A HIGH TORQUE DENSITY, DIRECT DRIVE IN-WHEEL MOTOR FOR ELECTRIC VEHICLES

Chukwuma Junior Ifedi

School of Electrical and Electronic Engineering

Newcastle University

A thesis submitted for the degree of

Doctor of Philosophy

June, 2013

Abstract

The use of in-wheel motors, often referred to as hub motors as a source of propulsion for pure electric or hybrid electric vehicles has recently received a lot of attention. Since the motor is housed in the limited space within the wheel rim it must have a high torque density and efficiency, whilst being able to survive the rigours of being in-wheel in terms of environmental cycling, ingress, shock, vibration and driver abuse.

Part of the work of this PhD involved an investigation into different slot and pole combinations in order determine a superior machine design, within given constraints based upon an existing in-wheel motor drive built by Protean Electric. Finite element analysis and optimisation have been applied in order to investigate the machine designs and achieve the optimum combination.

The main work of this PhD, presents a high torque dense machine employing a new method of construction, which improves the torque capability with a smaller diameter, compared to that of the existing Protean in-wheel drive system. The machine is designed with an open slot stator and using magnetic slot wedges to close the slots. Having an open slot stator design means the coils can be pre-pressed before being inserted onto the stator teeth, this improves the electrical loading of the machine as the fill factor in the slot is increased. The electromagnetic impact of the slot wedges on the machine design has been studied, also a method of coil pressing has been studied and the impact upon coil insulation integrity verified.

To ensure adequate levels of functional safety are met it is essential that failures do not lead to loss of control of the vehicle. Studies on a fault tolerant concept which can be applied to the design of in-wheel motors are presented. The study focuses on the ability to sustain an adequate level of performance following a failure, while achieving a high torque density. A series of failures have been simulated and compared with experimental tests conducted on a Protean motor.

Finally a prototype is constructed and tested to determine the true level of performance. The prototype is compared to a new motor built in-house by Protean and achieves an improved level of performance.

Acknowledgements

First and foremost I would like to thank my supervisor Prof. Barrie Mecrow for his guidance throughout the course of this research, he not only assisted in getting me a scholarship from the Power Electronic Drives and Machine group and provided me the opportunity to work with Protean Electric, he was also able to impart a lot of knowledge and critical thinking. I appreciate the input from my second supervisor Dr. Glynn Atkinson, who helped me during the early stages of building my finite element models and solving some problems I encountered during my work.

This work would not have been possible without support from Protean Electric, they provided me with sponsorship and the research idea, which became the outcome of this work. I would like to specially thank Simon Brockway, Gerry Boast, Chris Hilton, Dragica Kostic-Perovic, Al Fraser and Gunaratnam Sooriyakumar who provided me with the industrial supervision and help with undertaking the test on my prototype machine.

I thank Chris Manning for helping me with the mechanical aspect of my work such as coil winding and pressing, stator assembly and coil testing, just to mention a few. Also I will like to thank Jack Noble, Graham Ewart, Allan Wheatley, Luke Coates and Stuart Baker for when they had to step in and assist in some activities at the mechanical workshop.

I also will like to acknowledge Daniel Smith and Jamie Washington for how much I made their lives miserable, as they never turned me down every time I went to them with questions. Also to acknowledge Min Zhang, Christopher Spargo, Andrew Wechsler, Bassim Jassim, Alamoudi Yasser and Maher Algreer for the times we had discussions when trying to solve certain problems.

To save the best for last, I give huge thanks to my mother, brother and sisters for their support during my studies, and most especially my father, words are not profound enough to express how grateful I am for his financial support to see me through my educational life, my endeavours in life to date have been possible due to his presence.

Contents

List of figures

List of tables

Acronyms and symbols

EV	Electric vehicles
MMF	Magnetomotive force
SPP	Slot per pole per phase
EMF	Electromotive force
FE	Finite element
ICE	Internal combustion engine
LSV	Low speed vehicle
HEV	Hybrid electric vehicles
NEV	Neighbourhood electric vehicle
PM	Permanent magnet
RFM	Radial flux machine
SPM	Surface permanent magnet
IPM	Interior permanent magnet
AFM	Axial flux machines
IM	Induction machines
SRM	Switched reluctance machines
TFM	Transverse flux machines
CAN	Controller area network
MTBF	Mean time between failures
MTTF	Mean time to failure
BDV	Break down voltage
VB	Visual basics
2D	2 – dimensional
HCF	Highest common factor
PP	Pole pair
rms	Root mean square
C.S.A	Cross sectional area
SHC	specific heat capacity
SUV	Sport utility vehicles
NEDC	New European drive cycle
KPI	Key performance indicator

kp	Pitch factor
kd	distribution factor
kw	winding factor
m	harmonic number
n	coils per phase
α	pitch angle, angle of road inclination
δ	distribution angle
β	field weakening angle
X_d,X_q	d – and q – axis inductance
I_d,I_q	d – and q – axis current
V_d,V_q	d – and q – axis voltage
F_a	Acceleration force
K_m	Compensation factor
m_v	Vehicle mass
v_T	Velocity
F_{TR}	Traction force
F_{RL}	Road force
ρ	Density, resistivity
C_D	Drag coefficient
A	Frontal area
v_0	Head wind velocity
f	Tyre rolling resistance, frequency
g	Acceleration due to gravity
r,r_w	Radius
w_w	Wheel angular velocity
L	Inductance
Ψ	flux linkage
i,I	phase current
Φ	flux
N	number of turns
ω	electrical angular speed
R	Resistance
C	Capacitance
T	Torque
P	Power
N_{slot}	Number of slots
l_a	Axial length
A	Electric loading
B	Flux density
E	Electromotive force
H	Magnetic field strength
μ	permeability

l	width, thickness
d	Diameter
σ	Electrical conductivity
k	Thermal conductivity
z	Loss density
θ	temperature rise
J	Current density
K	Loss constant

Chapter 1

Introduction

1.1 Background

This project is an initiative between the Power Electronics, Drives and Machines research group at Newcastle University and Protean Electric; the project focuses on researching novel construction methods to further improve the torque capability of a high torque, low speed, fault tolerant permanent magnet machine, which is to be part of the Protean Electric in-wheel propulsion system, with the power electronic converter and drive motor as one compact packaged unit.

Protean Electric is a company that specialises on the development of advanced in-wheel electric drive systems for electric vehicles (EV) and recently showcased one of its in-wheel electric drive systems at the Auto-show; Auto Shanghai 2013. The electric drive system was fitted in a BRABUS hybrid vehicle, based on the Mercedes-Benz E-class, which is a hybrid system, jointly powered by an internal combustion engine and two of the Protean in-wheel electric drive motors, fitted into the two rear wheels.

Many companies and academic institutions today are focused on developing efficient, cost effective and modestly sized drive trains for EVs. Since the machine focused on in this work is to be applied as a direct drive in-wheel motor with no gearing, it is important that the correct machine topology is applied. The use of a permanent magnet machine as the drive motor has been the focus of most researchers, this is due to its inherent characteristic which include:

- A high torque density due to the use of the energy dense rare earth material.
- A relatively simple rotor structure and low rotor weight.
- A relatively low rotor heating.
- A high efficiency over its speed range.

These will be discussed further in the literature review, Chapter 2.

1.2 Electrical machine design study

The machine used to provide propulsion in the EV has to adhere to strict design constraints. This is because the energy source of the EV is the batteries, it is therefore important that the energy consumed by the machine when motoring is within a set design limit, so that the batteries can sustain the energy demand through the required drive range. The machine design has to deliver the torque required for traction, whilst maintaining a high level of efficiency over the expected speed range; the design of such a machine has to pay close attention to key aspects that can be detrimental to achieving the required performance level. These will now be outlined.

1.2.1 Machine losses

In order to achieve an efficient machine design, it is important to understand the components of the machine that contribute to the total loss. The sources of loss in a machine can be broken down into; copper loss from the current carrying conductors, iron loss in the lamination due to change of magnetisation flux at a given frequency, eddy current loss in the magnet, friction loss in the bearing and windage loss on the rotor surface. Depending on the machine technology applied, reducing these different losses can pose a difficult challenge, however they need to be reduced, else they can create large temperature rises in the machine and eventually lead to a failure in the machine. At low speed the machine is operated with its rated current, and copper loss is the dominant source of heat at this operating point, while at high speed the frequency of the magnetising flux increases and leads to an increased iron and windage loss. In permanent magnet motors, there is also a component of loss from the rotor magnet due to the spatial harmonics in the air-gap which leads to a drop in the magnet flux and in turn machine performance. There are other losses that should be considered in the machine, such as proximity loss due to the MMF enclosed by the winding, copper AC resistance loss and copper eddy current loss due to the magnet generated field.

1.2.2 Winding configuration

The winding configuration chosen is important to the machine design, it influences weight, torque density, air-gap harmonic distortion and speed range. Two basic types of winding choices exist for any machine; distributed and single tooth windings. Machines designed with distributed windings tend to exhibit better reluctance torque and near

sinusoidal varying induced voltage when compared to single tooth windings, however there is increase in copper loss and weight of machine with distributed windings [1]. The basic winding configuration can further be broken down into four groups [2-4]:

- Single layer, whereby each ends of a single coil occupies a full slot.
- Double layer, whereby the ends of two coils equally occupy a slot.
- Fractional slot, whereby the slot per pole per phase (SPP) is not an integer.
- Concentrated winding, whereby the coils of a phase are at one location.

The air-gap spatial harmonics can be attenuated by the layout of the winding, with the effect dependent upon the angle the windings of each phase span and their distribution. The factor that describes the span of the coil of a phase is termed pitch factor, a fully pitched coil is 180 electrical degrees and when the coil is short pitched, the angle between the start and return point of the coil is reduced by a given angle α, as shown in figure 1.1 (a). The distribution factor is the angle between two coils of one phase, this can be shown in figure 1.1 (b); C1, C2 and C3 are the coils that make up one phase. Equations 1.1 to 1.3 are used to calculate the winding factors of any type of machine; *kp* is the pitch factor, *kd* the distribution factor and *kw* the winding factor, *m* the harmonic number, α the pitch angle, δ the distribution angle and *n* the number of coils per phase.

$$kp_m = \cos\left(\frac{m\alpha}{2}\right) \tag{1.1}$$

$$kd_m = \frac{\sin\left(mn\delta/2\right)}{n\sin\left(m\delta/2\right)} \tag{1.2}$$

$$kw_m = kp_m \times kd_m \tag{1.3}$$

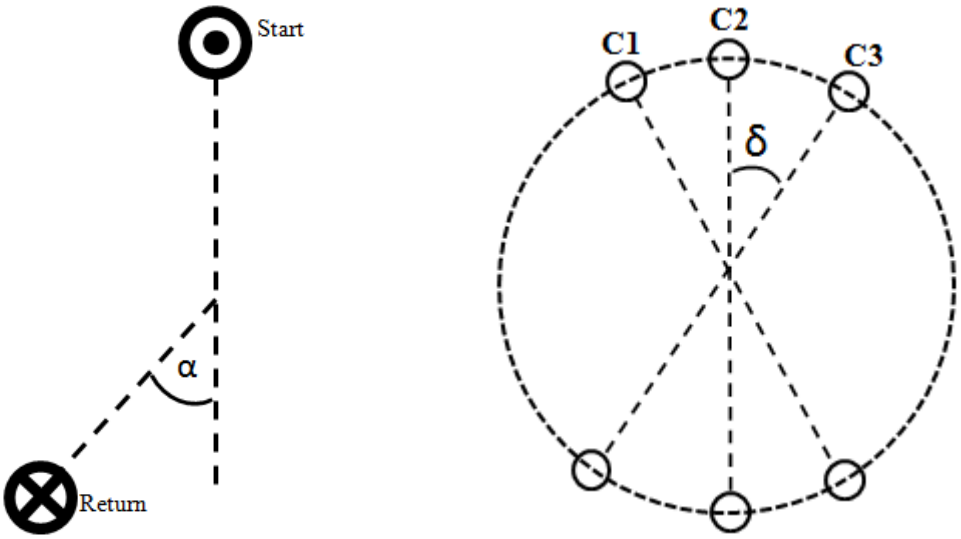

(a) (b)

Figure 1.1. Winding methods: (a) coil pitch, (b) coil distribution.

1.2.3 Machine field weakening

If the machine is to be used as a direct drive in-wheel motor the machine has to operate over the full speed range of the vehicle. When the machine speed is increased the back EMF in the machine increases in turn. At base speed the inverter voltage limit is reached, at this point to achieve a greater speed it is necessary to reduce the back EMF by reducing the field flux in the machine. Due to the fixed field flux from the magnets it is difficult to limit the field flux at speeds above base speed. The field weakening method is a way of extending the speed of the PM machine above the base speed, this method has been presented in previous works [5-7]. The method applies a component of the armature reaction flux in the negative d-axis that opposes the field flux from the magnets, this reduces the back EMF and allows the converter to push torque producing current into the machine above base speed. The field weakening capability of the permanent magnet motor is determined by the d-axis inductance and supply current [5], figure 1.2 shows a phasor diagram of a permanent magnet machine in its d and q-axis plane for a single phase; as seen from the phasor there exists an armature reaction component that opposes the magnet flux – X_dI_d. The set of equations derived from this phasor diagram in order to calculate the optimum field weakening angle – β between the supply current and back EMF is given from 1.4 – 1.6.

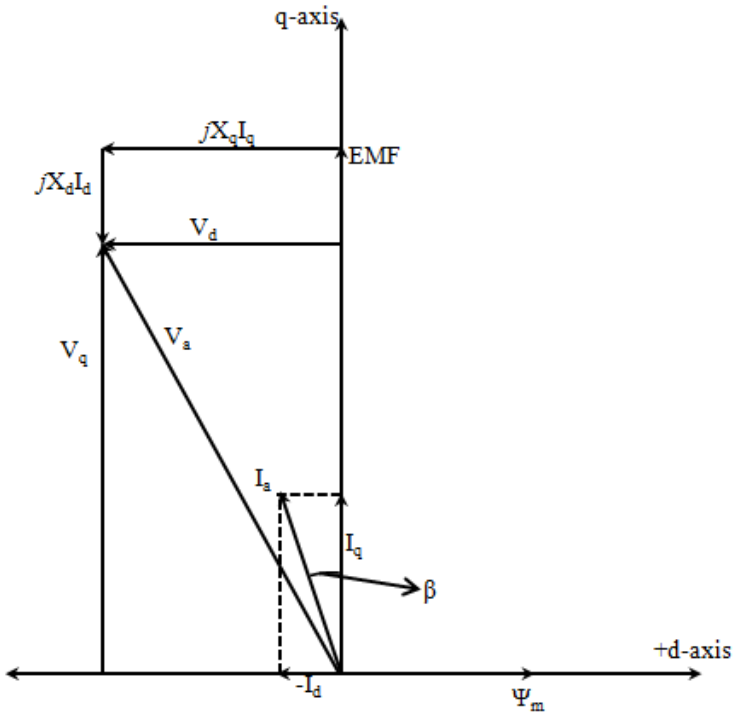

Figure 1.2. Machine phasor diagram.

$$V_a^2 = V_q^2 + V_d^2 \tag{1.4}$$

$$V_q = EMF - X_d I_d, \quad V_d = -X_q I_q, \quad I_q = I_a \cos\beta, \; I_d = I_a \sin\beta$$

$$V_a^2 = \left(EMF - X_d I_a \sin\beta\right)^2 + \left(-X_q I_a \cos\beta\right)^2 \tag{1.5}$$

Equation 1.5 can be solved at any operating point on the machine's torque – speed curve to determine the optimum field weakening angle – β.

1.2.4 Cooling methods

The method applied for cooling of a machine is vital to the machine performance, because the level of loading applied to the machine can be extended by improving the cooling system. The cooling method chosen is dependent upon the losses generated in the machine and the expected level of performance. The machine can either be cooled naturally or forced cooled. Forced cooling can be broken down into the following:

- Blown air, whereby air is blown over the outer surface of the by a fan.
- Wet cooling, whereby the machine component is flooded by a coolant.
- Water jacket.
- Spray cooling.

The housing of the machine can be optimised to improve heat removal by designing the outer surface to have fins in order to increase the surface area over which air is blown.

1.4 Methodology

The work to be carried out in this thesis concerns the electromagnetic design of a high torque dense machine for a low speed, fault tolerant application. In order to achieve the design and validate the model results, the following steps are followed:

- Carry out a review of available machine technologies in the market suitable for application as a high torque low speed machine.
- Carry out a design review and analysis of an existing Protean machine, to determine whether the performance can be improved for the given space limitation, also carry out a fault tolerant review of the Protean machine.
- Design modification of the existing Protean machine to improve performance for a reduced machine radius; this was achieved by carrying out an electromagnetic evaluation of different structural design variations and a thermal evaluation of the cooling method. The software tools used are Infolytica Magnet™ for FE electromagnetic evaluation, Infolytica OptiNet for FE electromagnetic optimisation, Infolytica ThermNet for FE thermal analysis and MotorCAD for analytical thermal analysis.
- Construction and testing of a prototype to validate the model results; the construction involved exploring a method of winding production to improve fill factor and full scale testing at various operating conditions
- Comparison of performance of the prototype machine to an existing Protean machine, having similar structure and back EMF constant.

1.5 Thesis overview

This thesis has been put together to present work done on the design and construction of a direct drive in-wheel motor. The thesis includes nine chapters, with chapters one and nine introduction and conclusion respectively. The thesis structure is as follows:

Chapter 2, which is a review chapter, looks at the advent of the EV, various projects carried out by industry to develop the EV, drive train topologies, issues associated with the use of in-wheel machine and selection and sizing of suitable drive machines for EVs.

Chapter 3 presents a design review and critique of a Protean in-wheel motor based on its electromagnetic performance and fault tolerance ability, also the fault tolerant design of a permanent magnet motor is reviewed by presenting relevant literatures.

Chapters 4 and 5 present the novel method of construction chosen for the new permanent magnet machine with improved performance, for a smaller wheel size. The design of the slot wedge and coil crushing of the stator windings are discussed.

Chapter 6 focuses on the electromagnetic design of the machine, having a slot wedge and crushed coils inserted on the stator tooth. The effect of having increased pole number is discussed and components of the machine that contribute to the loss in the machine are studied.

Chapter 7 presents work on the thermal analysis of the machine and the effect of temperature on the torque output of a machine when the pole and slot combinations are changed.

Chapter 8 presents test results of the machine designed with slot wedges, and also comparisons with an existing machine designed and constructed by Protean Electric.

Chapter 2

Electric Vehicles and their Associated Drive Train Design

In this chapter an up-to-date survey of the current state of the (EV) is presented, the benefits and the challenges associated with the EV and its contribution to the inner city environmental condition is discussed. The requirements the EV poses on motor design and the different motor design concepts used in the drive train are considered. The aim of this thesis is to present work done on an in-wheel motor design concept, so the survey will focus more on introducing the motor designs developed for the EV in-wheel application.

2.1 Background

The dependence on fossil fuel as a source of energy is ever growing in our world today. This is partly due to the extensive demand for more use of automobiles in developing countries around the world, such as China and India. In 2008 the number of passenger cars around the world was in the region of 850 million and growing, there is expected to be a 2.6 percent rise per annum in the number of passenger car ownership around the world [8]. With this high number of passenger cars, it was recorded in 2008 that the transport sector accounted for 55 percent of total oil consumption and is projected to be 88 percent of oil demand increase within the period of 2008 – 2035, where road is clearly the single most important system in the transport sector for oil usage [8]. This raises concerns associated with the environmental pollution within inner cities and as a result different countries have taken measures to put in place policies on environmental protection and conservation of energy. This can only mean an accelerated pace in the quest and enhancement of alternative energy as a source of propulsion for automobiles.

In recent years major researches in the automobile sector are focused in the advancement of electrical energy as the main source of propulsion for vehicles, hence the most talked about EV. The EV has its advantages over the conventional internal combustion engine (ICE) vehicles such as: more efficient source of propulsion and energy transfer, ability to capture braking energy and less pollution within cities. However it has its challenges, such as a shorter range compared to ICE vehicles and high initial cost due to the market price of the batteries, power electronics and the permanent magnets. It is a known fact that only 12-20 percent of the fuel fed into the input of an ICE in one cycle is available at the wheel as useful work, due to high transmission losses [9], but in the EV 75 percent or more of the energy from the battery is available at the wheel as useful work [10]. With all these in mind it is imperative for researchers to come up with an improved battery system and most importantly ensure the careful selection and design of motors with its associated drive train, so as to improve the drive range and cost problems.

It is often said that more power will need to be generated in the national grid to charge the EV, however this is not entirely true as there may be no need to increase the generating capacity from the power station. Load levelling can be used on the national grid, in which EVs are used during the day and plugged into the grid to charge at night during the off-peak periods [10].

2.2 Electric vehicles, past and present

The electric motor came into existence before the internal combustion engine, which means electric vehicles were around before ICE vehicles, however they started to decline during the oil boom when cheap gasoline was readily available [10]. The first battery powered electric vehicle was built in 1834 by Thomas Davenport, in 1838 Robert Davidson built the first battery powered locomotive and in the late 1800s and early 1900s electric vehicles started being manufactured in volumes [10]. A lot of electric vehicles were designed during that era by individuals and car companies and a good history of the various electric vehicles designed can be found in [11].

The prevailing challenge faced by the EV has always been the battery, as the drive range of the EV is limited by its capacity. However there has been tremendous improvement in the motor design and electronic controllers since the start of the electric vehicle in the 1800s. As electric vehicles couldn't compete with the ICE vehicles due to a limited drive range, they had to be employed more in low speed vehicles (LSVs) or neighbourhood electric vehicles (NEVs) for use within inner cities, battery-powered forklifts and golf carts [10] etc.

In the last decade more focus has been put into the research and development of electric vehicles, since the drive for a cleaner source of energy as a means of propulsion was revived. The challenges most researchers face since reinitiating the design and manufacture of electric vehicles have been on improving the drive range and speed of the electric vehicle. Figure 2.1 shows the different projects in electric vehicles by major vehicle manufacturers, from the early 1960s through to the early 1990s.

The 21st century has seen a huge development in electric vehicle manufacture, as improvement in power electronics and advancement of lithium-ion batteries came to play a major role in the development of electric vehicles. Most vehicle manufacturers have come up with electric vehicles: some of these vehicles are already in production and distributed for consumer use, whilst others are still concept vehicles for the future. A few of the electric vehicles currently present in the vehicle sector are mentioned below;

- the Chevrolet Volt, a plug-in hybrid vehicle manufactured by General Motors, which is marketed as the Opel Ampera in Europe, Vauxhall Ampera in the UK and Holden Volt in Australia and New Zealand. The concept of the hybrid vehicle was to have a gasoline engine driving a generator as a backup to improve drive range,

while the only mechanical connections to the wheels were from the electric motor [10]

- the Tesla Roadster is a pure battery power electric vehicle. It is designed as 2-door sports car by an electric car firm called Tesla Motors. The roadster has a range of 220miles per charge and is the first road battery electric vehicle to achieve such a range. However the cost of purchasing a roadster is high, which would lead to a low consumer demand for the vehicle [10]
- the Toyota Prius is a hybrid electric vehicle. It first went on sale in Japan in 1997 and then worldwide in 2000. It was the first mass-produced electric vehicle and has gone through a lot of development to improve the design. The Prius v and Prius c are new and improved version that are available in the market now [10]

The Nissan Leaf electric vehicle is already available to the market in few countries and still undergoing development for future upgrades. The Mitsubishi iMiEV Sport, Ford Focus Electric, Volvo (C30 and V60) and Renault (Fluence ZE and ZOE) are also electric vehicles which are still being developed to be released in the future. The Hybrid electric vehicle using gasoline is not the final solution for a cleaner energy as a source for vehicle propulsion, but will help to realise a future of pure electric vehicles because most of the drive components will have been properly developed.

2.3 Overview and topologies for EV drive train

There are different topologies established today to achieve electric traction in vehicles, different drive methods and sequences have been researched to make the drive train of the electric vehicle more efficient, in an attempt to improve its range. The different topologies range from hybrid electric vehicles (HEV) to pure electric vehicles; [12-14] presents a few electric motors designed for electric vehicles. The HEV is scarcely mentioned in this thesis, as the main focus of this work is the pure electric vehicle.

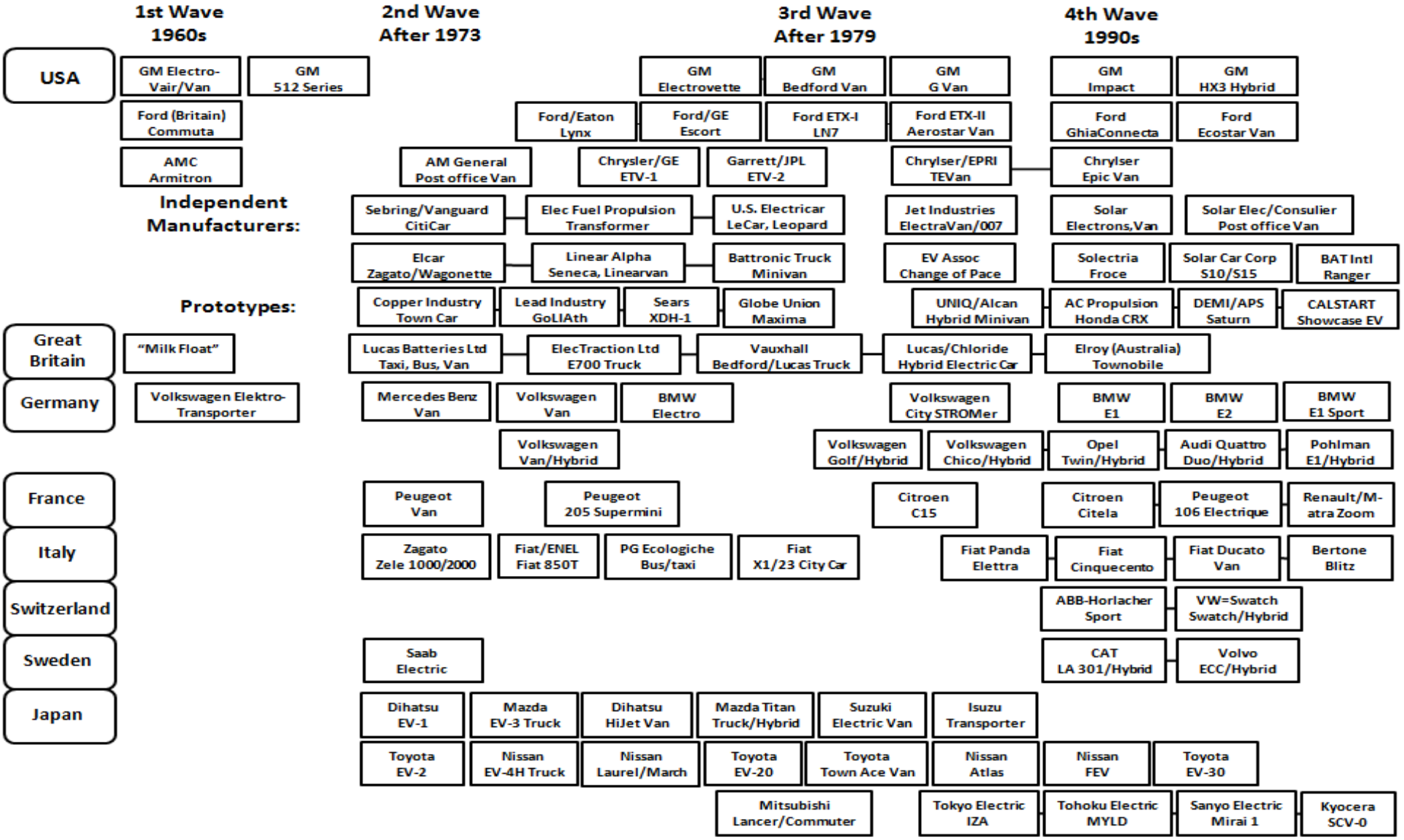

Figure 2.1. Electric vehicle projects by major manufacturers, from the early 1960s through to the early 1990s [10].

2.3.1 Hybrid electric vehicles

HEVs are vehicles that use different energy sources to achieve vehicle traction. They generally combine an electric motor and an internal combustion engine in such a way to maximize the strength of each at different points of the vehicles drive cycle. The power sources can be connected in different topologies as shown in figure 2.2 and the power trains work as follows [15];

- series hybrid, where the ICE is used to charge the batteries for the electric motor or power the electric motor directly and the electric motor is connected to the wheels
- parallel hybrid, where the ICE and electric motor are connected directly to the wheels of the vehicle in parallel and they are each sized for half of the drive power
- series/parallel hybrid, where the series and parallel hybrid are combined to achieve the advantages of both configurations. This has been found to be the most efficient method as it smartly switches between the ICE and electric motor to give the best and most efficient traction for the vehicle

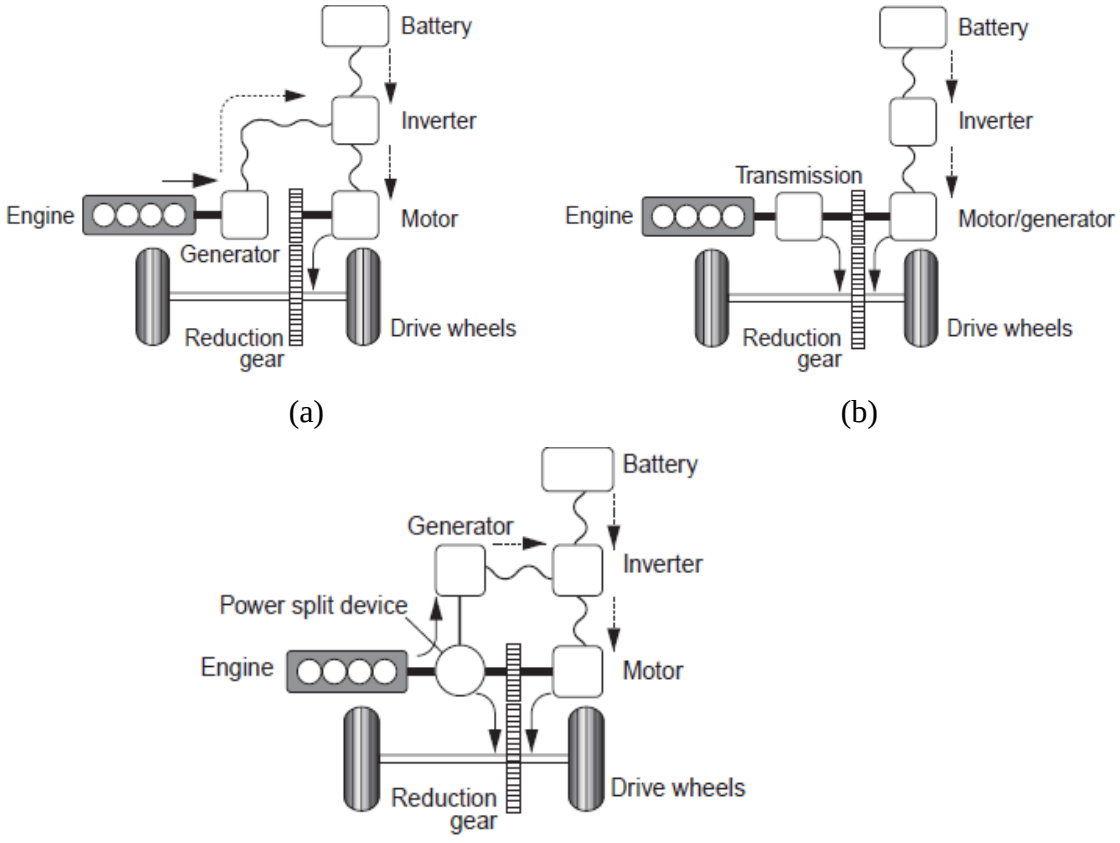

Figure 2.2. Power flow of hybrid electric vehicle drive train; (a) series hybrid, (b) parallel hybrid, (c) series/parallel hybrid [15].

2.3.2 Pure electric vehicles

Pure electric vehicles are designed with only one power source, which is electrical energy from a bank of batteries used to energise the electric motor(s) via a power electronic control system, for propulsion of the vehicle. There are different topologies for the pure EV, which can be grouped into two basic categories; an onboard motor connected to the wheel of the vehicle via a shaft and differentials, or an in wheel motor connected directly to the wheel(s) of the vehicle. Figure 2.3 shows simple layouts of the various topologies that can be found in the pure electric vehicle.

- in figure 2.3 (a), the topology shown is that employed during the early stage of EV design. At this early stage ICE vehicles had to be converted to EV, basically by replacing the combustion engine with an electric motor. The gearing system for this topology can come in two types; it can be designed as a fixed ratio type, or designed in the conventional way whereby the driver can shift the gear ratio using a clutch. The fixed gearing option cannot be used for ICE vehicles as it cannot achieve the required torque-speed curve of the vehicle. The advantage of the fixed gearing compared to the gearbox and clutch system is the number and weight of the mechanical parts are greatly reduced [16, 17]
- figure 2.3 (b) shows a topology which is commonly adopted by modern EVs and has a similar concept to the engine design of most ICE vehicles, where the vehicle has a front-engine in a transverse direction to the front wheels, commonly called a front-wheel drive [16, 17]. The electric motor and fixed gearing are coupled together as an assembly. There are two types to this drive configuration; a complex motor design (having two separately driven rotating parts) can be adopted, where the electric motor acts as a source of propulsion and speed differential to the wheels. Or by adopting a simple motor design and incorporating a mechanical differential to the drive assembly. This is obviously a trade off between complex motor design and assembly drive size and weight
- figure 2.3 (c) and (d) shows a unique topology where the drive train of the vehicle can be mounted in the wheel, which drastically reduces the mechanical transmission parts to the wheel. These topologies are known as the in-wheel or hub motor designs and wheel-speed differential is achieved electronically as the wheels are driven by separate motors. The motors can either be designed as a low torque – high speed motor, in which a fixed planetary gear is needed to step down the motor speed, or a high torque – low speed motor in which the motor is designed to have an outer rotor.

The fixed gearing used here is the planetary gear, which is favoured due to its advantage of high speed reduction ratio and an inline arrangement of input and output shafts [16, 17]

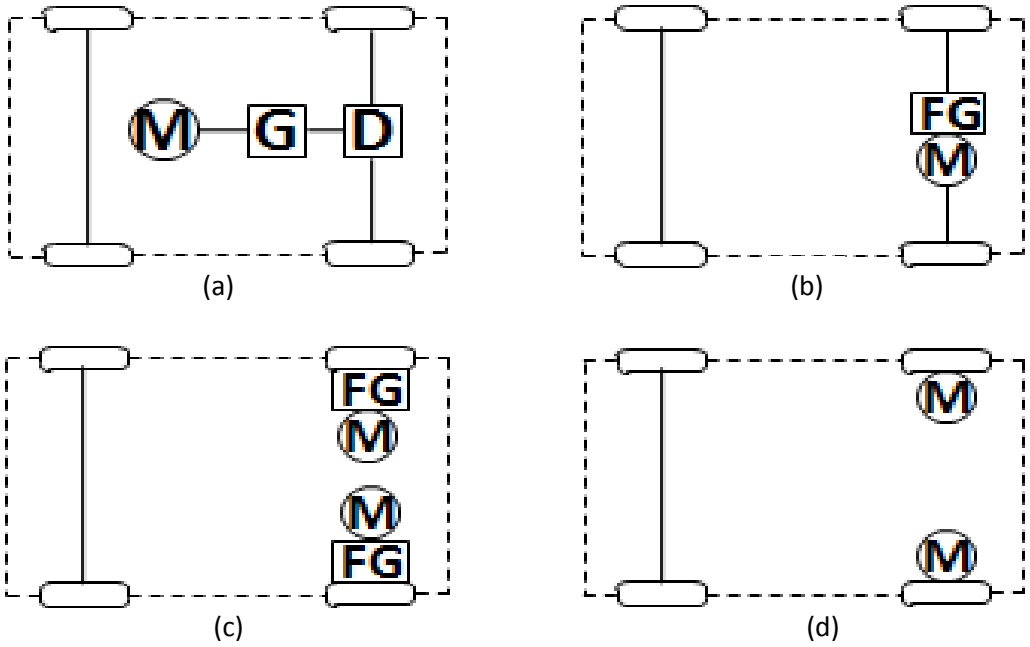

Figure 2.3. Pure electric vehicle drive train topologies; (a) motor, gear and differential, (b) fixed gear and motor, (c) in-wheel fixed gear and motor, (d) in-wheel motor [16].

2.3.3 In-wheel electric vehicles

The option of mounting the drive train of the EV in the wheel of the vehicle [18-25], ensuring that all of the motor's output power is available at the wheel without any mechanical transmission losses, is foreseen to be a very good choice for vehicle traction: figure 2.4 shows a complete assembly of the Protean In-wheel motor, integrated with its drive electronics. This is an interesting topology for the EV, which is receiving a lot of attention by researchers and industry: in-wheel motors designed for the EV are discussed in [26-33] as potential motor designs. Motors designed for this arrangement have to meet rigorous demands, with space limitations and driving environment forming key factors. There are significant advantages with adopting such a drive train topology, such as;

- releasing vehicle space for passengers, traction batteries etc
- the torque at each wheel can be independently controlled, giving true 4 wheel drive
- true wheel-slip based control allows improved vehicle response and shorter braking distances

- removal of drive train components gives vehicle designers greater freedom to design vibration free, more comfortable vehicles
- elimination of gears and differentials produces a simpler and more reliable overall mechanical design

Problems often perceived with in-wheel motors are related to ride and handling, due to an increase in the vehicle un-sprung mass, and safety issues when a motor fault occurs, developing a dangerous torque disturbance. More on the un-sprung mass will be discussed later in this chapter.

Figure 2.4. Protean Electric in-wheel motor assembly.

2.4 Designing an electric motor for EV

The design requirement for electric motors used in an electric vehicle application depends on the chosen drive train topology and the desired motor operating region. The work presented in this thesis focuses on the application of electric motors as an in-wheel direct drive for an electric vehicle. The following are typical requirements for selection and design of such drive motor [34-36];

- high instantaneous torque and continuous torque density
- high torque at low speed for starting and climbing
- fast torque response for use in braking (ABS)
- low cogging torque and torque harmonics for refined drivability

- high efficiency over constant torque and power range
- high fault tolerance
- good overload capability for uphill climbing

2.4.1 Vehicle and road load equations

In order to determine the ratings of the motor, it is important to analyse the forces that act upon a vehicle [10, 37]. This gives an idea of the vehicle performance and what level of traction is required at the wheels. The motor has to be rated to overcome the vehicle weight, aerodynamic forces on the vehicle and rolling resistance and gradient force from the road surface.

2.4.1.1 Vehicle weight

The utmost important factor in designing the EV is to keep the vehicle weight as low as possible. The battery pack in the EV contributes hugely to the weight of the vehicle, which has paved the way for further research into the material used for the vehicle body construction. The aim is to reduce the weight contribution from the vehicle body, so as to compensate for the weight gained from the battery pack. Newton's second law of motion is applied to determine the force (F_a) required to increase the speed of a given vehicle weight over a given time;

$$F_a = k_m m_v \frac{dv_T}{dt} \tag{2.1}$$

$$F_a = F_{TR} - F_{RL} \tag{2.2}$$

k_m is a compensation factor to account for the added inertia of the rotating components in the vehicle and is typically between 1.08 and 1.1 [37], m_v is the mass of the vehicle and $\frac{dv_T}{dt}$ is the vehicle acceleration. F_a at constant speed is always zero and F_{TR} is the traction force that has to be provided by the propulsion system (electric motor).

F_{RL} is the road force that has to be overcome by the traction force to keep the vehicle at the desired speed and it can be derived from the summation of the aerodynamic drag force, rolling resistance and gradient force.

2.4.1.2 Aerodynamic drag force

The aerodynamic drag force is the viscous resistance of the air acting against the motion of the vehicle. The equation for the drag force can be calculated as follows;

$$F_{AD} = \tfrac{1}{2}\rho(v_T + v_0)^2 C_D A \quad (2.3)$$

C_D is the coefficient of drag of the vehicle determined by empirical methods, typically between 0.2 and 0.4 [36, 37], A is the frontal area of the vehicle, ρ is the air density in kg/m^3 and v_0 is the velocity of the head-wind.

2.4.1.3 Rolling resistance force

At low speed, the rolling resistance force (due to the tire inflation and its contact with the road surface) is the major opposing force that has to be overcome when moving on a level ground. The equation for the rolling resistance force is given in (2.4) below;

$$F_{roll} = f \times m_v \times g \quad (2.4)$$

where f is the tyre rolling resistance coefficient, which increases with the vehicle speed and the tyre angle during cornering, m_v is the vehicle mass and g is the constant of acceleration due to gravity. The rolling resistance coefficient is 0.015 for concrete, 0.08 for a medium hard surface and 0.3 for sand [10].

2.4.1.4 Gradient force

The gradient or climbing force is the force to overcome for uphill climbing of the vehicle. The force is positive when climbing up a hill and negative when driving down a hill. The equation for this force is given as follows;

$$F_g = m_v \times g \times \sin\alpha \quad (2.5)$$

The angle α is the angle of inclination of the road.

The torque that has to be produced at the wheel by the motor can be derived by the equation below (2.6), where r_w is the wheel radius and w_w is the angular velocity [37];

$$T_{motor} = F_{TR} \times r_w \quad (2.6)$$

$$Power = T_{motor} \times w_w = F_{TR} \times v_T \quad (2.7)$$

2.4.2 Electric motor

The electric motor is the heart of the EV and when used as an in-wheel direct drive motor, must be able to produce the torque (T_{motor}) and power demanded by the vehicle, which can be derived from the equations above (2.6 & 2.7).

To illustrate employing a permanent magnet machine, the mechanism for torque generation in a machine can be explained from the stand point of the air-gap electromagnetic forces. Two separate sources within the machine must create flux; the armature reaction flux that creates a rotating magnetic field in the air-gap, due to the time changing current in the stator winding (figure 2.5 – a, showing peak current applied to phase A) and the permanent magnet materials attached to the rotor that creates a fixed field system which changes with rotor position. The flux of this fixed field system links the winding of the stator to create an electromagnetic force – EMF (figure 2.5 – b, showing position of maximum EMF in phase A). As the fixed field from the rotor magnets and the stator armature reaction flux interact, a net resultant flux is created in the air-gap and it is the skewing of this net resultant flux (flux creating a tangential stress on the rotor surface) that generates torque in the machine. This skewing effect is at a maximum at the point where the armature reaction flux and field flux are at 90˚ to each other. Finally the machine can act as a motor or generator depending on the rotor position relative to the net resultant flux in the air-gap. If the rotor position is behind the net resultant flux the machine will act as a motor (figure 2.6 – a) and vice versa if the rotor position is ahead of this net resultant flux the machine will act as a generator (figure 2.6 – b).

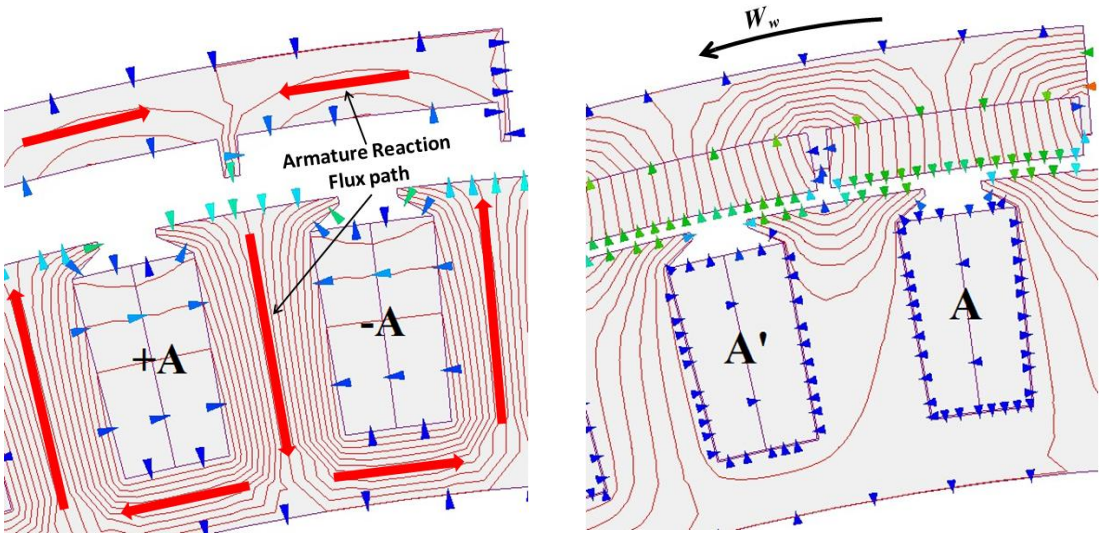

(a) (b)

Figure 2.5. Machine flux contour plot; (a) phase A armature reaction flux, (b) no-load magnet flux linkage.

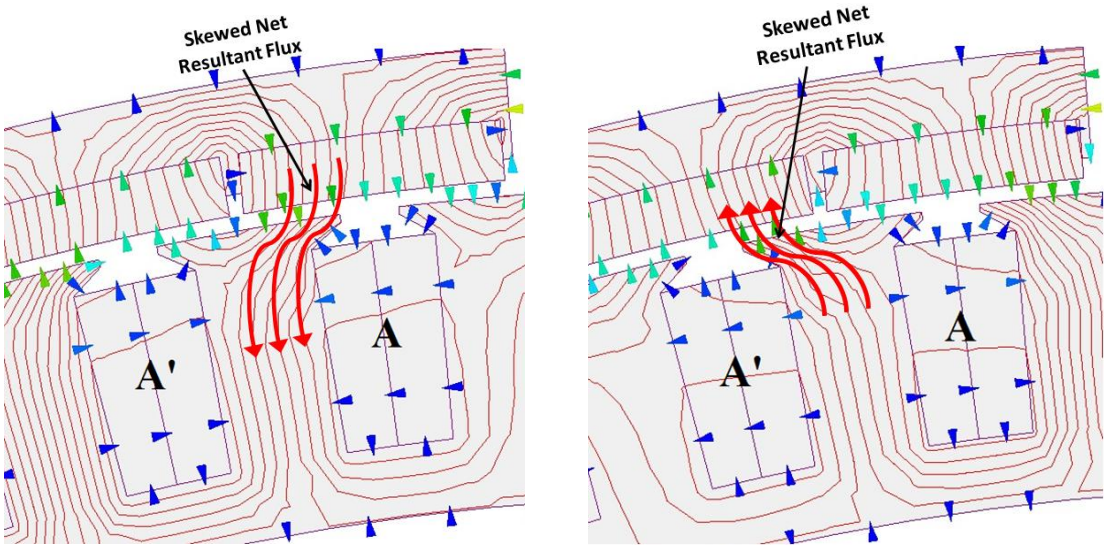

(a) (b)

Figure 2.6. Loaded machine flux contour plot; (a) motoring mode, (b) generating mode.

There are two methods to designing a high power density and high efficiency motor for use in this type of EV application; a high torque low speed motor or a low torque high speed motor with a reduction gear.

One of the driving factors behind the in-wheel application for the EV is to reduce the drive components and mechanical losses, so this work focuses on the high torque, low speed motor design [20, 38-42]. The motor has to operate efficiently and have high torque density: objectives which are difficult to simultaneously meet. With no gearing, the size and weight of the motor is larger than a geared motor (excluding the gear), as the motor has to generate the full wheel torque at low speed as required for acceleration from rest and uphill climbing. However with a careful motor design the size and weight can be minimised.

One way to minimise the weight of the motor is to have a high number of poles, resulting in very shallow core backs. Choosing an outer rotor design for the motor maximises the air-gap diameter and thereby minimises the shear force required at the air-gap for a given torque, which creates a "ring" type structure, opening up space in the centre of the ring for mechanical brakes and inclusion of power electronic models, figure 2.7 shows a general structure (Protean in-wheel motor structure). By employing concentrated, single tooth windings, with a fractional number of slot/pole/phase and optimal slot and pole number combination, the torque density can be maximised, with high slot fill factors and short end-windings, and also reduced copper loss [2, 3, 43-48].

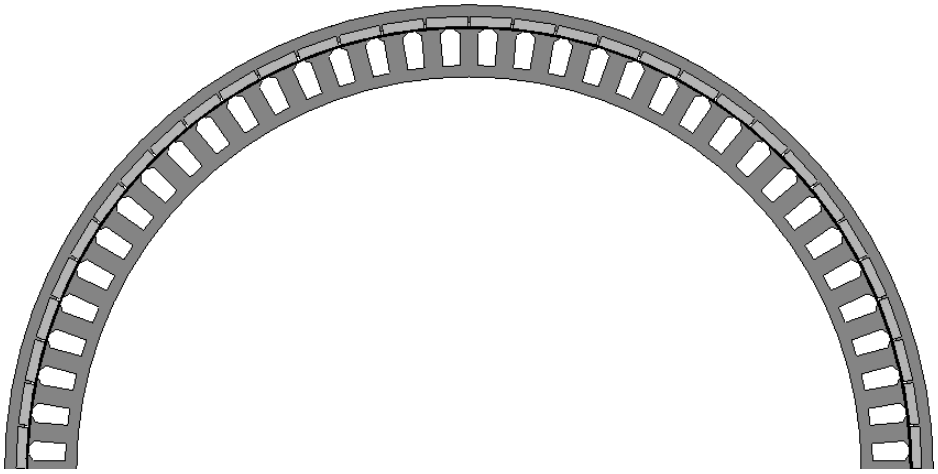

Figure 2.7. Ring type structure of outer rotor permanent magnet machine.

2.5 Survey of motor types suitable for EV

The choice of motor type used for the EV application usually depends on the cost, efficiency and operating region in the torque-speed curve for which the motor will be designed to operate. As shown in figure 2.8, there are two main regions in the torque speed curve of a machine; the constant torque region, where the machine operates at its rated torque (determined by the inverter current) until the base speed that is fixed by the inverter supply voltage, and the constant power region, where the machine is at its rated power and flux weakening or phase advance is applied to extend the machine speed. This region also depends on the machine's phase inductance. Finally there is a third region, where the machine reaches a critical speed (also known as the maximum speed), then starts to lose its rated power and the torque decreases proportionally with the square of speed at this region [35, 36].

The induction motor and permanent magnet motor are the common types of motor used in the EV in the market today, due to their inherent advantages and advancements in the technology behind their efficient operation. The DC motor was used during the early start of the EV and is not a favourable choice of motor type these days, due to its operational limitation. There are other types of motor that are proposed to be used in the EV application: switched reluctance motor, transverse flux motor and synchronous reluctance motor.

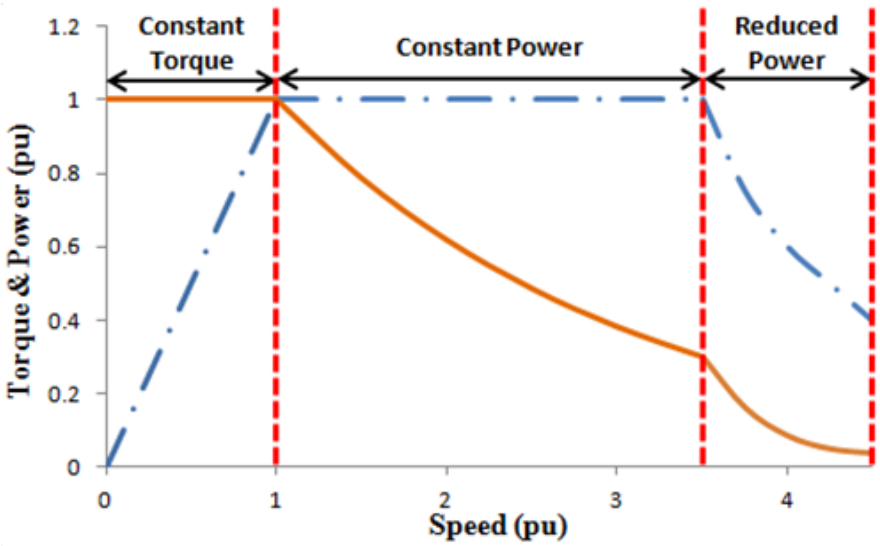

Figure 2.8. Ideal torque speed curve for a permanent magnet synchronous machine [35].

2.5.1 Permanent magnet machine

The permanent magnet (PM) brushless machine is a strong candidate for the EV application today. The torque density is very high, because of its simple and light weight rotor structure. Also the efficiency of the machine is very high compared to other machine types, when operating in the constant torque region. The PM machine is generally split into two types; the sinusoidal back EMF, also known as PM AC machine drive and the trapezoidal back EMF, also known as the brushless DC machine drives. Ideally it is desirable to apply a sine wave current to the sinusoidal back EMF machine and a square wave current to the trapezoidal back EMF machine, in order to maximize the torque density and efficiency and minimize the torque pulsation of the machine. Figure 2.9 shows a schematic of the PM machine and its drive.

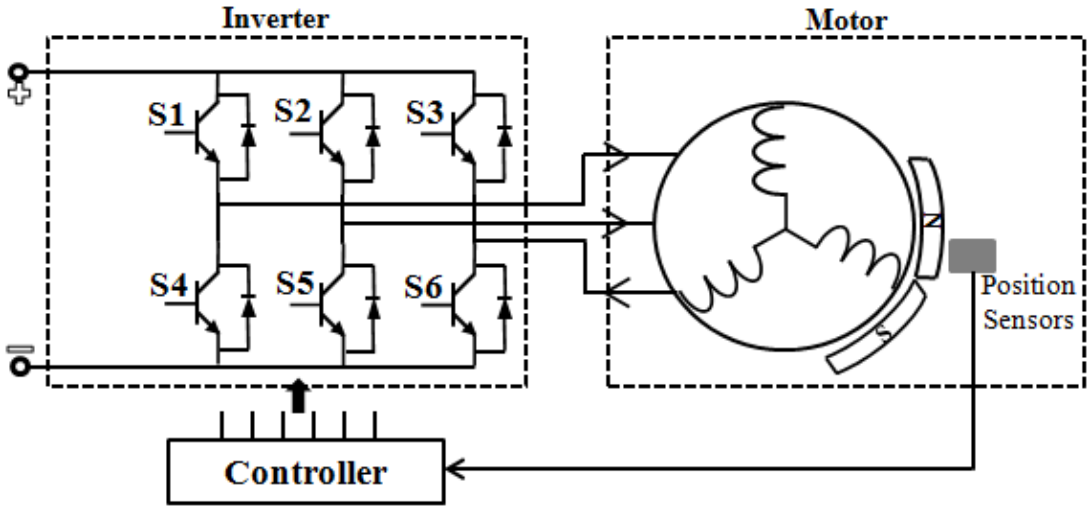

Figure 2.9. Permanent magnet machine and drive schematic [35].

The permanent magnet machine naturally has a short constant-power region due to the fixed field from the rotor magnets, which causes the machine back EMF to exceed the supply voltage as the speed increases past its base speed. However with the method of field weakening, the constant-power region can be extended by changing the current angle so as to create a negative d-axis current, which in turn creates a demagnetising component in the armature reaction air-gap field that opposes and weakens the magnet field as the speed rises. It is also worth mentioning that there is a limit to the negative d-axis current that can be applied at a given magnet temperature, so as to avoid irreversible demagnetisation of the magnets.

2.5.1.1 Radial flux machine

The radial flux machine – RFM [35, 49-52] is the most common topology of permanent magnet machine that is used today. There are different topologies that exist for the rotor design, depending on the magnet location. The magnets can either be on the surface of the rotor, inserted or buried in the rotor. The surface permanent magnet (SPM) machine is the most common topology used in machine designs. When an inner rotor design is used at high speed a retaining sleeve is used to prevent the magnets coming off the rotor. The SPM machine inherently has a low phase inductance, because the effective air-gap is a combination of the design air-gap and magnet depth. Also the d- and q-axis inductances of the machine are the same, which means the SPM machine doesn't have the advantage of utilising the reluctance torque created due to the difference between the d- and q-axis inductances. However with proper design of the synchronous reactance slot the phase inductance can be increased, also the construction of the SPM motor is simple, figure 2.10 (a) is a drawing of the SPM structure. The inset and buried permanent magnet (also called interior permanent magnet – IPM) machines are known to be a hybrid machine topology, as it combines both the magnetic and reluctance torque, which means the magnet mass can be reduced for the same power output of the SPM, however the electromagnetic loss in the rotor of the IPM machine can be significant. To fully utilise the reluctance torque distributed windings are generally preferred, due to distributed winding machines having lower leakage inductance than single tooth winding machines because flux does not easily fringe from one stator pole to another, leading to an increase in power factor, however there is a trade-off with weight and copper loss in the machine [53]. Most of the advantages of the IPM machine make the motor suitable for high speed operation in the constant power region. Figure 2.10 (b), (c) and (d) shows the general structure of the IPM.

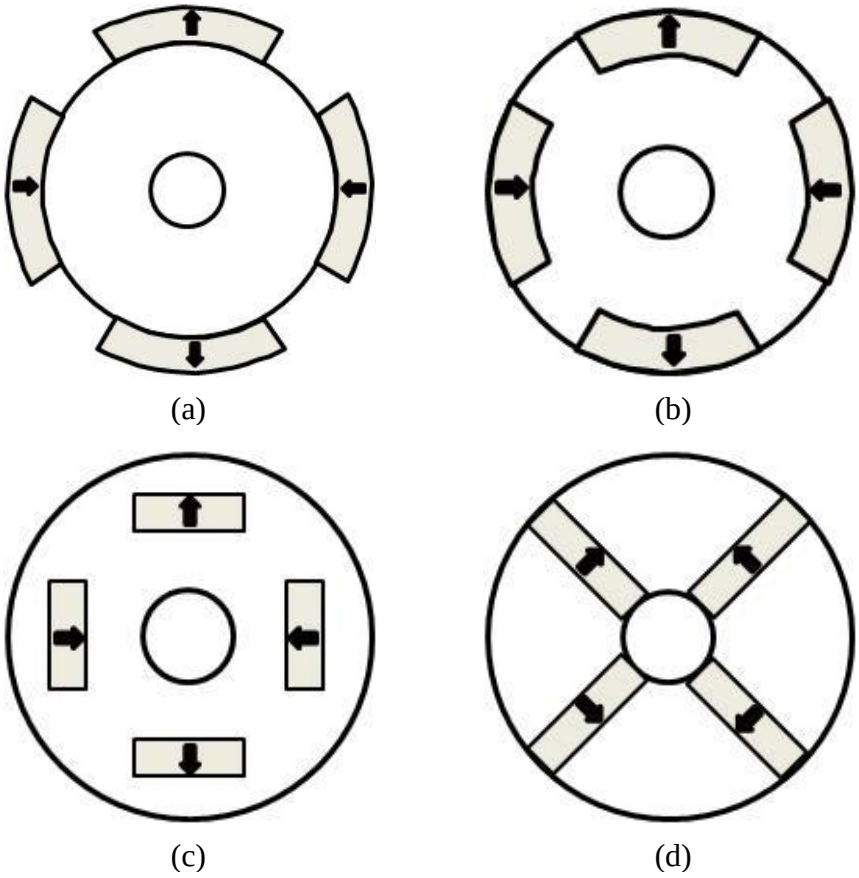

Figure 2.10. Radial flux machine topologies; (a) surface permanent magnet, (b), (c) and (d) interior permanent magnet [35].

2.5.1.2 Axial flux machines

The axial flux machine – AFM [54-56] has a "sandwich-like" arrangement, in which the air-gap flux travels in the axial direction, figure 2.11 shows an axial flux modulated machine. This machine is very suitable for application where there is limited axial space, where the "sandwich" shape is very advantageous. There are different topologies for this type of machine; a single-sided stator and a rotor, two stators and a single rotor and two rotors and a single stator. Manufacture of the AFM with slotted stators is difficult and inherently large axial forces exist between the stator and rotor.

2.5.1.3 Transverse flux machines

The transverse flux machine – TFM [57-59] is a type of machine that has its flux travelling in a 3-dimensional path around the machine parts, as described in [59], figure 2.12 is a transverse flux machine showing its flux path.

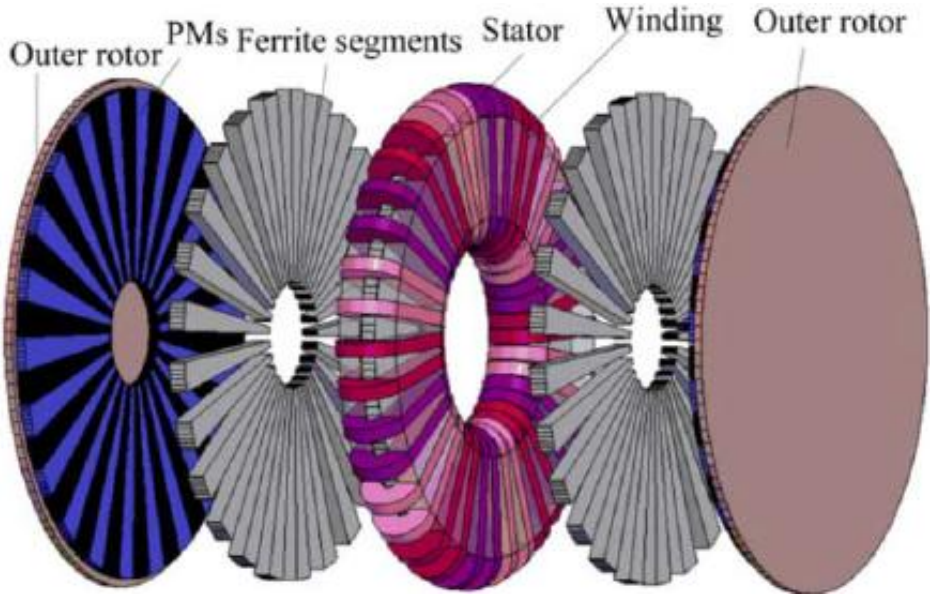

Figure 2.11. A novel Axial flux modulated motor [60].

They are usually designed for a high number of poles and due to the structure of the machine, the poles interact with the total armature reaction flux created. This increases the electrical loading, leading to very high torque density. TFMs are most suited for low speed applications where high torque is required. In [61-63] the TFM, AFM and RFM have all been compared in terms of performance. TFM machines generally have poor power factor, which means the VA rating of the inverter is overrated: the high pole number results in high electrical frequency, imposing restrictions on high speed operations.

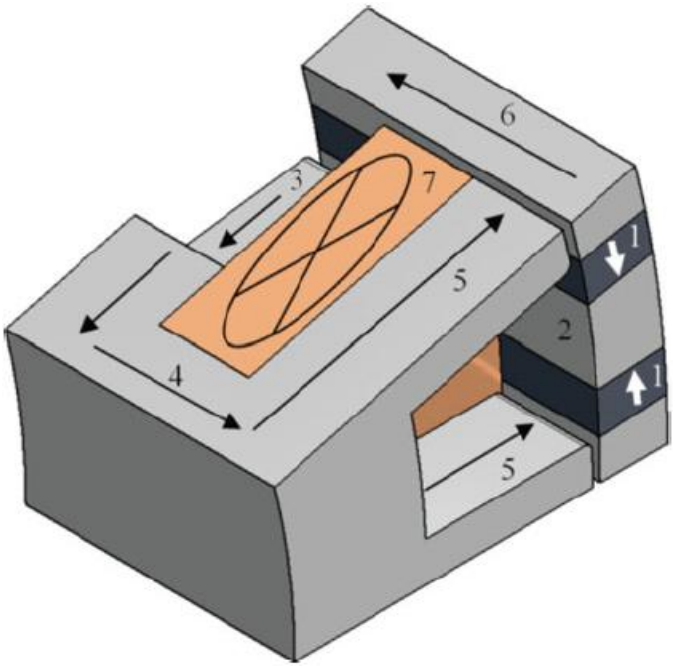

Figure 2.12. A cut-out section of a transverse flux machine [59].

2.5.1.4 Flux switching machines

This machine is typically grouped under the family of RFM, however its design principles can be applied to any type of permanent magnet machine mentioned above, putting it in a class of its own. Figure 2.13 shows a structure of this machine. The permanent magnets are located in the stator along with the armature winding, which makes the rotor have a very simple and robust salient pole structure [64-66]. The windings of the stator are usually concentrated on a single tooth and the magnets can be placed in the stator core-back, in between stator teeth or at the surface of the stator teeth. The torque capability of the flux switching machine can be very high, but the machine suffers from having a significantly high cogging torque.

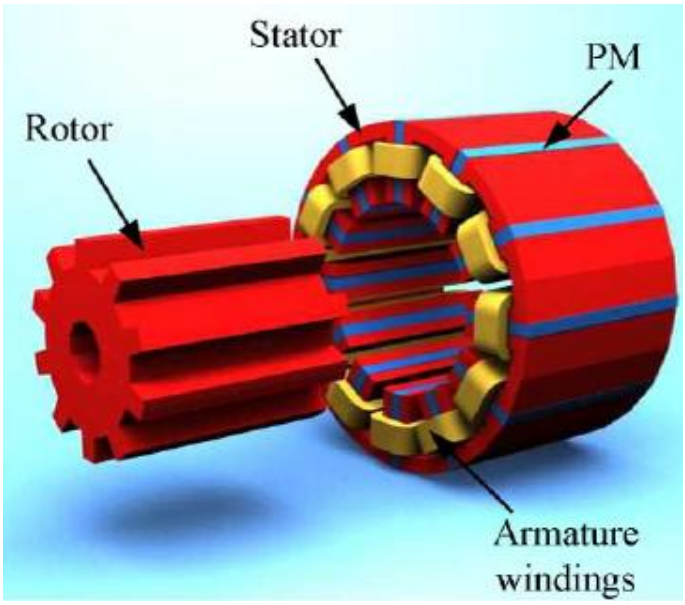

Figure 2.13. A flux switching permanent magnet machine [64].

As mentioned the permanent magnet machine is considered one of the most suitable type of motor for the EV; used by most of the vehicle manufacturer and intensively researched by a lot of academics.

2.5.2 Induction machine

Of all key motor types suitable for application to the EV, the induction machine (IM) has the most developed technology. The IM is a very rugged type of machine, has a relatively low cost and is easy to manufacture. The IM is very efficient in the constant power region, where low magnetisation current is required, also the constant power region can easily be extended to 4–5 times the base speed [35, 67]. However the IM has a lower torque density than PM machines and is less efficient at low speed, making it

unsuitable for a high-torque low-speed direct drive application to the EV, but suitable for a low-torque high speed application to the EV with a reduction gear.

The IM has been widely used by car manufacturers in USA and Europe, driven mainly by its inherent advantages and the desire to have a machine design that does not require the use of permanent magnets. In [68] performance comparisons have been carried out between the PMM, IM and switched reluctance machine.

2.5.3 Switched reluctance machine

The switched reluctance machine (SRM) is proposed to be an exciting choice of machine in the future of the EV application. The machine is inherently a fault tolerant machine as only a single phase is energised at a given time, which is a very important feature for the EV. The rotor is a simple robust iron structure without windings and magnets, which makes it suitable for any high speed application. The machine is made of just iron and copper, making it a low cost machine, however due to the need to have a small air-gap the manufacturing tolerances can be tight [35, 69]. With all these advantages are also some drawbacks associated with the SRM; the torque ripple in the machine can be very high due to its mode of operation and the machine suffers from very high acoustic noise, the inverter module of the machine is always oversized, which causes the cost of the entire system to be high and the rotor iron loss of the machine can be significantly higher than its rival machine technologies at high speed as reported in [68]. The SRM has not been employed by a lot of vehicle manufacturers, but is being researched by many academics.

As known the EV has a wide range of requirements, placing demands on the drive motor employed: in [9, 70] typical efficiency maps for optimum operation of different machine technologies are presented. Table 2.1 below shows the machine technologies used as a source of traction in some of the manufactured EVs and more of this information can be found in [16, 70].

Table 2.1. Motor technology used in manufactured vehicles.

Model	Power Rating (kW)	Drive Motor	Vehicle Model
Toyota Prius (Japan)	50	PM Motor	
Honda Insight (Japan)	9.7	PM Motor	
Nissan Altra/Leaf (Japan)	62 / 80	PM Motor	
Tesla Roadster/Model S (USA)	215	Induction Motor	
Lightning GT (UK)	150	PM Motor	
Ford Focus Electric (USA)	100	Induction Motor	
Mini E (Germany)	150	Induction Motor	
AC Propulsion eBox (USA)	150	Induction Motor	
Chevrolet Volt (USA)	111	PM Motor	

2.6 Un-sprung mass

Problems often perceived with in-wheel motors are related to ride and handling, due to an increase in the vehicle un-sprung mass. In [71-74] investigations show that even though the un-sprung mass increases from the addition of the motor to the wheel, it has no significant effect on the stability of the vehicle. The frequency analysis employed in the investigations show that the natural frequency of the vehicle driven with an in-wheel motor stays within accepted frequency limits, as will be expected by any driver of the vehicle. Figure 2.14 shows how the wheel was packed to increase the un-sprung mass, during an investigation performed by Protean electric and Lotus engineering on a 2007 Ford focus 1.6.

The work carried out in [71] presented studies on the various ground vehicle dynamic performance: ride, refinement, active safety and driveability. The ride performance is "*the ability of the vehicle to absorb any road disturbances*" [71] and is split into; primary, which is a low frequency (0 – 3Hz) vertical acceleration of the vehicle body on the suspension and secondary, which is a high frequency (above 3Hz) vertical acceleration of individual components such as wheels or power-train masses. Two vehicle mass conditions were simulated for the ride, on two road profiles; rough and smooth. Figure 2.15 shows the primary ride results and figure 2.16 shows the secondary ride result, with the key performance indicator (KPI) used as a scaling method, whereby 0 means poor performance and 10 an excellent performance; this indicates that the influence of un-sprung mass is small when compared to the type of road surface profile. The refinement performance is "*the ability of the vehicle to attenuate any noise and vibration*" [71]. Figure 2.17 shows the refinement KPI; increasing the un-sprung mass decreases the refinement KPI and can be expected to be very noticeable on a broken surface, also a reduction in bush stiffness can improve the refinement KPI [71].

Figure 2.14. Un-sprung mass experimentation by Lotus [74].

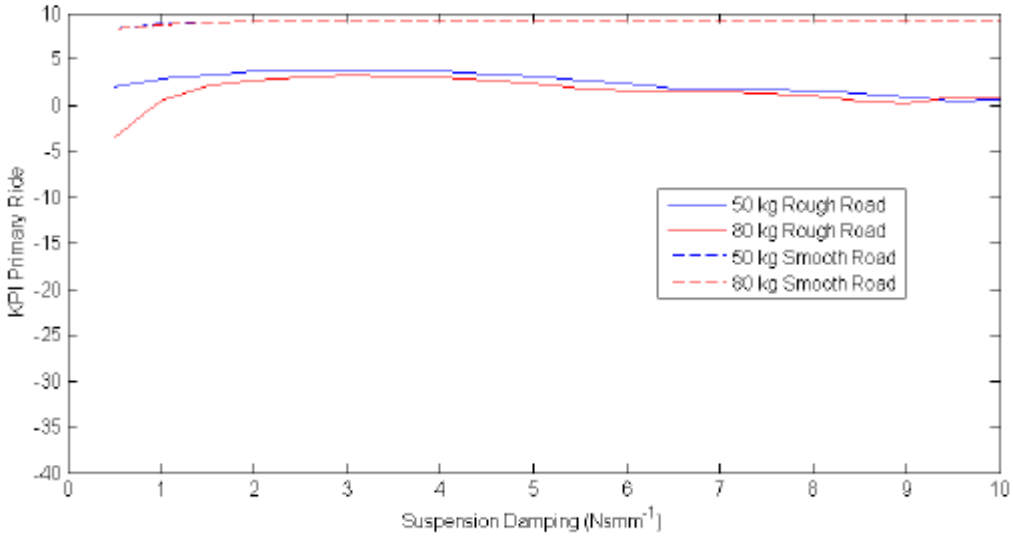

Figure 2.15. Suspension damping influence on primary ride KPI [71].

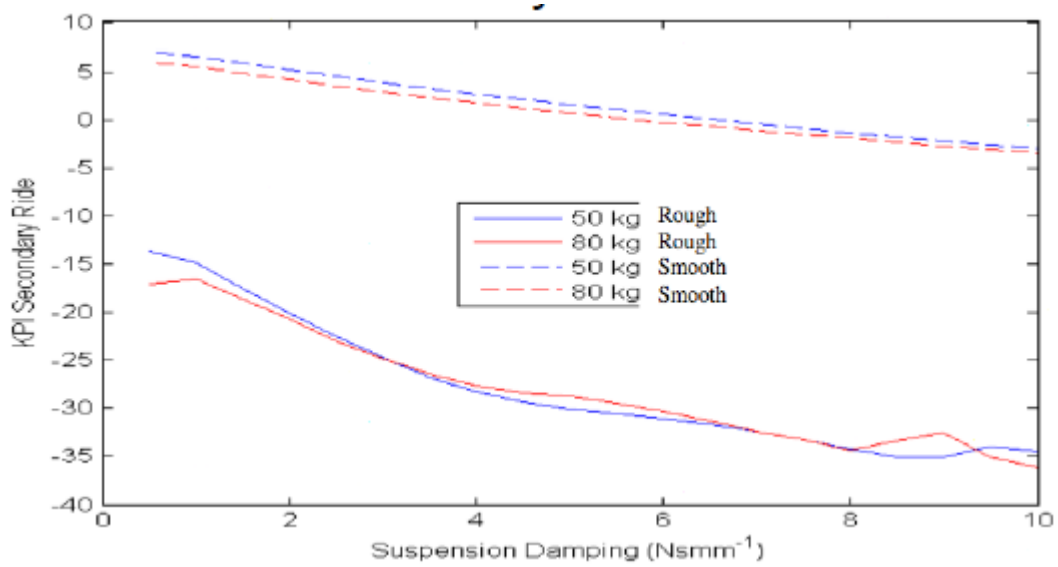

Figure 2.16. Suspension damping influence on secondary ride KPI [71].

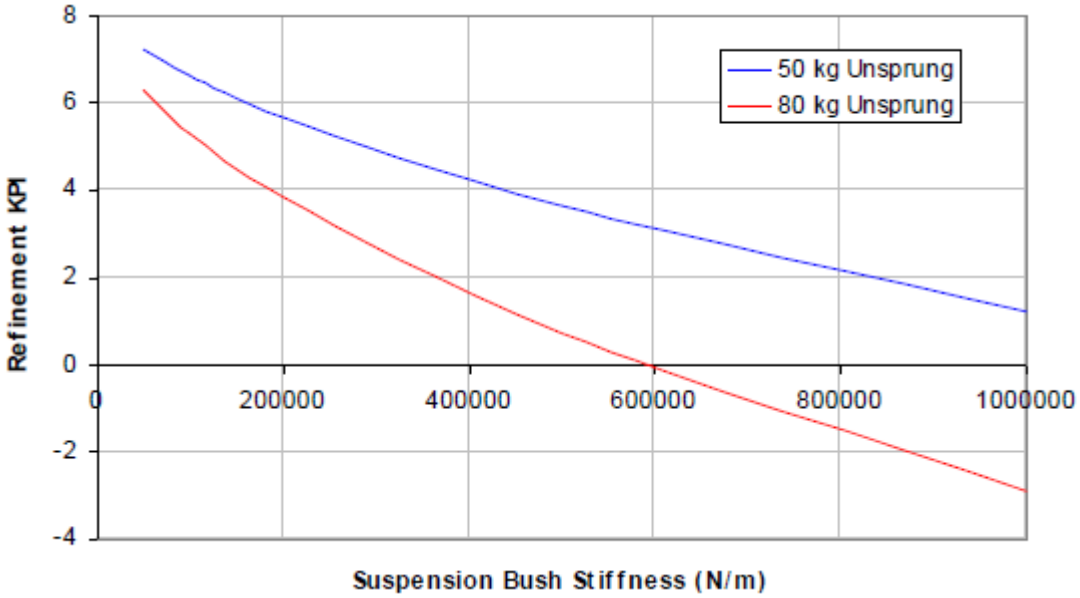

Figure 2.17. "Influence of suspension bushing aggregate fore-aft stiffness on refinement KPI" [71].

2.7 Drive cycle

The drive cycle test is a very important phase of machine validation, as after the machine has been designed and built, it is put through a drive cycle to determine the efficiency, speed response and battery consumption of the EV. The NEDC is the standard European drive cycle; made up of 4 consecutive ECE-15 (urban driving cycle) drive cycles repeated without interruption, then followed by one EUDC (extra-urban driving cycle) drive cycle at the end of the ECE-15 drive cycles [75]. Figure 2.18 shows

the NEDC drive, which basically depicts how the vehicle accelerates, cruises and decelerates over time.

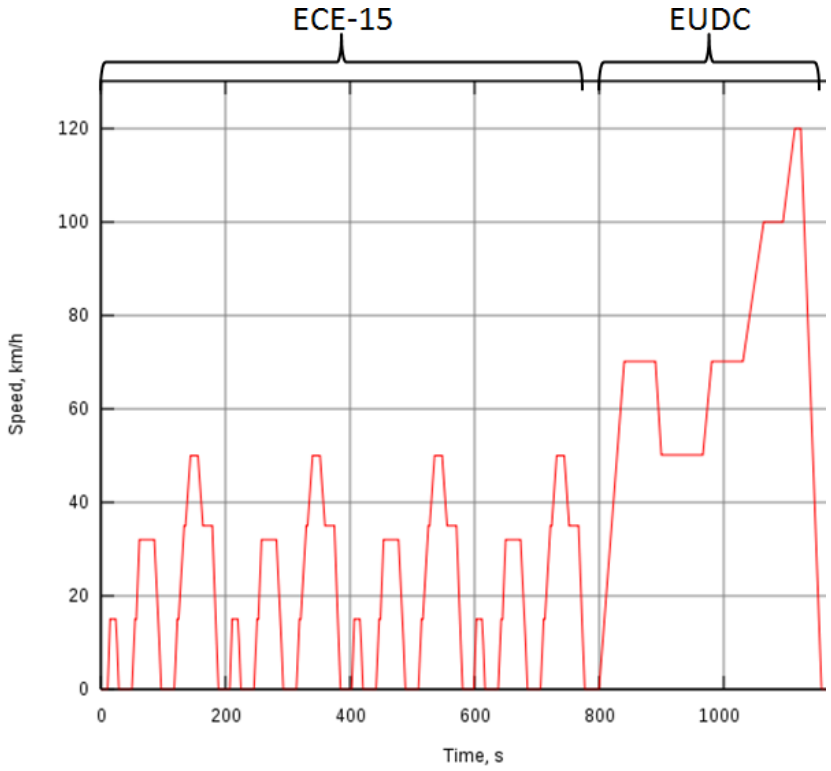

Figure 2.18. Standard european drive cycle (NEDC). [75]

2.8 Summary

An extensive review has been carried out to try and present a survey of the EV to date. Although the EV was in existence before ICE vehicles, it is still a growing technology that needs more research and development to increase its production and tackle most of the challenges facing it today. There are different processes that are involved in the design and selection of the drive motor for the EV and this section has presented the vehicle requirement for the design of a direct drive in-wheel motor. The equations involved in calculating the road forces acting on the EV were shown, which helps determine the motor rating. The selection of machine technology to be used for whatever demand posed by the EV is not straight forward; this section has presented the merits and demerits of all machine technologies that have been applied and can be applied to the EV. Clearly each machine technology has its distinct advantages and depending on the requirement, the chosen machine technology can be optimised to best meet the specification. Drive motors used by different car manufacturers have been presented and the power ratings of the motors given. PM and induction machines are the machines widely used by most vehicle manufacturers.

This work focuses on the design of a direct drive in-wheel electric motor, because wheel motors can offer very high performance, as they permit true independent control of the torque delivered by each wheel. An issue associated with the in-wheel motor is the added un-sprung mass and this issue has been addressed in this section. The motor technology selected for this work is the PM machine with an outer rotor topology.

Chapter 3

High Torque Density, Fault Tolerant Machine Design

The design options for achieving a torque dense motor for use as a direct drive in-wheel motor in an EV are presented; various slot and pole number combinations are investigated. The work in this chapter is focused on an existing Protean in-wheel motor, with the aim of carrying out an electromagnetic analysis to determine if it can be improved based on its output performance. Also the principles in achieving fault tolerance from the machine design perspective are discussed; various fault tests are carried out on the Protean in-wheel motor to determine the effect on performance. Safety is a major issue associated with the in-wheel motor, because a motor fault in one wheel of the vehicle can be catastrophic, as a dangerous torque disturbance will be developed by the motor. The high torque dense Protean in-wheel motor investigated in this work analyses a fault tolerant concept for the motor design, which is validated with model and test results.

3.1 Background

The use of in-wheel motors in a direct drive topology requires the development of a highly torque dense machine, while achieving high efficiency, fault tolerance, low cogging torque and low torque ripple. The design base speed imposed on the motor design for this work is relatively modest, so high pole number machines with permanent magnet excitation provide the best space utilisation and lowest mass. The motor employs concentrated, single tooth windings and fractional numbers of slot/pole/phase, which maximises the torque density.

Fractional slot/pole/phase machines generally introduce high contents of space harmonics in the air-gap MMF. The rotor losses, cogging torque and torque ripple can become a major issue if the slot and pole number combination is not appropriately selected. In [4, 48, 76-79] studies have been carried out to present the influence of the slot and pole number combination on these unwanted effects; different methods of minimising these effects and how choosing an appropriate slot and pole number are discussed.

Later in this chapter various slot and pole number combinations are investigated on an outer rotor permanent magnet motor design, with the aim of achieving high torque density for the direct drive in-wheel motor, which eventually shows how the Protean in-wheel motor was realised. Finally the optimal design was built with integrated drive electronics, which comes as a packaged unit. The Protean in-wheel motor is split into a series of three phase sub-motors, with each sub-motor operating independently of the other sub-motors. The idea of splitting into a series of three phase sub-motors is to incorporate a high level of fault tolerance in the machine, and this will be discussed in full detail later in this chapter.

The final motor build has been extensively tested and results will be presented here. To meet the required torque density the motor has to be adequately cooled. A water jacket is sited at the inner radius of the inner stator, providing intense cooling of the stator and the rotor has been designed to ensure that rotor losses remain very low.

3.2 Design options and method of optimisation

Before any motor design is carried out, a few basic design constraints must be imposed on the motor topology. The in-wheel motor has serious space limitations imposed on it. The design options, taken from the current design of the Protean motor must:

a) Have an outer rotor, coupled directly to the wheel hub.
b) Be capable of being split into series of parallel sub-motors, permitting redundancy during faults.
c) Have single tooth windings with very short end-windings: there is very limited axial length so the end-windings length of overlapped windings is too long.
d) Have a large number of poles, ultimately limited by the maximum electrical frequency of the inverter. The high pole number eliminates all but permanent magnet topologies, as induction and reluctance machines would require excessive magnetising current.
e) A radially shallow rotor, which limits the rotor magnet arrangement.

3.2.1 Design optimisation

In this work a range of design options are compared, ensuring they are within the topology limitation defined above. In order to be certain that the comparison is rigorous, each design is formally optimised using an evolutionary based optimisation routine within a commercial finite element package (Infolytica Magnet). [80, 81] talks about how the evolutionary method of optimisation is carried out. The outcomes of the optimisations are explored in this work to make sure the final results are as expected.

The dominant parameter for optimisation is the mean torque per unit volume which can be achieved within a specific efficiency and temperature rise and within specific dimensional constraints. However, other parameters must be kept within acceptable limits. These include:

- cogging torque
- torque ripple
- unbalanced magnetic pull

There are also constraints imposed by the need to avoid any danger of magnet demagnetisation and the need to limit any fault current and field weaken, which places requirements upon the per unit inductance.

There are two critical design points:

a) Maximum continuous operating torque. This critical thermal point occurs when driving up a very steep, long hill.
b) A short term overload torque requirement, used when accelerating. The duration of this short term condition is well within the thermal time constant of the machine and

so does not pose thermal problems: however, the motor must be electromagnetically capable of achieving this condition.

In order to build the model for optimisation a script file has to be generated to parameterise each vertex path of the machine. The script file has equations input into it in order to calculate the winding loss as a function of the slot depth and tooth width. The formal design optimisation procedure was adopted, maximising the torque capability for a fixed winding loss, corresponding to condition (a) above. Ideally the optimisation would be for a slot peak temperature rise, taking into account the thermal performance differences between different designs and incorporating the thermal effect of iron loss. In practice it was found that the temperature rise due to iron loss was quite small, because there is a very good thermal path between laminations and water coolant: however, failure to account for thermal differences as the slot number is varied is a significant limitation which will be addressed in future work.

In addition to fixing the winding loss for the optimisation, the following hard constraints were imposed;

- maximum outside diameter
- minimum inside diameter
- fixed air-gap length
- maximum overall axial length, including end-windings

3.2.2 Parameters for optimisation

The optimisation process fixes the following:

- stator inside diameter (340 mm)
- rotor outside diameter (400 mm)
- axial length, including end-windings (56.6 mm)
- air-gap length (1 mm)
- winding slot fill factor (0.36)

The following parameters were variables:

- tooth width
- stator core back depth
- tooth tip span
- slot depth

- magnet depth (up to 5.0 mm)
- magnet arc
- magnet insertion depth

These parameters are illustrated in figure 3.1. Optimisation was achieved for a fixed overall stator winding loss of 1800W, using sinusoidal winding currents. Each optimisation calculated the mean torque over an electrical cycle so that results were unaffected by torque ripple caused by cogging or back emf harmonics.

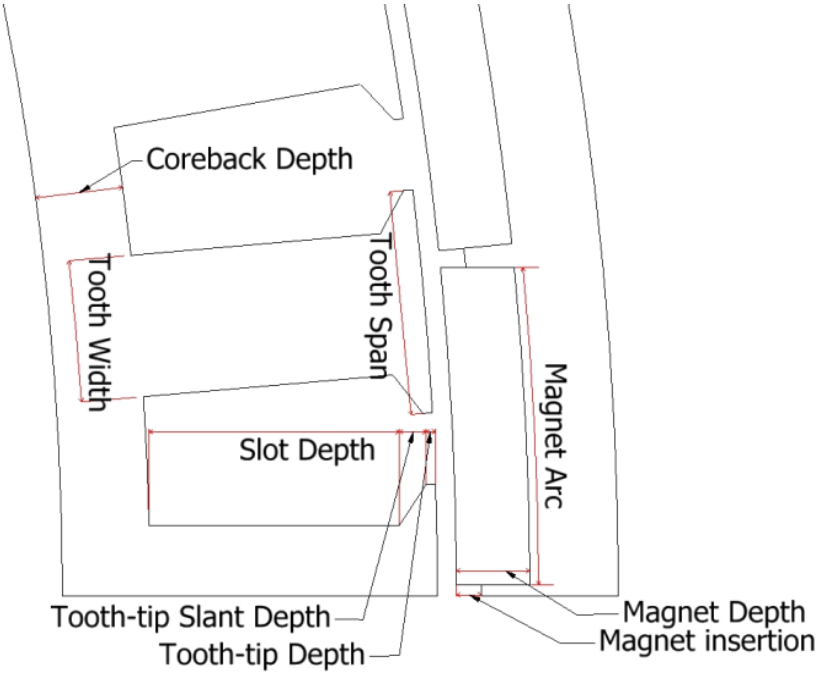

Figure 3.1. Parameters set for optimisation.

The optimisation was commenced from a range of starting points in order to check that it always converged upon the same solution. The results for any one pole and slot number always produced almost identical optimised mean output torque for a given loss, but with minor parameter variations, indicating that there were a range of designs of similar performance.

3.3 Selection of slot and pole number

The selection of slot and pole number combination which are to be considered for optimisation must take into account:

a) ability to split into separate sub-motors
b) ability to withstand demagnetisation
c) effect upon rotor heating

Since the overall axial length of the motor is fixed, the slot number also affects the lamination axial length. As the number of slots decreases, each coil increases in size and so the end-winding standout increases, so that the stack length has to decrease.

The range of different pole and slot combinations chosen for optimisation is shown in table 3.1. Initial verification was done to ensure the combinations chosen have a balanced air-gap rotating magnetic field, by calculating the electrical slot pitch angle, then drawing phasor diagrams to represent the electrical angle between each slot, and rearranging them in such a way that the slots that make up one phase have a resultant phasor, which is 120 electrical degrees from the resultant phasor of the slot that make up the next phase [82, 83]. All of the options are chosen to allow splitting into a minimum of four sub-motors for fault tolerance. The number of teeth varies between 36 and 72, whilst the number of poles ranges between 40 and 64. The configurations chosen generally give good winding factors with high harmonic reduction and consequently low cogging torque.

Table 3.1. Motor configurations.

Number of teeth	Number of poles	Number of sub-motors	Teeth per sub motor	Poles per sub motor
72	64	8	9	8
60	64	4	15	16
36	48	4	9	12
54	60	6	9	10
45	50	5	9	10
36	40	4	9	10

3.3.1 Harmonics elimination

As the ratio of the number of teeth to number of poles comes closer to unity the fundamental pitch factor rises. Thus the 60 tooth, 64 pole option has the highest fundamental winding factor (Table 3.2). Equally, the 36 slot, 48 pole machine has the lowest. For this latter design every coil of any one phase lies at the same electrical angle (there is one coil per phase per pole pair). The consequence of this is that there is very little attenuation of induced harmonic voltages. All other topologies combine a high fundamental winding factor with good harmonic attenuation of all induced harmonics up to the 11^{th}. They are therefore seen as particularly attractive.

Table 3.2. Winding factor for slot and pole combinations.

No. of Teeth	No. of Poles	Winding factor for different harmonics				
		1^{st}	5^{th}	7^{th}	11^{th}	13^{th}
72	64	0.945	0.140	0.061	0.061	0.140
60	64	0.951	0.173	0.111	0.046	0.021
36	48	0.866	0.866	0.866	0.866	0.866
54	60	0.945	0.140	0.061	0.061	0.140
45	50	0.945	0.140	0.061	0.061	0.140
36	40	0.945	0.140	0.061	0.061	0.140

3.3.2 Unbalanced magnetic pull and cogging torque

All the designs, with the exception of the 45 slot machine, have an even number of slots. They therefore exert no unbalanced magnetic pull, assuming the rotor is concentrically placed around the stator.

The frequency of the cogging torque generated is given by the product of the number of teeth and poles, divided by their highest common multiple factor. Table 3.3 shows how the cogging torque is at a very high pole number for most designs, with the 60-64 design having the highest frequency of 720 pole pairs in one mechanical revolution.

Table 3.3. Cogging torque frequency.

No. of Teeth	No. of Poles	Cogging torque lowest pole pair number
72	64	576
60	64	720
36	48	144
54	60	540
45	50	450
36	40	360

3.4 Optimisation results

It is interesting to analyse the optimisation results, in order to understand why the optimisation outcome is as chosen from the optimisation tool. There were some consistent trends that can be seen from the optimisation:

- The magnet depth output from the optimisation was always 5.0mm; the maximum allowed.
- Magnet arc was always large, in the range of 154 – 171 degrees, to produce the maximum back EMF; saliency effects remained virtually insignificant.
- Tooth width was always minimised to give a flux-density in the range of 1.92 to 2.01 Tesla when loaded and around 1.5 Tesla on no-load.
- Rotor and stator core back depths were reduced to the magnetic lower limit, except where they met the mechanical minimum allowed.

As the ratio of number of slots to number of poles dropped, the electric loading increased because the teeth became progressively over pitched, permitting more overall slot area. It was anticipated that this would produce more torque, but the increased slot area produced longer end-winding standouts, thereby forcing a shorter lamination stack length.

Figure 3.2 illustrates the optimised designs and table 3.4 shows the stack lengths produced. It is notable that the 36 slot design can have 23% less stack length than the 72 slot machine, because of its long end-windings. This has a large impact upon torque capability.

3.4.1 No-load back EMF

For the design comparison the magnitude of the EMF constant was kept the same for all models by changing the number of turns. Spatial harmonics in the air-gap flux density produced by the magnets result in time harmonics in the back EMF. Figure 3.3 shows the line-line back EMF at 1200rpm and figure 3.4 shows the harmonics spectrum for the various optimised designs, derived from the FE results. As expected, there are only 5^{th}, 7^{th}, 11^{th} and 13^{th} harmonics and, for all configurations except the 36 slot 48 pole, these harmonics are less than 1% of the fundamental.

Table 3.4. Active length for various slot numbers.

Slot number	72	60	54	45	36
Active length (mm)	50.0	47.3	46.2	42.9	38.4

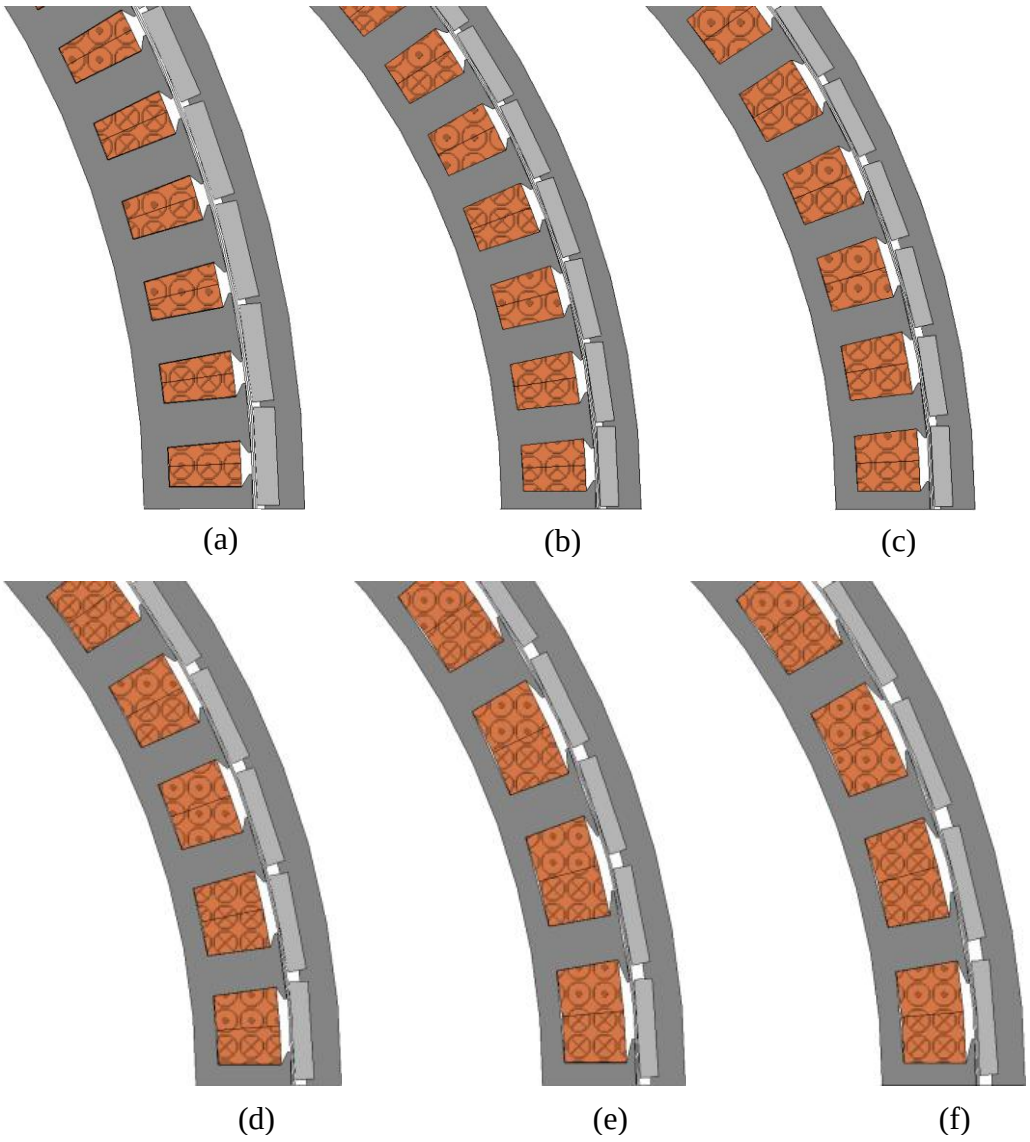

Figure 3.2. Geometrical structure for various combinations; (a) 72slots/64poles, (b) 60slots/64poles, (c) 54slots/60poles, (d) 45slots/50poles, (e) 36slots/48poles, (f) 36slots/40poles.

Table 3.2 shows how, unlike the other designs, the 36 slot 48 pole design has no significant harmonics reduction through the winding factors, so this result is to be expected. Back EMF harmonics in the 36 slot 48 pole design will give rise to running torque ripple at six times the electrical frequency.

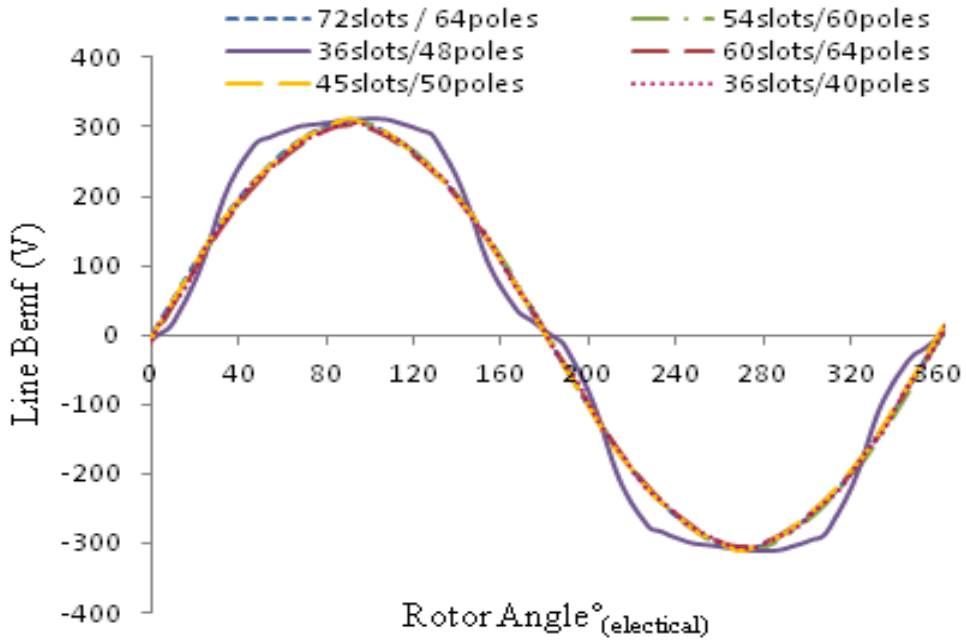

Figure 3.3. Waveform of line back EMF at 1200rpm.

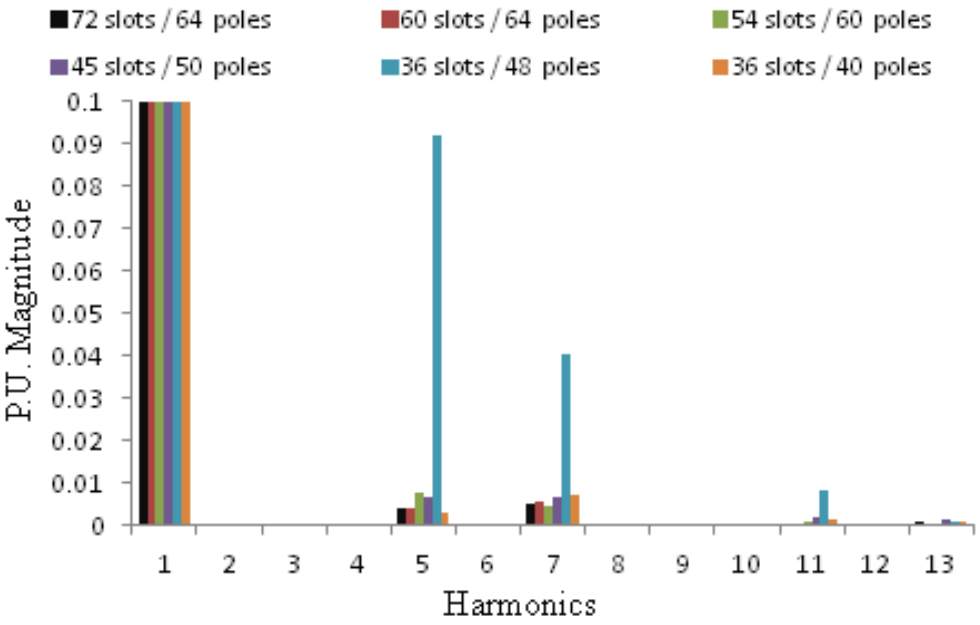

Figure 3.4. Harmonics in back EMF for various combinations.

3.4.2 Cogging torque

The driver of an electric vehicle is surprisingly aware of even modest cogging torque when running very slowly or parking. The mass of the vehicle and compliance in the drive chain will damp out very high frequency harmonics, but they cannot be ignored. For this reason cogging needs active consideration. Cogging torque is not explicitly included in the optimisation process, but is simply observed on the optimised designs. Figure 3.5 shows the results derived from the finite element simulations. Firstly, it should be noted that all the simulations produce very low cogging torque of 1Nm or less.

The frequency of the cogging is also seen to be in agreement with the values given in table 4.

It should be noted that the simulation assumes that the rotor is perfectly central, that all dimensions are exact and that all magnets have equal magnetisation. In practice the tolerances on a production motor are likely to give significantly greater cogging torque than predicted in this ideal case.

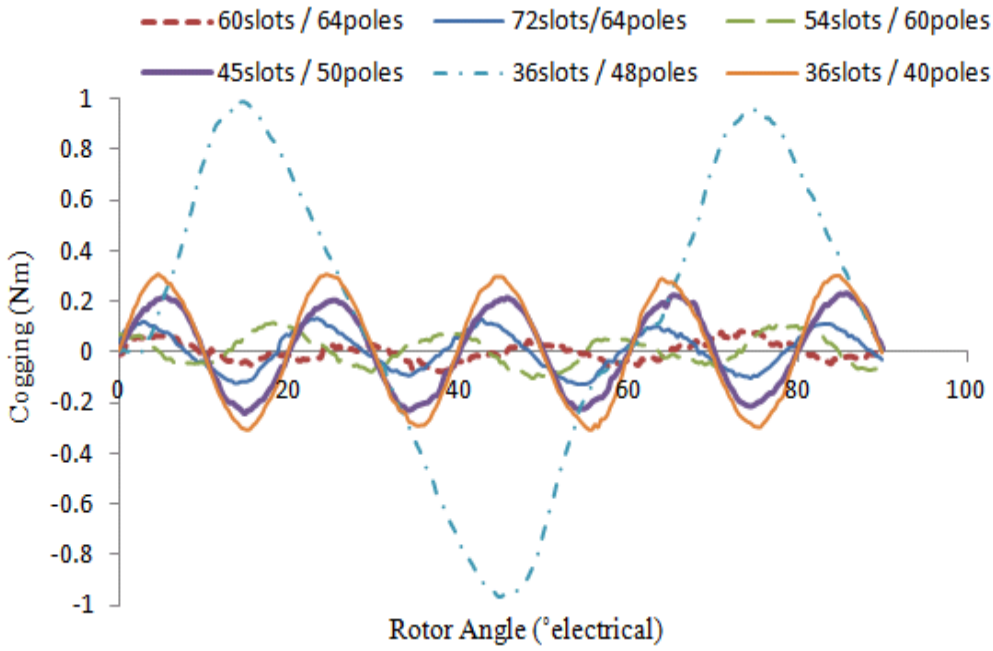

Figure 3.5. Cogging torque for various combinations.

3.4.3 Mean torque

Table 3.5 shows the mean torque produced by each design. Mean torque outputs vary between 426 and 499 Nm. In general the designs with higher pole numbers have the highest mean torque capability; this does not mean that there is no limit to the increase in pole number, as the pole number is limited by the operating frequency and the fixed outer diameter will cause the degraded magnet air-gap flux density (as the magnet arc gets smaller) to limit the torque. The poorest performance comes from the 36 slot machines, and the reason for this is simple: they have longer end-windings, which results in 23% shorter stack length than the 72 slot machine. There is less than 4% difference between all the other designs, indicating that the optimum design is not particularly sensitive to pole number, once the slot number exceeds 45 slots.

Table 3.5. Mean torque, magnetic and electric loadings.

Slots	Poles	Electric loading (A/m)	Mean Torque (Nm)
72	64	56500	499
54	60	66400	482
36	48	70100	455
60	64	63900	488
36	40	80900	426
45	50	75100	483

It is interesting to note that the lower pole number designs have reduced magnetic loading and increased electric loading than the high pole numbers. This can be seen in table 3.5 and in figure 3.2: low pole number designs tend to have relatively wider slots than teeth. The reason this occurs is thought to be due to the space taken up by the stator and rotor core backs. This would become prohibitively large in lower pole number designs unless the flux per pole is limited. Consequently the flux per pole remains almost independent of pole number, with similar width teeth for all designs.

The 72 slot, 64 pole machine – Protean in-wheel direct drive motor still shows better performance compared to the other designs, indicating that the optimum design for the given constraints and limitations has been achieved in the Protean motor. This combines the highest torque capability with the lowest cogging torque and minimal space harmonics in the back EMF. The slots in this design are relatively narrow, which is also likely to improve the thermal performance compared to the other designs.

3.5 Protean in-wheel motor

Table 3.6 shows the specification of the existing Protean in-wheel motor drive, revealing a high demand, torque dense arrangement. The topology is that of a 3-phase, radial field, permanent magnet, outer rotor, in-wheel motor, with each in-wheel motor split into eight sub motors: figure 2.4 is a blown out drawing of the Protean in-wheel motor. A series of these motors have been built and extensively tested in a variety of vehicles, ranging from a Volvo C30 to a Ford F150 SUV. In both of these vehicles the motors were placed in all four wheels, giving true four wheel drive.

Table 3.6. Wheel motor drive specification.

Peak Output Power	80 kW
Continuous Output Power	54 kW
Peak Output Torque	800 Nm
Continuous Output Torque	475 Nm
DC Supply Voltage	380 V
Overall motor axial length	56.6 mm
Overall diameter	420 mm
Maximum speed	1400 r/min
System mass (inverter + motor)	31 kg

The hub motor receives a torque demand from the vehicle controller via CAN communications protocol. The torque demand is 1/8th of the total hub motor torque demand since there are 8 sub-motors within each hub motor, each producing 1/8th of the total motor torque. The torque demand is distributed to each of the 8 micro-inverters, where each micro-inverter drives a sub-motor. The micro-inverter and associated sub-motor are independent from the others in the hub motor except for the common CAN interface signal and the shared DC bus connection and, of course, the permanent magnet rotor. The CAN interface signal is opto-isolated at the micro-inverter to prevent a CAN fault on one inverter affecting the CAN interface to the other micro-inverters. Each micro-inverter has its own DC bus bulk capacitance and driver circuits, and is individually fused to the DC bus, so that an inverter or sub-motor fault that results in large DC bus current will blow the DC-bus fuse and hence isolate the fault from the other micro-inverters in the hub motor. An overview of the architecture is illustrated in figure 3.6.

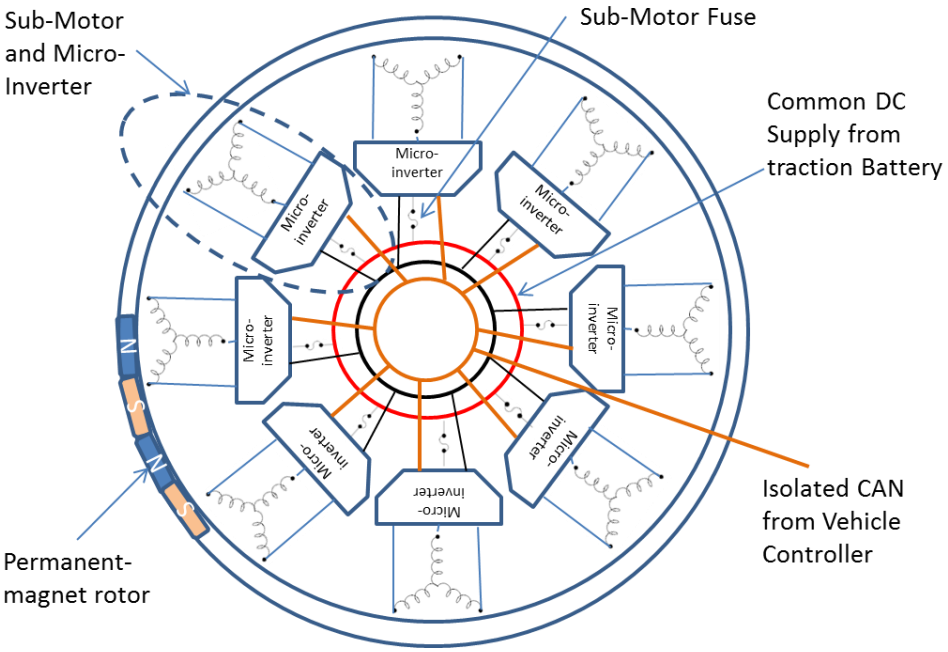

Figure 3.6. Overview of micro-inverter and sub-motor architecture.

A finite element model of the machine was developed and validated against measurement. This model is two dimensional in nature and therefore does not accommodate fringing and leakage at the axial ends of the machine. A time stepping method is used so that harmonic fields are represented and variations in torque with position can be determined.

Figure 3.7 shows a finite element plot of the machine under load, and figure 3.8 compares the variation of mean torque with current for the complete motor, whilst operating at rated speed. Two dimensional modelling tends to overestimate the performance by up to 10%. This is primarily a result of the failure to model end effects in a relatively short machine. At high currents there is a modest element of saturation, reducing the torque constant slightly. The machine back emf has low harmonic content, primarilly due to the nature of the winding, and so torque ripple remains low when the motor is supplied with sinusoidal current, figure 3.9 shows a plot of the measured and modelled phase back EMF and modelled line back EMF at a speed of 1200rpm.

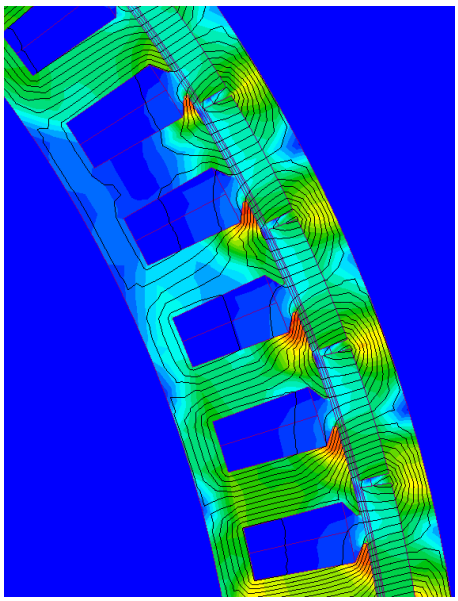

Figure 3.7. Loaded motor flux and flux density distribution.

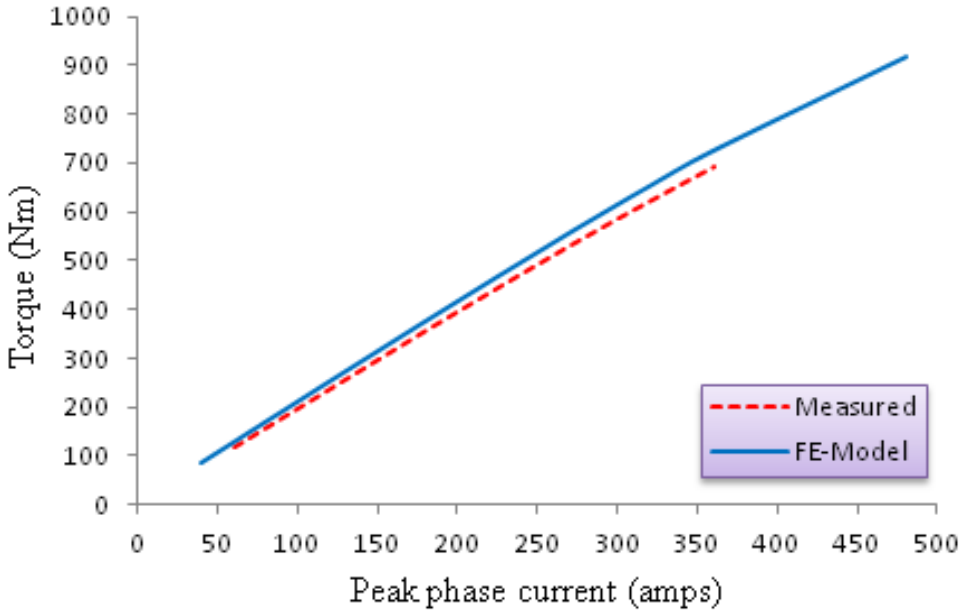

Figure 3.8. Motor torque performance versus electric loading (complete motor).

3.6 Protean machine drive cycle test

This section presents simulation results of the motor against the NEDC (new european driving cycle), provided by Protean. The simulation took into account a typical vehicle mass of 2000kg, powered by only two of the four in-wheel motors. Figure 3.10 shows the motor speed as it follows the ECE-15 drive cycle, along with its torque response and figure 3.11 shows the motor speed as it follows the EUDC drive cycle, along with its torque response. In motoring mode, the mean efficiency was found to be 78% through the entire drive cycle. The battery consumption of the vehicle was 200Wh/km.

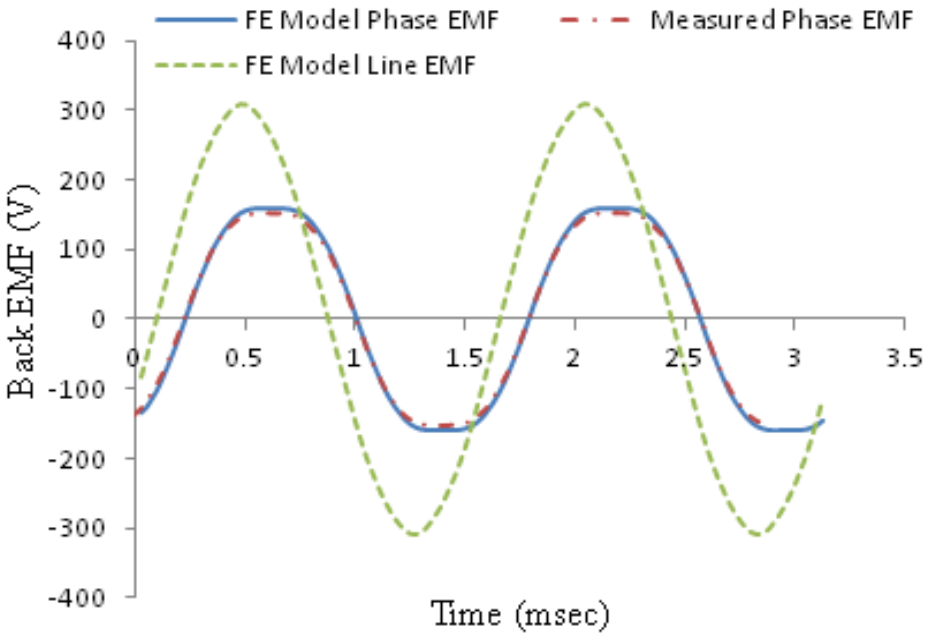

Figure 3.9. Phase and line back EMF at 1200rpm.

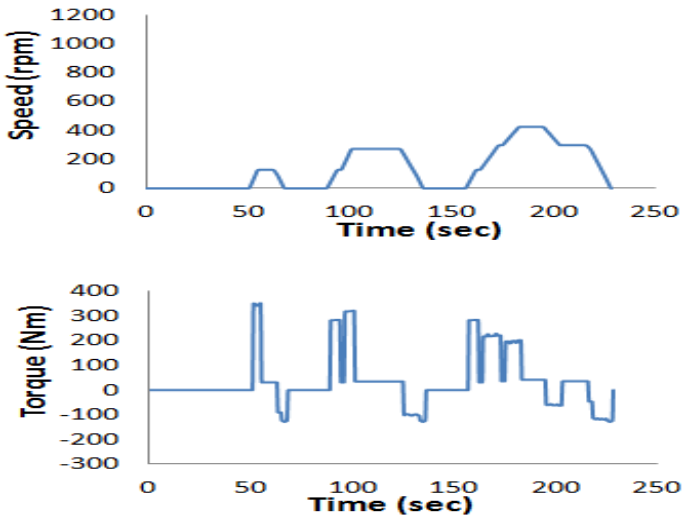

Figure 3.10. Motor response to ECE-15 vehicle drive cycle.

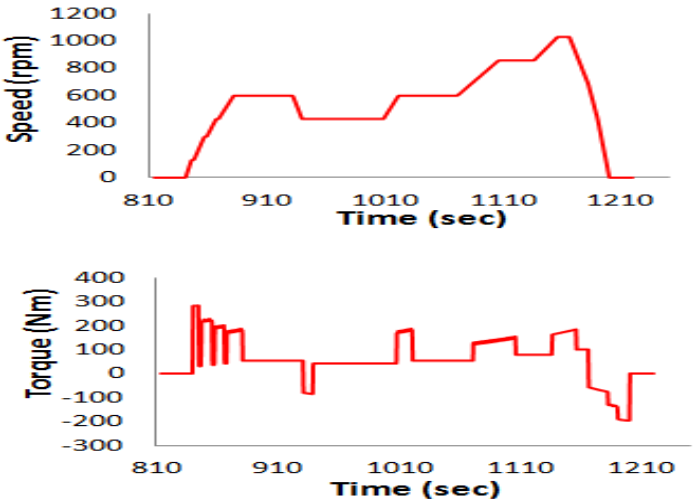

Figure 3.11. Motor response to EUDC vehicle drive cycle.

3.7 Background

Fault tolerant concepts in machine design have been considered by the aerospace industry, where high power density, availability and reliability are major design requirements. Most of the fault tolerant machines presented in past research works are for application in the aerospace industry, but the ideas behind the fault tolerant design in these machines can be applied to the machines designed for use in the EV. However the difference between the two applications is the cost that can be associated with the machine drive: due to the market demand the machines designed for the EV have to be cost effective to ensure the EV is well priced to compete in the automotive world. The reliability of conventional industrial drives is of the order of 10^5 hours between failures (often termed mean time between failure – MTBF or mean time to failure – MTTF) [84-86], corresponding to 3,000,000 miles at 30 miles per hour. This is clearly well beyond the life of most vehicles and offers the promise of increased reliability over the ICE. However the environment of an in-wheel motor is far from benign: the motor is sealed against water and dust ingress and designed to withstand shock loads. Having independent in-wheel motors gives a level of redundancy, so that there is also a "limp home" capability in the event of any motor drive failure.

A sudden fault in one wheel of the vehicle can lead to a drag torque or braking torque being generated in one wheel of the vehicle and can cause loss of vehicle control, which can be catastrophic at high speeds. System studies carried out by Protean have revealed that a large disturbance torque of 280Nm or more could lead to loss of vehicle control, and so the system must be designed to virtually eliminate such a possibility. Most of the work on fault tolerant design [87-93] focuses on having a high number of phases, but fails to address the issue of large torque disturbances arising. The fault tolerant machine design studied in this work has taken into account the need to minimise this torque disturbance. The short circuit fault is the type of fault considered in this investigation, since this type of fault leads to a braking torque. Open circuit faults only result in high torque ripples and loss of torque, but do not cause braking torque, so they are not considered in this study. However the open circuit faults are managed by introducing a level of redundancy in the machine, whereby the machine still produces rated torque by applying an overrating factor to each phase during the machine design, which compensates for the loss of a phase or sub-motor.

3.8 Fault tolerant design requirements

The main faults that can occur in a machine are:

a) Winding open circuit.
b) Winding short circuit; turn-turn, phase-ground or at winding terminals.
c) Power device failure; either open or short circuit.
d) Capacitor failure; open or short circuit.
e) DC bus open or short circuit.

The probability of a winding short circuit fault is not as high as power converter faults or a machine terminal short/open circuit fault. However it is important to design the machine to limit such faults, and their propagation and reduce the possibility of loss of operation. Vibration due to mechanical and electromagnetic forces, coil crushing and heat are conditions that machine coils are exposed to naturally or by design choice, which gradually degrades the integrity of the coil insulation and may lead to the mentioned winding faults. In order to achieve a fault tolerant design it is important to have; physical, electrical, magnetic, thermal isolation between phases and a large per unit phase inductance [88, 94-97].

The switched reluctance machine naturally meets the requirements of fault tolerance, because only one phase is excited at any given time and, if there is a short circuit fault in a phase, it is automatically disconnected if the fault current is large enough to break the electrical continuity in the phase winding. However, since the coils of two phases can occupy the same slot, thermal coupling can cause fault propagation. The PM machine has to be designed specially to improve its fault tolerant capability, as the source of excitation that drives the fault current cannot be removed due to the fixed excitation of the rotor magnet. From work presented in [96] fault tolerance in a PM machine can be achieved by: having a surface permanent magnet reducing the mutual flux, a one per unit phase inductance to ensure the fault current of a phase doesn't exceed the machine rated current, concentrated windings for elimination of physical contact between phases and one phase winding per slot to increase the thermal isolation. In [98, 99] the authors present a method to select an optimum slot and pole number combination for a fault tolerant machine design, whereby the magnetic coupling between phase windings can be limited. The SRM and the PM machine have been compared in [100] to determine their fault tolerant capabilities, and it shows the PM machine can match the SRM in this design aspect.

3.9 Fault tolerant design of protean wheel motor

Splitting the 72slot/64pole motor into eight sub-motors introduces a level of redundancy in the motor to help achieve fault tolerance. This fault tolerant concept is important to limit the level of braking torque generated by the motor during a fault, which is a major concern in terms of vehicle safety, as these motors are to be fitted in the wheel of the vehicle. This is a motor design aspect that has not been addressed in most fault tolerant motor designs. Each sub-motor is a 3-phase motor in its own right, with its own three phase inverter and windings, which operates independently of the other sub-motors.

3.9.1 Braking torque and fault tolerant factor

When a sub-motor is faulted, it introduces only 1/8th of the braking torque of a complete motor, whilst the other sub-motors can continue to produce motoring torque. The machine is expected to produce rated torque even when one sub-motor is lost and in [96] an equation for fault tolerant overrating factor was developed, $(n/(n-1))$, where n is the number of sub-motors in the case of the motor presented in this work. Splitting into 3-phase sub-motors, rather than single phase ones is preferable because each sub-motor draws constant power. The loss of one sub-motor does not result in significant distortion of the supply current of introduction of significant output torque ripple. So each sub-motor is overrated by one seventh, because the overall system must continue to perform with only seven of the eight sub-motors still healthy. From the vehicle point, the braking torque from the occurrence of a fault in one sub-motor is anticipated to be low, since there are four in-wheel motors driving the vehicle, which means there are 32 sub-motors in effect.

3.9.2 Per-unit inductance

To achieve a significant per-unit inductance, careful design of the motor's synchronous reactance slot (slot opening) has to be carried out. This inductance acts to limit the maximum fault current in the motor winding and later in this chapter the fault current produced in the motors being optimised presented. Two dimensional (2-D) modelling was used to compute the motor fault currents and drag torques, however this two dimensional model fails to incorporate the end-winding inductance. So a single three dimensional (3-D) model was constructed to determine the end-winding inductance of the motor. Figure 3.12 is a section of the motor, showing the model used for the calculation of the end-winding inductance. The calculated end-winding inductance was

then incorporated into the two-dimensional FE model as external impedance in series with the windings.

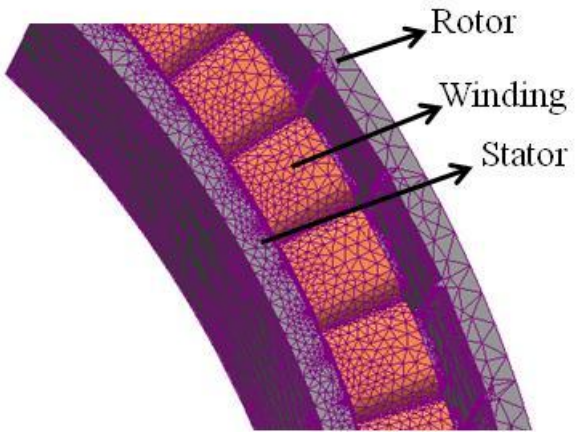

Figure 3.12. 3D-FE element size.

The winding per-unit inductance can be calculated from equation 3.1 below;

$$L_{pu} = \frac{L_{actual}\,\hat{i}_{rated}}{\hat{\Psi}_{magnet}} \tag{3.1}$$

The L_{actual} is the phase inductance calculated from the FE model. The phase per-unit inductance is shown in table 3.7 below.

Table 3.7. Per-unit phase inductance calculation.

$\hat{\psi}_{mag}$ **(wb-turns)**	$\hat{i}_{rated}$ **(A)**	L_{actual} **(mH)**	L_{rated} **(mH)**	L_{pu}
0.0453	30	0.94	1.51	0.62

3.10 Fault performance of the protean machine

In this section simulated and measured results for different fault scenarios are presented, with the test motor running on open circuit and the drag torques and fault currents recorded at different speeds for the various fault scenarios.

The test rig set up is shown in figures 3.13 and 3.14. The test motor (Protean PD18) is driven from a dynamometer, with an inline torque transducer. A toggle switch via a contactor is used to implement the different range of winding failures, so as to ensure the fault is removed before the thermal limits of the phase winding is exceeded.

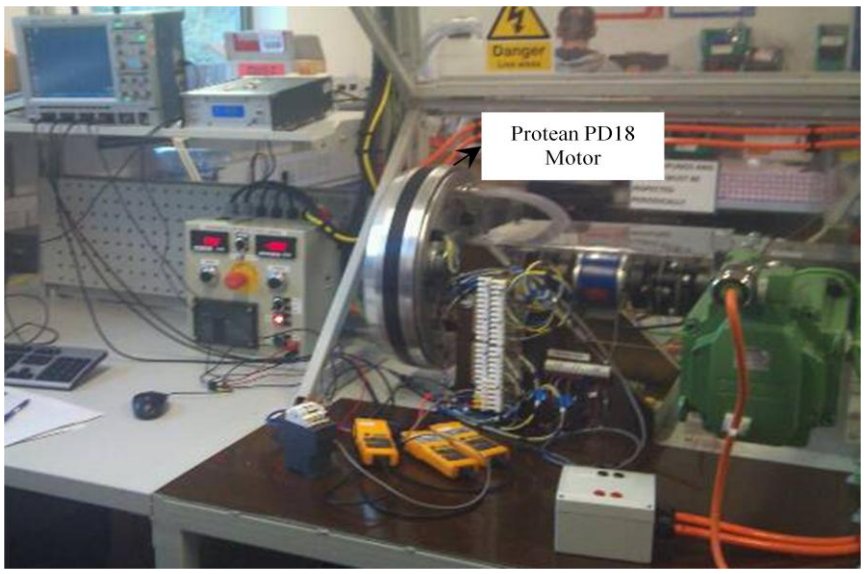

Figure 3.13. Test rig setup and measuring devices.

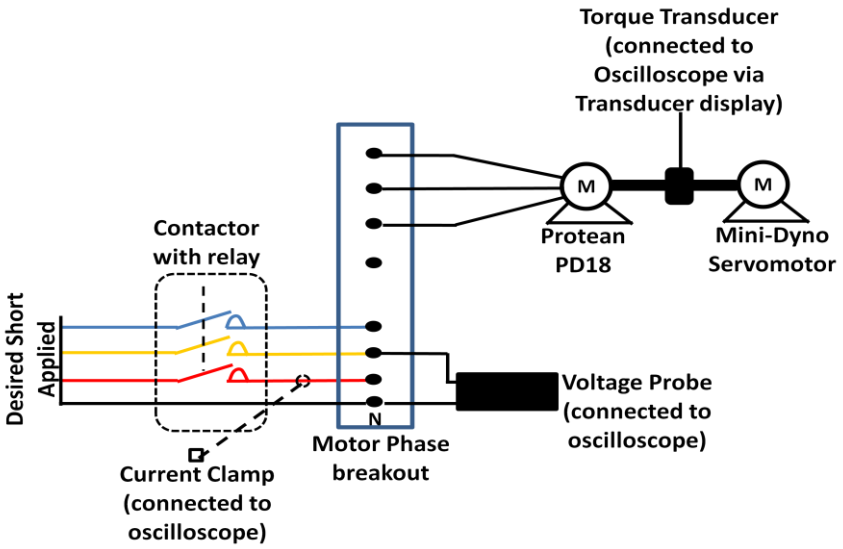

Figure 3.14. Schematic of test rig and shorting arrangement.

All simulation results were derived from 2-D FE time stepping models, with the end-winding inductance and resistance included as a lumped parameter with the phase coils, as shown in figure 3.15. Figure 3.16 shows the structure of the FE model for one sub-motor, with each phase winding consisting of 3 coils. Each sub-motor has eight poles, nine slots and spans 45 degrees around the periphery of the machine.

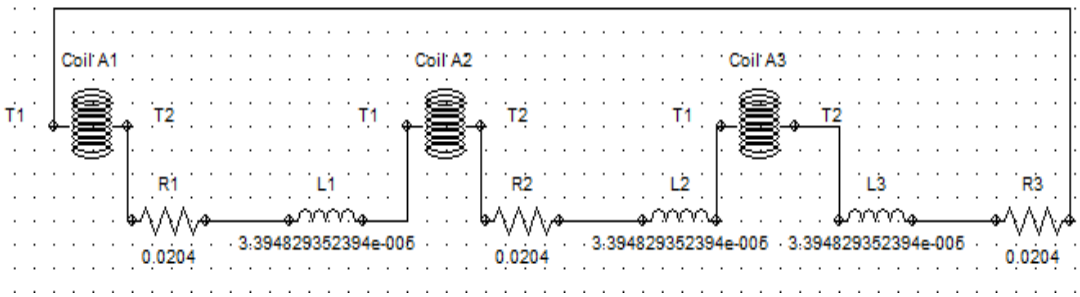

Figure 3.15. Lumped circuit parameters for winding short circuit calculation.

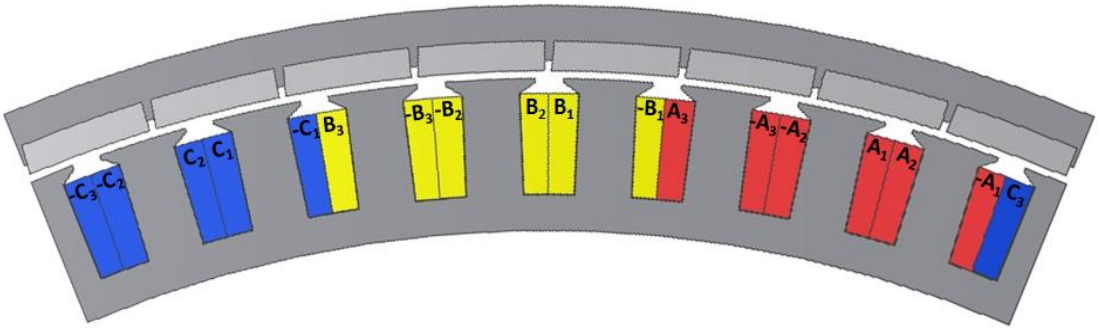

Figure 3.16. Section of the 72slot/64pole machine design (9slots/8poles).

3.10.1 Single phase fault

This fault occurs between the terminal of one phase and the star point for one sub-motor. This type of fault can conceivably arise from degradation of the winding insulation. The braking torque for this fault scenario has a large degree of ripple, due to the unbalanced nature of the fault, but when rotating at all but the lowest speeds, the frequency of the ripple is about several hundred Hertz or larger and will not be observed by the vehicle driver. Also the torque transducer measurement bandwidth of the braking torque is typically much less than the braking torque ripple frequency and so the ripple is not observed in the measurements.

Figure 3.17 shows the finite element predictions and the measured mean braking torque as function of speed, whilst figure 3.18 shows the variation of the peak steady state fault current with speed, when a single phase of one sub-motor is shorted.

The peak braking torque is 17Nm and occurs at a rotational speed of 80revs/min. This braking torque has a magnitude less than the maximum allowed torque disturbance and is likely to pass completely unobserved by the vehicle driver. Figure 3.19 shows the measured fault current that flows for a shorted phase at the designed base speed of 1200revs/min. The steady state current is limited by the phase inductance and is within

the thermal limit of the motor and the transient state of the current is due to the discharge of the stored magnetic energy of the coil inductance.

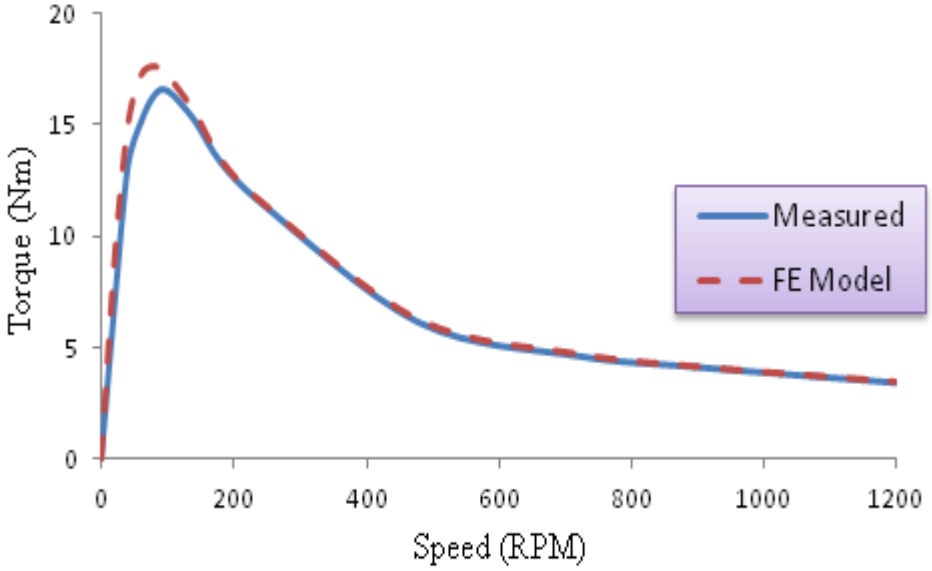

Figure 3.17. Mean drag torque versus speed for a single phase short-circuit, in a sub-motor.

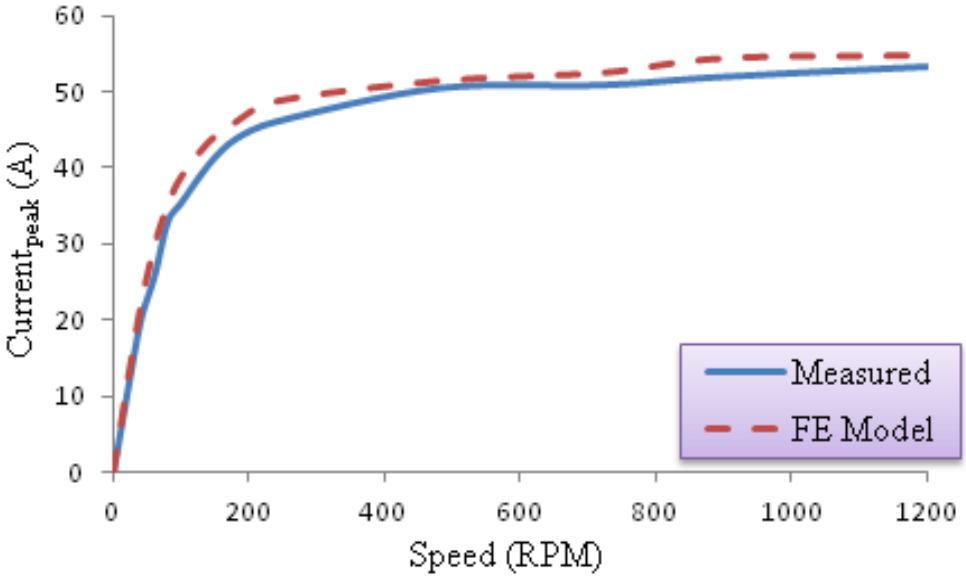

Figure 3.18. Fault current versus speed for a single phase short-circuit, in sub-motor.

The sole source of excitation that drives the fault current is the magnet flux, as the fault investigation was done at no-load. So the short circuit current can be determined using equation 3.2 below:

$$i_{sc} = \frac{j\omega N \hat{\phi}}{R + j\omega L} \tag{3.2}$$

At low speed: $i_{sc} = j\omega N\hat{\phi} / R$ - the current rises with rotor speed.

At high speed: $i_{sc} = N\hat{\phi} / L$ - the current is not speed dependent.

The braking torque is derived from the power loss equation ($P = i_{sc}^2 R$) and is obtained from the equation below:

$$T_{drag} = pp\left(\frac{jN\hat{\phi}}{R + j\omega L}\right)^2 \omega R \tag{3.3}$$

Where pp is the number of pole pairs, ϕ is the magnet flux, N is the number of turns, ω is the electrical angular speed and L and R are the winding inductance and resistance of the shorted winding section.

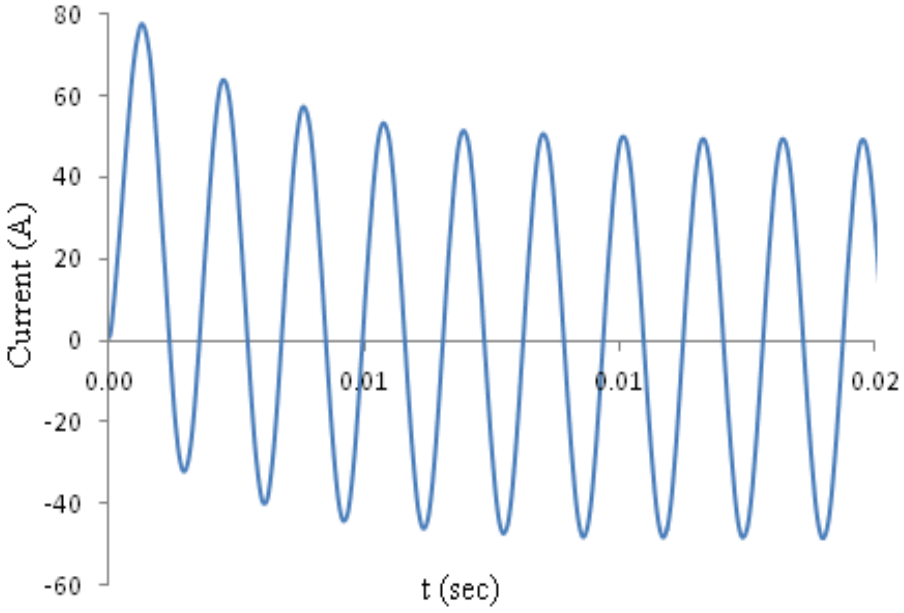

Figure 3.19. Measured short circuit current for single phase short at 1200rpm, in a sub-motor.

3.10.2 Three phase fault

A three phase symmetrical fault is most likely to be caused by a failure in the power electronic converter, resulting from shorting of the DC link due to either capacitor or device short-circuit failure. As shown in figure 3.20 this fault scenario produces a larger braking torque, which is predictably about three times that of a single phase short. As seen again in this fault scenario, the peak braking torque occurs at low speed: the peak braking torque of 50Nm is less than one fifth of the allowable disturbance and does not

pose a risk to the vehicle safety. Figure 3.21 shows the variation of peak fault current with speed, which once more is within the thermal capability of the motor. Because the fault is symmetrical the braking torque has no significant oscillations, as shown in figure 3.22.

The braking torque in this case is almost DC, with very little oscillation in the torque waveform, due to the balanced nature of the fault. The graph of braking torque is shown for this fault scenario at 80revs/min, where maximum braking torque is obtained. It is interesting to note that the brake torque quickly settles to 50Nm, with a small dip after 0.8 seconds in the measured waveform. The cause of this dip is simply a result of the speed of the driving motor dropping slightly, as the drive motor is set to operate in speed control mode, and is of no major significance.

If the motor and drive system had been of more standard form, rather than the eight sub-motors the peak braking torque would have been 400Nm, which is well beyond the 280Nm at which loss of control becomes a serious issue.

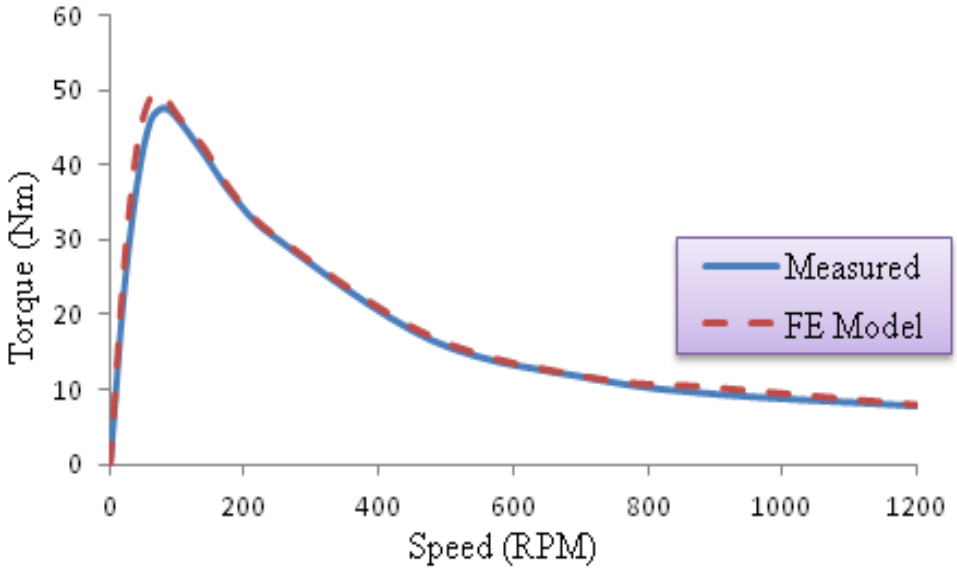

Figure 3.20. Mean drag torque versus speed for a three phase symmetrical short-circuit, in a sub-motor.

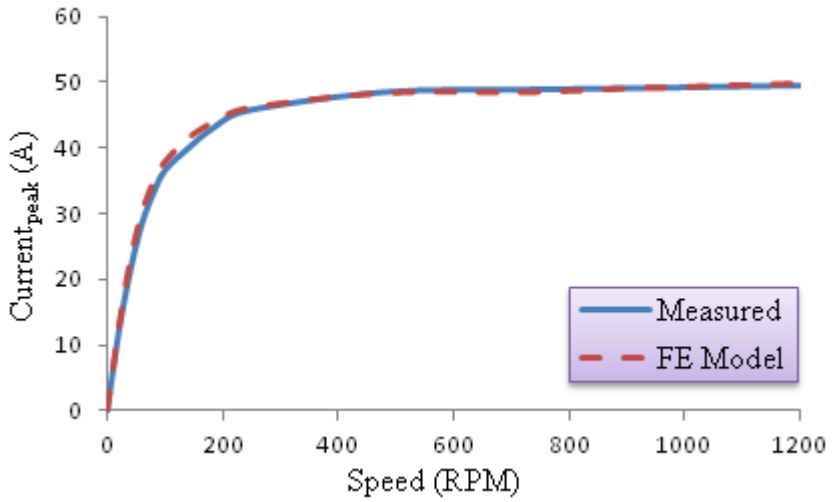

Figure 3.21. Short circuit current versus speed for a three phase symmetrical short-circuit, in a sub-motor.

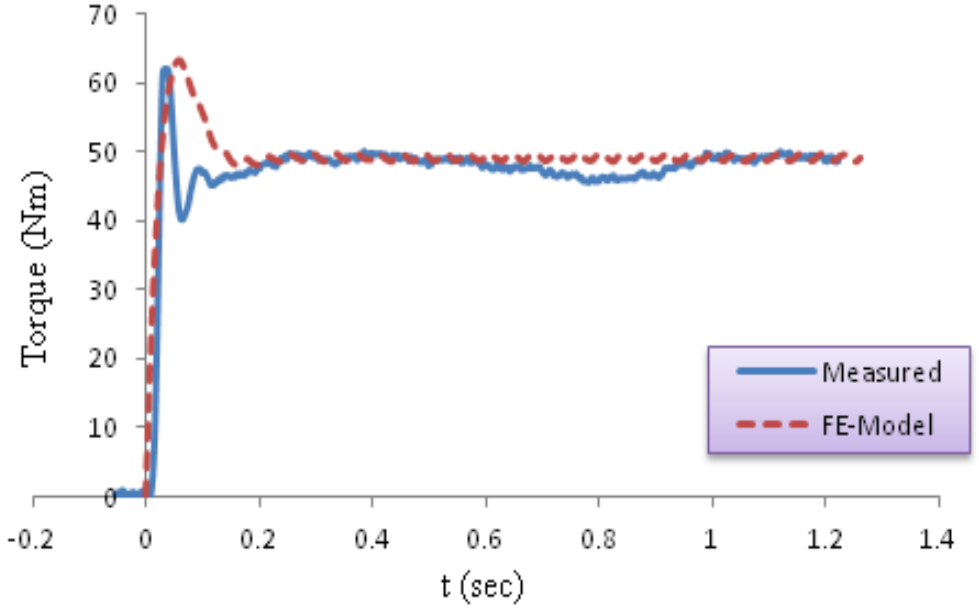

Figure 3.22. Drag torque as a function of time with a symmetrical three phase short-circuit occurring at 80rpm, in a sub-motor.

3.10.3 Effect of single coil short

A single coil short circuit is likely to occur due to degradation of winding insulation. This type of fault can lead to fault currents of large magnitudes flowing in the winding compared to the single and three phase faults, as the impedance limiting the current is reduced and the excitation driving the fault current remains the same. This can also lead to demagnetisation of the magnets, depending on the operating temperature of the machine. Figure 3.23 (a) and (b) show the magnetic flux plot for no-load and single coil

fault respectively. As seen, the magnetic flux linking the coil is effectively reduced to about 16% of the magnet flux linking the faulted coil. Most of the flux linking the faulted coil shunts around the magnet, while little of the flux travels across the stator tooth tip or links the coil. The level of flux density across the tooth, magnet and rotor back iron is shown, and can be used to judge the possibility of magnet demagnetisation. The flux linking the adjoining coils are slightly affected, but this will not drastically reduce the EMF of these coils. The braking torque produced due to this fault instance is of very low magnitude, figure 3.24 shows an FE simulation of this torque.

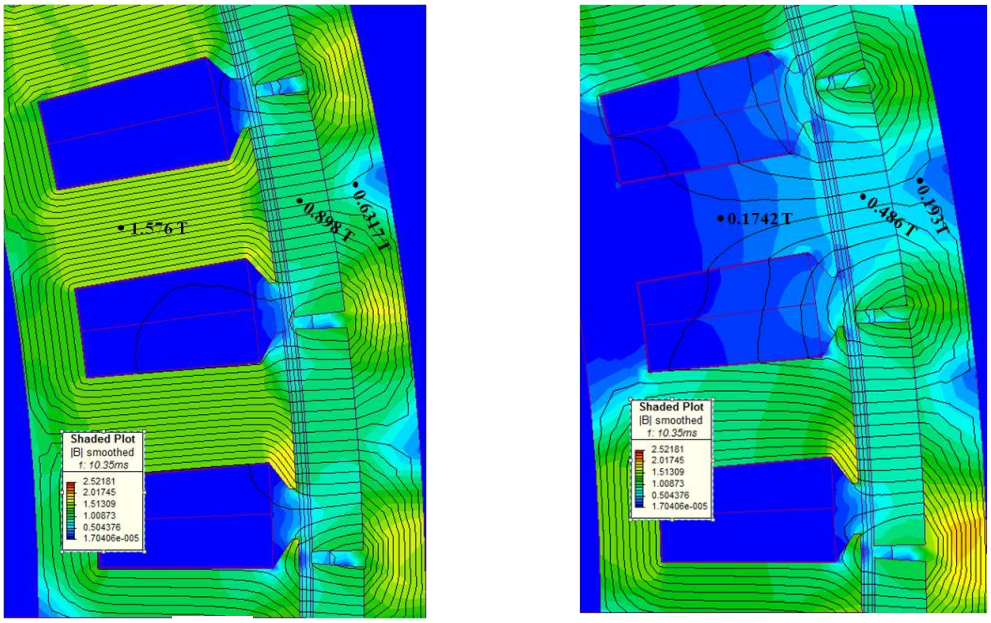

(a) (b)

Figure 3.23. Machine flux density and contour plot at 1200rpm; (a) no-load magnet flux, (b) short circuit applied to coil directly underneath a magnet.

3.10.4 Inter-turn fault

Turn-turn faults can result from degradation of the winding insulation. No measurements were undertaken for this condition, as it is practically difficult to access a single coil in the machine assembly. However a finite element model was built to simulate this fault condition. The fault creates a large current in the shorted turn as shown in figure 3.25. The fault current is an order of magnitude greater than the thermal limit of the machine and will cause thermal overheating of the winding. The reason that such large currents are created is that the single turn has a very low inductance; ($1/N^2$ of the coil inductance) – where N is the number of turns of one coil, which means that the current is limited solely by the resistance of the turn. The investigations in [94, 101] discuss methods to manage a single turn short circuit, to prevent winding melt down.

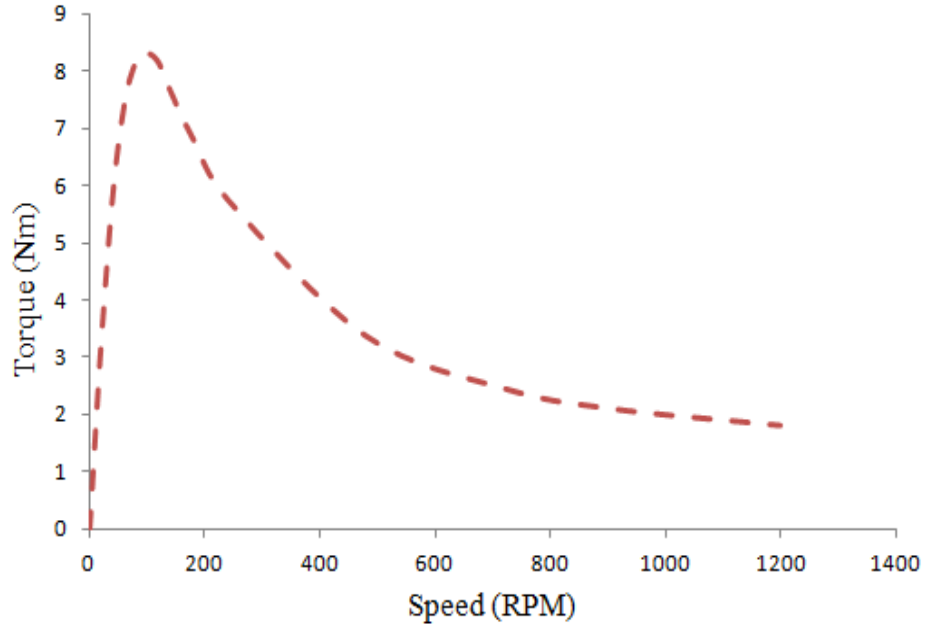

Figure 3.24. Mean drag torque versus speed for a single coil short-circuit, in a sub-motor

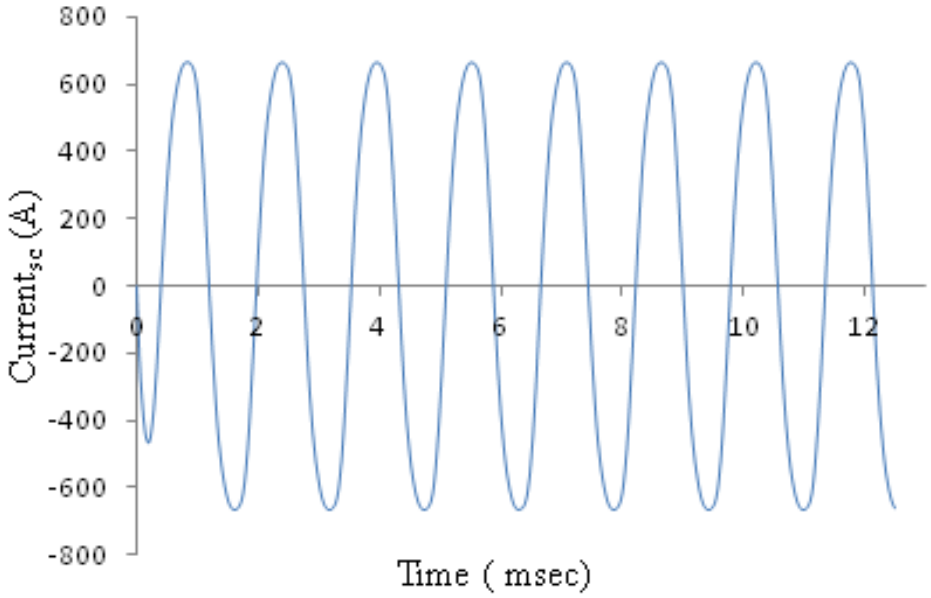

Figure 3.25. Simulated short circuit current for an inter-turn short at 1200 rpm, in a sub-motor.

Although the shorted turn carries a very large current it was found that the fault creates a very small braking torque of only 2Nm. This is because the net air-gap MMF of the fault remains very small.

3.10.5 Fault result analysis

The fault tolerant concept studied here has been applied to a machine designed as a high torque low speed machine, used as an in-wheel direct drive motor in an EV. The results presented on the different fault scenarios can be summarised as follows:

- there are no faults which result in a serious torque disturbance. Indeed, it is unlikely that the driver will even notice the occurrence of any of the above failures
- the FE simulation provides a remarkably accurate prediction of the braking torque and fault current resulting from various fault scenarios
- the largest braking torque occurs with a symmetrical short-circuit of a complete sub-motor
- the largest fault current occurs with a single turn short-circuit, but the resulting brake torque is very low
- it is noticeable from different fault scenarios that the braking torque (drag torque) variation with speed is rather like an induction motor characteristic. The peak torque disturbance occurs at low speed, where its effect is not dangerous to the vehicle control: at high speed the torque disturbance of a single sub-motor short circuit can be as low as 10Nm in the entire machine and is therefore relatively benign, as it may not even be noticed by the vehicle driver
- it can be seen that the short circuit current increases with increasing speed, but converges at a certain speed as the fault current is no longer dependent on the speed of the rotor. At lower speed the short circuit current is limited by the winding resistance and rises as speed rises, while at high speeds the short circuit current is limited by just the phase inductance and becomes independent of speed. This is demonstrated in equation 3.3, for short circuit current below
- machine temperature can alter the speed at which the peak braking torque occurs: the peak braking torque occurs at the speed where the resistance is equal to the reactance for the fault scenario considered (derived by differentiating the equation of drag torque – equation 3.3, with respect to speed and equating to zero), since the resistance is a function of temperature, as the temperature rises the resistance of the winding rises for the shorted phase(s), which means the drag torque occurs at a higher speed and vice versa

3.11 Preventing fault propagation

To prevent the propagation of any type of fault, it is essential that the fault in one sub-motor has little or no impact on the performance of an adjoining sub-motor, so that the healthy sub-motor can continue to perform at its optimum design point. This requires that the magnetic coupling between two adjacent sub-motors must be as low as possible. However the coils of two sub-motors share the same slot which means the coils can be thermally coupled. Figure 3.26 below shows the phase back EMF of a sub-motor, before and during a phase short-circuit fault, applied to the sub-motor adjacent to it. The phase back EMF drops by 3.3%, with no significant change in phase, which indicates that the healthy sub-motors can continue to operate, even during a fault on an adjacent sub-motor.

The flux plot in figure 3.27 (a) and (b) shows the no-load flux plot and short circuit fault applied to the phase C in sub-motor 1 respectively. This goes further to confirm that the flux linking the phase A in the adjacent sub-motor 2 is not significantly affected, which proves that the measured result agrees with the FE simulated model.

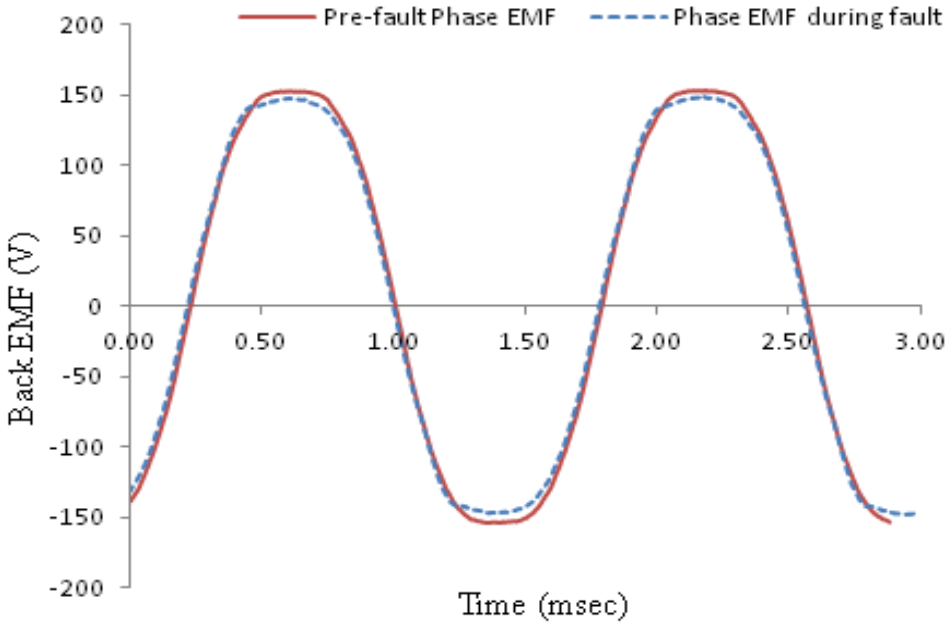

Figure 3.26. Measured pre-fault and during fault phase back EMF in an adjacent un-faulted sub-motor.

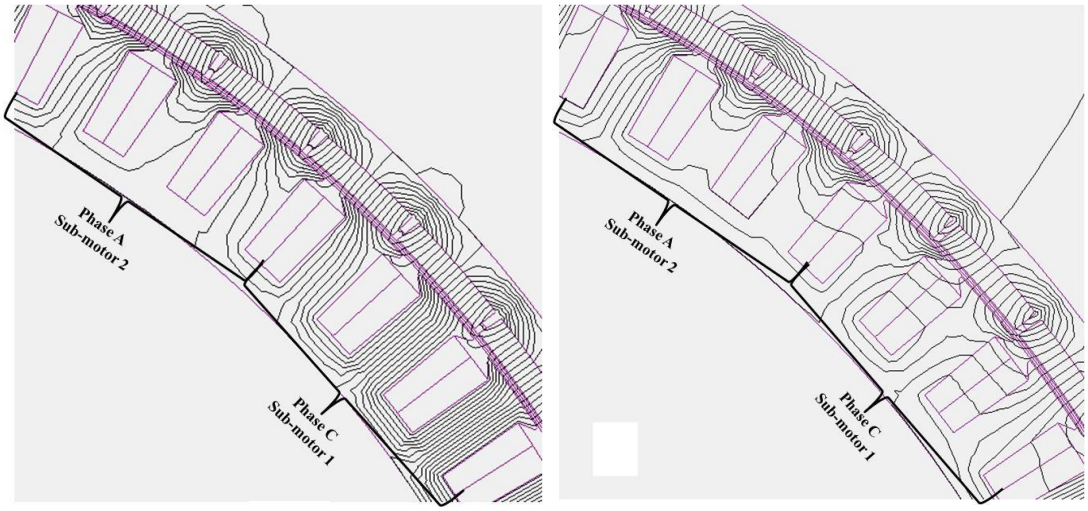

(a) (b)

Figure 3.27. Machine flux contour plot showing peak back EMF in phase A; (a) no-load magnet flux, (b) Phase C (sub-motor 1) short circuited.

3.12 Conclusion

The choices of slot and pole number combination for a motor suitable for an in-wheel electric vehicle drive application are analysed and discussed. The various electromagnetic aspects of a machine that is affected by the slot and pole number are also mentioned, with referenced works to further highlight the subject. A simulation against a standard drive cycle was done on the demonstrator motor. Also the methods and steps used for optimisation of the different slot and pole number were also discussed. Splitting the machine into a series of sub-motors has been shown to limit the brake torque in the event of a fault occurring at in the motor.

The financial cost of producing a motor split into eight parts, rather than only one, lies only in the need to bring out more connections to the power electronic converter. Because the inverters are closely integrated with the motor, this cost is trivial. However, the requirement to split the inverter into eight separate units has greater impact. It keeps the current drawn by any one power device at a manageable level, with relatively low current connectors, but the number of components in the entire system is greatly increased.

Safe operation is essential and it is important that there is no loss of vehicle control following failure of one motor. The work presented in this chapter has demonstrated for the first time that a high performance in-wheel motor can be produced with intrinsically safe characteristics, whereby the level of drag torque generated during fault can be

limited. This is achieved through a fault tolerant system architecture and electrical motor design that provides for high availability and ensures that no single fault drag torque exceeds 280Nm for over 100ms, as per the system functional safety requirement. The main thrust of the rest of this thesis is to improve the electromagnetic performance of the Protean in-wheel motor presented in this chapter by looking at novel method of construction of permanent magnet machines.

The demonstrator motor has been extensively simulated and tested for a number of different fault scenarios. It has been shown through both simulation and experiment that the peak torque disturbance following a fault is less than 20% of the value which is likely to cause control problems for the driver. This very low value is achieved through a combination of design for an appropriate inductance to limit fault currents and through dividing the motor into a series of eight independent sub-motors. Without this division the fault torque is predicted to be eight times higher i.e. 400 Nm, which is 40% greater than safety permits. Experiment has shown that the sub-motors are only very weakly coupled magnetically, so that failure of one sub-motor should not significantly affect the operation of others.

Chapter 4

Stator Design; Improving Machine Performance

The main work of this PhD research involves taking the previously designed Protean electric motor and exploring novel methods of construction, in order to improve the performance of the machine without jeopardising the machine's reliability, fault tolerance and also to reduce the diameter of the machine to fit a small rim size. The machine component that has been researched deeply in this work is the stator; a simple castellated stator design having open slot, with a magnetic slot wedge to close the slot and pre-pressed windings to improve the slot fill factor. Since the overall diameter of the machine is to be reduced, this means the rotor design will deviate from the previous Protean electric motor construction. This section will present the effect of the slot wedges on the machine performance and compares the slot wedge stator to a conventional partially closed slot stator.

4.1 Introduction

In order to improve the performance of a permanent magnet machine with fixed diameter and axial length, there are three main design parameters which can be varied;

a) the magnetic loading, which can be improved by changing the magnet air-gap flux density
b) the electric loading, which can be improved by changing the fill factor of the stator slot, so the slot current density is reduced or the slot turns number increased
c) the cooling capability, which means the current into the stator winding can be increased

To improve the performance of the machine studied in this work, a novel method of construction has been researched, using the FE method for magnetic modelling of electric machines. The research involved achieving the optimum performance for a high torque density machine, whose stator has pre-pressed coils placed onto each tooth of the stator and using slot wedges to hold the coils in the slots to prevent the coils moving due to any acting forces and also provide magnetic linkage compensation.

Slot wedges can be non-magnetic or magnetic, the choice to use magnetic slot wedges impacts the magnetic performance of the machine; reducing proximity loss, reducing cogging, increasing leakage flux and increasing magnet induced voltage. Magnetic slot wedge has inferior mechanical properties to non-magnetic slot wedges and the choice varies between manufacturers (non-magnetic wedges are widely used in North America). The magnetic wedge typically consists of a high percentage of iron powder, and due to the presence of the iron powder the slot wedge becomes brittle, causing it to be more susceptible to failing compared to the non-magnetic wedge. In [102, 103] failure analysis was presented on a motor, which was due to the magnetic slot wedge failing and causing the motor to go out of service. Any mechanical vibration on the motor causes moving of the slot wedge and over time this movement gets bigger in magnitude and leads to the slot wedge failing. When one slot wedge has been lost, the electromagnetic forces in the motor will cause damage to the other slot wedges within the vicinity. The driving environment for the in-wheel motor is far from benign, and mechanical vibration might be an issue for the slot wedges.

To prevent the slot wedge from failing it is important that the magnetic and thermal stress is kept within the accepted limit with mechanical and electromagnetic vibration minimised. Also [102] specifies the use of a "wet process" when fitting the wedge.

4.2 Effect of wedge structural design

Having a magnetic slot wedge as part of the stator design can on one hand improve the flux linkage into the teeth at no-load by providing extra path for flux, and on the other hand can reduce the flux linkage into the teeth at no-load by shunting the magnet flux across the air-gap [104]. With all these in mind and the aim of understanding the influence of one on the other, the cross-sectional shape and depth of the wedge will be researched, and also to achieve an optimum wedge design for the machine to be built for this work.

4.2.1 Effect of wedge thickness

The influence the wedge thickness has on the machine performance is studied, when the machine is running on no-load. Time stepping 2D FE analysis was used to get the machine no-load loss and flux linkage and static 2D FE analysis was used to determine the inductance for different wedge thickness.

The flux-linkage of the coil is directly influenced by the thickness of the wedge and depending on the machine geometry and slot and pole combination, the effect of this wedge thickness on the flux-linkage is small, as shown in figure 4.1. The wedge thickness was varied between 1mm and 3.2mm in steps of 0.2mm. The machine is a 72slot/64pole machine and it is clear that there is an optimum wedge thickness, but the changes in the flux-linkage are not significant as the wedge thickness is varied.

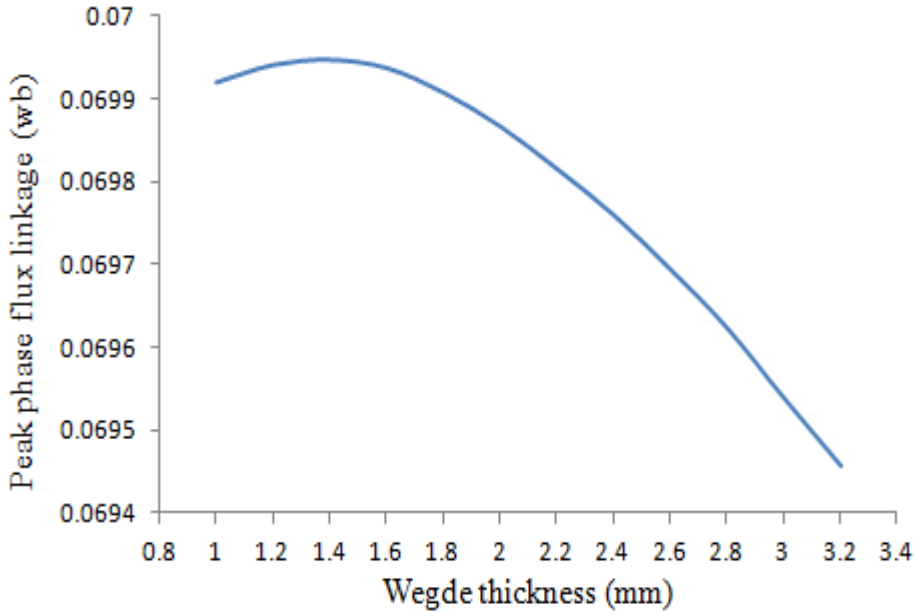

Figure 4.1. Variation of flux linkage due to magnet flux, with magnetic wedge thickness.

The flux density perturbation can be minimised when using wedges, which can in turn reduce induced magnet eddy current. The no-load losses considered are the stator iron, magnet and slot proximity losses; as the wedge thickness is varied significant change in the magnet and slot proximity losses can be observed, while the change in stator iron loss is very insignificant. Figure 4.2 shows the variation in these losses; the slot proximity loss increases as the wedge thickness is reduced, this is due to how much of the magnet flux penetrates the wedges, exposing the windings to this varying field. Figure 4.3 shows the magnet loss due to the slotting effect; this depicts the magnitude of the magnet eddy current loss with wedge thicknesses of 2.2mm and 1mm, the magnitude is lower with 2.2mm wedge thickness as the variation of the air-gap flux density when the magnet is under the slot then under the tooth is lower, this is because more flux is conveyed into the tooth via the wedge when the thickness increases. Figure 4.4 shows the variation of the phase inductance with wedge thickness; as expected this is a linear relationship, as more flux is encouraged to circle around the wedge.

The cogging torque is expected to be reduced as the thickness of the wedge is increased, because the change in air-gap reluctance with position is minimised. From the total no-load losses, it can be concluded that any wedge thickness of 2.2mm and above will be a good design choice, however there isn't much added to the machine performance or mechanical strength of the wedge with a large thickness above 2.2mm, so 2.2mm was chosen as a final value for the thickness.

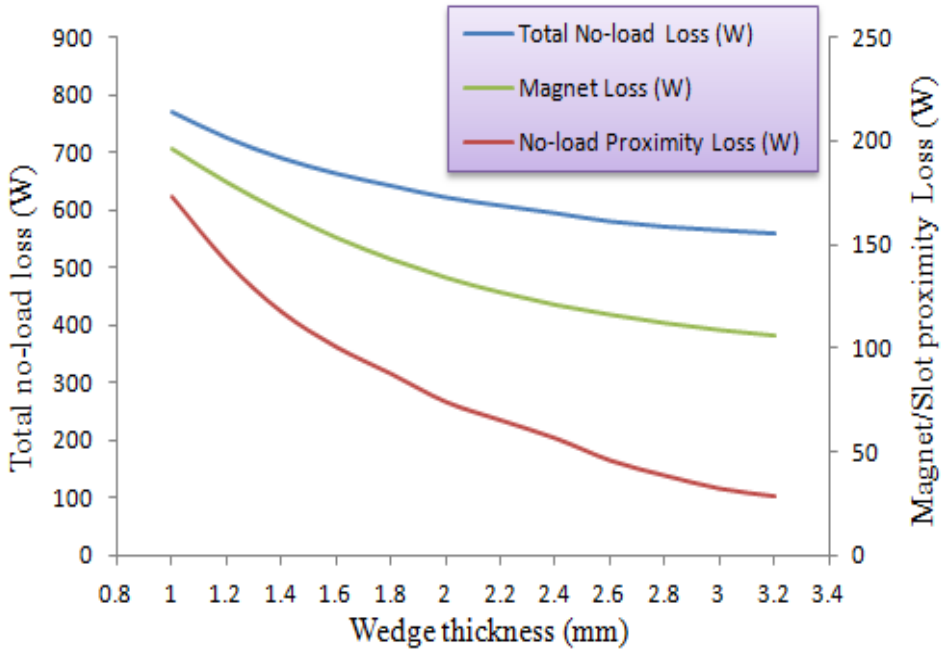

Figure 4.2. Variation of no-load losses with magnetic wedge thickness at 630rpm.

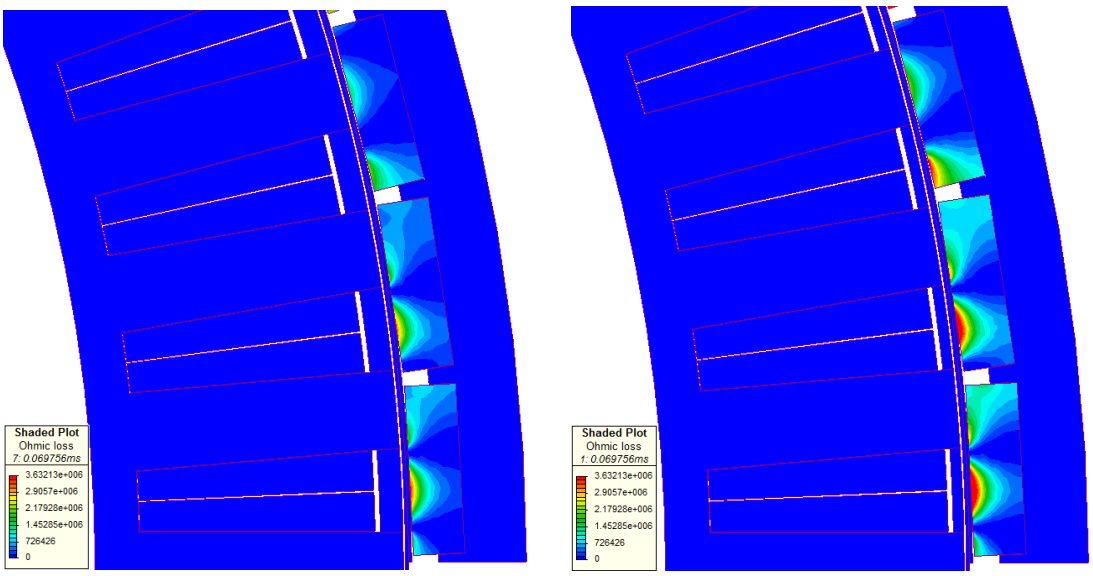

(a) (b)

Figure 4.3. Machine eddy current ohmic loss distribution at 630rpm; (a) wedge thickness of 2.2mm, (b) wedge thickness of 1mm.

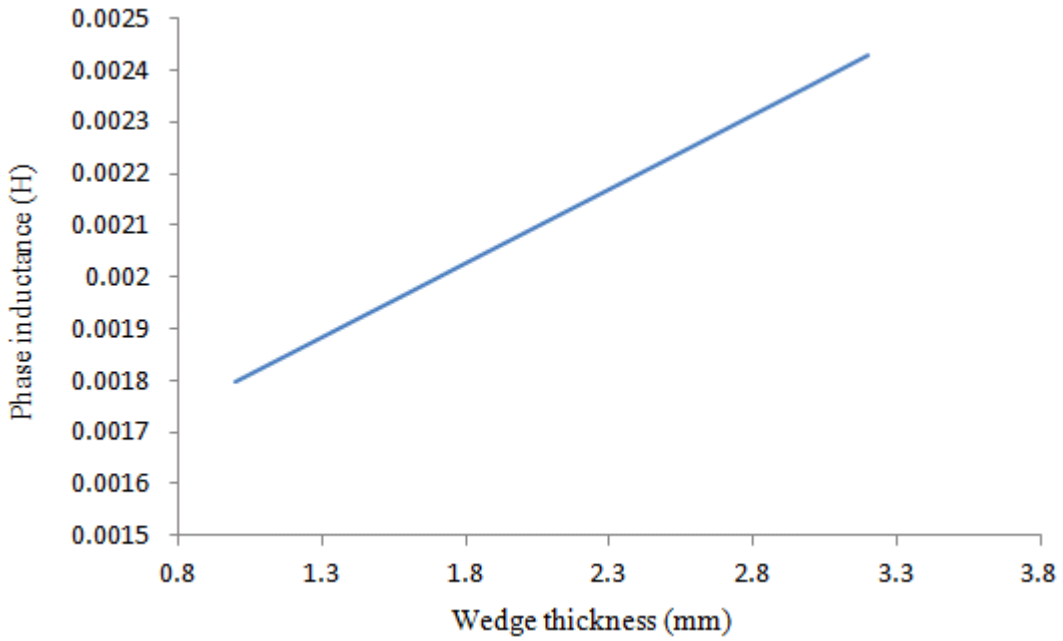

Figure 4.4. Variation of phase inductance with magnetic wedge thickness.

4.2.2 Effect of wedge shape

The wedges can be shaped in different ways depending on their effect on stator tooth saturation, the ease of cutting the required shape and fitting them into the machine during production. Due to the chosen thickness of the wedge, the effect of wedge shape upon stator tooth saturation is of no significance, hence making it of low priority when deciding what shape of wedge to use. Figure 4.5 shows the various wedge shapes and method of insertion onto the stator tooth, while figure 4.6 shows the line – line back

EMF for the various types; evidently the wedge shape has no effect on electromagnetic performance of the machine, as mentioned earlier.

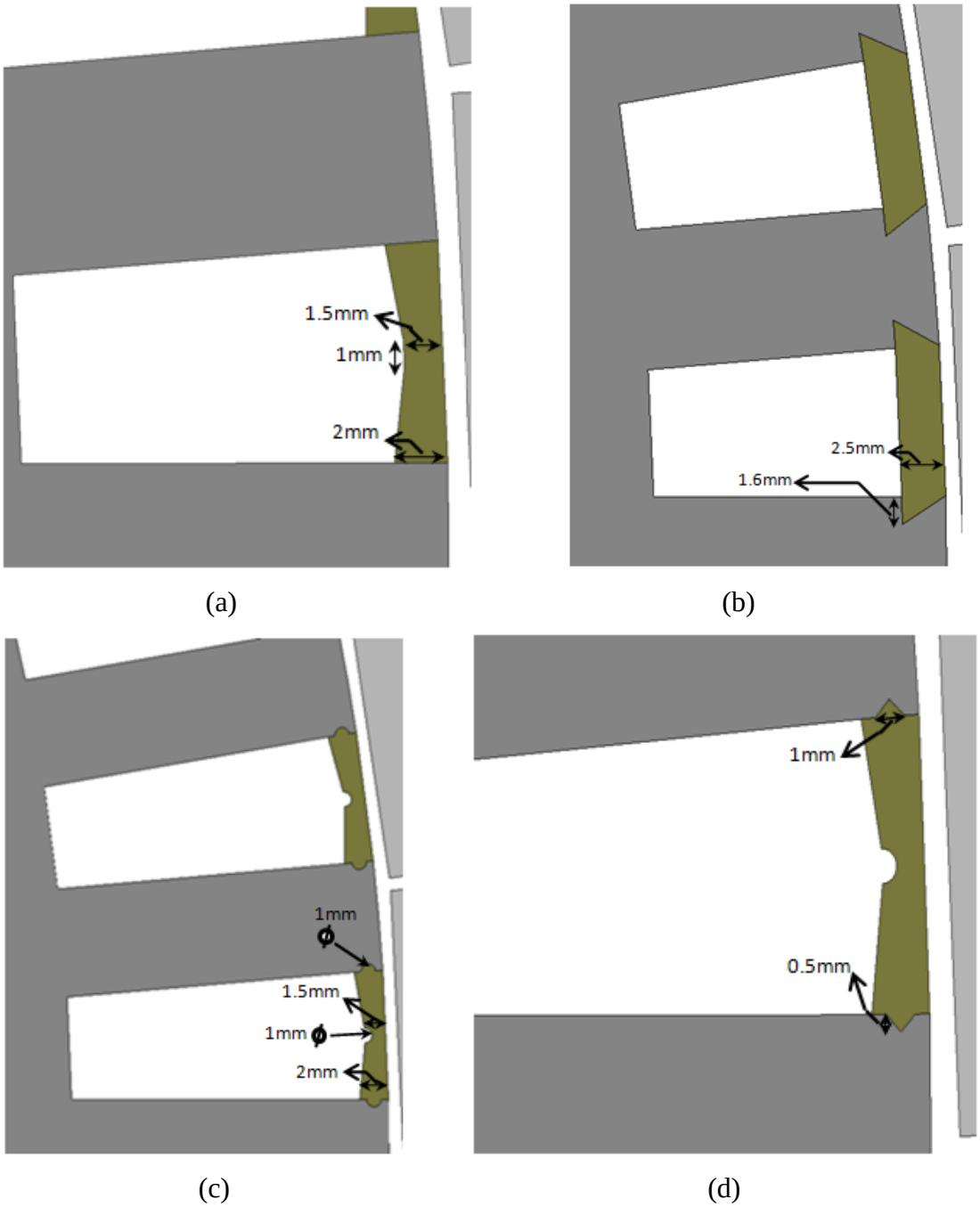

Figure 4.5. Wedge shapes and method of insertion into stator tooth; (a) wedge type 1, (b) wedge type 2, (c) wedge type 3, (d) wedge type 4.

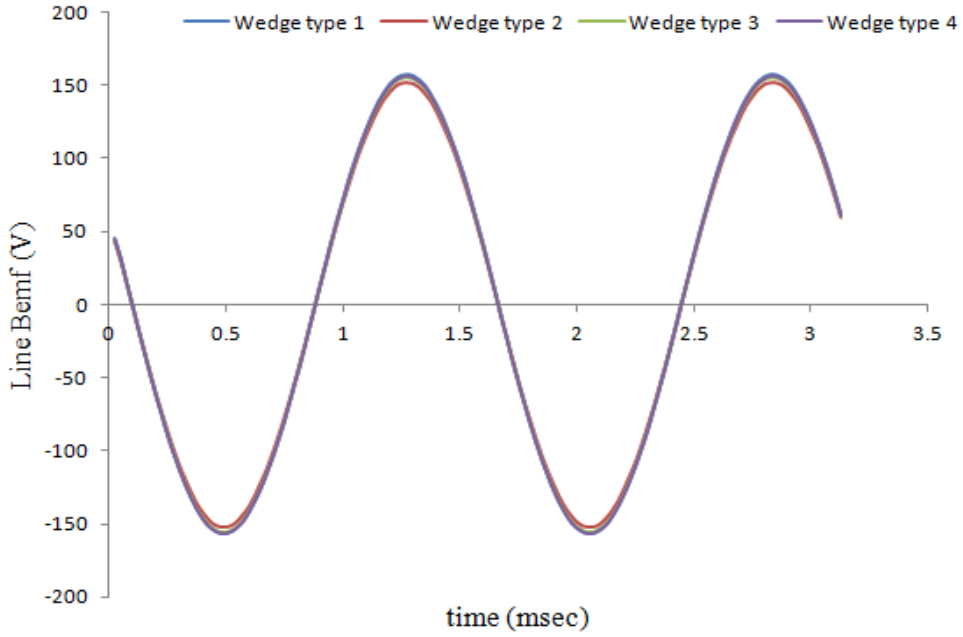

Figure 4.6. Line – line back EMF for the various wedge shapes, at 630rpm.

The milling process of the wedges makes it possible to have only a few design shapes, it is also important that for high volume production the wedge shape can easily be cut at the precise angle so as to be in perfect tolerance with the teeth notch. In [105] different possible wedge designs are discussed presenting their pros and cons; the trapezoidal design is the easiest shape to mill and has been proposed as the design choice for the machine, figure 4.7 shows the trapezoidal wedge.

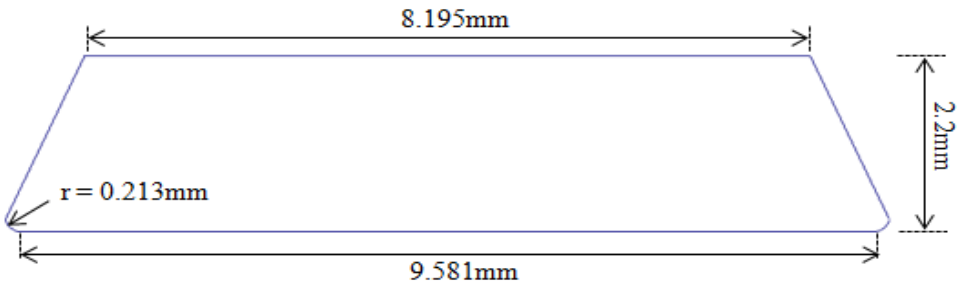

Figure 4.7. Slot wedge structural design.

It is a design consideration to have round edges at the base of the trapezoidal wedge design, to ease insertion of the wedge into the slot. The wedge fitting on the stator tooth is shown in figure 4.8, the wedges have been cut at the appropriate tolerance so as to fit tight enough into the stator tooth notch but not too tight that it is hard to slide into the tooth.

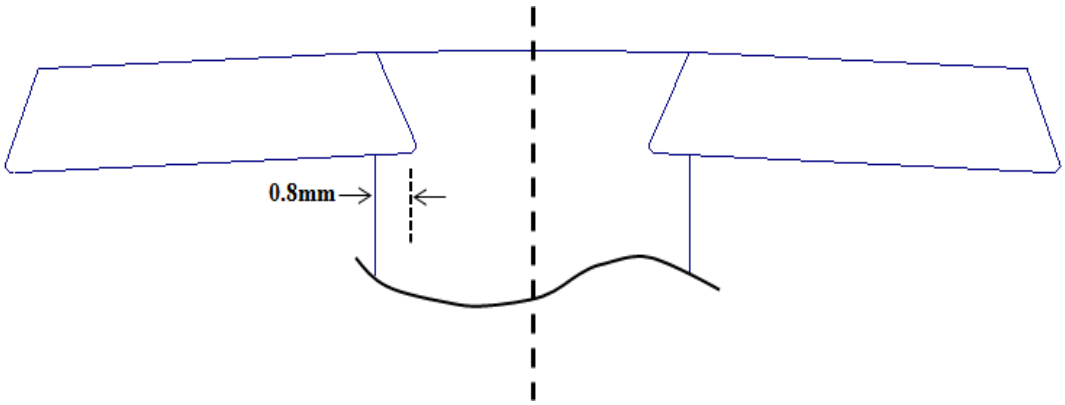

Figure 4.8. Slot wedge tooth penetration and tooth tip design.

4.3 Comparison of the magnetic influence of slot wedge

The design method chosen for the slot opening influences the magnetic circuit path of the machine and can improve or degrade the magnetic loading and other properties of the machine. The comparison done in this section includes; an open slot, a semi-open slot and slot wedge design; the fill factor chosen for the various designs was 0.62, although this high fill factor cannot inherently be achieved with the tooth tip design, but for the purpose of this comparison all things are kept similar. This high fill factor is achieved by pre-pressing the coils before placing onto the stator teeth; this will be discussed fully in the next chapter. Figure 4.9 are images of the different slot opening design structures to be compared in terms of the following properties; total no-load losses, flux linkage, inductance and no-load space harmonics in the back EMF.

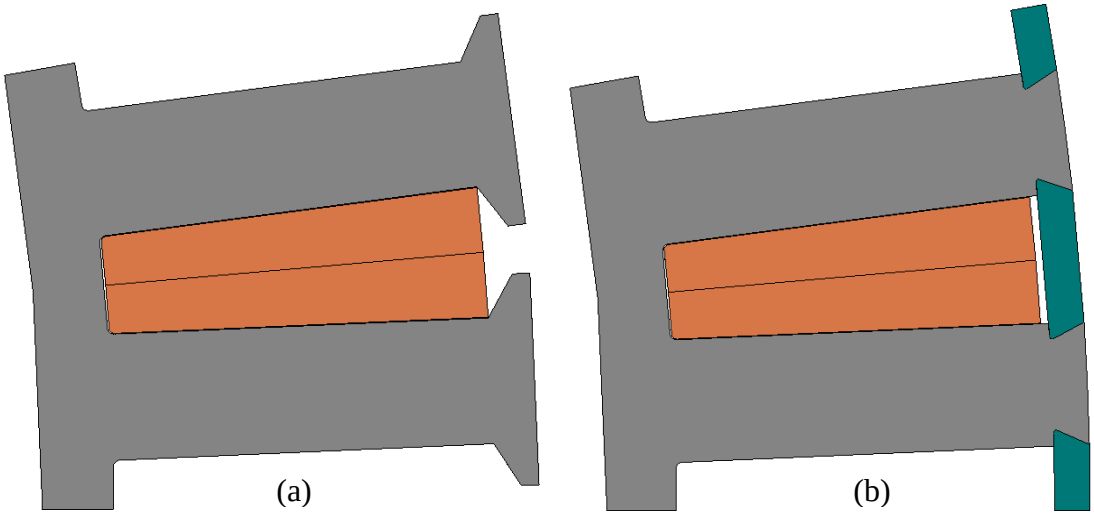

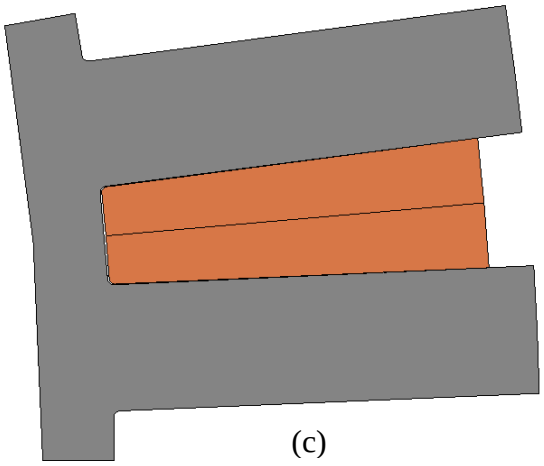

(c)

Figure 4.9. Machine slot opening designs; (a) design with tooth tip, (b) design with slot wedge, (c) design with open slot.

The no-load losses are expected to be a lot worse in the open slot design, due to the large change in position of the air-gap flux density caused by the slotting effect, this results in increased slot proximity and magnet eddy current losses. Table 4.1 shows the total no-load losses for the entire machine for the various slot opening designs shown in figure 4.9 above; the stator iron loss has no significant change for the different designs, as mentioned the slotting effect causes the magnet loss to be worse in the slot wedge and opens slot designs, also the winding loss is worse in these designs due to the exposure to the air-gap field variation and the eddy current loss in the slot wedge is only 0.000088% of the total no-load loss in the slot wedge machine design, so its contribution to the total no-load losses is of no significance.

Table 4.1. Total no-load losses in machine.

	Stator Iron Loss (W)	Magnet Loss (W)	Winding No-load Proximity Loss (W)	Wedge Loss (W)	Total Loss (W)
630rpm					
Tooth Tip Design	380.27	42.54	6.07	N/A	428.88
Slot Wedge Design	399.95	150.53	67.53	0.00055	618.02
Open Slot Design	398.06	293.5	79.33	N/A	770.89
1600rpm					
Tooth Tip Design	1524.66	280.13	34.44	N/A	1839.22

Slot Wedge Design	1619.06	977.25	460.89	0.0035	3057.2
Open Slot Design	1608.54	1908.25	536.66	N/A	4053.46

The spatial harmonics of the magnet flux in the air-gap are a function of the slot opening, because the slot opening acts to create a non-sinusoidal waveform of the air-gap field, so it is expected that the spatial harmonics changes when the slot opening design changes. Figure 4.10 shows the air-gap flux density for the various designs. However it is worth mentioning that depending on the winding configuration on the machine's stator, the spatial harmonics are attenuated and might not be influential in the torque ripple of the machine. The result of the air-gap flux density was obtained from probing the air-gap flux density of a FE static solution.

The line – line back EMF was obtained from a transient with motion model for the various designs and is shown in figure 4.11 below. As seen the highest peak back EMF was achieved in the design with an open slot design. This was checked by analysing the average peak flux density in the tooth directly underneath a magnet in order to calculate the back EMF of a phase, the average peak flux density in the tooth are; 1.557T for the tooth tip, 1.5866T for the slot wedge and 1.6002T for the open slot design. Figure 4.12 shows the harmonics content in the back EMF and the lowest fundamental is seen in the tooth tip design. It can be inferred that due to magnet flux shunting, the least flux is linked into the tooth in the tooth tip design compared to the slot wedge design, this can observed in figure 4.13 by counting the flux lines in the teeth. Due to the tooth saturation where the slot wedge penetrates the tooth in the slot wedge design, the open slot design shows the most flux linkage of all three designs, as can be seen in the back EMF waveform. Finally figure 4.14 shows the phase inductance variation for the different slot opening designs; as expected the tooth tip design has the highest value of phase inductance due to the increased flux shunting across the tooth tip when compared to the other designs.

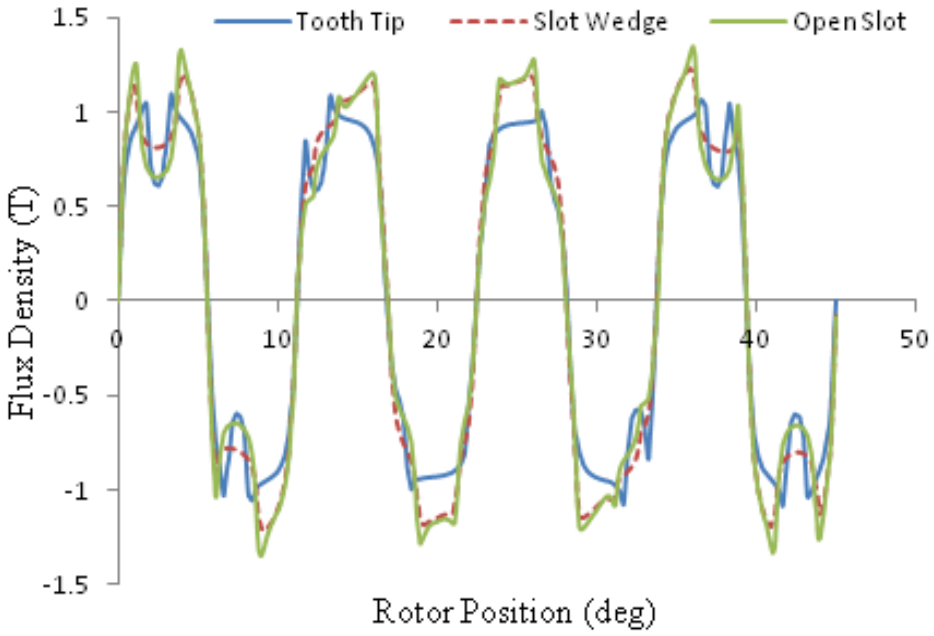

Figure 4.10. Magnet air-gap flux density for the various slot opening designs.

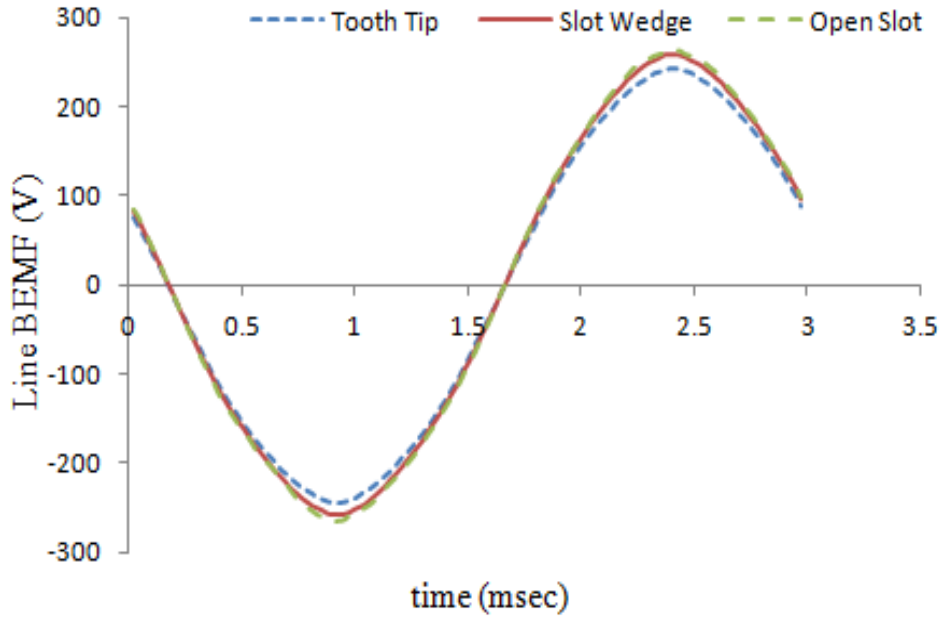

Figure 4.11. Line back EMF at 630rpm.

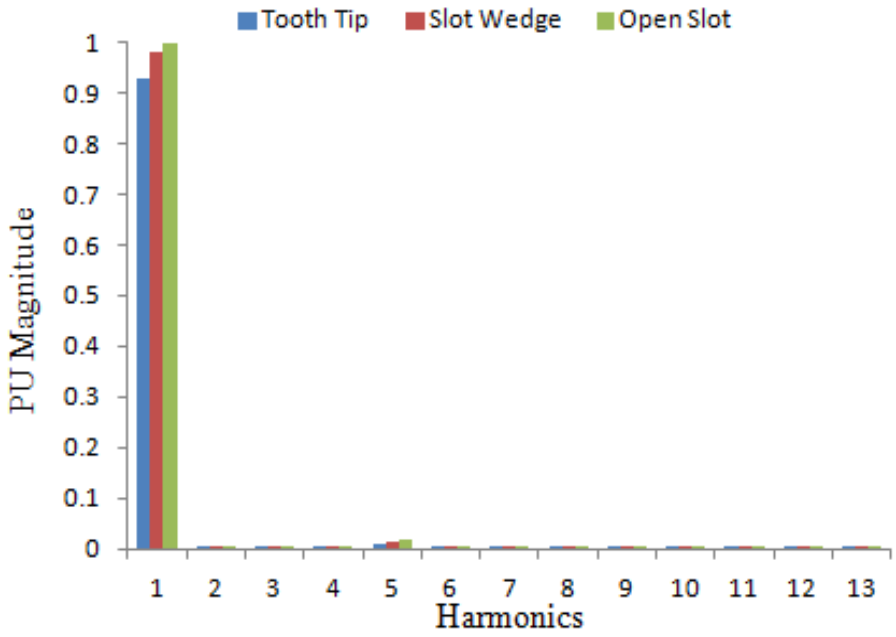

Figure 4.12. Line back EMF harmonic content for the various slot opening designs.

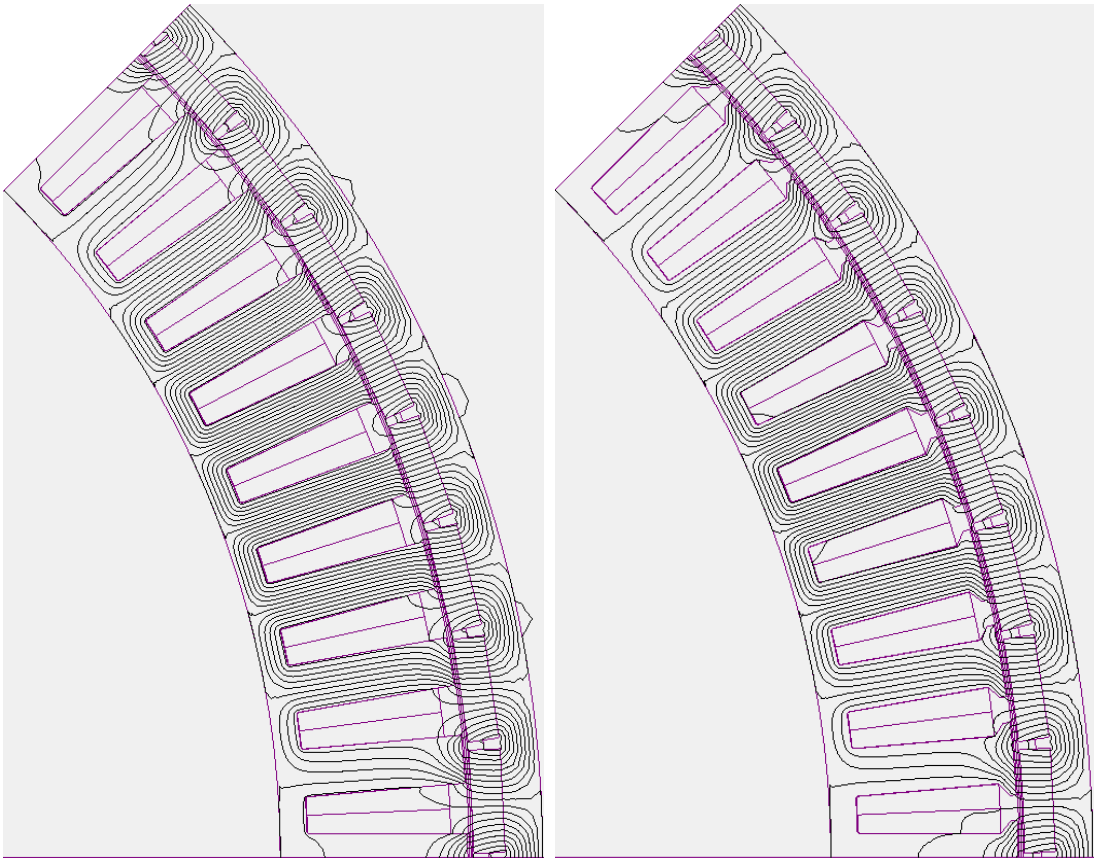

(a) (b)

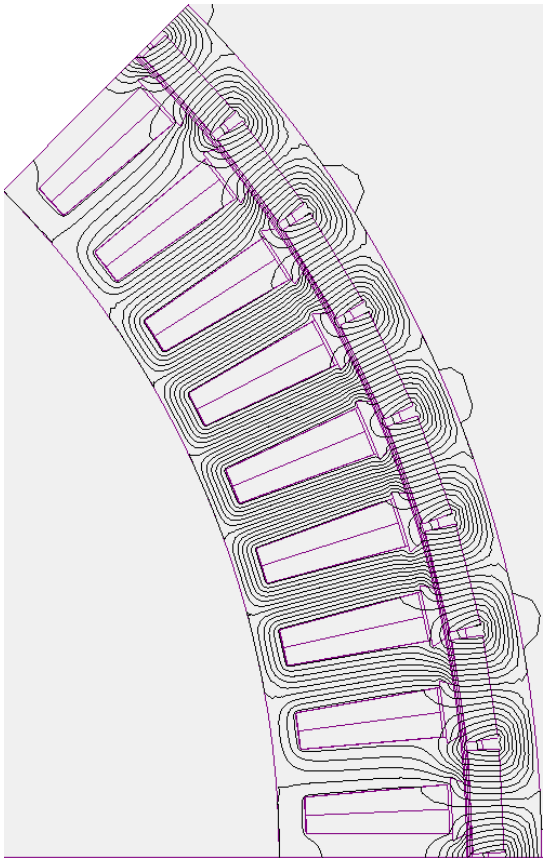

(c)

Figure 4.13. Contour flux plot for various designs; (a) design with open slot, (b) design with tooth tip, (c) design with slot wedge.

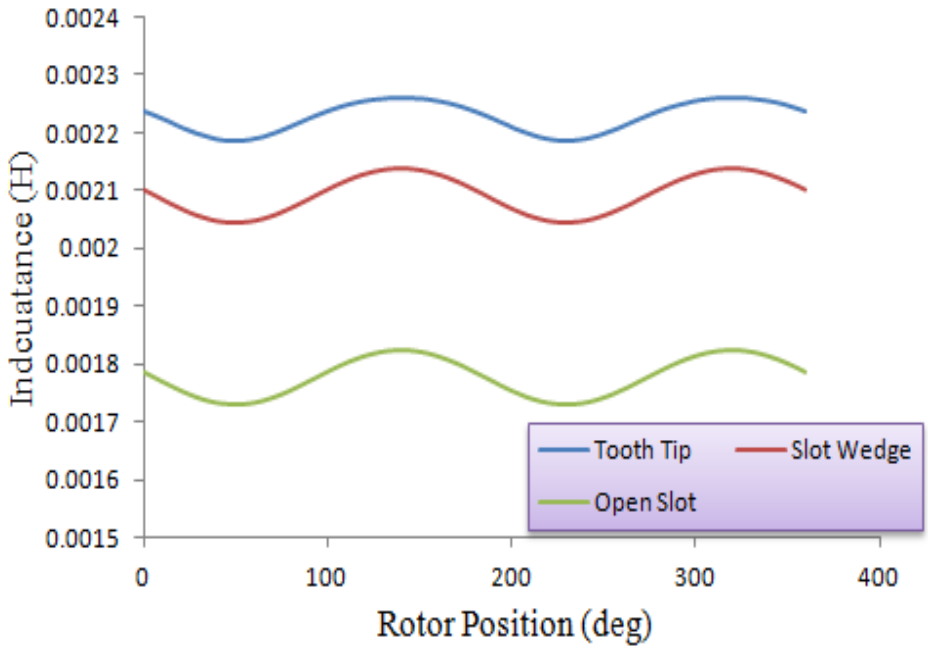

Figure 4.14. Inductance variation with rotor position for various slot opening designs.

The torque against the sum of the AC copper loss and magnet loss at a speed of 630rpm was obtained from the FE model and peak phase current from 0 amps to 40 amps in

steps of 5 amps was applied; figure 4.15 shows a graph comparing all the different slot opening design. At light loading the tooth tip design has the least loss at the same torque output, but as the machine loading is increased the torque per AC copper and magnet losses in the tooth tip design starts getting worse compared to the other designs.

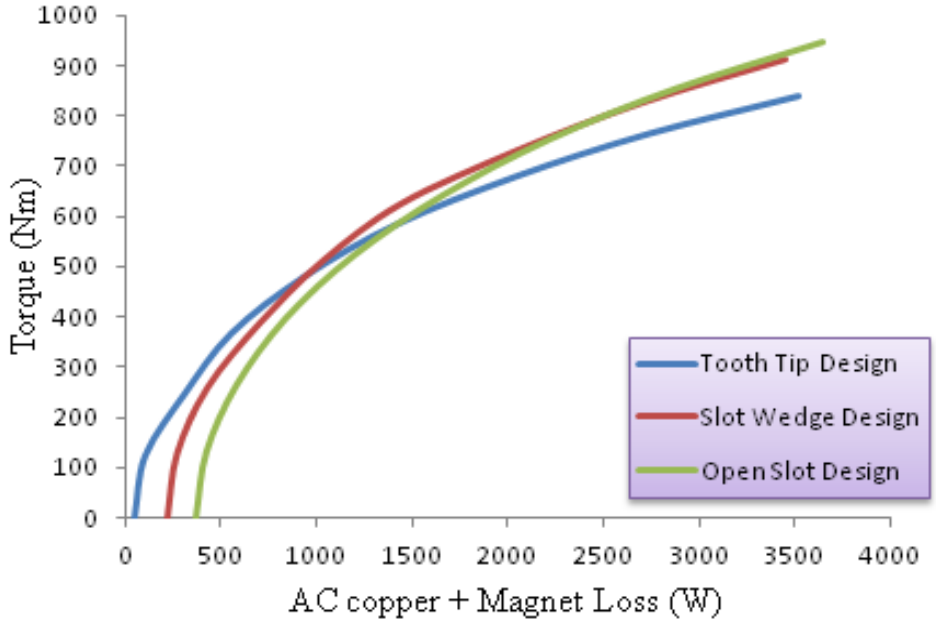

Figure 4.15. Torque against Copper and magnet loss at a speed of 630rpm.

4.4 Slot wedge properties

The electromagnetic benefits of using magnetic wedge over non-magnetic type has been presented in the previous sections, also how the wedge shape is chosen has also been discussed.

In the past conventional magnetic wedges were milled out of layered laminated materials. When small forces act on the wedge this will lead to delaminating of the wedges and eventually complete machine failure [105], as shown in figure 4.16.

Figure 4.16. Delaminating of a laminated magnetic wedge [105].

4.4.1 Wedge manufacturer selection

The magnetic wedge was chosen as the wedge to be used in the motor design. Samples of wedges were obtained from two magnetic wedge manufacturers; SPIndu wedges from Austria and Camawi wedges from India. FE analysis was applied to check the effect of the wedges on the magnetic properties of the machine, figure 4.17 below shows the BH-curve for the two wedge materials, which was used to create new materials in the FE software to represent the wedge component.

The effect that both slot wedges have on the machine performance was established, which allows selection of the best wedge type. The magnetic field strength across the slot wedge was calculated to get the flux density; with a peak current of 26.2A, the MMF in the slot (66 turns) is 1732A-turns and assuming there is no flux drop down the tooth or flux leakage, the magnetic field strength across the slot wedge is 225000A/m. Using the BH-curve below the flux density for the SPIndu wedge is 0.675T and 0.85T for the Camawi wedge.

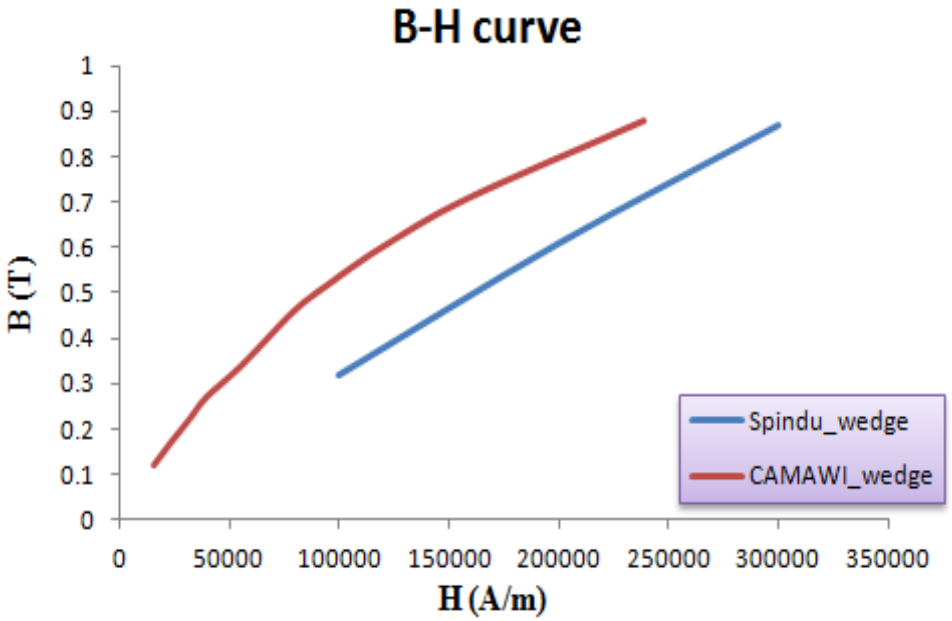

Figure 4.17. B-H curves for the SPIndu and Camawi wedges.

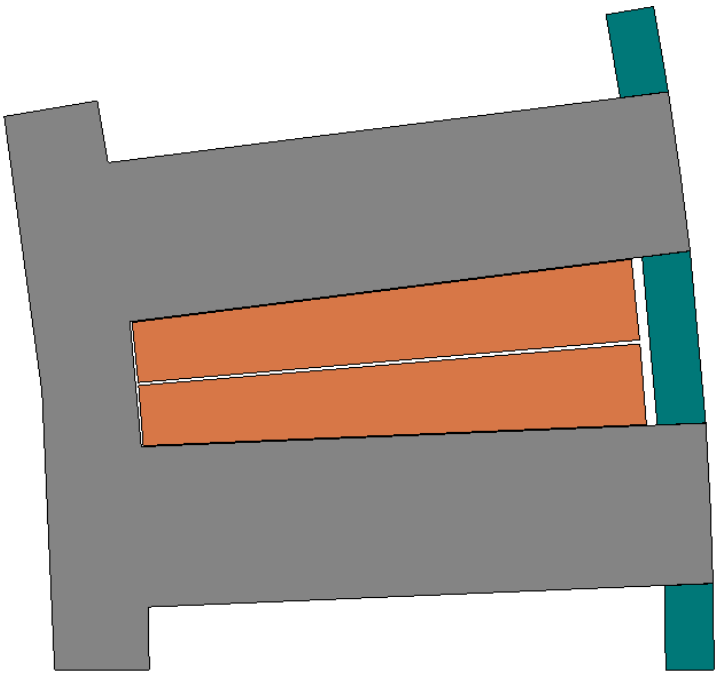

Figure 4.18. FE model used for analysis of the magnetic slot wedge.

The FE Model in figure 4.18 above is used to calculate the flux density across the slot wedge, when the peak current of 26.2 is applied to the winding. The flux density across the slot wedge is calculated to be 0.583T for the SPIndu wedge and 0.776T for the Camawi wedge. The reason the calculated values are different from the FE model values is because the calculated values does not consider the MMF drop along the tooth. Since the main drive for the machine design is to improve the torque performance, the FE model was used to calculate the average torque performance; the average torque when the SPIndu wedge is used is 82.42Nm and 82.02Nm when the Camawi wedge is used. There is no significant variation in performance when either of the wedge types is used, so the SPIndu wedge was chosen for the motor design, due to ease of sourcing.

4.4.2 SPIndu wedge

The SPIndu wedge is claimed to be a breakthrough in magnetic wedges manufactured by the SPIndustries, it has an extremely good mechanical property compared to the conventional magnetic wedge. The SPIndu wedge is isotropic having the same mechanical constancy in all direction, because the wedge is manufactured by using a rolled glass cloth, pressed along with a mix of iron powder and resin at a predetermined press magnitude [105].

The wedge is expected to last for the motor life time at the rated temperature: a variety of tests have been carried out on the SPIndu wedge. The SPIndu wedge used for the wedge study is called the SPInduwedge F HP, which is a class F material with an

operating temperature of 155˚C and has a flexural strength of 370Mpa at 23˚C and 210Mpa at 155˚C from a bending test carried out on the wedge. The various tests done on the wedge are: bending test (flexural strength and module elasticity), delamination test (caused mainly by fitting the wedges by hammering them in) and heat deflection temperature [105]. As compared to the conventional magnetic wedge, the SPIndu wedge has a different way of delaminating, this is shown in figure 4.19; this was as a result of carrying out a cleavage test, whereby a load is applied to the wedge and it is show that the SPIndu wedge has a different type of fracture to a conventional wedge, only a small area of the wedge is damaged and the internal structure of the wedge remains intact [105].

Figure 4.19. Test SPIndu wedge after mechanical failure [105].

4.5 Conclusion

The use of non-magnetic and magnetic slot wedges in different types of machine application has been discussed in this section, presenting the pros and cons of the two types of slot wedge compositions. The magnetic slot wedge has been employed in the machine design studied in this thesis, with electromagnetic studies carried out to present the advantages of having the magnetic slot wedge and slot wedge materials from two separate manufacturers have been compared. The SPIndu Wedge from an Austrian manufacturer was chosen as the wedge to be used in the machine and technical report from the manufacturer presented in [105]. Research into the shape and thickness of the wedge was carried out and a wedge thickness of 2.2mm has been chosen. The advantages of having the machine designed with the wedge are; simple stator construction can be employed and the coils can be pre-wound and pressed to improve the slot fill before being placed onto the stator tooth, pre-wound coils are discussed fully

in chapter 5. Also it has been shown that not much is lost in terms of electromagnetic performance when a machine is designed with slot wedge, as the slot wedge conveys additional flux into the tooth even when the magnet is not underneath the tooth, however there is significant rise in the magnet eddy current loss and winding loss due to the magnet field.

Chapter 5

Stator Design; Coil Pressing and Integrity Tests

With the stator slot opening design studied in Chapter 4, it makes it possible to pre-press the stator coils before sliding them onto the stator teeth, this will help improve the slot fill factor of the machine. This section presents the work conducted on pressing the stator coils and carrying out tests to check the integrity of the coils. The constraints and challenges involved with pressing the coils will be discussed, such as the level of pressure applied during the crushing process, whereby the shape of the cross-section of the wire can be altered.

5.1 Introduction

The slot fill factor can be greatly increased when pressed coils are used, this in turn can be used to reduce the current density of the winding and can thermally or electrically improve the torque of the machine. In [106], the method of pressing the coil is presented, showing the length of the end-winding arc, as shown in figure 5.1.

In this work, there are constraints and challenges imposed on the total axial length of the coil. The machine has to fit into a small envelope of the wheel, this poses a limit on how far the over-hang can extend. A new method of pressing the end-winding has been investigated. The slot area of the stator makes it difficult to get a high fill factor, also there is a certain level to which the coil can be pressed before the insulation integrity is jeopardised: this must be considered. The bending radius and crossovers are key areas to focus on when the coils are pressed, as these are potential weak points.

An Ansys model showing deformation and stress points when a coil is pressed will also be shown, along with a detailed picture of a cut-through section of the actual coil, showing the wire cross-sectional shape after pressing.

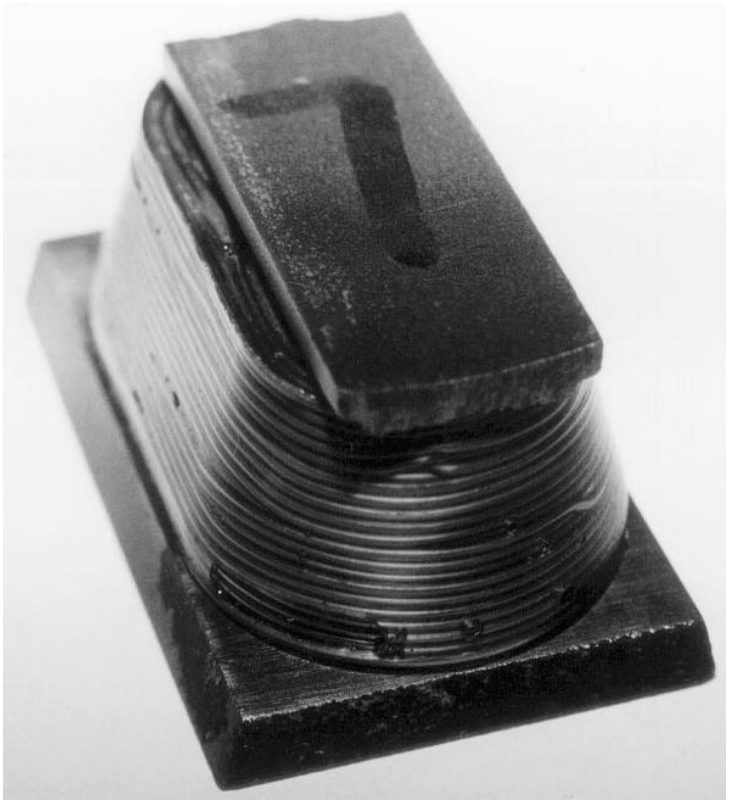

Figure 5.1. Prepressed winding used in a powdered iron core, permanent-magnet machine [106].

5.2 Winding and pressing of coils

In order to produce the coils the stator dimensions have to be known, figure 5.2 shows the stator dimensions and the design of the stator will be presented later in Chapter 6. The coils wound for the machine are to have 33 turns and a coil that is not pressed typically has a slot fill factor of 0.43 (bare copper), so for a slot area of 164mm^2 the conductor diameter will be 1.17mm. The slot fill factor to be achieved after the coil pressing is 0.62 (bare copper), so for the same slot area of 164mm^2, the conductor diameter is expected to be 1.4mm.

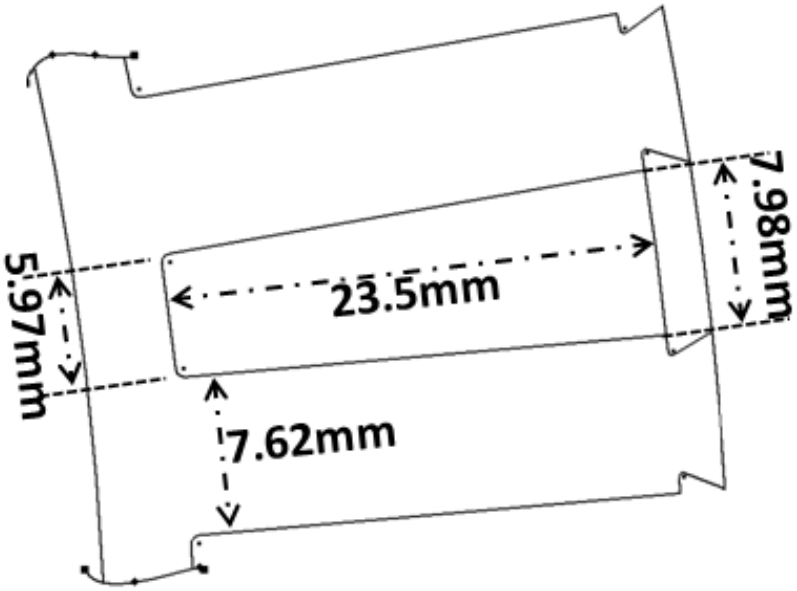

Figure 5.2. Stator dimensions for coils wound and pressed.

Figure 5.3 shows the tool (with its components) used in pressing the coil, the tool is made up of a die having a cavity in which the coil is pressed, a punch that is used to push the coils into the die cavity and a bobbin onto which the coil is wound, dimensions of the pressing tool are shown in appendix C.

Figure 5.4 shows a coil being wound on the winding machine and the coils are wound in two layers, one layer consists of 17 turns of a wire having 1.48mm diameter, therefore the total height of that layer will be 25.16mm and the width of the two layers is 2.762mm, as shown in figure 5.5. The coil is then pressed to a height of 23mm (defined by the depth of the stator slot) and half the slot width, which is 3.655mm at the top and 2.65mm at the bottom, as shown in the pressing tool drawing (appendix C). This gives an idea of how much the coils are compressed.

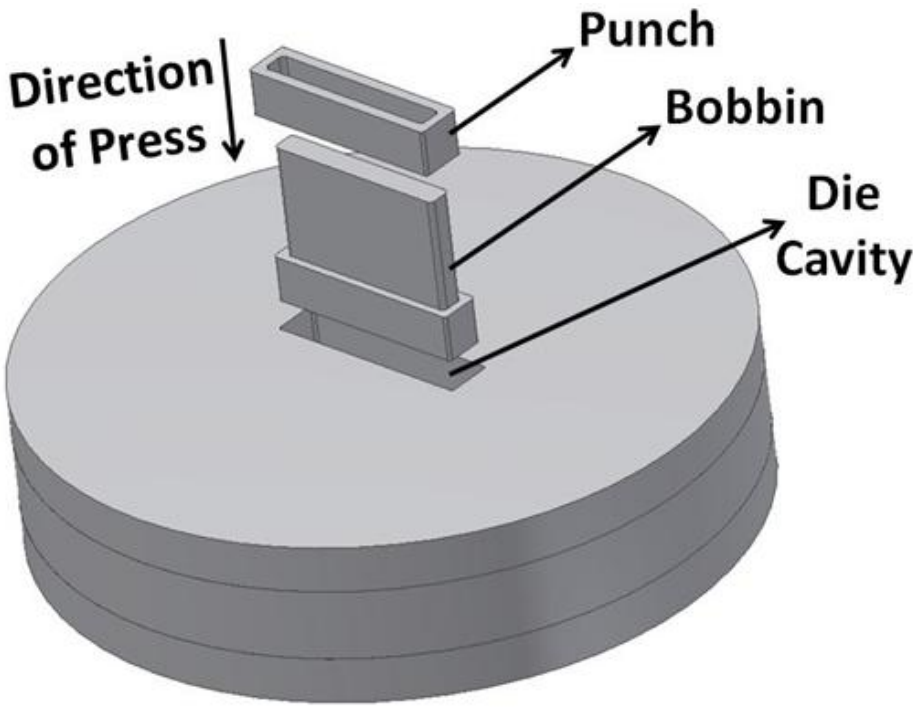

Figure 5.3. Press Tool, showing the different parts.

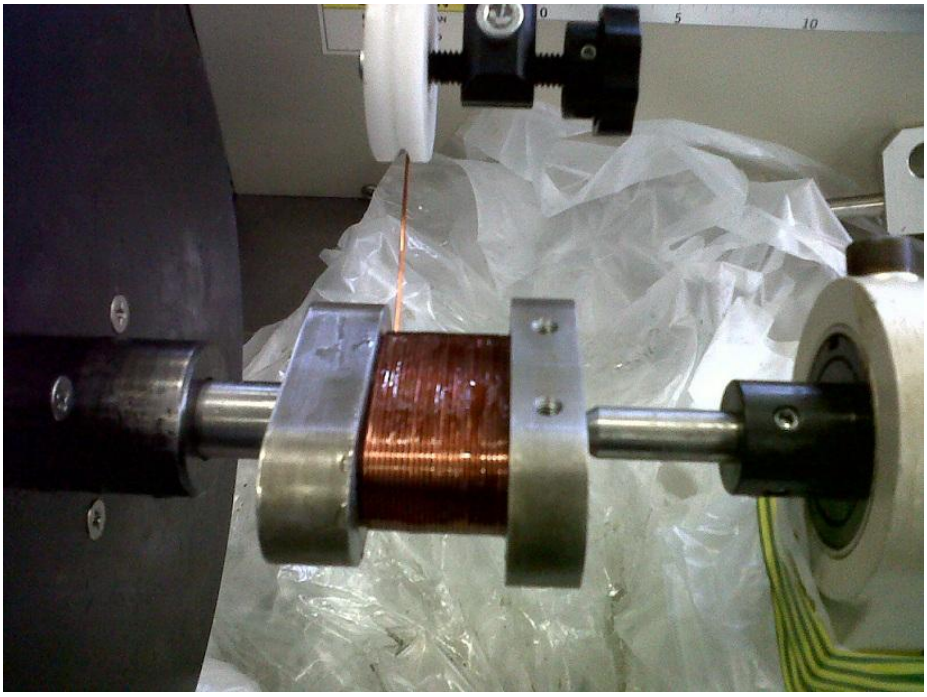

Figure 5.4. Machine coil winding.

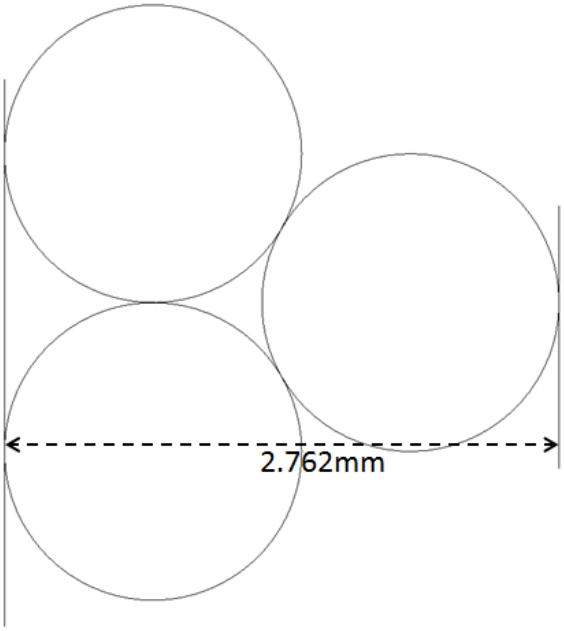

Figure 5.5. Initial coil winding.

5.3 Effect of coil pressing

When a coil is pressed the shape of the cross-sectional area changes from its circular nature to a hexagonal one, which develops sharp edges where the insulation could crack and present weak spots for failure on the wire, this can be seen in figure 5.6.

The FE package Ansys was used to carry out an FE stress analysis to determine how the applied force propagates across the turns of the coil, the main stress points and the shape of the conductor when pressed. For simple modelling, seven turns were assumed in the die cavity to reduce computation time of the FE calculation.

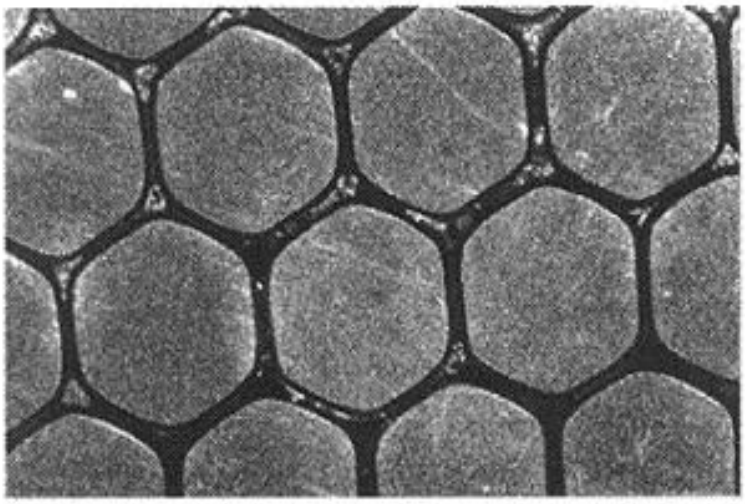

Figure 5.6. Cut through section of pressed coil, at a pressure of 800MPa [106].

In Ansys an explicit dynamic model was setup as follows:

- Explicit materials were chosen to be used for the different components (conductor, insulation and steel), table 5.1 gives the mechanical properties for these materials.
- The contacts between the components are very important; a bonded contact was applied between a conductor and its insulation, a frictional contact was set between wire enamel and die, wire enamel and punch with a friction coefficient of 0.2, this value of friction coefficient is usually between 0.1 and 0.2 when considering the interaction between wire enamel and steel and finally between the punch and die a frictionless contact was applied.
- The body interaction between the components are also important; the body interaction between a conductor and its insulation was of a bonded type set as unbreakable, and the body interaction between adjacent moving contacts was of a frictionless type.
- The mesh size is the most important aspect of an FE solution, due to the unit measurement of the conductors and insulations very small mesh sizes have to be used; a face sizing mesh with element size of 1mm was applied to the punch and die on the X-Y plane, a face sizing mesh with element size of 0.09mm was applied to the punch, die, conductor and insulation along the Z axis and finally a contact sizing was used between a conductor and its insulation, with an element size of 0.09mm. The mesh size of 0.09mm was chosen due to the thickness of the wire enamel, surface contacts and accurate stress and deformation modelling of the wire enamel, figure 5.7 shows the element size of the wire.
- A fixed support was applied to the surface underneath the die which introduces a force of reaction acting in the positive Y- axis.
- A displacement support was applied to the X-Y plane of the conductors and insulations, with the Z component held at 0mm (restricted from moving in the Z axis) and also to the X-Y plane of the punch and die a displacement support was applied with the X and Y component set to 0mm.
- A load pressure of 120MPa was applied on the top surface of the punch in steps of 12MPa.
- For the analysis settings; maximum number of cycles is set to $1e^{+7}$ and end time is set to 0.5ms; figure 5.8 shows the geometry of the turns in the die and how the loads and supports were applied to the model and figure 5.9 shows the dimensions, with wire diameter of 1.48mm.

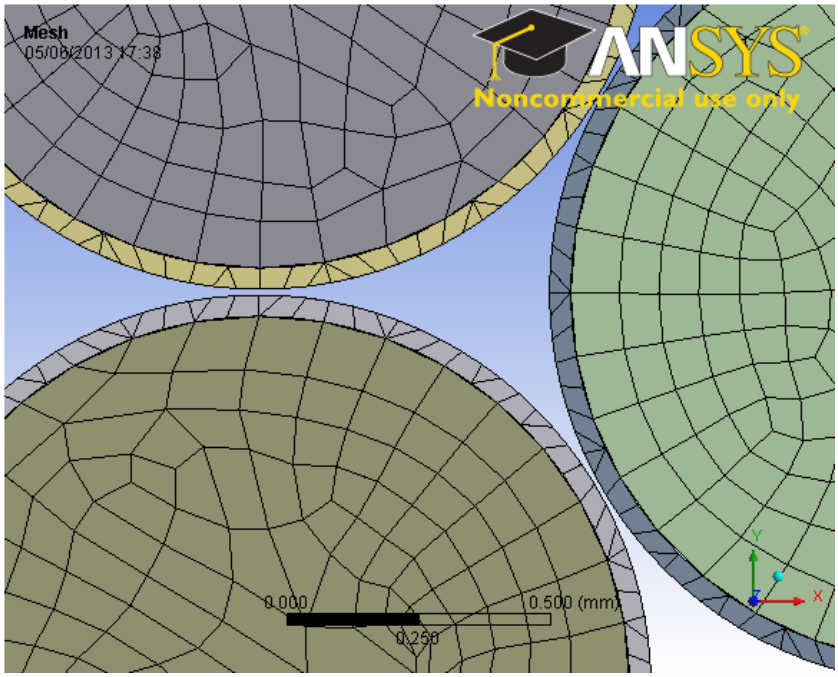

Figure 5.7. Meshing for wire enamel.

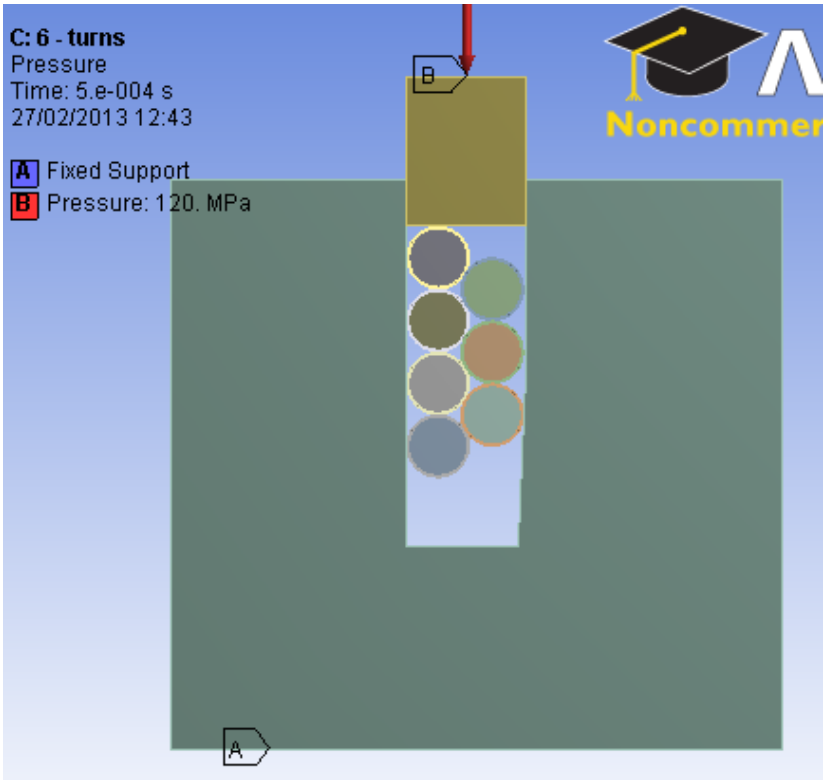

Figure 5.8. Geometry of coil pressing model.

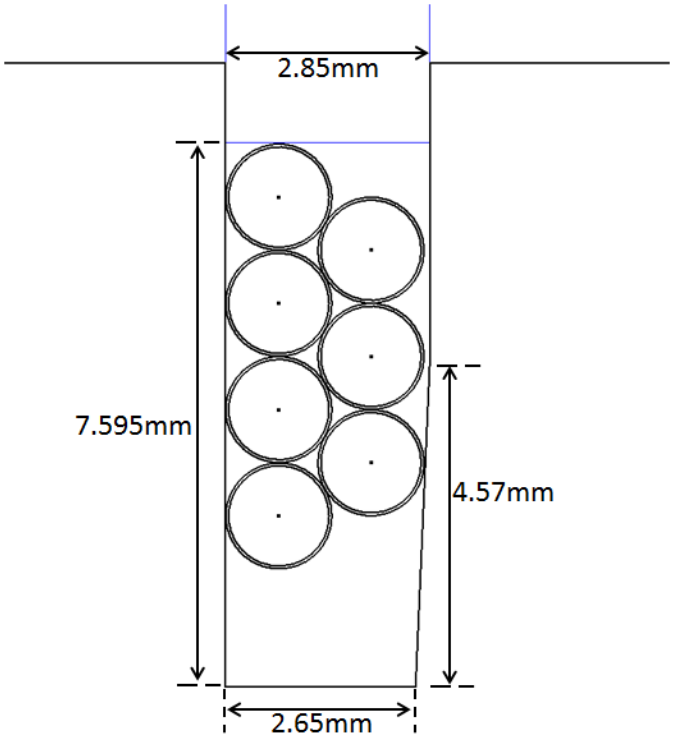

Figure 5.9. Dimensions for coil pressing model.

Table 5.1. Mechanical property of materials.

Material	Shear Modulus (GPa)
Copper	47.7
Insulation	28
Steel	81.8

From figure 5.10 and 5.11 below, it can be seen how the conductors are affected as the pressure applied on the punch propagates across the turns; the bottom turn and the top turn experience the most pressure (which is the reason for using the sacrificial aluminium pieces at the top and bottom of the coil). In figure 5.10 the maximum pressure occurs on the wire enamel at a value of 798MPa, on the turns placed at the top and bottom of the die cavity. The pressure on the coil at the points where the coils come in contact with the side of the die wall is high with a value of 690MPa, so to prevent the insulation damage at these points the die cavity has to be greased or polished to limit this damage. The insulations have different deformations, depending on the location of the conductor in the slot, as seen the insulations are most flattened at the sides that come in contact with the die and punch, however it is worth noting that the top two turns

(shown in figure 5.11) have been flattened at their point of contact with each other and this may reduce the dielectric strength between these two turns, leading to a leakage current flowing between the two turns. The limitation of the model is the inability to tell how the conductor insulation is affected, because of the insulation thickness of 0.08mm, which means the meshing element should be set very small but this will cause the computation time to increase significantly; the model solved for approximately 70hours.

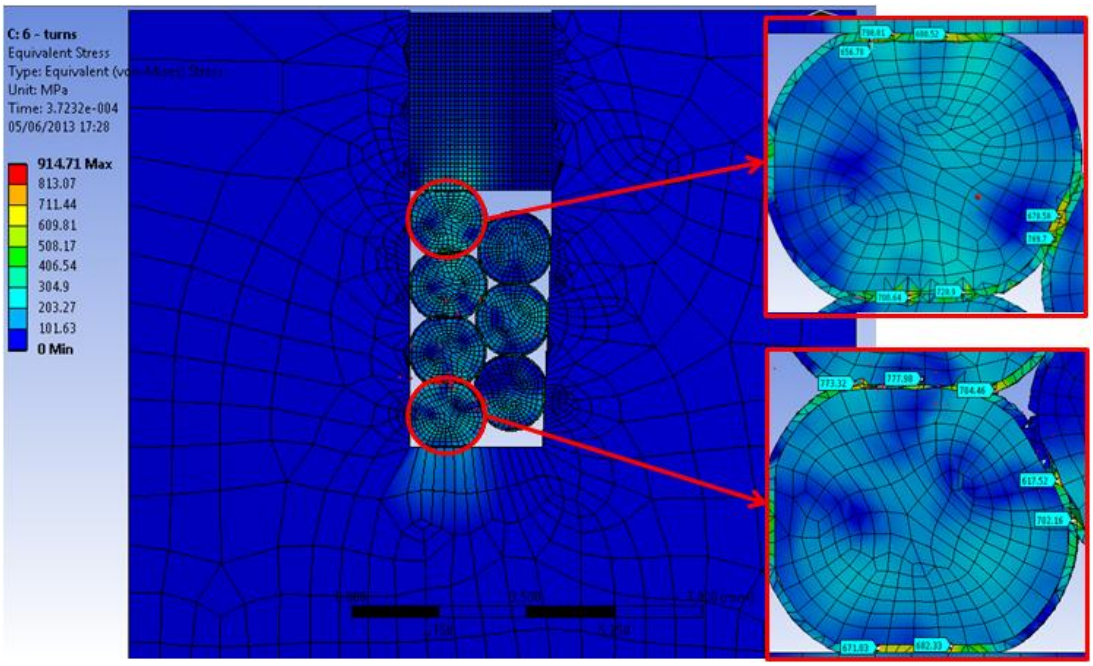

Figure 5.10. Equivalent stress of coil pressing model.

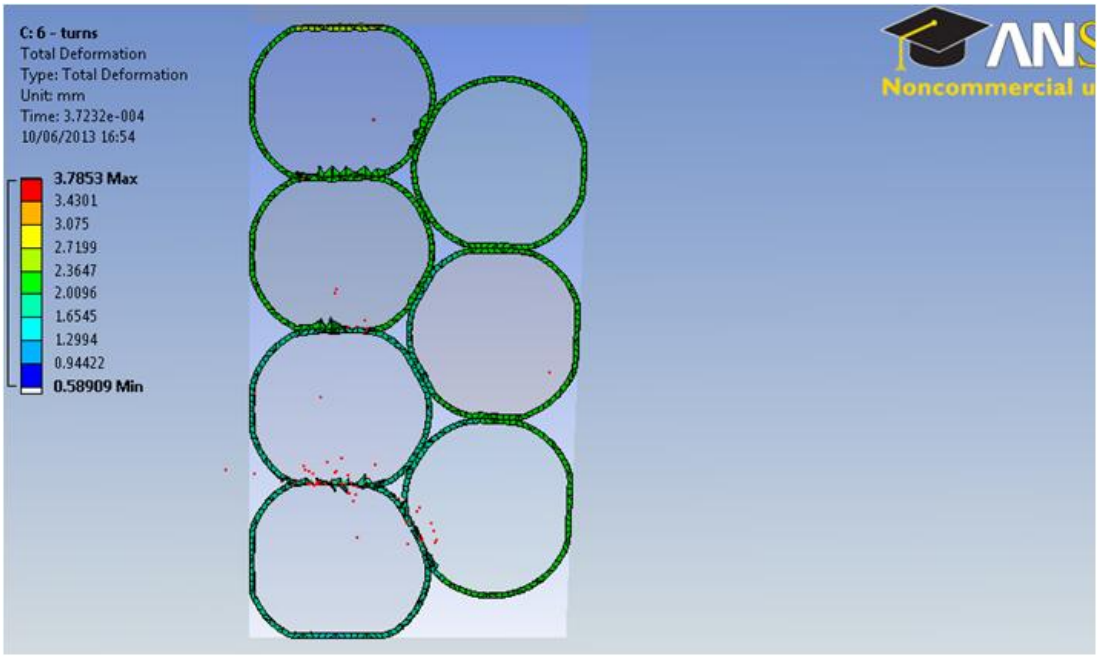

Figure 5.11. Deformation of coil enamel.

5.4 Coil pressing process

The process of winding and pressing the coils will now be described, by outlining the various important factors considered during the coil winding and pressing process;

- A bobbin is first wrapped with a non-sticky insulting film (0.05mm thick) before the wire is wound on the bobbin, this prevents direct contact between the wire and the bobbin and to allow easy separation of the bobbin from the pressed coil.
- The coils were wound using the winding machine in manual mode so that a consistent winding pressure could be applied. This method also prevents the coil turns from bowing on the flat axial surface. After this process the coil is wrapped in tape to prevent direct contact with the die cavity surface.
- The cavity of the die is lubricated using white lithium grease, so as to reduce the friction between the coil and the die cavity wall.
- This bobbin (with the coil wound around) is now placed into the die cavity, a thin layer of sacrificial aluminium piece is inserted at the bottom and top of the bobbin – this serves to distribute the force uniformly across the turns of the coil, as the top and bottom turns will experience the most force of compression compared to the middle turns.
- The punch is slid on top the bobbin so it sits on top of the coil as shown in figure 5.3, it is important that the punch and bobbin are aligned straight in the die cavity.
- With the aid of an hydraulic press the punch is pushed down onto the coil, which together with the bobbin penetrates deep into the die cavity – as seen in figure 5.3 the die has three layers, the middle layer has its cavity 23mm deep and is tapered all the way at an angle of 2.5˚ when viewed from the side of the end-winding.
- The punch is pushed down until its (punch) bottom is flush with the top of the middle layer of the die, and at the same time the bottom surface of the bobbin is flush with the bottom surface of the die.
- Having ensured the coil has been pressed to the required height, the bobbin is pushed from the top of the hollow punch down out the bottom of the die, with just the coil left in the middle layer cavity of the die.
- The die is turned downside up and the pressed coil is pushed out of the die. It is important to inspect the coil to make sure the insulation at the bends and the crossovers is not damaged.

Pressing the coil with the wire end terminals can cause damage to the insulation, so a means to press the coil without pressing the end terminals had to be developed; two slots were cut into the top of the die, down to the top of the middle layer, the coil end terminals slide into these slots as the coils are pressed. Also two blue plastic sections (polyurethane tufset) were screwed to the top of the die, which helps align the turns of the coil properly and prevent them from moving about before they are compressed in the die cavity. Figure 5.12 shows a picture of the die detailing the slots and the blue plastic on the top of the die; the screws on the periphery of the die are used to hold the top layer of the die to the bottom layers, because the die has been cut in two parts. The material used for the die, punch and bobbin is D2 tool steel, that was not hardened or polished.

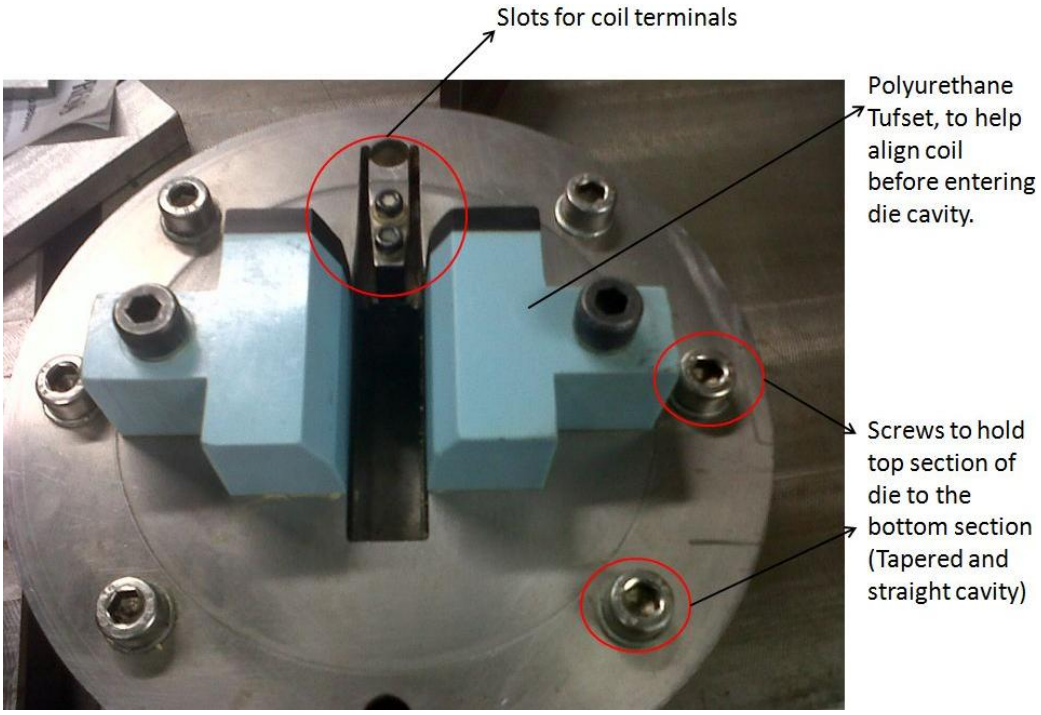

Figure 5.12. Picture of die.

It is important to have a large bending radius on the end of the coil, as shown in figure 5.1, to prevent any insulation damage due to bending and crushing at the ends. Having a bending radius that is too small can lead to the insulation at the outer end of the wire to stretch and break. However, due to the constraint on the length of the overhang of the coils being made, it is important to test different bending radii on the coils; having a bending radius greater than the diameter of the wire was found to introduce no breaks in the insulation at the bend of the coil. Figure 5.13 shows a picture of a sample coil wound and crushed for the purpose of this work, a bending radius of 1.6mm was chosen

for a wire diameter of 1.48mm. This is significantly smaller than the radius shown in figure 5.1.

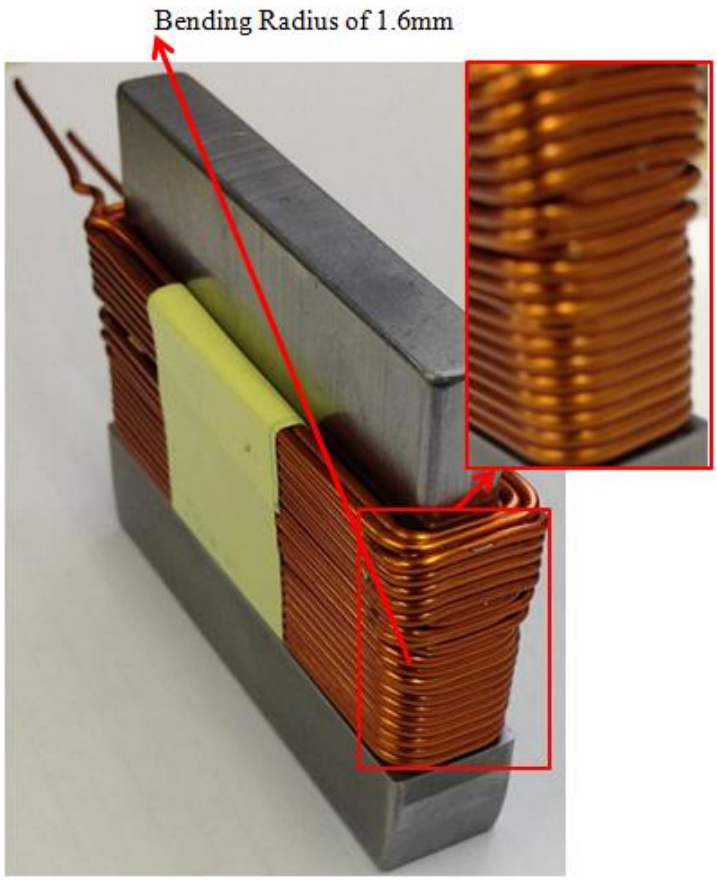

Figure 5.13. Sample of pressed coil for machine design with slot wedge.

A cut through section of a sample pressed coil, which has 33 turns and a fill factor of 0.62 (bare copper) is shown in figure 5.14. The pressure applied to the coil was 21MPa; the coils were wound in two layers, so it is not straightforward to say that the conductors take the shape of an hexagon, however from figure 5.14 (a), where the conductors come in contact with each other it can be seen that the conductors become close to hexagonal. In figure 5.14 (b), the conductors form irregular shapes: it can be inferred that this is due to the displacement of the conductors as they were pressed in the die cavity and this distortion is likely to lead to insulation failure. In order to fix this, it is important that the turns of the coil are held properly in place before pressing the coil.

Finally it was discovered that the wires are not necessarily produced with the enamel in excellent condition, which is shown in figure 5.15, showing some insulation damage at different points along a wire 300mm long. These imperfections were present when leaving the supplier.

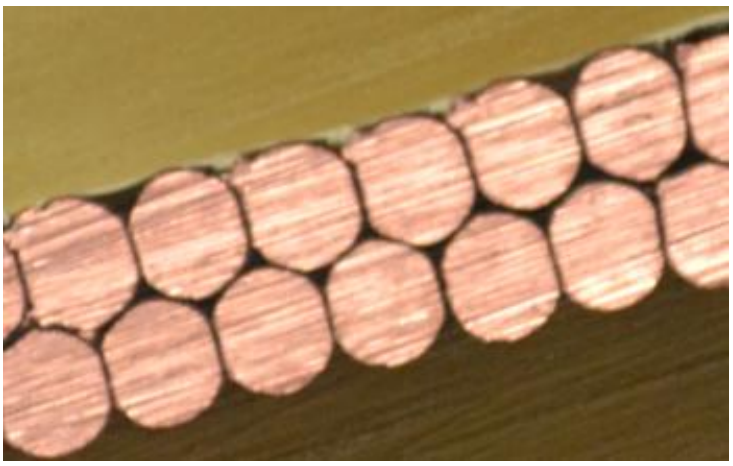

(a)

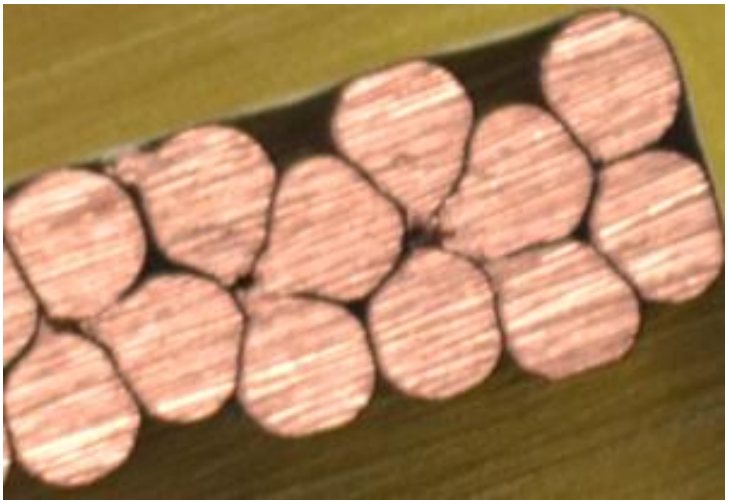

(b)

Figure 5.14. Cut through section of test coil: (a) hexagonal cross-section, (b) irregular shapes due to coil displacement during pressing.

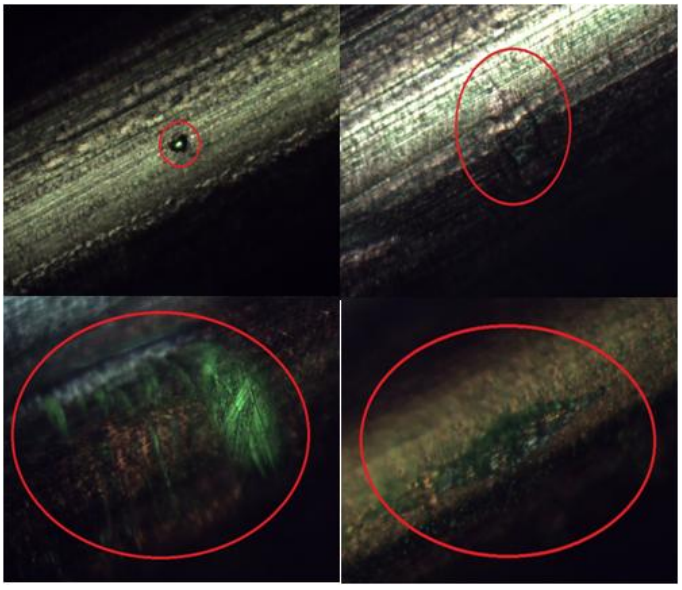

Figure 5.15. Insulation damages on wire of length 300mm.

5.4 Insulation life expectancy

A motor is usually expected to operate safely for a period of 10 years or more [107]. In aerospace and automobile applications, the safety and reliability factors are of upmost importance in motor design, as failure of the electric motors can be catastrophic. One possible risk introduced by pressing the coils is the reduction of the insulation breakdown voltage (BDV), which can lead to inter-turn short circuit; the wire used for this work is called the MAGNETEMP® – CA200 [108], grade 2 wire having a BDV of 1.5KV. The reduced BDV when the wire is crushed is expected to be well above the operating DC link voltage of the power electronic converter, however no wire enamel BDV was found in this work.

Failure modes in motors are categorised in two ways; electrical (weakening of insulation) and mechanical (rotor deflection or bearing wear) [107]. Electrical failures typically occur due to stator coil and slot liner insulation degradation, which leads to inter-coil short or coil to ground-wall short. So it is important to provide the right level of stator slot wall insulation, taking into consideration the operating temperature (as temperature is one of the main degrading factors for the insulation) and the motor operating voltage.

Typically the insulation life adequacy is determined practically by thermal life testing of the insulation material and checking the dielectric breakdown voltage as the insulation ages. Methods for accelerated thermal life testing of insulation by thermal cycling have been established [109]. In [109] a thermal life test was performed. The conclusion of the work was that the dielectric breakdown voltage of the insulation material remains unaffected as long as the temperature class of the insulation material is not exceeded. The deterioration of the insulation material is usually a chemical reaction caused by temperature, Arrhenius came up with an equation [110, 111] used to determine the life expectancy of the insulation material based on how the thermal ageing affects the chemical reaction of the insulation.

$$L = \log_{10^{-1}}[B/T - A] \tag{5.1}$$

Where;

L time in hours

A, B constants for insulation under consideration (provided in insulation temperature chart)

T absolute temperature of insulation in degrees K (273 + degrees C)

The insulation life of the slot liner – Nomex type 410 can be estimated, as information regarding this is available from manufacturers. The data sheets [112] provide some information of the slot liner insulation material used. Figure 5.16 shows the insulation life in hours as a function of temperature, which is provided for the Nomex insulation material. The experiment conducted for this chart was carried out within a temperature range of 220˚C to 320˚C with the Nomex liner insulation maintaining a dielectric strength of 12kV/mm. This chart helps estimate the expected life of the insulation at the given operating condition; the operating temperature in the slot is 155˚C, the insulation thickness is 0.18mm and expected life is 73000000hours.

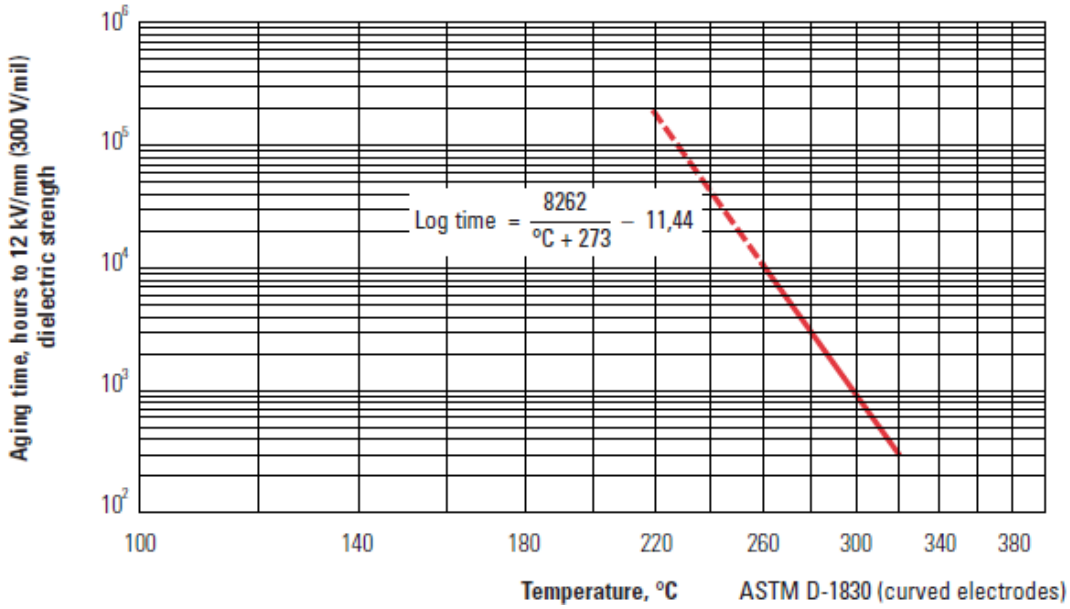

Figure 5.16. Nomex Insulation; Useful life Vs Temperature Chart [112].

5.5 Coil testing (ground wall and inter-turn)

The conventional method of testing a coil is to carry out a Mega-ohm, PI or HiPot test to check for any leakage current at $\leq$ 1kV, this checks the slot liner dielectric strength to ensure the slot wall insulation is well rated to prevent any coil to ground wall fault. However no conventional method is available to test a pressed coil to ensure the wire enamel can withstand an inter-turn fault, since it is expected that the insulation between turns will be weakened. Baker Instrument Company (an SKF group company) introduced coil testing equipment, which can be used to carry out a series of tests that

includes a surge test to detect any weakness between turns of the coil, and also gives an indication of the coil inductance.

The principle of the surge test involves applying a high current impulse to the coil that has a fast rise time. This high rise time current impulse creates flux that induces a voltage difference between adjacent loops of wire within the coil. If the wire enamel between two adjacent turns is broken or too weak to withstand the level of voltage difference, then there will be an arc between the two turns. This can be seen as a change in the surge waveform measured from the test; figure 5.17 shows the standard shape of the surge waveform when there is an arc between two adjacent turns and the change in the waveform can be seen at the start, which is viewed on a display that comes with the test equipment [113]. The surge waveform is a depiction of the voltage across the test leads of the test equipment, an indication of an inter-turn fault is a shift, and/or decrease in the amplitude of the waveform.

The surge waveform has a close relation to the inductance of the coil, which is the primary factor that influences this surge waveform. The waveform can be said to be of a ringing type, which is typical of an RLC circuit. This comes from the coil's inductance and resistance and the test equipment comes with an inbuilt capacitance, hence the ringing waveform that decays with time at a resonant frequency as described by equation 5.2 below.

$$Frequency = \frac{1}{2\pi\sqrt{LC}} \tag{5.2}$$

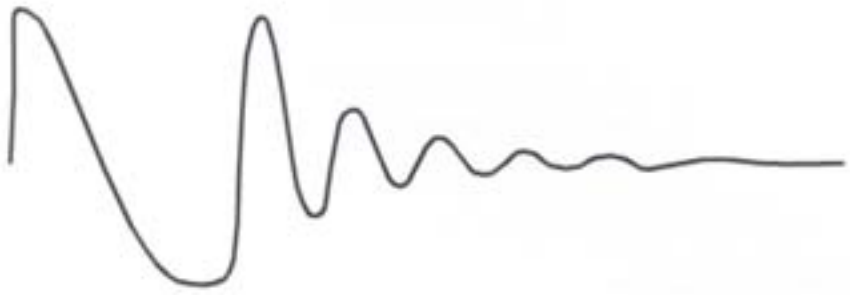

Figure 5.17. Surge waveform that shows an arc due to damage between two adjacent turns [113].

The inductance of a coil is a function of the coil geometry, number of turns and the material that is place in the core of the coil. Looking at equation 5.2 it can be seen that the inductance is inversely proportional to the frequency, so if the coils are not pressed in similar patterns it will be seen in the frequency of the surge waveform. So in the

event there is a weak dielectric strength between two adjacent turns if the voltage potential is large enough to cause an arcing and an eventual short circuit, this will lead to a decrease in the number of turns of the coil and hence a reduction in its inductance.

All 72 coils of the machine were tested and the few that failed the surge test were replaced. Figure 5.18 shows the series of test that can be carried out on the coil, which also represents the surge waveform for a healthy coil. The way the test process is set up, requires that the surge test be done on a master coil that is thought to be in a fully healthy state and the waveform of the surge test stored as a master, which acts as a reference for all other coils being tested. For the surge test two leads from the Baker test equipment are connected to the two terminals of the coil; as seen from figure 5.18 the polarity of the voltage applied to the coil terminals is reversed and the waveform for lead 1-2 (RED) and lead 2-1 (BLUE) are recorded. The pulse to pulse error area ratio (P-P EAR) is the method applied to the coil testing to compare and make sure that the coils have the same properties, indicating a healthy or failed coil; this applies a number of voltage pulses to the coil and looks for a difference between each pulse. The coil P-P EAR should be within +/-10% of the saved master coil, because the coils should have similar shape, zero crossings and amplitude [113]. Also it can be seen that the mega-ohm and HiPot were all carried out at different voltage levels.

The test data presented in figure 5.19 performed on a faulted coil shows the surge waveform. The voltage pulse was at a peak of 1900V before the P-P EAR exceeded the set maximum, which was then reported as a failure, also the difference in time of the two half of the first cycle can be likened to that of figure 5.17.

Results Summary		**Test Date/Time 01/05/2012 12:53:34**	
Test ID:	**Coil Test**	Repair/Job #	
Tested By		Tested For	
Room #		MCC	
Model	**A**	State	**Coil**
Memo	**Coil 69_replacement**		
Temp Status	**No Test Performed**	**PI Status**	**No Test Performed**
Temp		Volts (V)	**0**
Resist Status	**No Test Performed**	DA Ratio	**0.0**
L1-L2 (Ohms)	**0**	PI Ratio	**0.0**
L2-L3 (Ohms)	**0**	**HiPot**	**PASS**
L3-L1 (Ohms)	**0**	Volts (V)	**2980**
Max Delta R %	**0.000**	I(µA)	**0.10**
Coil 1 (Ohms)	**0**	Resist (Mohm)	**30764**
Coil 2 (Ohms)	**0**	**Surge Status**	**PASS**
Coil 3 (Ohms)	**0**	Peak Volt(V) L1	**2820**
Megohm Status	**PASS**	Peak Volt(V) L2	**2820**
Volts (V)	**1000**	Peak Volt(V) L3	**0**
I(µA)	**0.02**	Max P-P EAR(%)	**5.2/5.0/--**

Resist (Mohm)	41820	EAR 1-2/2-3/3-1(%)	0/--/--

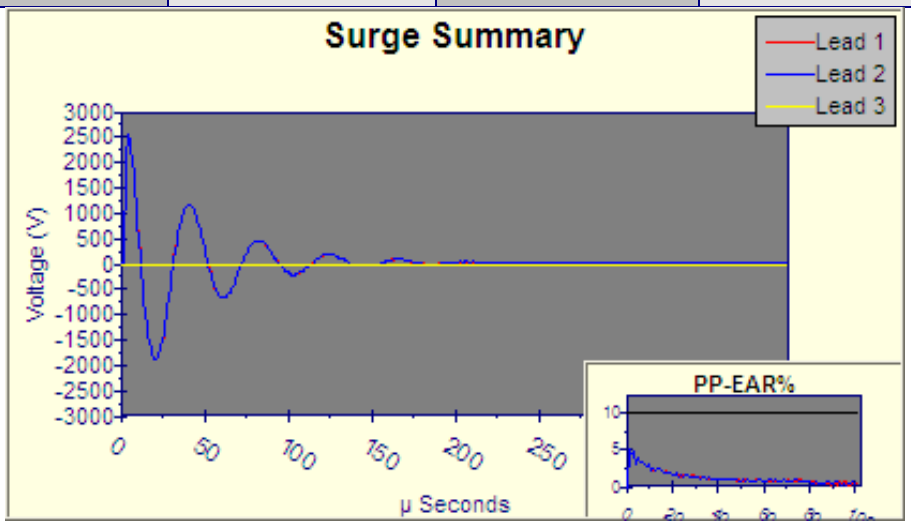

Figure 5.18. Complete test of coil, with the surge test compared to master coil.

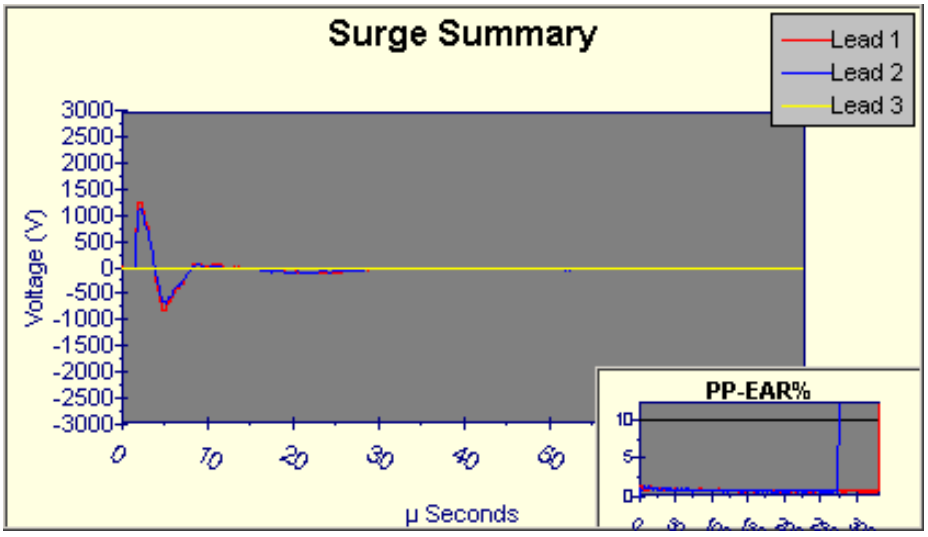

Figure 5.19. Surge test of a faulty coil.

5.6 Conclusion

In Chapter 4 the method of stator construction was presented, having an open slot with a magnetic wedge to cover the slot. This method of stator construction allows the coil to be pre-pressed before being inserted onto the teeth of the machine. The process of coil pressing has been investigated here, and as seen the pressing of the copper coil does not hinder the coil integrity. It was found that when the coil is pressed the top and bottom layers experience greater forces when compared to the middle turns, so a sacrificial layer of aluminium was placed at those positions to reduce the level of deformation.

An estimation of the insulation life expectancy can be carried out, however it is difficult to tell how the insulation of the coil has been affected as the coils are pressed. As a

future work on coil pressing it is important to have experimental results to validate life expectancy against depth of press; where life expectancy in hours is plotted against the depth of pressing in millimetres (or the level of pressure in MPa) applied to the coil. Various test carried out on the pressed coils for the actual machine build have been presented, the tests were conducted using the Baker Instrument AWA.

Chapter 6

Model Design of High Torque Dense Machine having Magnetic Slot Wedge

The magnetic and structural design considerations of the three-phase, outer rotor permanent magnet machine, having a simple open slot design closed with a magnetic wedge and pre-pressed coil are presented in this chapter. The machine stator design employed has a single tooth concentrated winding, with a coupled rotor having surface mounted magnets and a high pole count. The complete machine optimisation and analysis is carried out, along with studies of different slot and pole number combinations with magnetic wedges. The machine has been designed to fit an 18-inch wheel and it was part of the initiative to downsize the Protean machine presented in Chapter 3 to fit this wheel size. The machine prototype built and tested has its results presented later in Chapter 8.

6.1 Introduction

The FE models solved were built using a Visual Basic (VB) script file; the VB script codes were written to change the structural design of the model by simply changing the parameters (pole and slot number, tooth width, machine diameter, etc). In order to save simulation computation time, the models were built at the line of symmetry and the appropriate boundary conditions set. To improve the simulation accuracy, the model boundary air was split into four parts; stator and rotor air-boxes that encompass the stator and rotor respectively, and the static and rotating air-gap that make up the two sections of the model air-gap. The mesh of the static and rotating air-gap were then set to have a maximum element size of 0.5mm, to accurately model the rate of change of the magnetic field in the air-gap. The FE model solutions applied to obtain the desired results were; static 2D, transient with motion 2D and time harmonic 2D.

6.2 Design variations with change of slot and pole number combination

The slot and pole number has a profound influence on the machine parameters of the permanent magnet machine, as discussed in Chapter 3. In [114] the effect of changing the pole number on the slot area and flux per pole was presented; these two quantities affect the electrical and magnetic loading of the machine, as the electrical loading depends on the available slot area and the flux per pole depends on the amount of flux that links a tooth from the magnet pole. If the pole number is doubled, the stator flux per pole is halved and if the air-gap diameter and slot current density remains the same, the torque output of the machine is not changed. However this is an ideal case, as there are other design variations that are affected when the pole count is changed, which in turn influences the machine torque output.

Increasing the pole and slot number of a machine has the following effect on the machine design and construction variations [114, 115]:

- The machine electrical frequency is increased for the same speed as the pole count is increased, this will lead to increased stator iron losses, however the magnet loss and end-winding loss are reduced with increased pole count as the circumferential path of the magnet eddy current and end-winding length are reduced.
- The machine core-back can be reduced with an increase in pole number, as the magnetic path at the core-back will not carry as much flux with the core-back

reduced, the machine air-gap diameter can be increased for the same outer diameter, leading to an increase in output torque and reduced weight of stator and rotor iron.

- The higher the pole count the smaller the magnet arc, which leads to an increase in the shunting and fringing of flux between two magnets and between the magnet and tooth respectively; this causes the air-gap flux density to look more sinusoidal (as will be shown later) and thereby reducing the fundamental component of the spatial harmonic.
- The cogging torque is reduced as the pole count is increased, because the highest common factor between the slot and pole combination is increased.
- The risk of magnet demagnetisation is reduced as the pole count is increased, as the armature reaction is reduced.
- The construction and assembly of the machine with higher pole count is more intense and expensive as the component count is increased and the sizes of the components are decreased.

A simple comparison has been carried out between three different machine slot and pole combinations; a 36slot/32pole (the protean 72slot/64pole downsized by a factor of 2), a 36slot/24pole and a 12slot/8pole design. A double layer, single tooth winding was adopted and a quarter of the machine was modelled for this comparison. The machine model with 36 slots has three coils per phase and that of the 12 slots has one coil per phase. The magnets for all the models span 85.91% of the complete pole pitch (180˚), since the magnets in the modelled section are even in number, an even periodic boundary condition was chosen. Figure 6.1 shows the different topologies considered for the purpose of describing the effect of the pole and slot combination; the core-backs of the machines were not varied, the number of turns for the various designs were kept at 20turns, while maintaining the same fill factor of 0.62 and a zoomed picture of the magnet air-gap field is shown.

As seen the slotting effect in the air-gap flux density is reduced in the 36slot/32pole model, as the air-gap flux density is more sinusoidal; this is due to the shunting and fringing effect of the magnet flux, the peak air-gap flux density for the 36slot/32pole is 0.75059T, 36slot/24pole is 0.80884T and 12slot/8pole is 0.85638T. Also it can be seen that the core-back depth for the models with a high pole count should be a lot smaller.

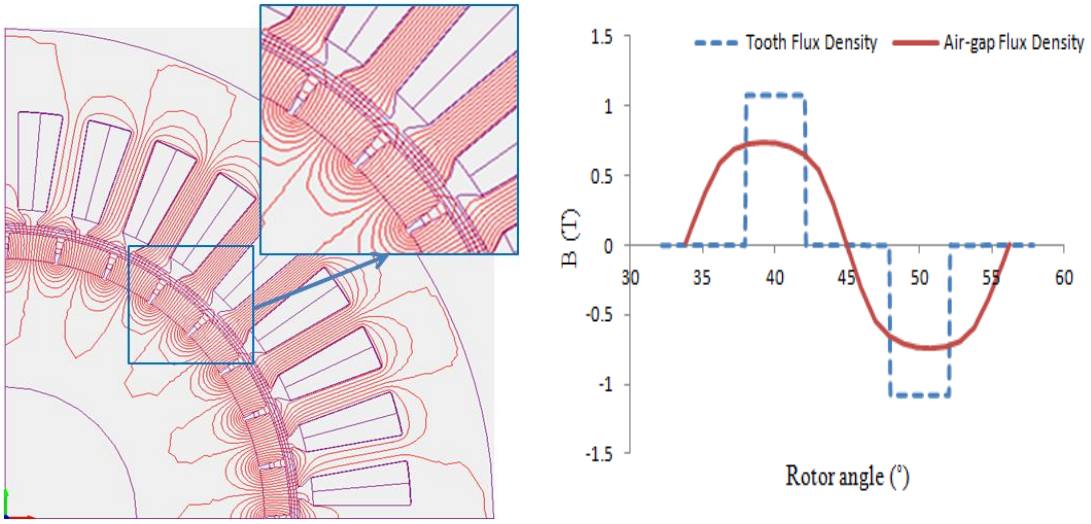

(a) 36slots / 32poles

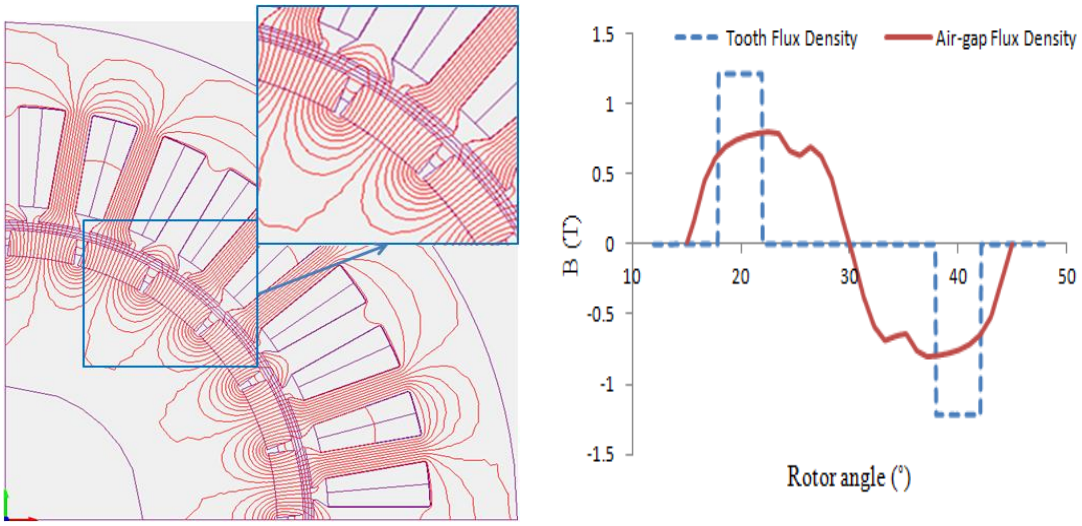

(b) 36slots / 24poles

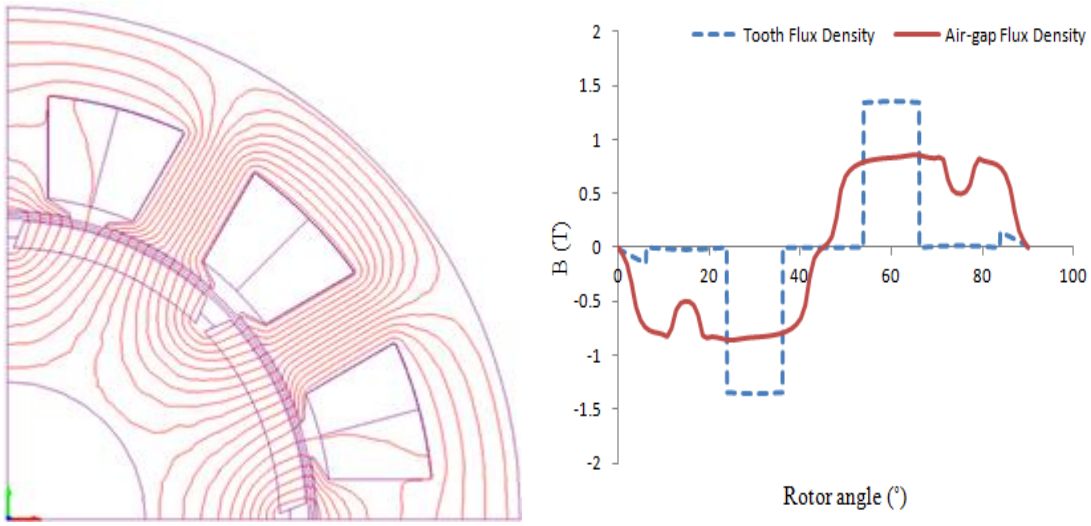

(c) 12slots / 8poles

Figure 6.1. Flux contour plot lines, air-gap and tooth flux density, at no-load.

The 36slot/24pole and the 12slot/8pole both have a slot per pole per phase (SPP) of 0.5 with a fundamental winding factor of 0.866, which means the coils that make up a single phase all lie at the same electrical angle (no winding distribution) and a pole pair spans a total of three stator teeth, while the 36slot/32 pole has a SPP of 0.375 with a fundamental winding factor of 0.9452. Machines topologies with a SPP value of 0.5 typically have a high attenuation of the 3rd harmonic but the harmonic order is increased in the 5th and 7th, while those with a SPP of 0.375 have a reverse effect. This can be seen in the harmonic spectrum of the phase back EMF shown in figure 6.2, however it is worth noting that the 3rd and all triplen harmonics are not present in the line back EMF, as they would all cancel each other.

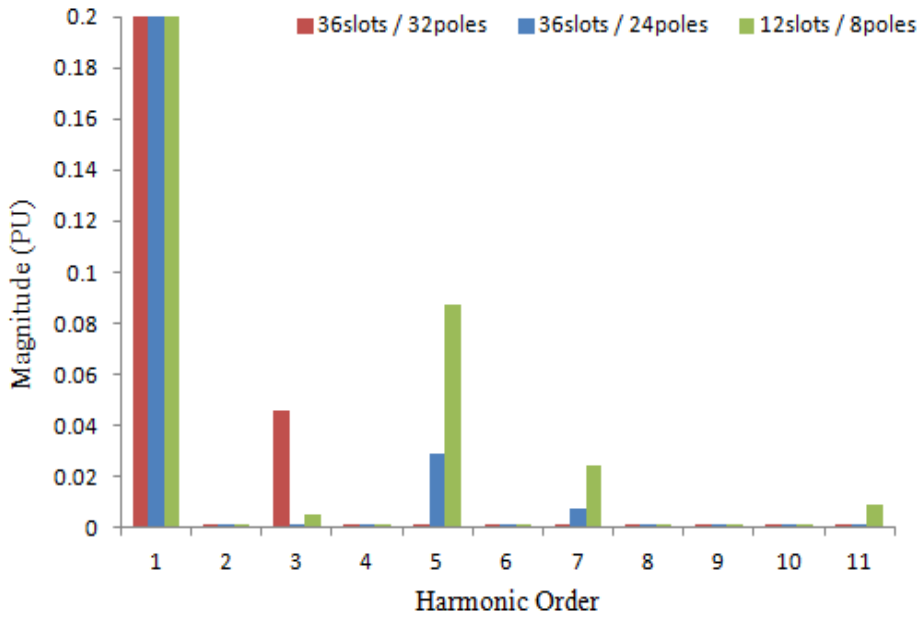

Figure 6.2. Harmonic spectrum of phase back EMF.

6.3 Evaluation of slot and pole combinations for slot wedge machine design

Having studied the effect of changing the pole count has on the winding harmonics, this section presents an evaluation of the pole and slot combinations chosen for the machine design with a magnetic slot wedge.

The slot and pole combinations selected must conform to the limitations and requirements developed for the purpose of this work. Two types of slot and pole combinations were modelled; one type that has more poles than slots and the other type with more slots than poles. Table 6.1 shows the various combinations chosen for

investigation; the number of teeth varies between 72 and 36, whilst the number of poles varies between 64 and 40, and the minimum number of sub motors has to be four. The combinations chosen typically have good winding factors with proper harmonic attenuation, except for the combinations with a SPP of 0.5 and 0.25 and consequently low cogging torque, due to the high cogging torque lowest pole pair number. Equation 6.1 is used to calculate the cogging torque lowest pole pair number. Table 6.2 presents the values calculated for the cogging period and winding factor harmonics.

$$Cogging_{pp} = \frac{N_{slot} \times PP}{HCF\{N_{slot}, PP\}} \tag{6.1}$$

Where PP is the pole pair number and N_{slot} is the slot number.

Table 6.1. Motor configurations for slot wedge design.

Number of teeth	Number of poles	Number of sub-motors	Teeth per sub motor	Poles per sub motor
72	64	8	9	8
72	60	6	12	10
72	48	8	9	6
63	56	7	9	8
60	64	4	15	16
60	56	4	15	14
54	60	6	9	10
54	48	6	9	8
45	50	5	9	10
45	40	5	9	8
36	48	4	9	12
36	40	4	9	10

Table 6.2. Fundamental design parameters for slot and pole combination.

Number of teeth	Number of poles	Coils per sub-motor per phase	SPP	Cogging pole pair	Harmonic winding factors			
					1^{st}	5^{th}	7^{th}	11^{th}
72	64	3	0.375	576	0.945	0.140	0.061	0.061
72	60	4	0.4	360	0.808	0.058	0.058	0.808
72	48	3	0.5	144	0.866	0.866	0.866	0.866
63	56	3	0.375	504	0.945	0.140	0.061	0.061
60	64	5	0.312	960	0.951	0.173	0.111	0.045
60	56	5	0.357	840	0.951	0.173	0.111	0.045
54	60	3	0.3	540	0.945	0.140	0.061	0.061
54	48	3	0.375	432	0.945	0.140	0.061	0.061
45	50	3	0.3	450	0.945	0.140	0.061	0.061
45	40	3	0.375	360	0.945	0.140	0.061	0.061
36	48	3	0.25	144	0.866	0.866	0.866	0.866
36	40	3	0.3	360	0.945	0.140	0.061	0.061

6.3.1 Optimisation of chosen slot and pole combination

The outer and inner diameters of the machines were fixed, along with the air-gap diameter and with the overall axial length (which includes active length and over-hang). This is due to the environment in which the motor is to be placed, as the wheel diameter is fixed and the inner stator is to be fitted around an existing water jacket. As the number of slots change the slot area and consequently the length of over-hang changes, so to carry out a justified comparison within the set limits, the active length of the machine has to be reduced as the slot number is reduced in order to maintain the given overall axial length. The optimisation of the various designs was achieved by adopting the formalised design optimisation procedure presented in Chapter 3, the limits for the optimisation are given below:

- Stator inside diameter – 302 mm
- Rotor outside diameter – 386 mm
- Total axial length; including over-hang – 67.3 mm
- Air-gap diameter – 362 mm
- Air-gap length – 1 mm

- Wedge depth – 2.2 mm
- Winding slot fill factor – 0.62
- Total machine winding loss – 2074 W

The magnetic slot wedge has been studied in Chapter 4 and so is not included in this optimisation. Figure 6.3 shows the various structural parts parameterised to be optimised. The optimisation was setup to apply a sinusoidal current over one electrical cycle and obtain the mean torque. A number of parameters were allowed to randomly vary within a defined range, the process was repeated several times; it was identified that a range of optimised variables generated very similar performance, a post-optimisation check to validate a chosen optimised structure was conducted. To keep the back EMF constant for the various slot and pole combinations, the number of turns were changed where appropriate.

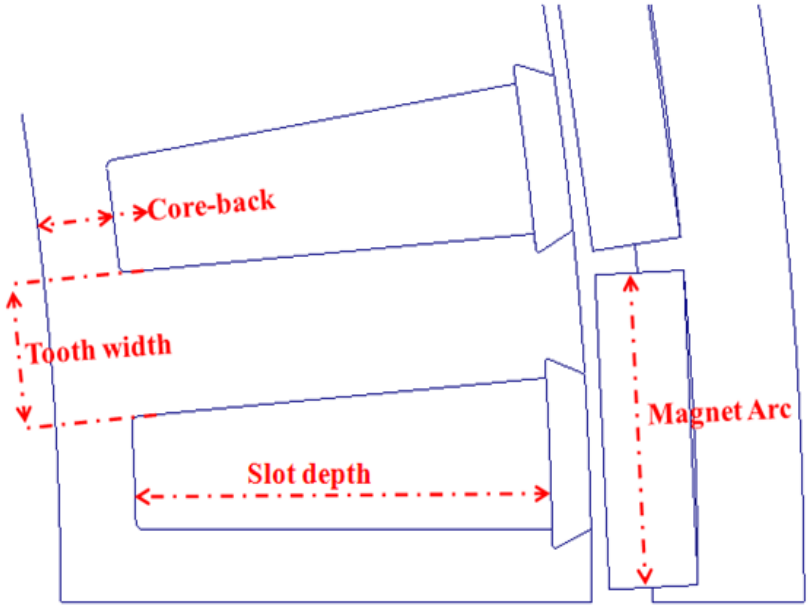

Figure 6.3. Parameters set for optimisation.

6.3.2 Results of optimisation

Given the radial limits of the machine models, the core-backs of the stator and rotor are limited in how deep they are allowed to be; this means that the tooth width of the machine will not increase significantly as the slot number decreases, which in turn means the topologies with lesser slot number will tend to have bigger slot areas and the tooth is chosen close to its saturation limits. As the slot area increases the over-hang gets longer, to maintain the same overall axial length the active axial length has to be reduced as the slot area gets bigger. Figure 6.4 illustrates the structural and magnetic

variations of the optimised slot and pole combinations obtained from a static 2D solution. The flux density graph plotted over a sub-motor of the complete machine model is shown, table 6.3 presents the change in stack length, the number of turns per coil and the no-load flux density in the air-gap and teeth. The slot and pole combinations employ a high level of magnetic loading in the air-gap, the teeth and core-back are reduced to their lower magnetic limits as can be seen in figure 6.4. The combination of 36slot/48pole presents a peculiar case where the air-gap flux density peaks at a higher value than that of the teeth.

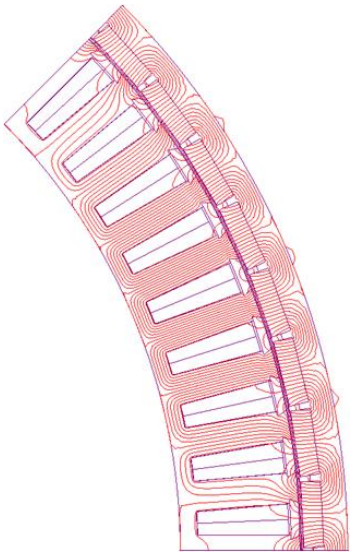

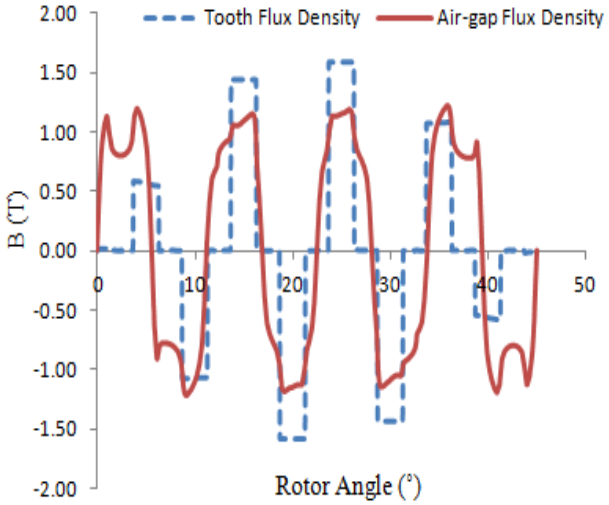

(a) 72slots / 64poles

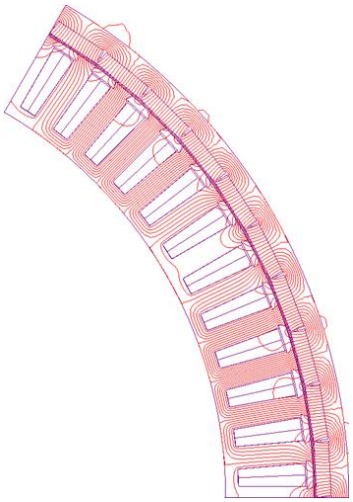

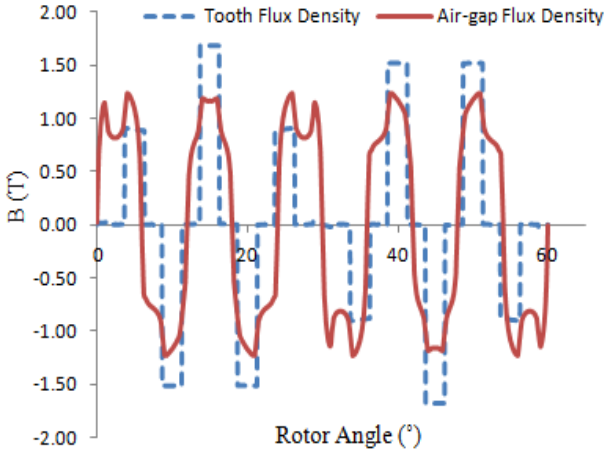

(b) 72slots / 60poles

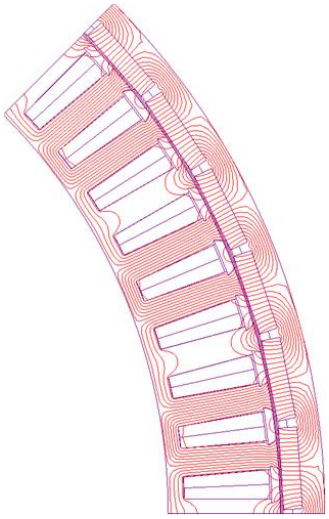

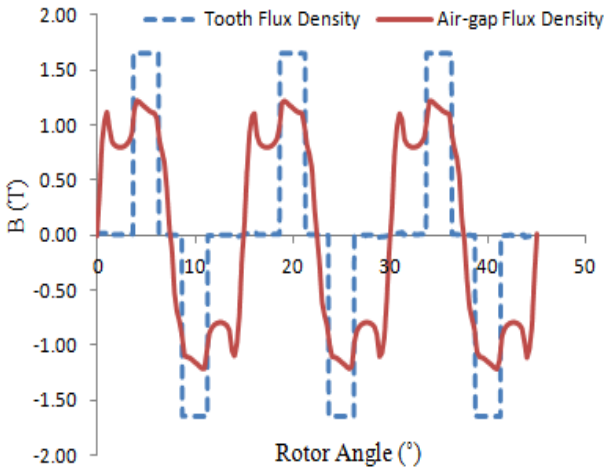

(c) 72slots / 48poles

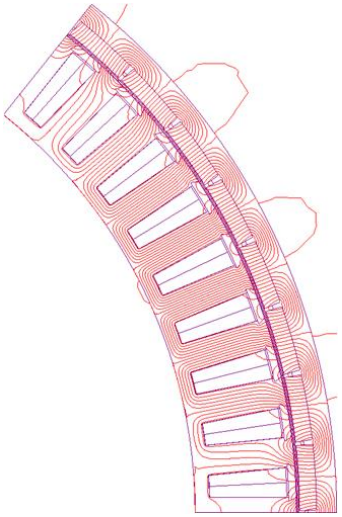

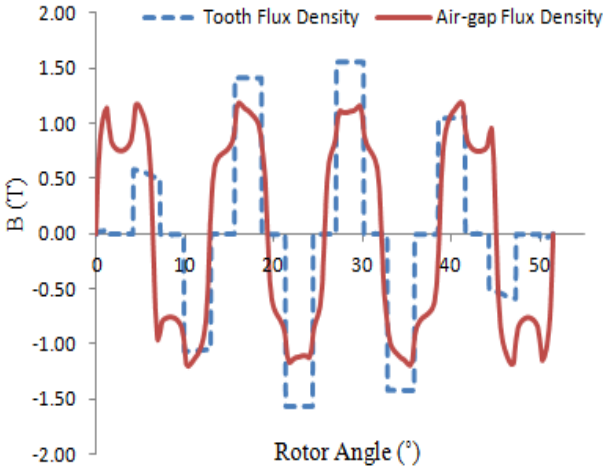

(d) 63slots / 56poles

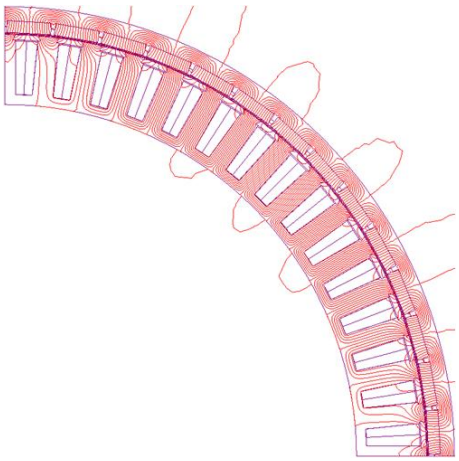

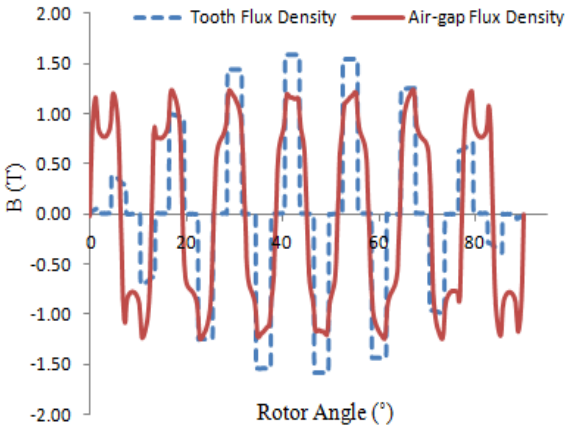

(e) 60slots / 56poles

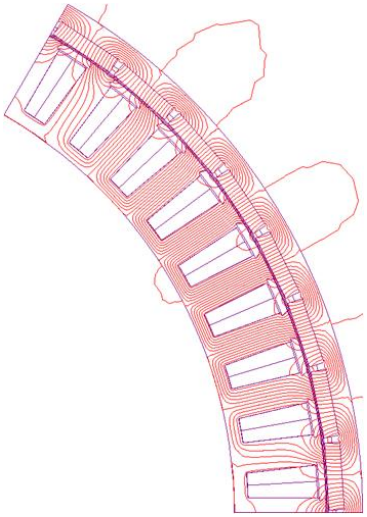

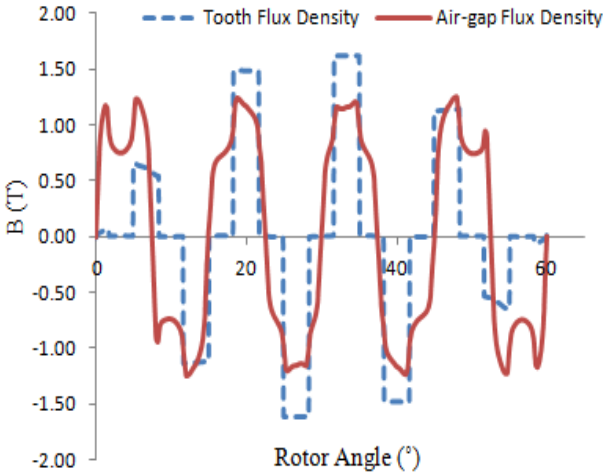

(f) 54slots / 48poles

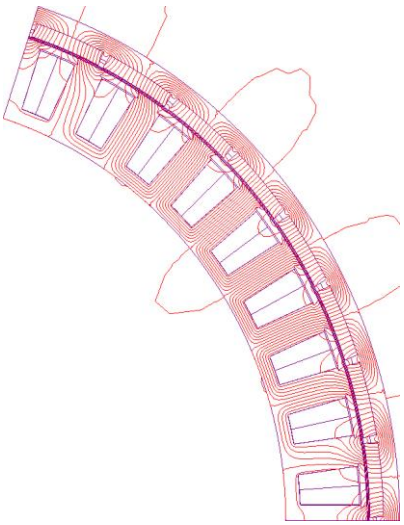

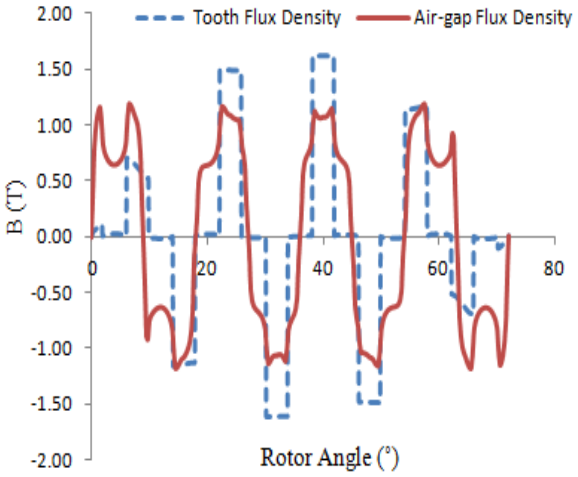

(g) 45slots / 40poles

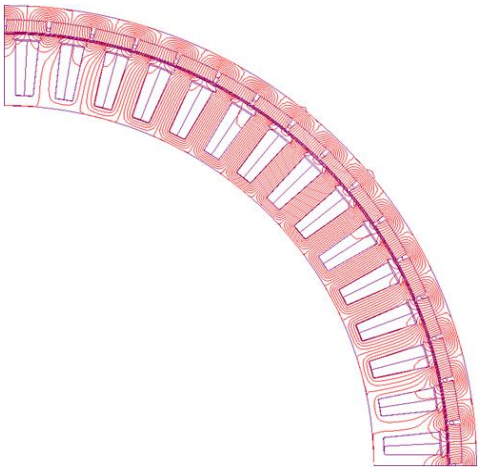

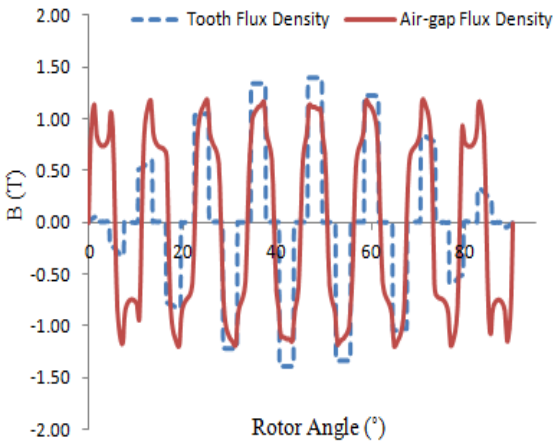

(h) 60slots / 64poles

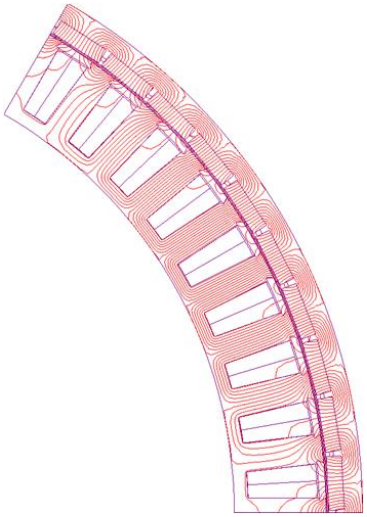

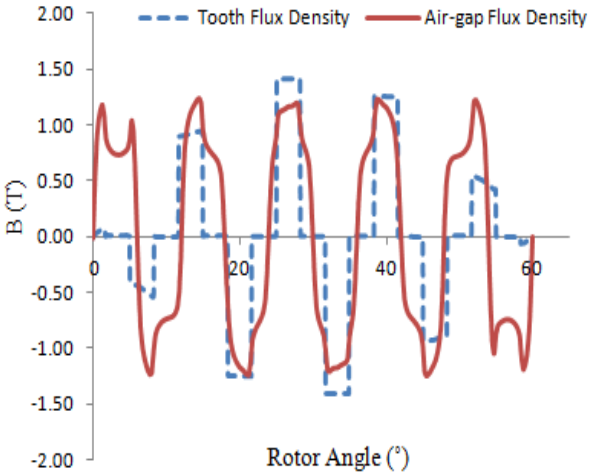

(i) 54slots / 60poles

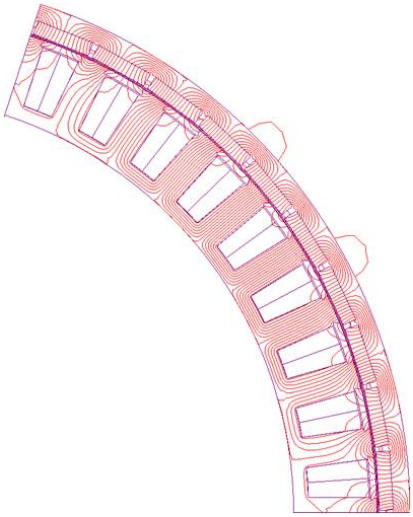

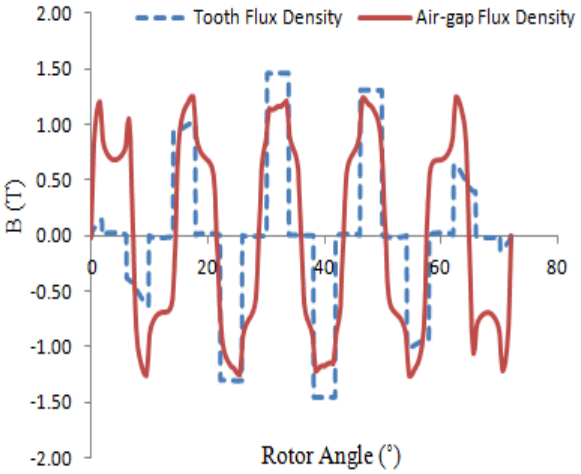

(j) 45slots / 50poles

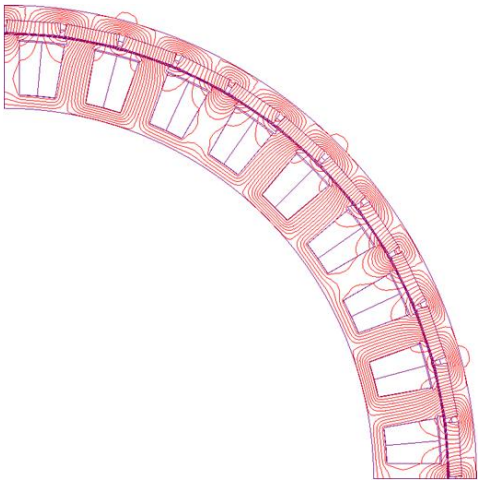

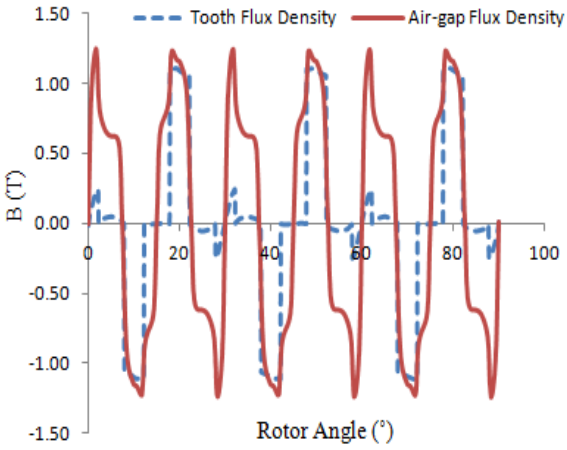

(k) 36slots / 48poles

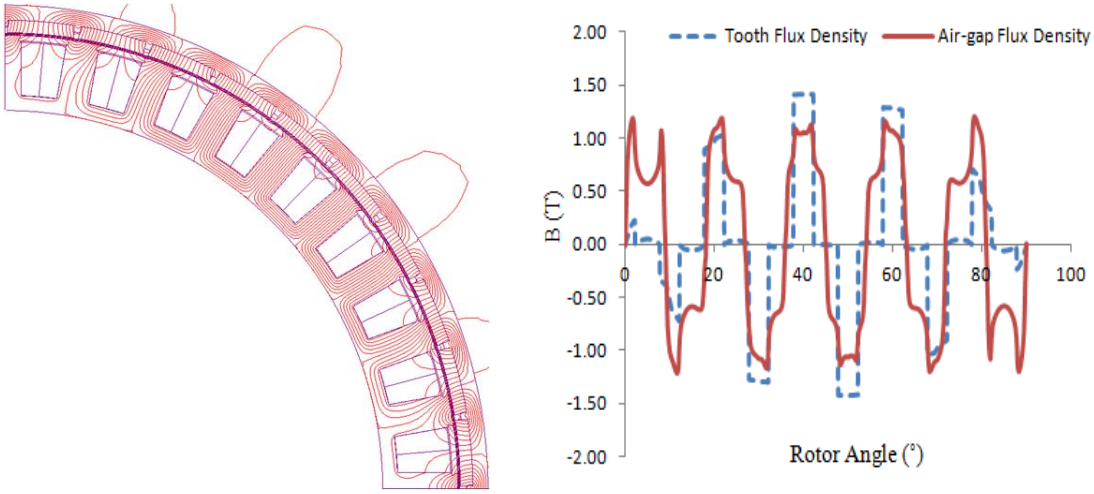

(l) 36slots / 40poles

Figure 6.4. Flux contour plot lines, air-gap and tooth flux density, at no-load.

Table 6.3. Axial length and turns per coil.

Number of teeth	Number of poles	Axial length (mm)	Turns per coil
72	64	58.3	33
72	60	58.3	30
72	48	58.3	34
63	56	56.4	34
60	64	55.6	21
60	56	55.6	20
54	60	54.46	35
54	48	54.46	35
45	50	51.16	37
45	40	51.16	41
36	48	46.7	41
36	40	46.7	44

The axial lengths vary with the change in slot number; the lowest slot count designs with 36 slots have a 19.9% shorter stack length than the highest slot count designs with 72 slots. So this is expected to have an effect on the torque capability of the machine, since the torque is proportional to the unit volume of the rotor as shown by the generalised electrical machine torque equation – equation 6.2; where B_{g_fund} is the peak

of the fundamental air-gap flux density derived by Fourier analysis of the air-gap flux density in figure 6.4, A_{rms} is the electric loading per unit periphery, r the rotor radius, l_a the axial length, N the series turns per phase for the complete machine and I is the phase current.

$$T_m \propto \hat{B}_{g\_fund} A_{rms} \times \pi r^2 l_a \tag{6.2}$$

$$A_{rms} = \frac{6NI}{2\pi r}$$

6.3.2.1 Back EMF waveform distortion

Since the back EMF constant was kept constant by changing the number of turns; the peak values remain unchanged, however the back EMF waveforms contain harmonics, diminished by the winding attenuation of the spatial harmonic contents of the air-gap that link the winding. The rms value of the back EMF can be calculated by equation 6.3, although this will not give a very accurate value due to the non-sinusoidal nature of the EMF waveforms. Φ is the peak of the linked phase flux in the modelled sub-motor, N is turns per coil and f is the electrical frequency.

$$E_{rms} = 4.44 \times \hat{\phi} N \times f \times k_w \tag{6.3}$$

Figure 6.5 shows the line back EMF at a speed of 630rpm for the various optimised designs, derived from a 2D transient with motion simulation and figure 6.6 is the harmonic spectrum of the line back EMF. It can be seen that some non-triplen harmonics exist as expected, but these harmonics have a magnitude that is less than 2% of the fundamental in all designs except the 36slot/48pole and 72slot/48pole. The 72slot/48pole design in particular has a large 5^{th} harmonic, which is about 11.69% of the fundamental harmonic.

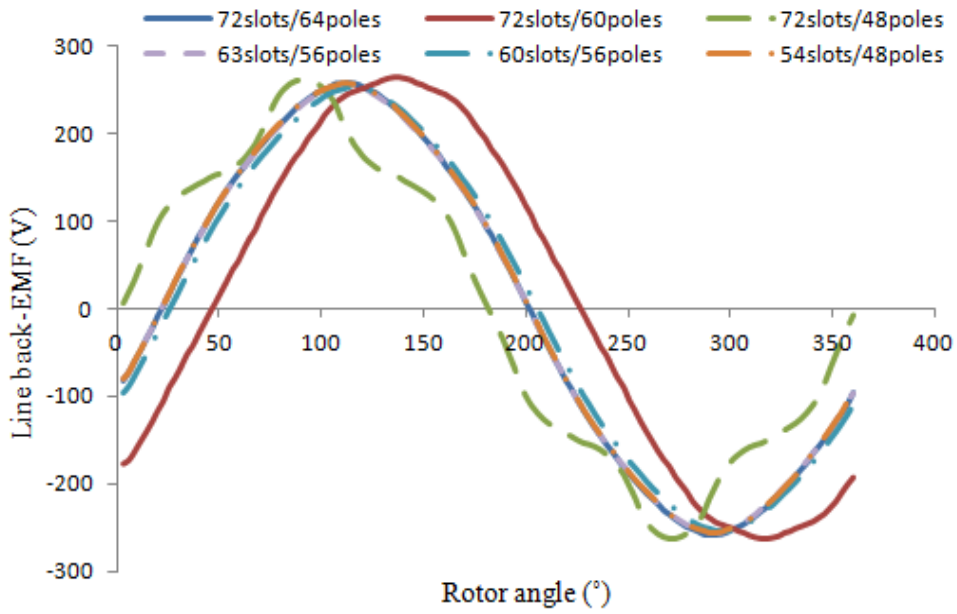

(a) 72slots/64poles, 72slots/60poles, 72slots/48poles, 63slots/56poles, 60slots/56poles, 54slots/48poles.

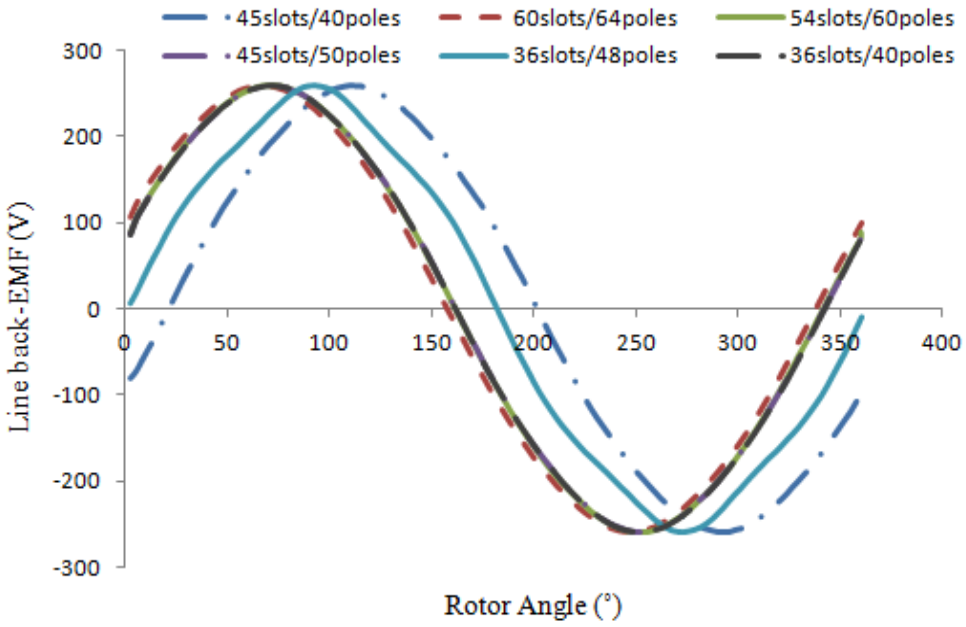

(b) 45slots/40poles, 60slots/64poles, 54slots/60poles, 45slots/50poles, 36slots/48poles, 36slots/40poles.

Figure 6.5. Line back EMF at 630rpm for the chosen slot and pole combinations.

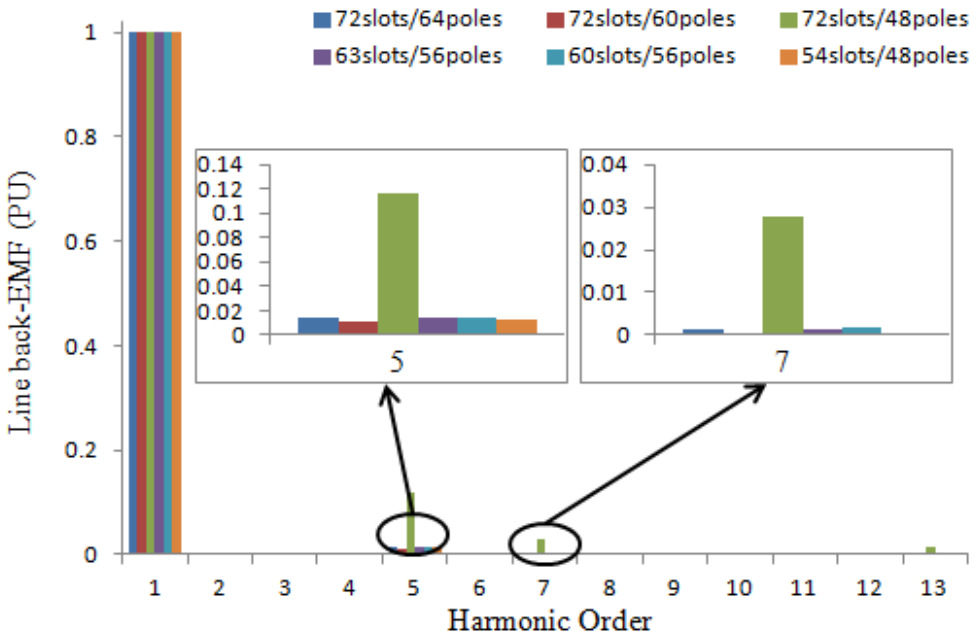

(a) 72slots/64poles, 72slots/60poles, 72slots/48poles, 63slots/56poles, 60slots/56poles, 54slots/48poles.

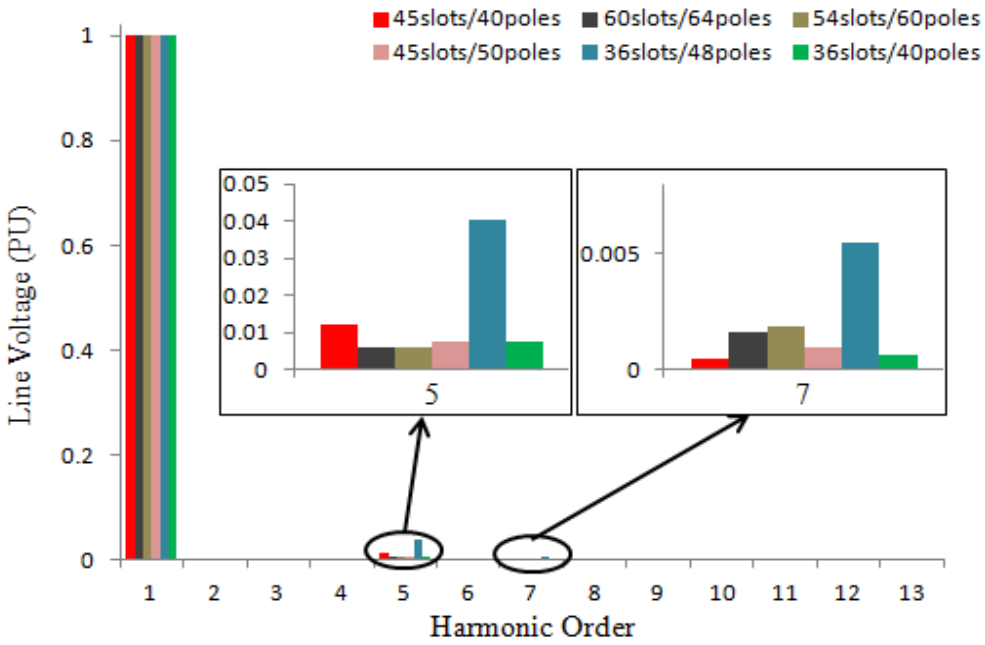

(b) 45slots/40poles, 60slots/64poles, 54slots/60poles, 45slots/50poles, 36slots/48poles, 36slots/40poles.

Figure 6.6. Harmonics in line back EMF for the chosen slot and pole combinations.

6.3.2.2 Electromagnetic torque and torque disturbances

With the exception of oscillatory cogging torque, the surface type permanent magnet machine analysed, produces torque solely due to the voltage induced in the winding by the magnets, this induced voltage interacts with the winding current to produce

mechanical torque. Equation 6.4 describes how the mechanical torque can be derived from computation of the phase back EMF and armature phase current, where β is the phase displacement between the back EMF and current waveform and ω_{mech} is the angular displacement of the rotor over a given time.

$$T_m = \frac{3E_{rms}I_{rms}\cos\beta}{\omega_{mech}} \times submotors \qquad (6.4)$$

The mean torque produced by the different designs as the winding loss changes was investigated; figure 6.7 shows the torque against the winding resistance loss for the complete machine. The designs that have similar performance and the best of all the combinations are the 72slot/64pole and the 54slot/60pole.

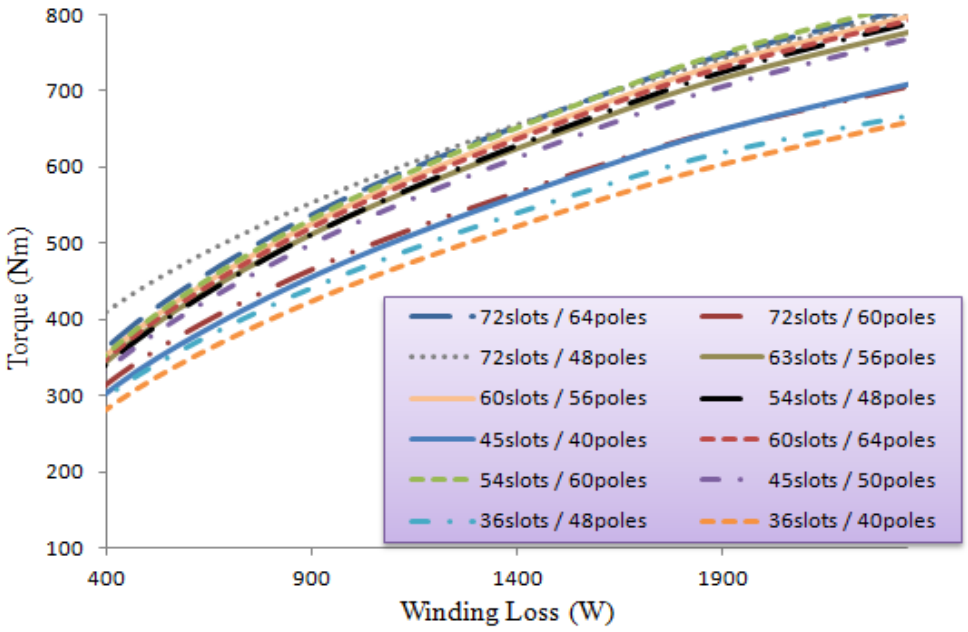

Figure 6.7. Plot of torque against winding resistance loss for slot and pole combinations.

The 54slot/60pole design is a strong candidate of all the combinations considered; this is due to its use of a high electric and magnetic loading, its electromagnetic performance is not influenced significantly by the 6.6% reduction in its axial length compared to the 72slot/64pole design. The 72slot/48pole design at low electric loading produces better torque than all other designs, but when loaded to the rated operating point (2074W – winding loss) the performance drops off below the 72slot/64pole and 54slot/60pole designs due to saturation in the stator teeth. The other designs with closer performance to those mentioned above are the 60slot/56pole and 60slot/64pole designs. Again it can be seen that the 36 slot machines produce the poorest performance, as the reduction in

stack length is significant enough to impact the performance. When the slot number exceeds 45 slots, the performance of all the machine combinations are fairly close showing less than 4.6% difference, with an exception of the 72slot/60pole machine.

Table 6.4. Mean torque output.

Number of teeth	Number of poles	Mean Torque (Nm)
72	64	773.44
72	60	673.05
72	48	769.02
63	56	742.51
60	64	757.09
60	56	761.56
54	60	777.12
54	48	751.57
45	50	732.01
45	40	673.96
36	48	640.15
36	40	625.74

Torque ripple is an important factor to consider that can be a draw back with some machine designs; the torque produced by the various machines over one electrical cycle is shown in figure 6.8. The excitation torque ripple can be quantified using equation 6.5. The factors that create torque ripple and disturbances are as follows [116]:

- Interaction of asynchronous spatial and time harmonics between the air-gap field created by the armature excitation and air-gap field created by the rotor magnets; so even with a sinusoidal current in the stator winding, the field setup in the air-gap has high content of spatial harmonics due to the slotting effect and tooth tip saturation.
- The variation of reluctance to the tooth and slot interacting with the air-gap field created by the magnet flux; this torque is usually felt when the stator winding is not energised and the rotor flux changes with position.

$$T_{ripple}(\%) = \frac{T_{\max} - T_{\min}}{T_{\max}} \times 100 \qquad (6.5)$$

The machines with the worst torque ripple are the 36slot/48pole and the 72slot/48pole machines as seen from the torque waveforms; this is due to the poor attenuation of the air-gap harmonics in the back EMF waveform. Since the current put into the windings of the machines is balanced and sinusoidal, but the back EMF is not sinusoidal, so the torque ripple produced by the machine will be due to the distortion of the back EMF waveform.

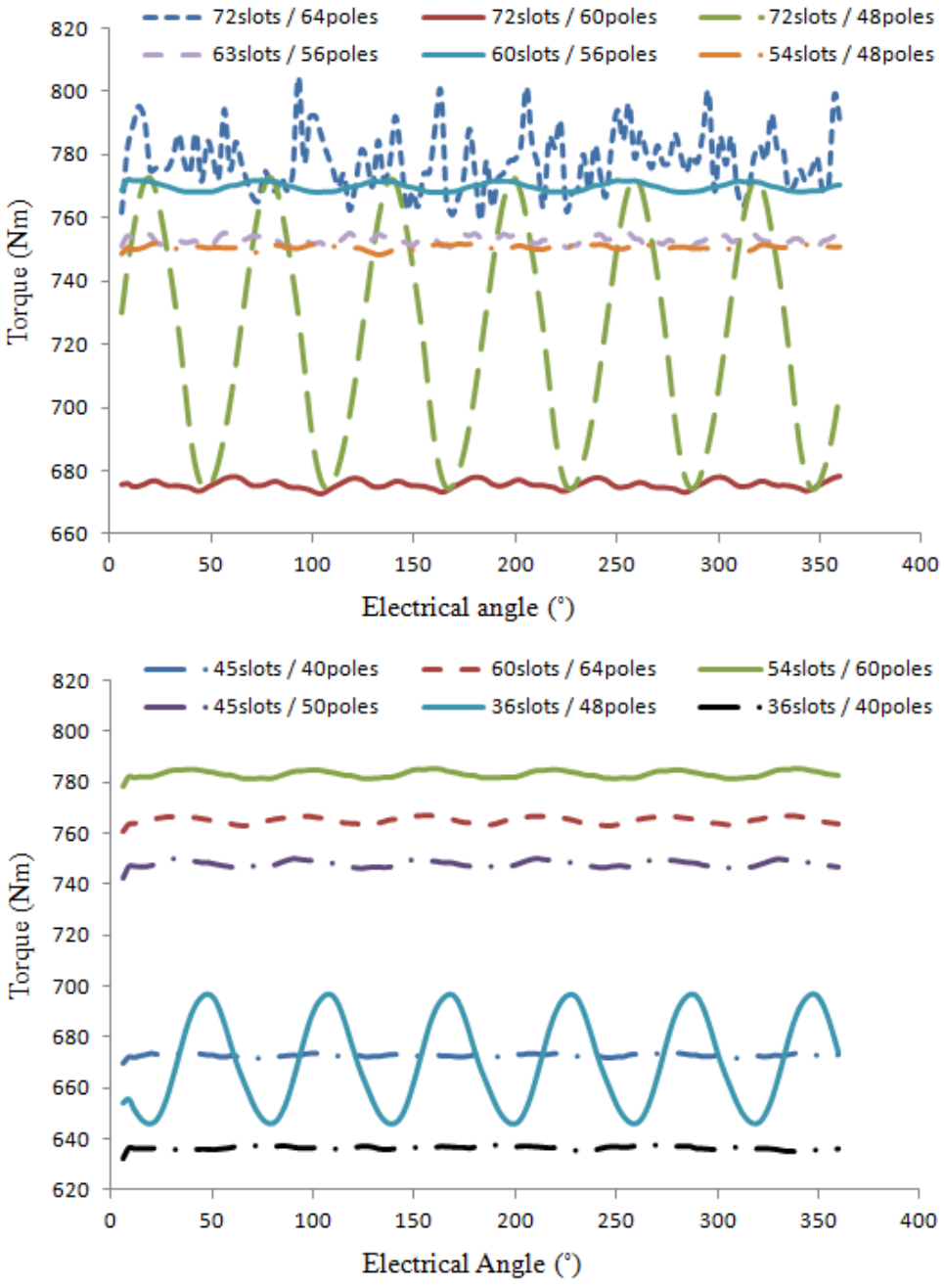

Figure 6.8. Torque output at 630rpm.

The 72slot/64pole machine was chosen for future study, as will be seen in the following sections of this chapter, this is also partly because it is in line with the existing electronics.

Along with the 72slot/64pole machine, the 54slot/60pole machine also presents a good level of performance, which could be analysed in future work.

6.4 72slot/64pole stator slot MMF harmonics

The advantages of having a concentrated fractional slot machine have been discussed in Chapter 2, however the stator MMF of such a machine produces a high level of space harmonics in the air-gap. This is due to the current in the stator winding producing a magnetic field in the air-gap that contains both space and time harmonics. Ignoring the time harmonics, the distortion in the stator MMF air-gap field is caused by the slotting effect of the machine, flux concentration at the edges of the teeth and the chosen slot and pole combination [76, 117]. The high order space harmonics that rotate asynchronously with the rotor cause an increase in the rotor losses, depending on the strength with which they penetrate the rotor.

The stator MMF slot harmonics were obtained from an FE model for the 72slot/64pole machine. The FE model was set up by applying a sinusoidal current in the phase windings and the magnet components disabled. This was then solved for a 2D transient solution. After solving the model, a set of mathematical equations were applied to determine the tangential H-field produced by the stator winding MMF, which was Fourier analysed to generate the harmonic contents that make up the stator air-gap H-field. The set of mathematical equations were implemented using Matlab, which can control the Infolytica MagNet™ software to extract the field strength in the x (H_x) – and y (H_y) – axis. The tangential H-field is then obtained from H_x and H_y by using equation 6.6. Figure 6.9 shows the variation of the tangential H-field with position, when the winding current is at a maximum in phase A and negative half in phases B and C.

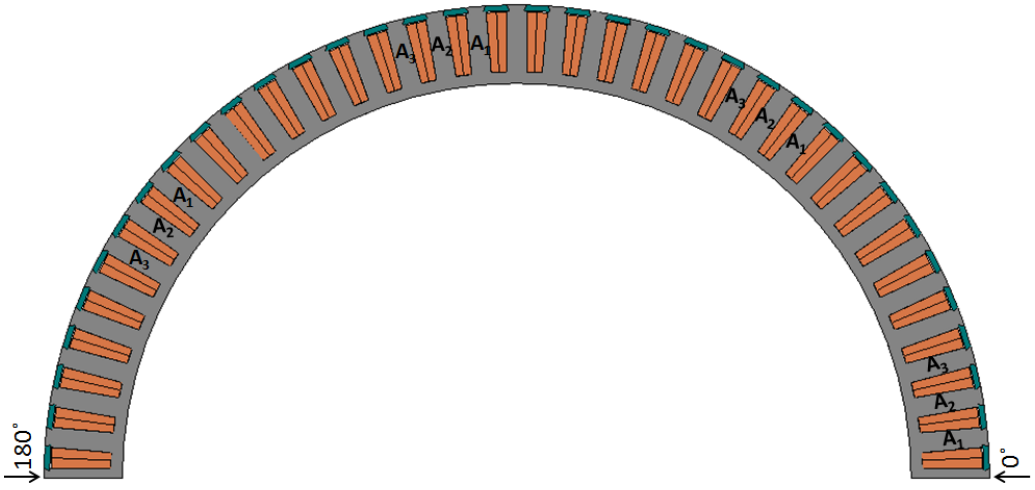

(a)

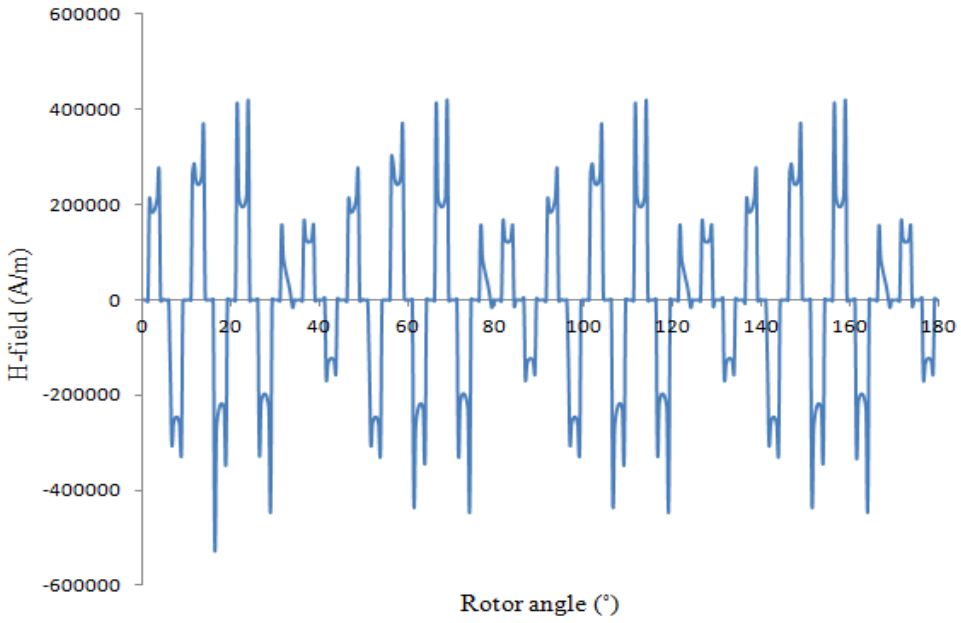

(b)

Figure 6.9. Variation of tangential H-field with position: (a) stator structure, (b) stator H-field waveform.

$$H_{\tan gential} = H_x \cos(\theta + 90) + H_y \sin(\theta + 90) \qquad (6.6)$$

In figure 6.10 the harmonic spectrum of the stator tangential H-field for the complete machine (as in figure 6.9 – b above) is shown. As expected the torque producing harmonic is the 32nd harmonic for the complete machine, also all harmonics are a multiple of the 8th harmonic, as the machine is 8 identical 9slot/8pole sub-motors. There are sub-harmonics (owing to the fact that the torque producing harmonic is of a high harmonic number) present and a high magnitude of the 40th harmonic that contributes significantly to the rotor losses.

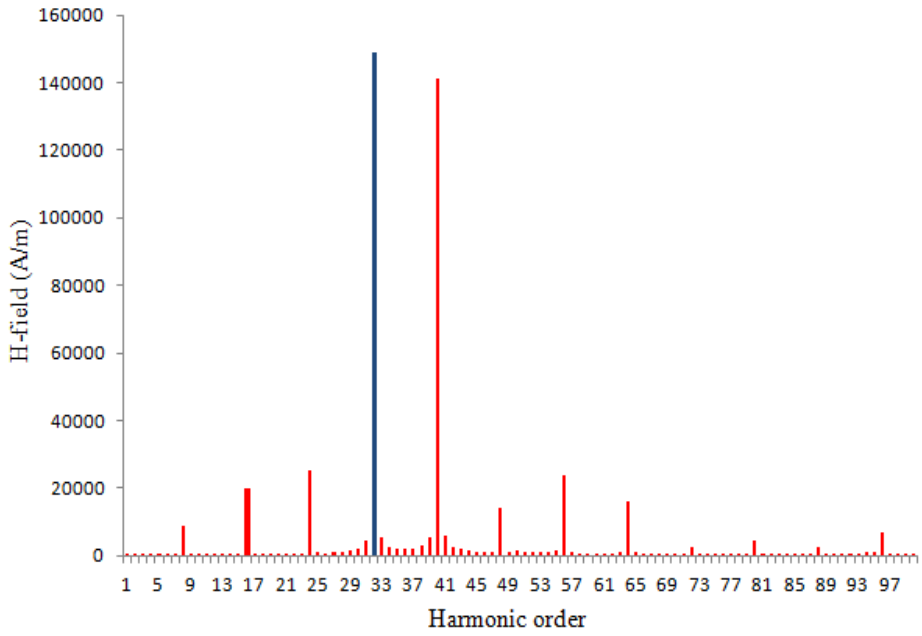

Figure 6.10. Stator slot MMF harmonics.

6.5 72slot/64pole slot loss

The slot loss for an AC machine can be separated into its individual components they are; proximity loss due to the arrangement and shape of coils enclosed in the slot, loss due to the varying air-gap field and conduction loss due to the resistance of the wire. A time-harmonic 2D simulation was solved to determine the contribution of the various loss components.

A method called the square-field-derivative for computing the proximity eddy current losses in the slot of a machine made up of round wires was derived by the author of [118], as shown in equation 6.10. The method analyses the time dependent field enclosed by the current carrying conductors of the slot, which cuts across each conductor in the slot and induces an eddy current that circulates within each conductor, leading to increase in heat loss within the conductors. Figure 6.11 shows the enclosed H-field setup by the current carrying conductors, showing the enclosed H-field variation with the slot depth. Equations 6.7 to 6.9 are also relevant to the calculation of the proximity loss in equation 6.10; N is the number of turns enclosed within the H-field, ω is the electrical frequency, μ_0 is the permeability of free space, l_a is the axial length of the conductor, l is the slot width (ignoring any MMF drop in the stator iron), d_c is the conductor diameter and ρ_c is the conductor resistivity.

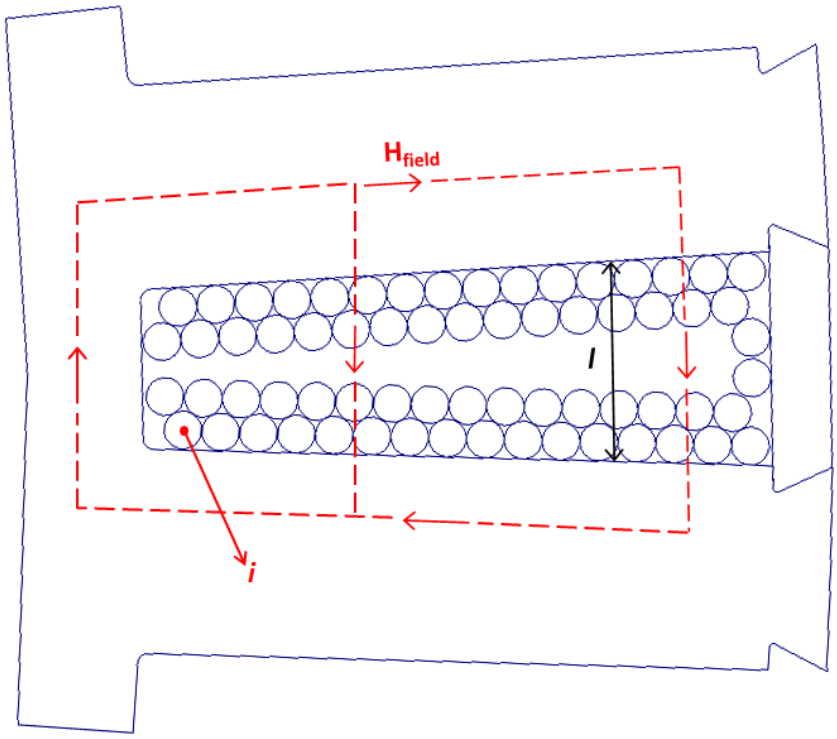

Figure 6.11. Slot conductors and MMF setup by the conductors.

$$H = {N \times I \sin(wt)}/{l} \tag{6.7}$$

$$B = \mu_0 \times H \tag{6.8}$$

$$\left(\frac{dB}{dt}\right)^2 = \frac{\omega^2 \times \mu_0^2 \times N^2 \times I^2 \cos^2(wt)}{l^2} \tag{6.9}$$

$$P(t) = \frac{\pi l_a d_c^4}{64 \rho_c}\left(\frac{dB}{dt}\right)^2 \tag{6.10}$$

Figure 6.12 shows the magnitude of the eddy current in the conductors solely due to the flux setup by the excitation current in the turns of the slot; it can be seen that at the bottom of the slot the eddy current circulating in each conductor is at its lowest because the MMF enclosed is only that of a few conductors, as compared to the layer of conductors at the top of the slot (closest to the air-gap) that encloses a larger MMF. In figure 6.13 the proximity loss variation with the current applied to the coil for the complete machine at a frequency of 336Hz is shown; this shows the loss square relation with current and the same relation can be said for the supply frequency.

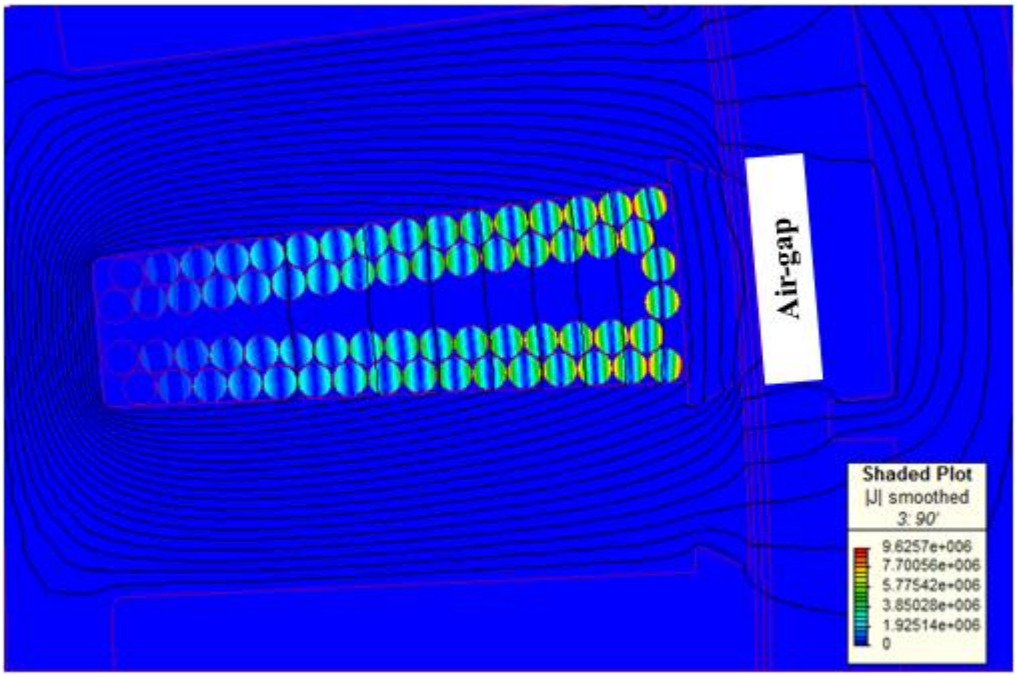

Figure 6.12. Eddy current in conductors and slot MMF.

The variation in the air-gap field due to the magnets also contributes to the slot loss due to the exposure of the top layer of the winding to the air-gap field; this always has to be considered and is dependent on the design of the stator tooth tip, FE result of the variation of this loss component with speed will be presented later in Chapter 8. In figure 6.13, the offset of the total slot loss at zero winding current is as a result of this loss.

Finally the conduction loss (I^2R) due to the resistance of the conductor is hugely important, this can be seen in figure 6.13. For a DC supply the conduction loss is solely due to the DC value of the coil resistance, which can be calculated by the simple coil resistance equation (6.11). However for an AC supply it becomes more computational, as the value of the resistance is affected by the skin effect of the conductor due to the supply frequency, this causes the current to flow in a smaller area of the conductor, which changes the resistance of the current path. Equation 6.12 is applied to calculate the depth of the conductor skin; C.S.A is the conductor cross sectional area, f is the supply frequency and σ is the conductivity of the material. Figure 6.13 shows the total slot loss of the complete machine as it varies with the phase current, at a frequency of 336Hz.

$$R_{DC} = \frac{2 \times N \times l_a \times \rho_c}{C.S.A} \tag{6.11}$$

$$d_{skin} = \frac{1}{\sqrt{\pi f \mu_0 \sigma}} \tag{6.12}$$

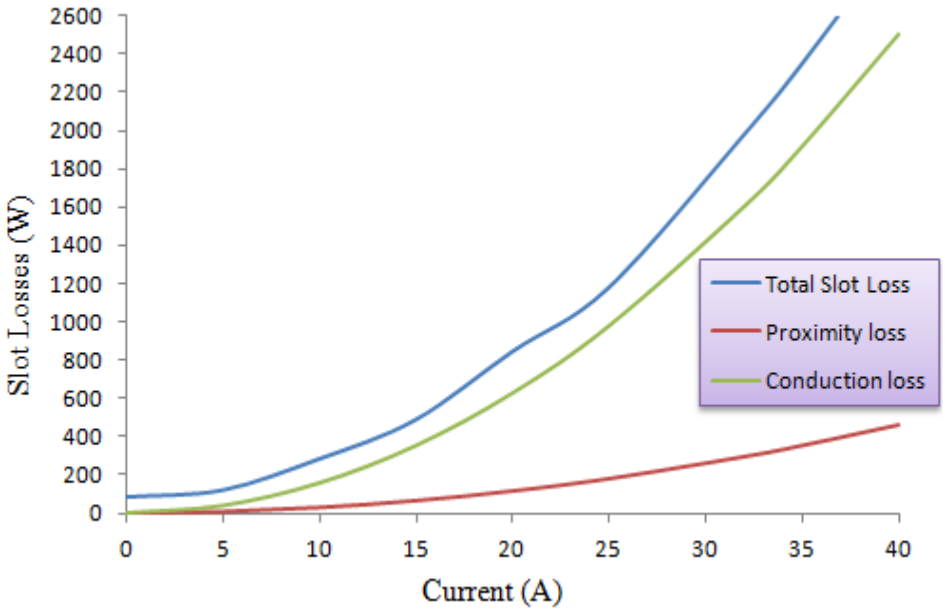

Figure 6.13. Components of winding loss in the complete machine at 630rpm.

6.6 72slot/64pole torque vs speed graph

The torque – speed curve for the complete machine is shown in figure 6.14, this was obtained from an FE model by solving a 2D transient with motion. The field weakening equation (1.5) derived in chapter 1 was applied to determining the field weakening angle, which was then applied to the FE model by phase shifting the angle between the supply current and back EMF. Table 6.5 shows the field weakening angle – β at various speeds and the resulting per unit d and q – axis inductances obtained at a terminal line voltage of 360Vpeak and peak phase current of 32A. Equation 6.13 was applied to determine the machine's power output. When the machine is operating in the field weakening region and a negative d-axis current is applied, there is a possibility that permanent or partial demagnetisation of the magnets could occur. Demagnetisation is investigated later in the next section.

$$P_{out} = T_m \times \omega_{mech} \tag{6.13}$$

$$L_{(q,d)}(pu) = \frac{\omega L_{(q,d)} I_{(q,d)}}{E_f} \tag{6.14}$$

Table 6.5. Field weakening angle and reactance.

Speed (rpm)	L_q (pu)	L_d (pu)	β (˚)
100	0.9697	0	0
200	0.9697	0	0
300	0.9697	0	0
500	0.9697	0	0
700	0.951	0.1812	11.28
900	0.8277	0.4827	31.4
1100	0.7088	0.6322	43.03
1300	0.6137	0.7172	50.74
1500	0.5387	0.7703	56.25
1700	0.4788	0.8056	60.42
1900	0.43	0.8303	63.67

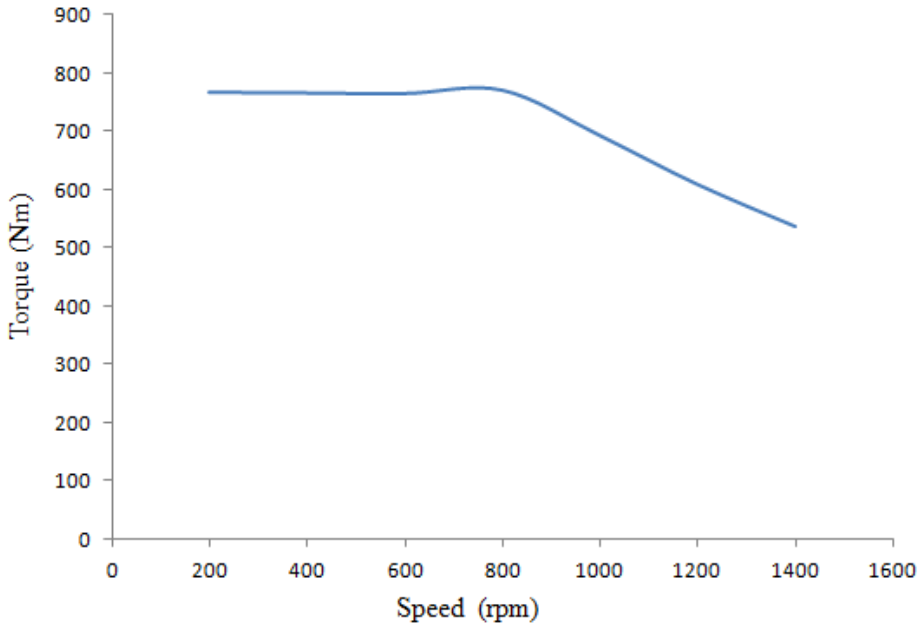

Figure 6.14. Torque – speed curve obtained from FE calculation.

6.7 Magnet demagnetisation

Partial or complete demagnetisation of the magnets in the permanent magnet machine is an important issue to consider. In the field weakening region negative d-axis current is applied to act against the magnet reducing the back EMF of the machine if the current is

too high, this can cause demagnetisation. The operating temperature and magnetic circuit are also factors that can cause the partial or irreversible demagnetisation of the magnets. Figure 6.15 shows the hysteresis curve (or demagnetisation curves) in the second quadrant for the neodymium-iron-boron magnet used in the machine construction. The magnet will have its load line from the origin, the gradient of this line is a function of the permeance of the magnetic circuit in which the magnet has been placed, with no external field applied to the magnet by the machine's stator winding. When the load line crosses the intrinsic curve above the knee point at any given temperature it is said that the magnet is operating at a safe linear region and can return to the residual flux density of the magnet. If the load line crosses below the knee point of the intrinsic curve then the magnet will experience an irreversible demagnetisation due to the relative recoil permeability of the magnet causing the magnet to behave in a linear manner at any temperature [119]. During normal machine operation, the normal curve determine how the magnet is loaded in the machine and when the magnet operate anywhere close to the knee point on the normal curve then there is possibility of causing an irreversible demagnetisation, as the knee point on the normal curve corresponds to the knee point on the intrinsic curve. The load line can be drawn from any point on the x-axis, depending on the demagnetising field applied by the stator winding.

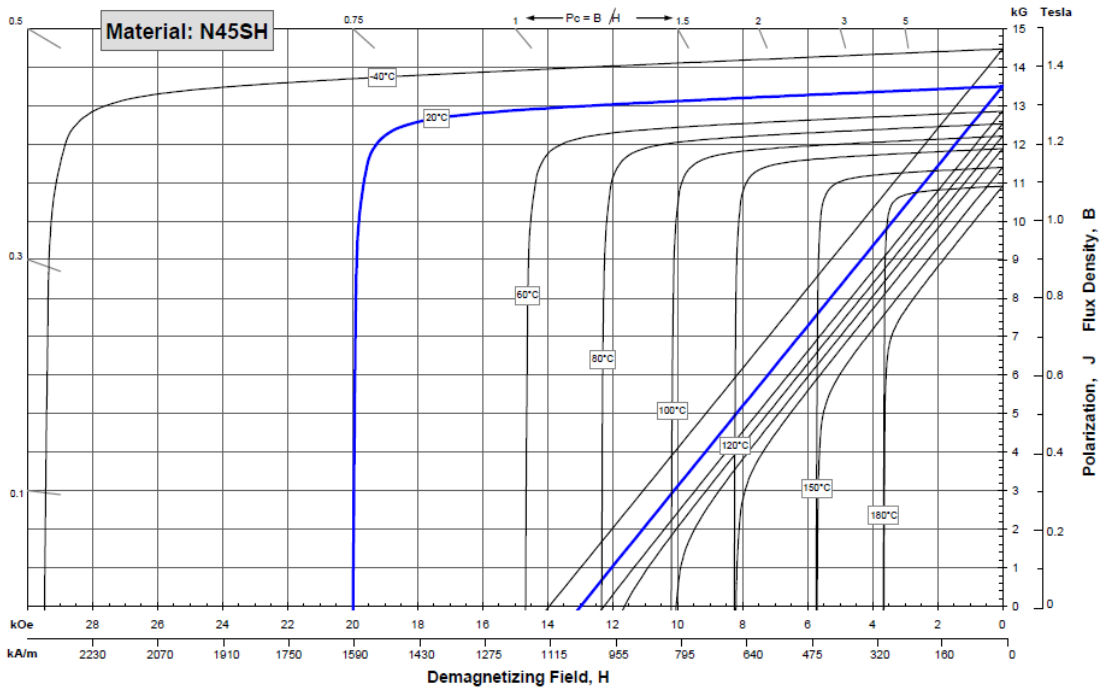

Figure 6.15. Magnet Characterisation B-H curve [120].

A 2D static solution of FE model to determine the demagnetisation of the magnet has been solved; an operating temperature of 150˚C was chosen for the magnet with the

rotor rotating at a speed of 1600rpm. The negative d-axis current applied to the machine was -19.3A and the magnet was placed at the d-axis of the phase (directly underneath a tooth), to which this current was applied. The magnet's demagnetisation flux density threshold for this operating temperature was 0.6T. Figure 6.16 shows the magnet flux density plot; it can be seen that the magnet flux is reduced to 0.6652T at the edges of the magnet exposed to the air-gap, which means the magnet is not likely to experience any permanent demagnetisation at this operating point.

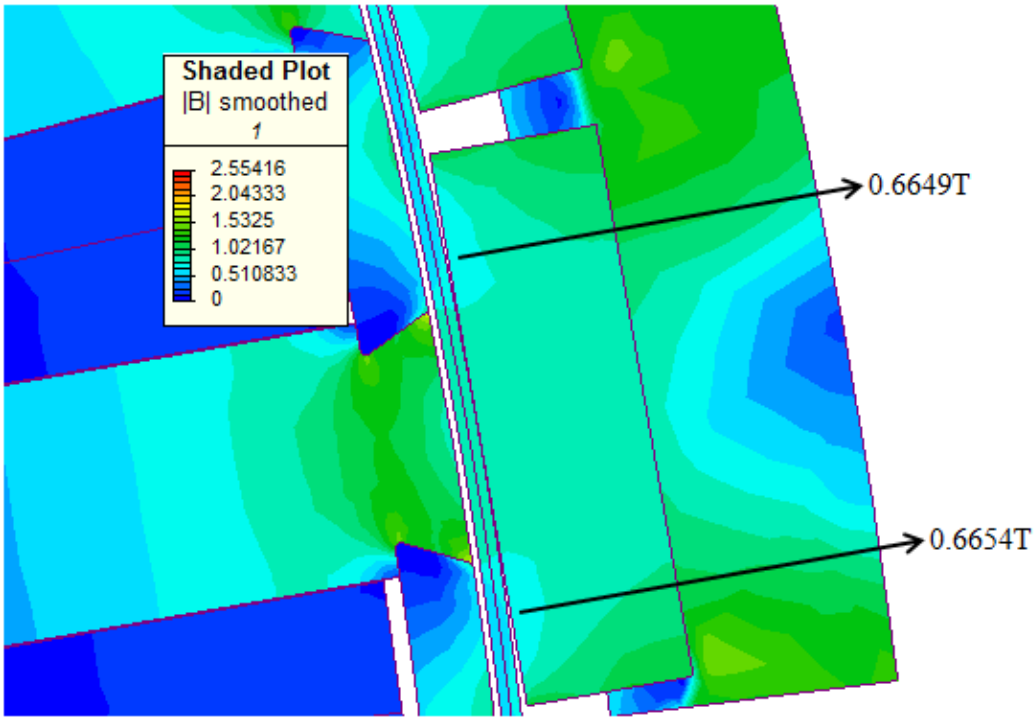

Figure 6.16. Magnet flux density due to negative d-axis current in stator winding.

6.7.1 Magnet coating

The electromagnetic effect of having a coating around the magnet was investigated. Magnets are susceptible to corrosion depending on the environment in which they are used, this can lead to the magnet breaking down into its powder form. The coating material studied is copper nickel; having a conductivity of 2000000siemens/m and a thickness of 0.03mm around the magnet. Figure 6.17 shows the eddy current circulating within the magnet coating; a 2D transient with motion solution was applied with the with a peak current of 34A. The eddy current density in the magnet coating was calculated to be 11.5A/mm^2 at this operating point.

The total losses calculated in the magnets are 1328W within the magnets and 114W for the magnet coatings, at a speed of 1200rpm. The loss in the magnets when the coating is not applied around the magnet is 1349W also at the speed of 1200rpm, which indicates

that the coating does not do much in shielding the magnets from the air-gap field. The total magnet loss increases by 6.88% when the coating is applied to the magnet, which leads to an increased magnet temperature.

The magnets are axially split into five segments; this reduces the eddy current loss in the magnets by increasing the total resistance path in which the eddy current flows, in turn reducing the eddy current that flows around the magnets.

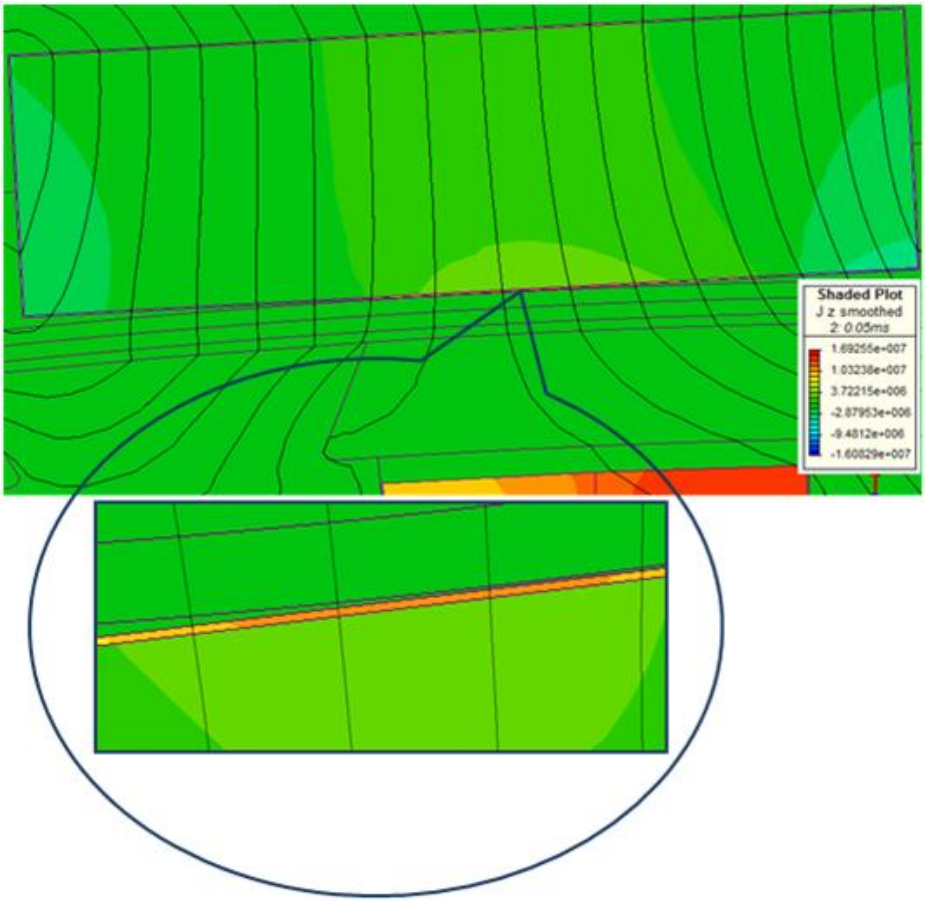

Figure 6.17. Eddy current in magnet coating.

6.8 Conclusion

The design effect of having a high pole number in the machine was discussed in this section and the possible design variations with regard to having a high pole number highlighted. Different pole and slot combinations for the machine design with compressed winding, having slot wedges have been studied. The 72slot/64pole and 54slot/60pole machines showed the best performance with the 72slot/64pole machine producing better performance at low current loading of the two machines.

Further electromagnetic analysis was conducted on the 72slot/64pole machine, to determine the machine performance and the source of losses in the rotor and stator slot. Compared to a conventional slot opening design, having a slot wedge at the tip of the tooth can cause an increase in the slot loss by exposing the conductors to the varying field from the air-gap and also introduces high content of space harmonics that increases the rotor magnet loss.

The possibility of magnet demagnetisation was studied by considering operation under field weakened conditions, at a given magnet temperature. Finally due to the environment in which the machine is to be used, the use of coated magnets was studied and its effect on the magnet loss highlighted. The magnet coating has to be made as thin as possible so as to prevent a significant drop in the flux linking the coils from the magnets.

Chapter 7

Machine Thermal Analysis

This chapter discusses thermal analysis of the 72slot/64pole machine design. At first the various slot and pole number combinations discussed in the previous chapter were parameterised and optimised for a given slot temperature rise, with the main objective of improving the mean torque output. The electromagnetic FE modelling and optimisation tools used in the previous optimisation were also used for the slot temperature optimisation. Finally the 72slot/64pole machine was modelled using motorCAD, in order to predict the heat flow in the machine from the thermal resistance network. With the information obtained from motorCAD a FE thermal analysis was conducted using ThermNet™, in order to study the temperature drop caused by the slot liner and any air-gap between winding and tooth.

7.1 Introduction

The thermal aspect of machine design is very important, as this is the factor that limits the maximum output performance of most machines. This is especially the case in a machine used for an in-wheel direct drive electric vehicle application, where a high continuous torque rating is required and the machine has to be capable of delivering a certain peak overload torque for a short period of time. The temperature within the machine is directly related to the thermal resistance properties and the losses in the machine. The losses that can be generated in a machine have been discussed in the introduction.

There are different methods which can be used to cool a machine, in this work water cooling was used, with a water jacket around the inner surface of the stator. At low speed, high torque, the bulk of the heat loss is generated in the slot, as large currents are passed into the windings. Due to the thermal path from the slot out to the water jacket it is difficult to cool the machine effectively at low speed. However at higher speed, the heat loss is larger in the iron core as the current into the winding is reduced and the high frequency increases the iron loss, the temperature rise for a given total loss is reduced, making the cooling at high speed more effective.

There are three modes of heat transfer in a machine; conduction, convection and radiation. The heat is transferred from the slot via the tooth and onto the stator core back by conduction, and then finally the heat is removed from the stator core back into the atmosphere by convection or radiation. A temperature gradient can be plotted within a machine to spot the areas within the machine were temperature drops are introduced due to the poor thermal conductivity of the material or medium.

7.2 Optimisation of various slot and pole number combinations

The previous optimisations performed on the different slot and pole combinations only considered the winding loss of the machine, however as the pole number changes, so does the iron loss for a given speed, which in turn changes the temperature rise in the slot. In this section, work on optimising the various slot and pole combinations for a given slot temperature rise is presented.

7.2.1 Initial assumptions and optimisation method

The model was scripted for a fixed slot conductor current density, as the stator dimensions vary a new slot area is calculated and subsequently a value of peak current

is applied to maintain the same conductor current density. However at the end of each iteration process, a new value for current density is calculated based on the likelihood of the slot temperature exceeding the preset limit. The varied parameters set for this optimisation are similar to those for the previous optimisation presented in figure 6.3 of Chapter 6, except in this case the magnet arc was a fixed value. The optimisation limits imposed in the previous optimisation were adopted here, although the stator inner diameter was set to 282mm.

The temperature of the machine was assumed to be at a steady state, so that the simple lumped thermal resistance network could be created. This calculates the various temperature drops within the machine, as well as highlighting the nodes where the losses generated add to the heat flow. Figure 7.1 shows the simple thermal resistance network, it was assumed that the stator is directly coupled to the water jacket (the water jacket was held at a temperature of ***50˚C***), thereby excluding the effect of the temperature drop between the stator and water jacket due to roughness of the surface and contact resistance. The thermal resistance network in figure 7.1 has been derived from the slot heat flow mechanism shown in figure 7.2.

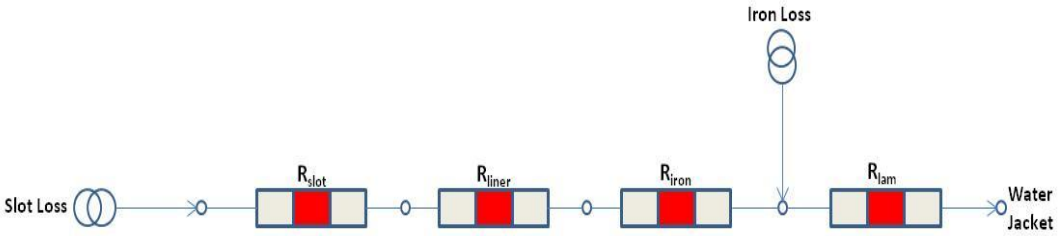

Figure 7.1. Lumped Thermal Resistance Network showing Heat Flow

- R_{slot} is the total slot thermal resistance.
- R_{liner} is the slot wall liner thermal resistance.
- R_{iron} is the thermal resistance due heat conduction in the lamination.
- R_{lam} is the thermal resistance due to convection out the stator lamination.

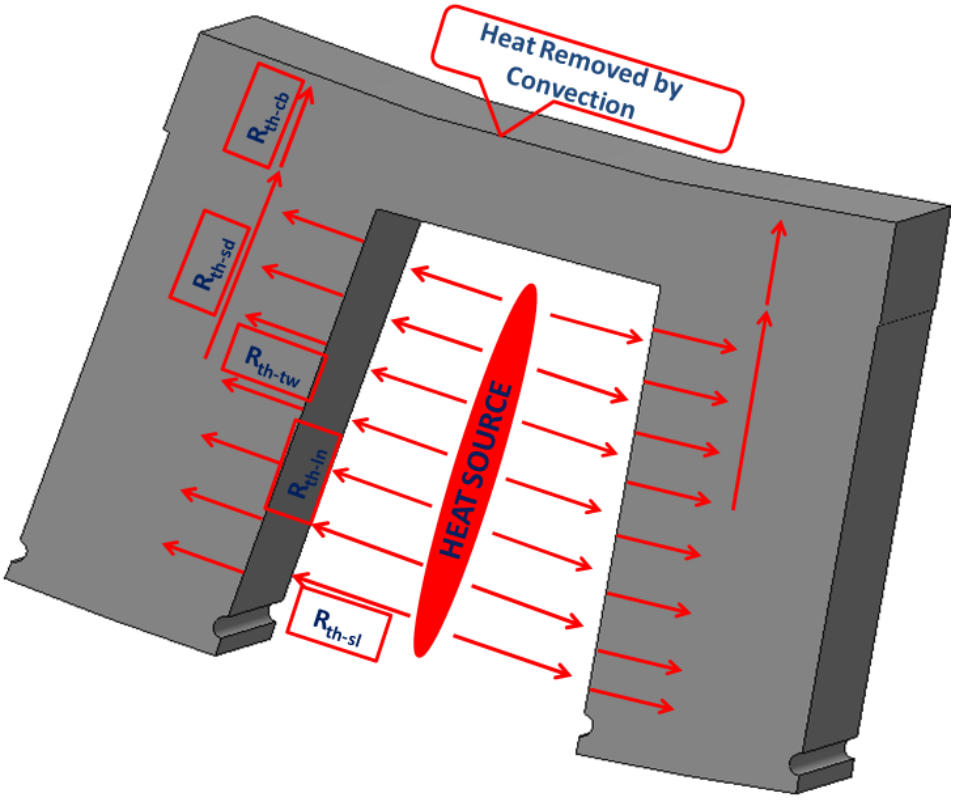

Figure 7.2. Thermal path for heat removal from the slot; R_{th-sl} - slot thermal resistance, R_{th-ln} - liner thermal resistance, R_{th-tw} - half-tooth thermal resistance, R_{th-sd} - half slot depth thermal resistance, R_{th-cb} - core-back thermal resistance.

A peak slot temperature of ***180˚C*** was set as a limit for the optimisation.

Slot Resistance (*R_{slot}*): Calculating the thermal resistance of the slot is not a simple process, as an equivalent thermal conductivity of the slot has to be obtained based on the contents of the slot. The thermal resistivity of the copper is assumed to be negligible as its value is extremely low compared to any other component that makes up the slot content (such as air, impregnation or wire insulation). As the fill factor of copper increases the equivalent thermal conductivity of the slot increases. Dickinson [121] presented a conductivity factor, which is multiplied by the conductivity of air (0.026W/˚C/m), to get the effective thermal conductivity of machine with high slot fill factors. The value of conductivity depends on the shape of copper, method of winding and the compounds surrounding the copper. For this optimisation it was assumed that the slot was potted with an epoxy having a conductivity of 0.2W/˚C/m and the insulation of the copper wire was also assumed to have a conductivity of 0.2W/˚C/m. An equation used to derive the effective slot conductivity will be presented later in this section, based on the conductivities mentioned above.

Equation 7.1 was used to calculate the equivalent thermal resistance of the slot. The constants of the equation vary from a potted to an un-potted slot and for a potted slot the values for the constants are as follows: *a = 0.1753, b = -0.0282, c = 0.3973*. These constants were obtained in [121] by curve fitting on an FE model result of the slot thermal conductivity factor over a range of fill factor values, using the thermal conductivity for epoxy and copper insulation stated above. If the conductivity of the epoxy and copper insulation is changed, then the constants for calculation of winding equivalent thermal conductivity will change.

$$K_{winding} = \frac{K_{air}}{a + b.(\%\, fill\_factor)^c} \tag{7.1}$$

Equation 7.5 is used for calculation of the slot thermal resistance and was derived from equations 7.2 to 7.4 that describes the temperature rise due to conduction; where *Z* is the loss density, *w* is length of slot width considered, *l* is the total slot width and $k_{winding}$ is the equivalent winding thermal conductivity.

Assuming all the heat that flows out of the conductor is equal to the heat generated, and all heat travels out the sides of the slot, giving a one dimensional problem, equation 7.2 is obtained.

$$k\frac{\partial^2 T}{\partial l^2} = -Z \tag{7.2}$$

The general solution to equation 7.2 is:

$$T = \frac{-Z}{2k}l^2 + c_1 l + c_2 \tag{7.3}$$

Where c_1 and c_2 are constants, dependent upon the boundary conditions. If the problem is symmetrical, then we can assume that $T = T_0$ at $l = 0$ and $l = w$, c1 and c2 are given below.

$$T_0 = c_2 \text{ and } c_1 = \frac{Zw}{2k}$$

Apply c_1 and c_2 in equation 7.3, gives:

$$T_{rise} = \frac{-Z}{2k}l^2 + \frac{Zw}{2k}l\,; \qquad l = w \text{ so,} \tag{7.4}$$

$$T_{rise} = \frac{-Z}{8k} w^2 = \frac{loss \times w^2}{8k \times slot\_volume}$$

$$\therefore R_{slot} = \frac{w^2}{8k_{winding} \times slot\_volume} \quad (7.5)$$

$$w = slot\_width - 2 \times liner\_thickness$$

Liner Resistance (*$\mathbf{R_{liner}}$*): The slot liner resistance is comparably easier to derive, the temperature drop across the slot liner increases with increase in the thickness of the slot liner. Electrical insulators are generally poor thermal conductors, which makes it important to consider the temperature drop across the liner. The slot liner used in the model was 0.00018m thick and with conductivity of ***0.14W/°C/m***.

Equation 7.6 calculates the slot liner thermal resistance, where *k* is the slot liner thermal conductivity and *l* is the thickness of the slot liner.

$$R_{liner} = \frac{2l_{liner}}{k \times Area_{liner}} \quad (7.6)$$

$$Area_{liner} = slot\_depth \times axial\_length$$

Lamination Conduction Resistance (*$\mathbf{R_{iron}}$*): The heat generated in the slot has to flow through the stator tooth and up the core back by conduction before being removed by convection on the stator outer surface. The thermal conductivity of the lamination used is ***28W/m/°C***. It is assumed that all the heat generated in the slot flows out the side of the slot. To get an average value for the heat removed from the slot, only half the tooth depth and half the tooth width is considered for calculation.

The thermal resistance of the stator tooth can be calculated using equation 7.7, where D_{half_slot} is half the depth of the slot and $Area_{1/2tooth\_la}$ is the product of half the tooth width and axial length. Equation 7.8 is for calculation of the thermal resistance drop at the stator core back.

$$R_{iron\_1} = \frac{2D_{half\_slot}}{k \times Area_{1/2tooth\_la}} \quad (7.7)$$

$$R_{iron\_2} = \frac{l_{coreback}}{k \times Area_{coreback}} \quad (7.8)$$

Lamination Convection Resistance (*$\mathbf{R}_{lam}$*): Heat is removed from the outside surface of the lamination by convection. The equation for the thermal resistance of the lamination will be given in the next section. A heat transfer coefficient of 3280W/m^2/°C was assumed, which is obtained from the motorCAD model built for the thermal analysis of the machine.

Equation 7.9 was derived for calculation of the thermal resistance due to convection at the stator lamination core back; starting from equation 7.10 of temperature rise due to convection, where *h* is the heat transfer coefficient.

$$T_{rise} = \frac{loss}{h \times Area} \tag{7.9}$$

$$Area = axial\_length \times slot\_pitch\_arc$$

$$\therefore R_{lam} = \frac{1}{h \times Area} \tag{7.10}$$

From knowledge of the various thermal resistances, a general equation for the peak temperature in the slot can be derived by adding the temperature rise across the various thermal resistances to the temperature of the water jacket, as shown in equation 7.11. The slot loss only considers the DC winding loss, ignoring the end-winding length. The iron loss in this calculation is a value obtained from the iron loss per unit slot pitch of the stator (the total stator loss divided by the number of teeth). It must be noted that this stator iron loss is an approximate value and in a real system the loss is not uniform all around the stator lamination.

$$T_{slot}{}^{o}C = water\_jacket{}^{o}C + slot\_loss \times (R_{slot} + R_{liner} + R_{iron\_1} + R_{iron\_2} + R_{lam}) + Iron\_loss \times R_{lam} \tag{7.11}$$

Since the winding temperature is fixed at 180°C, the thermal limiting torque can always be calculated for each iteration process of the optimisation by applying a factor to account for the temperature deviation away from the allowed peak slot temperature of 180°C. The method for determining the thermal limiting torque is shown from equations 7.12 to 7.14 and equation 7.15 is used to calculate the new slot current density due to the peak slot temperature set.

$$\theta_{allowed}{}^{\circ}C = T_{slot}{}^{\circ}C - T_{water-jacket}{}^{\circ}C \tag{7.12}$$

$\theta_{allowed}{}^{\circ}C$ is the maximum allowed temperature rise from the slot and stator core due to the water jacket at the stator core-back.

$$\theta_{winding-allowed}{}^{\circ}C = \theta_{allowed}{}^{\circ}C - \theta_{iron-loss}{}^{\circ}C \tag{7.13}$$

$$\theta_{iron-loss}{}^{\circ}C = Iron\_loss \times R_{lam}$$

$\theta_{winding\text{-}allowed}{}^{\circ}C$ is the allowed temperature rise of the slot and $\theta_{iron\text{-}loss}{}^{\circ}C$ is the temperature rise due to the iron loss, while $\theta_{winding\text{-}actual}{}^{\circ}C$ is the actual temperature rise calculated from the current applied in the winding.

$$\theta_{winding-actual}{}^{\circ}C = slot\_loss \times R_{slot} + slot\_loss \times R_{liner} + slot\_loss \times R_{lam}$$

$$\therefore Torque_{\theta\_limit}(Nm) = Torque_{calculated} \times \sqrt{\frac{\theta_{winding-allowed}{}^{\circ}C}{\theta_{winding-actual}{}^{\circ}C}} \tag{7.14}$$

$$\therefore J_{\theta\_limit}(A/m^2) = J_{calculated} \times \sqrt{\frac{\theta_{winding-allowed}{}^{\circ}C}{\theta_{winding-actual}{}^{\circ}C}} \tag{7.15}$$

Equation 7.14 is the final torque output objective to be maximised for the fixed slot temperature for each iteration process of the optimisation. Equation 7.15 gives the actual current density of the slot after the correction factor has been applied.

7.2.2 Optimisation result

A few trends can be observed from the final optimisation of the various slot and pole combination:

- The slot width tends towards a smaller value to reduce the temperature drop across the slot, as it was assumed that the heat is removed from the slot through the sides
- The slot depth tends towards a larger value in order to have available slot area to get a good level of electric loading in the machine, despite the decrease in slot width
- The temperature drop in the lamination is not significant, so the core-back depth tends towards the maximum limit of the inner stator radius, in order to reduce the core-back saturation.

The final structural designs for all the combinations can be seen in figure 7.3, and it is evident that the tooth width was made wider and slot width narrower to reduce the temperature drop in the machine. A comparison of the stator dimensions when the

optimisation was conducted for a fixed slot loss and the optimisation for a fixed winding temperature can be seen in Appendix B.

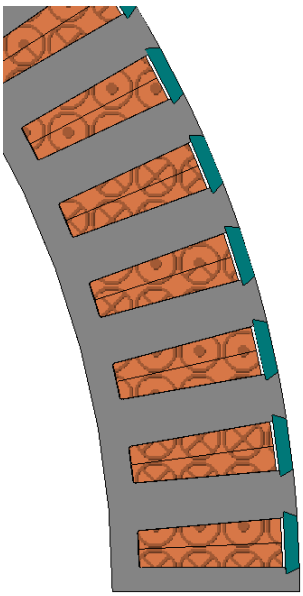

(a) 72slots/64poles

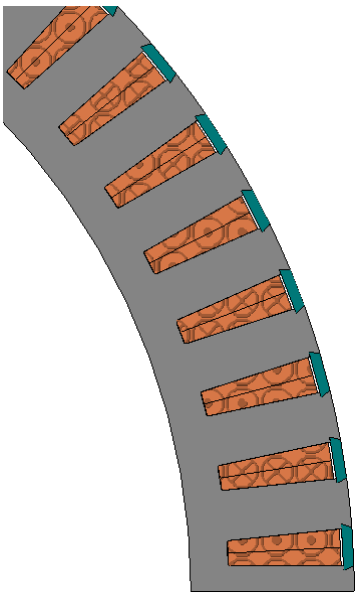

(b) 60slots/64poles

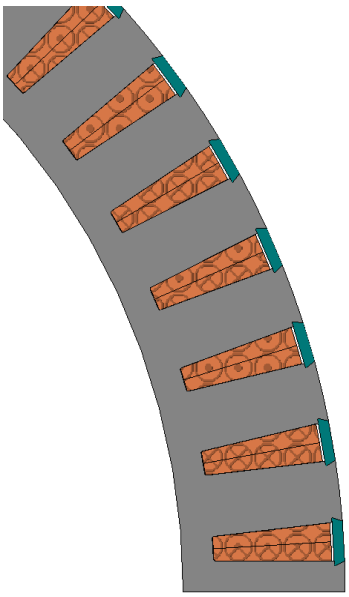

(c) 54slots/60poles

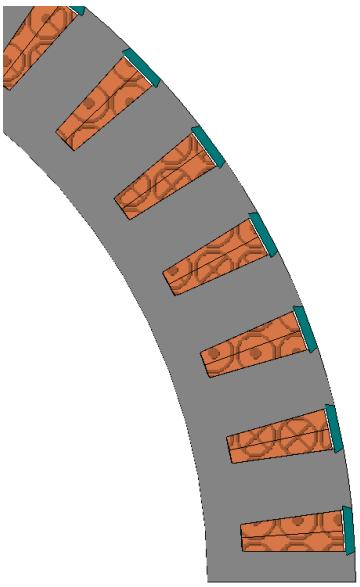

(d) 45slots/50poles

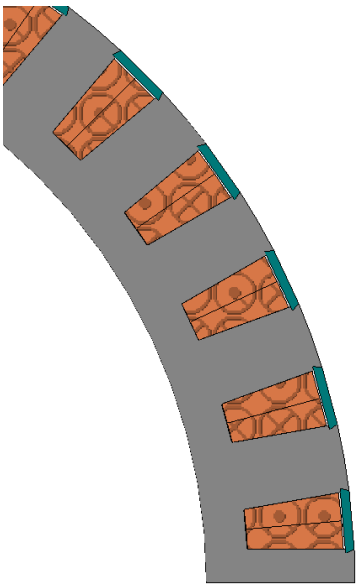

(e) 36slots/48poles

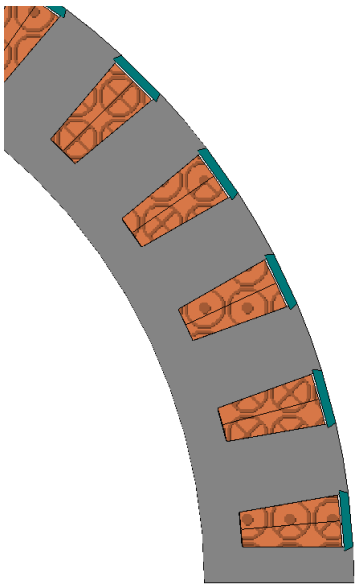

(f) 36slots/40poles

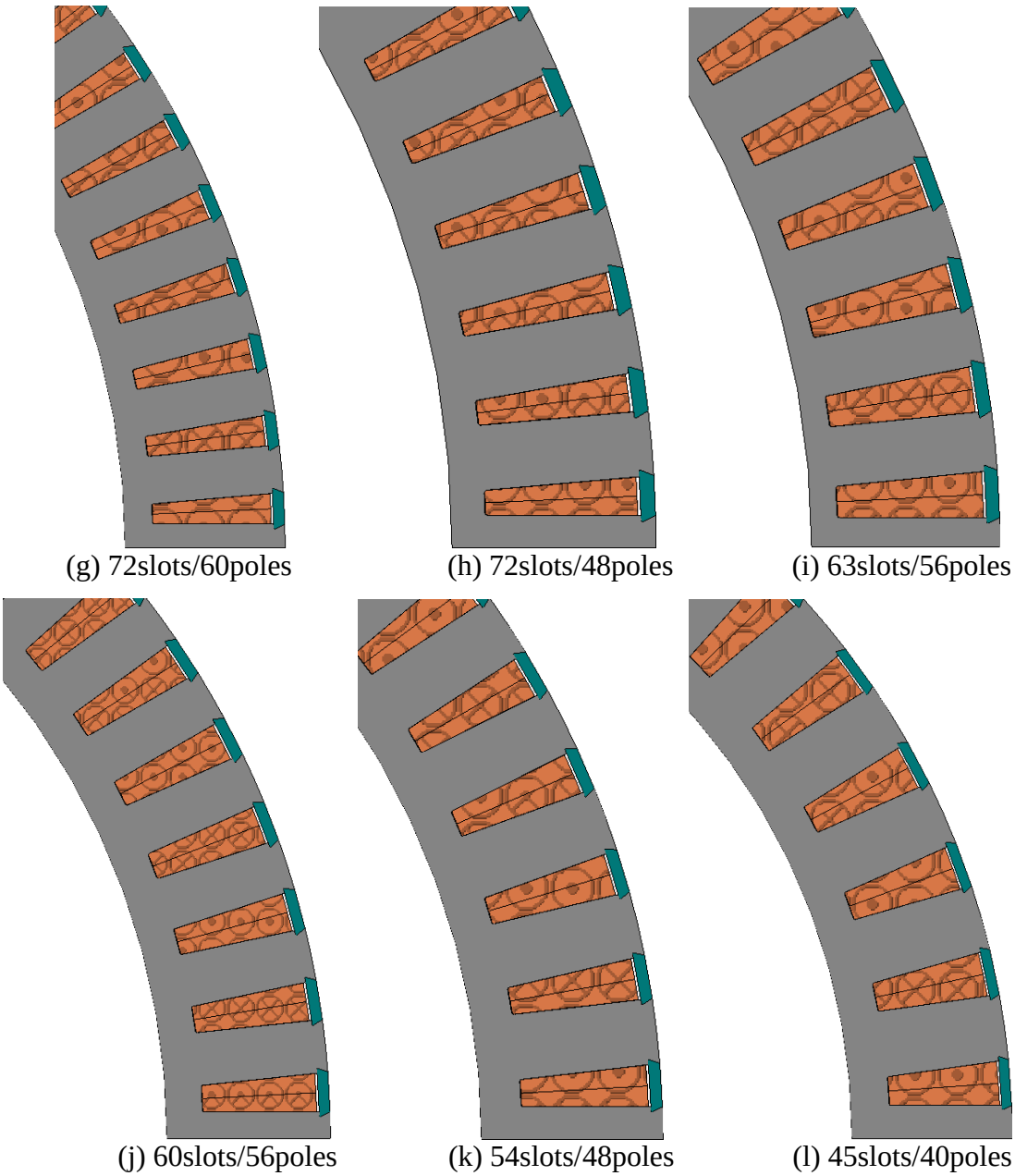

Figure 7.3. Geometrical structure after optimisation for fixed slot temperature.

Figure 7.4 is a graph showing the torque output variation with slot temperature. The 72slot/64pole machine produces a higher torque for a given temperature, and its geometrical dimensions are similar to the final machine construction. The machine designs with a slot number of 45 and below show the worst performances, as they have a relatively large slot width. This has a large impact in the ability to remove heat from the slot, also their short axial length introduces a recognisable limit on the electromagnetic capabilities.

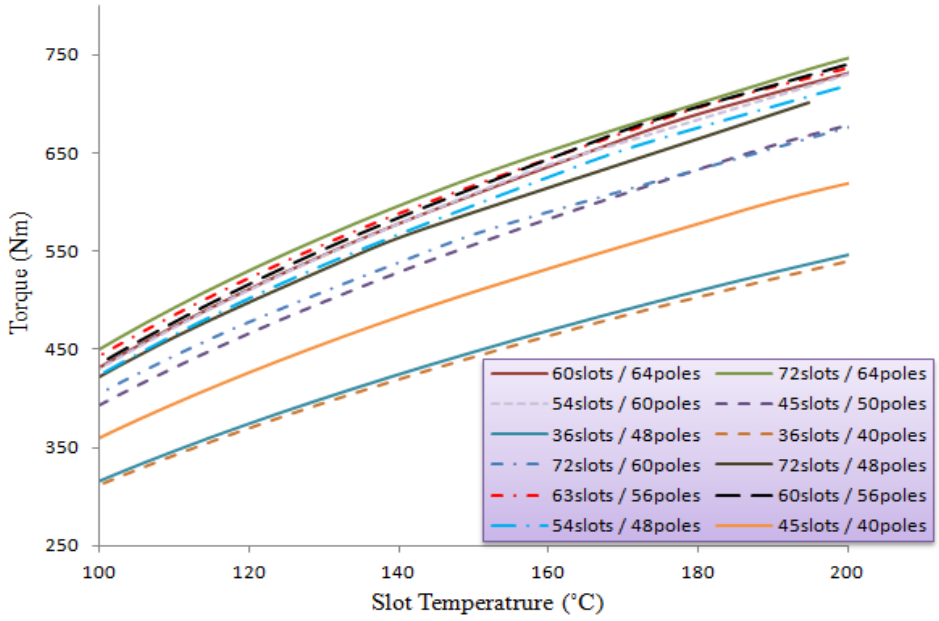

Figure 7.4. Torque variation with slot temperature.

7.3 Thermal model design

It is important to model the thermal network of the machine as accurately as possible, in order to determine the areas that cause temperature drops within the machine. Two models were developed for this work; first a motorCAD model [122] to help build a thermal network of the entire machine, with information of the cooling method and casing, then a FE model was built using ThermNet™ to analyse the temperature variation within the slot.

7.3.1 MotorCAD model

The thermal modelling of any machine is not a straightforward process, it often requires input from the actual measurement from the machine prototype. The motorCAD model acted as a starting point for understanding of the machine's thermal behaviour. Figure 7.5 shows the machine thermal assembly, built in the model. Within the model, the motor orientation was set so that its axle was horizontal to the ground and a shaft spiral groove was chosen as the method of passing water in and out of the cooling channel. An electromagnetic FE model was solved at a speed of 100rpm and a winding current of $24.18A_{rms}$ (representing an actual current value from machine testing) to obtain loss data, which was used as the motorCAD thermal model loss input. Table 7.1 shows the parameters for the cooling channel.

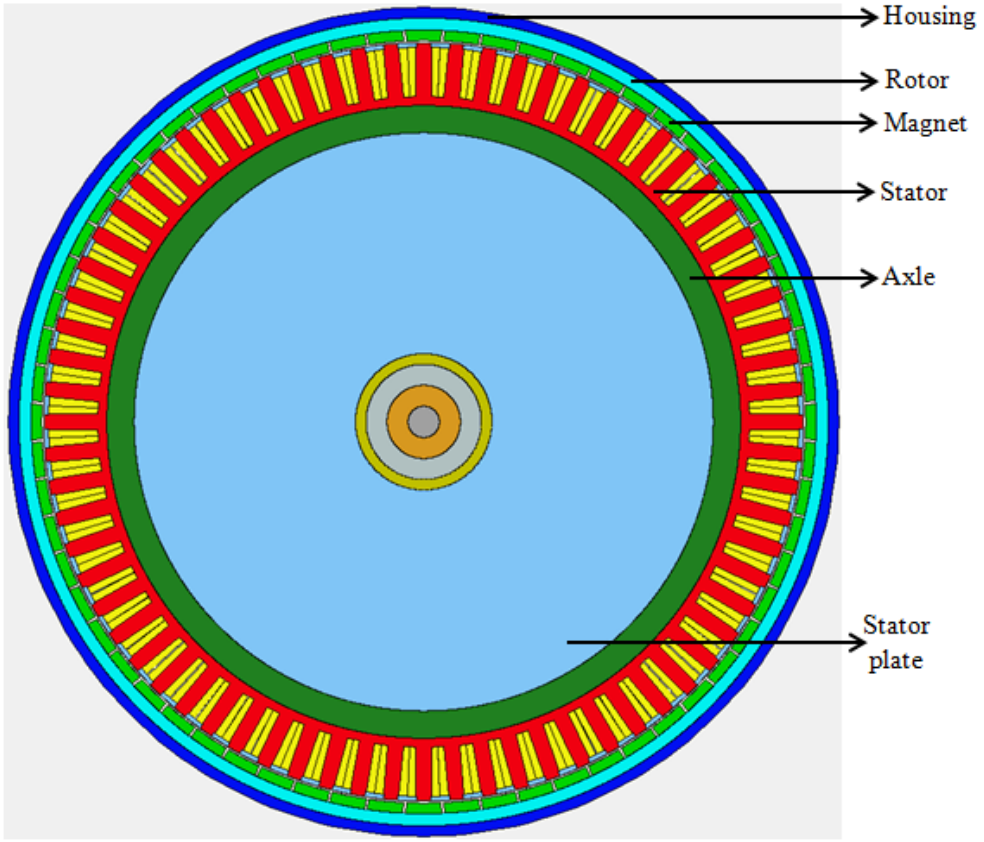

(a) Radial view

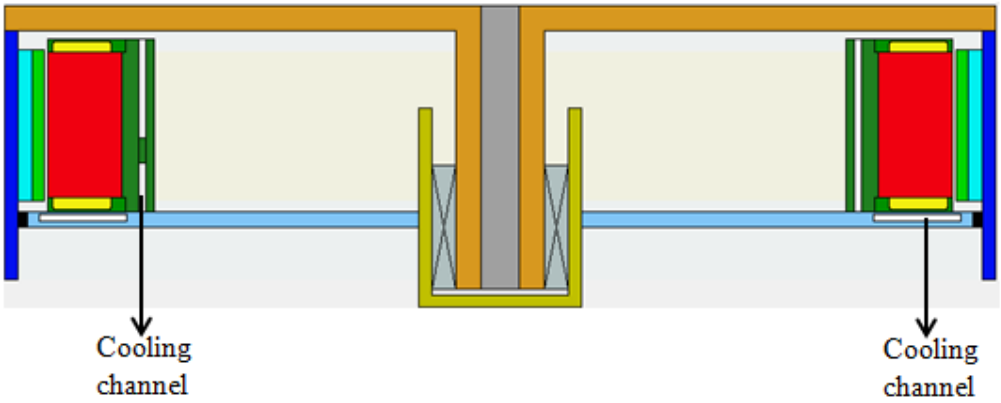

(b) Axial View

Figure 7.5. Thermal Model using motorCAD.

Table 7.1. Machine cooling characteristics.

Fluid volume flow rate (litre/sec)	Inlet temperature (˚C)	Heat transfer coefficient ($W/m^2/^{\circ}C$)	Duct wall roughness
15	50	2515	0.0025

Figure 7.6 shows the steady state thermal network, solved from the thermal resistance network; there are various heat sources around the machine, but the main source of heat is in the stator winding, and the model has split the copper loss in the winding into its active and end-winding quantities. It can be seen from the figure that the hottest spot in the machine at the given speed is the stator winding and this winding temperature varies across the slot, with the centre of the slot having the maximum winding temperature. In order to ensure the solution was accurate, an iterative process was adopted to make sure that the generated loss convergences at the same value between the thermal model and the electromagnetic FE model. Finally it was checked that the end-winding temperature from the model was similar to the measured end-winding temperature at the given operating point. Table 7.2 gives the full steady state temperature at the nodes in the machine.

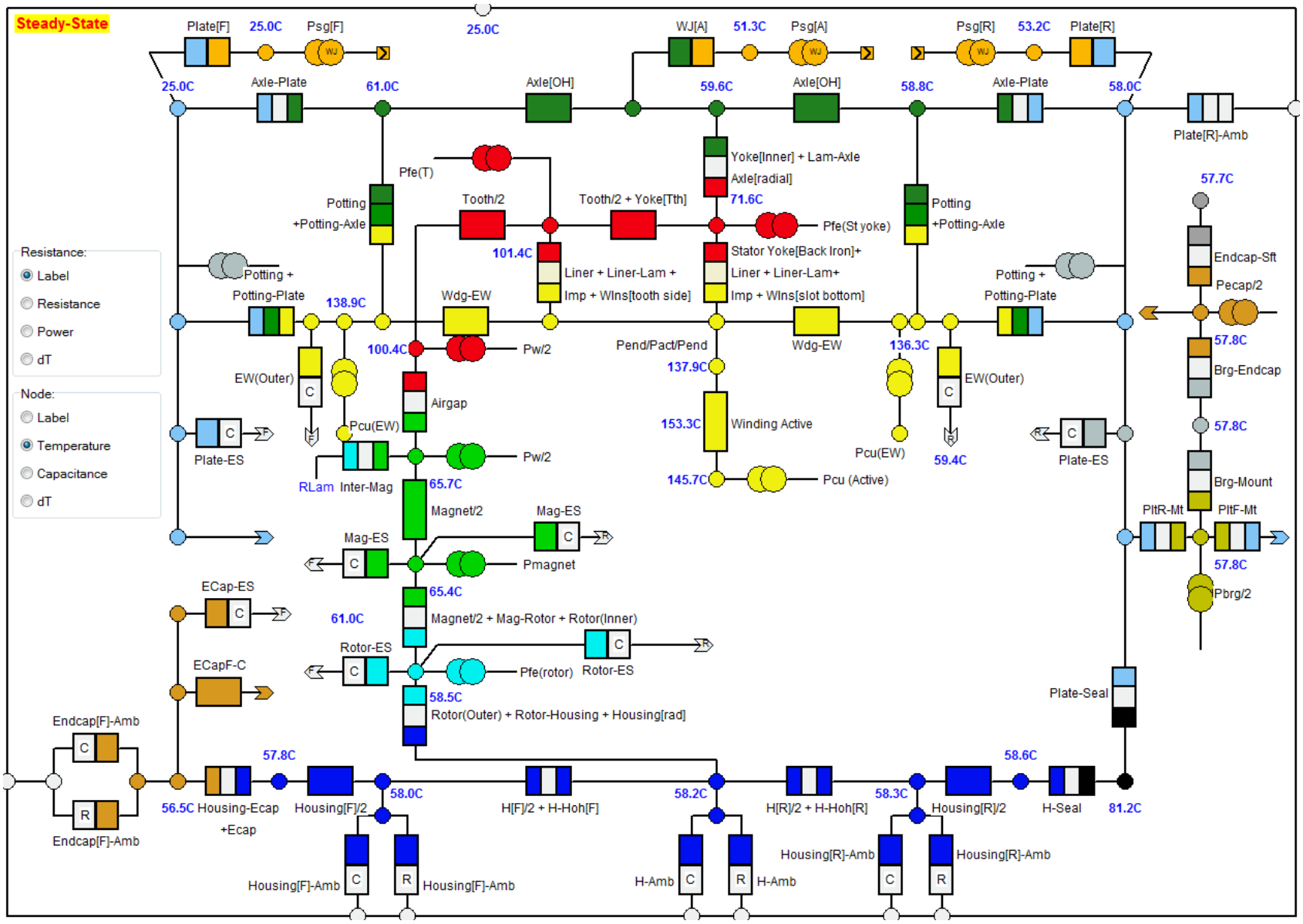

Figure 7.6. Steady state thermal resistance network.

Table 7.2. Solution for steady state temperatures.

Front		Active		Rear	
Node	**Temp (˚C)**	**Node**	**Temp (˚C)**	**Node**	**Temp (˚C)**
T [housing – overhang (F)]	58	T [ambient]	25	T [housing – overhang (R)]	58.29
T [housing – front]	57.79	T [housing – active]	58.23	T [housing – rear]	58.59
T [endcap – front]	56.46	T [stator lam (back iron)]	71.57	T [endcap – rear]	25
T [bearing – front]	57.79	T [stator lam (tooth)]	101.4	T [bearing – rear]	25
T [axle Ohang – front]	60.97	T [stator surface]	100.4	T [axle Ohang – rear]	58.77
T [axle – front]	25	T [rotor surface]	65.65	T [axle – rear]	25
T [endspace – F]	61	T [magnet]	65.35	T [endspace – R]	59.43
T [EWdg (F)]	138.9	T [rotor lamination]	58.51	T [EWdg (R)]	136.3
T [end winding average]	142.2	T [axle – centre]	59.64	T [maximum]	153.3
T [winding maximum]	153.3	SG fluid average temp [A]	51.27	T [minimum]	51.27
T [winding average]	145.7	T [active winding maximum]	153.3		
T [winding minimum]	136.3	T [active winding average]	146.8		
		T [active winding minimum]	137.9		

7.3.2 ThermNet™ model

In order to understand the winding thermal behaviour and how heat flows out the slot of the machine, an FE thermal model was built using ThermNet™, this model will also be essential in studying the temperature drop across the gap between the winding and stator tooth. The accuracy of the ThermNet™ model is dependent on the temperature distribution and heat flow around the machine obtained in motorCAD. With all the information gathered, a segment of the stator enclosing two slots was modelled in ThermNet™ to analyse the slot temperature distribution. A small section of the steady state thermal network shown in figure 7.6 was used to find the inputs. Figure 7.7 shows the section of the thermal network, highlighting the useful temperature and power loss applied to the ThermNet™ model.

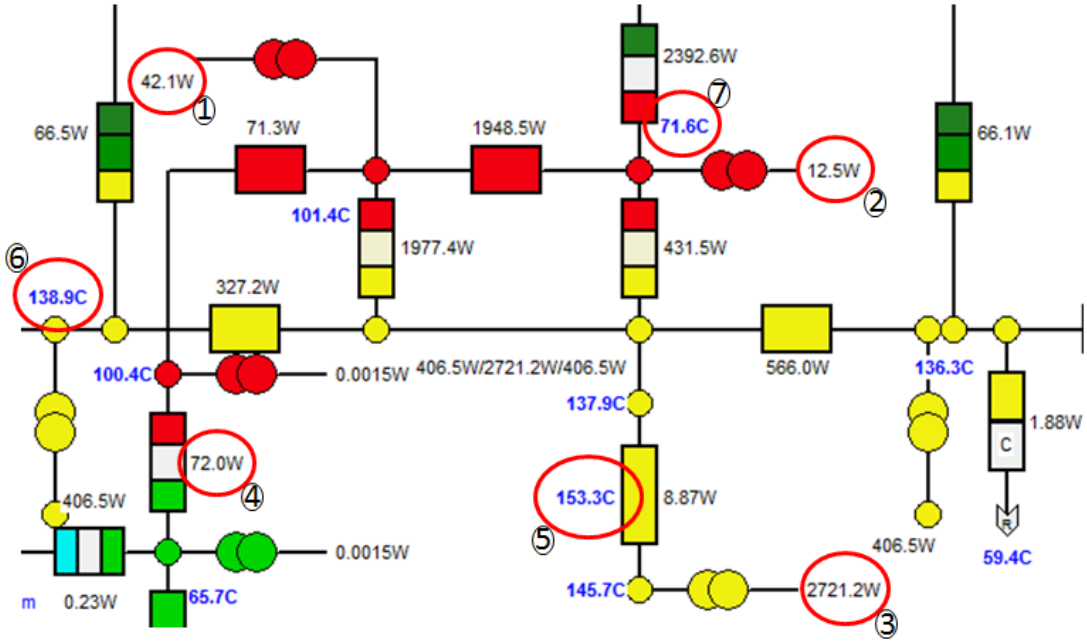

Figure 7.7. Thermal network showing temperature and power losses

The following steps explain how the motorCAD model in figure 7.7 was developed:

a) From measured data of the actual machine, the maximum steady state end-winding temperature was 138.9˚C with an excitation current of 34.27A_{pk} applied to the winding per sub-motor (figure 7.7 – 6).

b) An FE electromagnetic model was solved with the same excitation current to obtain the iron and magnet loss information, which was fed into the motorCAD model as shown in figure 7.7. The stator loss was fed into the model – (1) stator teeth loss and (2) stator core-back loss.

c) The DC resistance copper loss was calculated and applied to the motorCAD model, also shown in figure 7.7 – (3), the winding resistance was calculated at the modelled winding temperature.

d) The potting of the winding and gap between liner and tooth were adjusted by changing the value of potting goodness in the motorCAD model, till the end-winding temperature converged at the value obtained from measurement, as shown in figure 7.7 – (6).

e) The liner to tooth gap which is basically an air-gap was found to be 0.066mm in the model and the potting goodness of the slot potting was 0.9, this value is an indication of how much air bubbles are present in the slot after potting.

Using the temperature information obtained from figure 7.7 on the active winding (5), heat flow across the air-gap (4) and stator core-back temperature (7), a model of the stator segment was modelled in ThermNet™, this can be seen in figure 7.8.

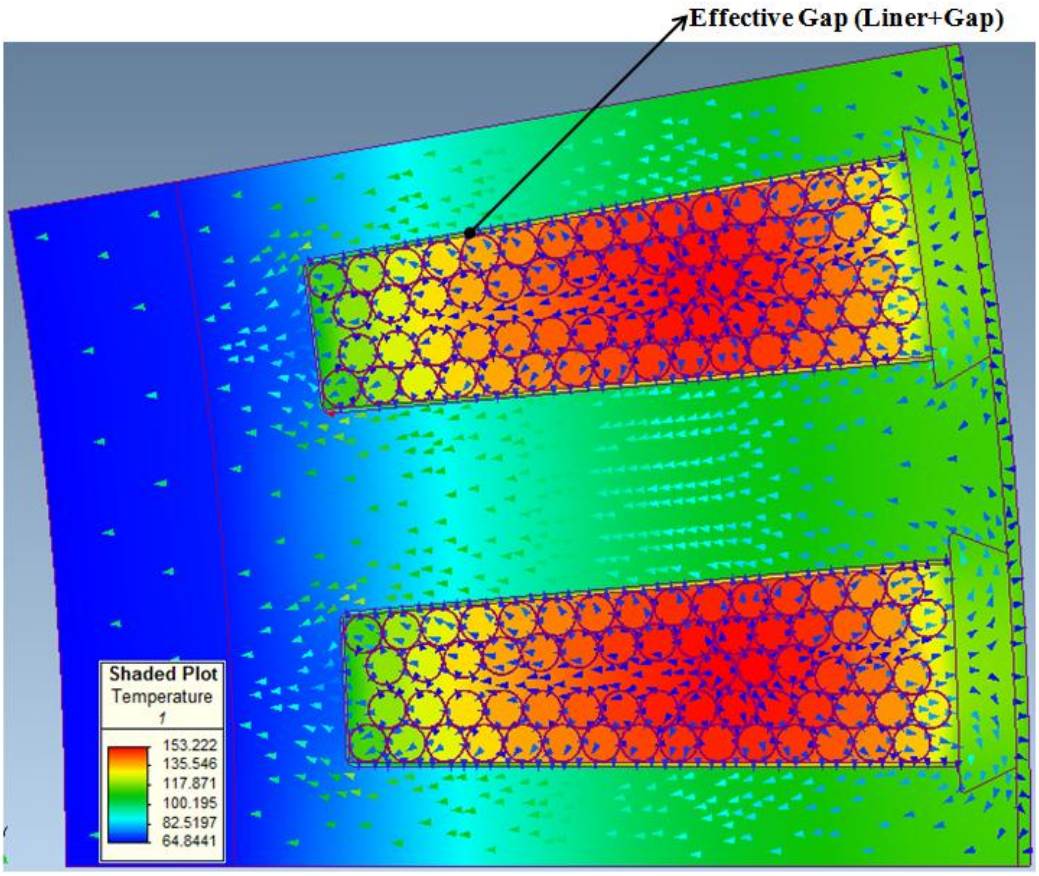

Figure 7.8. Temperature distribution and heat flow in stator

The thermal FE model was solved to obtain the temperature distribution, heat flow and the length of the gap between the slot liner and tooth, which is expected to have a high thermal resistance. The input into thermal FE model is the loss density of the various

components that introduces losses in the machine while under operation, a copper loss density of 6.42MW/m^3 was applied to each conductor, derived from applying a current of 24.24A$_{rms}$ to the coil resistance calculated using equation 7.16, at a temperature of 145.8˚C, which was obtained from the motorCAD model (figure 7.7).

$$R_\theta = R_{20}(1+\alpha(\theta-20)) \tag{7.16}$$

R_θ is the resistance at the given temperature θ, and α is 0.00393/˚C.

The ThermNet™ model was used to estimate the size of the gaps which inevitably exist between the slot liner and tooth, as outlined below:

Figure 7.8 is a steady state model showing the temperature distribution and heat flow in a segment of the stator which is 1/36 of the complete machine, enclosing two stator slot pitches. The effective thermal conductivity of the gap between the winding and tooth was varied in the thermal FE model, to ensure the hottest spot in the winding has a temperature of 153.2˚C (the same as obtained from the motorCAD resistance network, 5 – figure 7.7), this information is then used to calculate the thickness of the gap between the liner and tooth. The environmental and boundary conditions were applied to the thermal FE model to ensure the temperature at the core-back was 71.36˚C (similar to the motorCAD model, 7 – figure 7.7). The heat flow out of the stator into the air-gap was found to be 2W: from the motorCAD model the heat flow to the air-gap was 72W (4 – figure 7.7), since 1/36 of the complete machine was modelled the value of 2W is correct, assuming the heat flow from the stator into the air-gap is evenly distributed around the stator outer periphery. The effective thermal conductivity (K_{eff}) of the gap between the winding and tooth was found to be 0.0426W˚C^{-1}m^{-1}, an estimation of the gap between the liner and tooth can now be obtained as the thickness and thermal conductivity of the liner is known.

The gap between winding and tooth is considered to be a lumped homogeneous material then the following equations describe the effective resistance of the air and liner between the slot and laminations (R_{eff}):

$$R_{eff} = \frac{l_{liner}}{K_{liner}A_{liner}} + \frac{d}{K_{air}A_{air}} \tag{7.17}$$

$$\Rightarrow \therefore R_{eff}\,\alpha\,\frac{l_{liner}}{K_{liner}} + \frac{d}{K_{air}}$$

Where, K_{liner} is the thermal conductivity of the slot liner material, K_{air} the thermal conductivity of air, l_{liner} the thickness of the liner and d the thickness of the air-gap between liner and laminations. If the material was made up of only slot liner then

$$R_{eff} \alpha \frac{l_{liner}}{K_{liner}}$$

In this case the gap is made up of both air and slot liner, therefore for a liner thermal conductivity of 0.14W˚C^{-1}m^{-1}, an air thermal conductivity of 0.02W˚C^{-1}m^{-1} and a slot liner thickness of 0.18mm the effective thermal conductivity can be calculated as follows:

$$K_{eff} = K_{liner} \times \left(\frac{l_{liner} \big/ K_{liner}}{\frac{l_{liner}}{K_{liner}} + \frac{d}{K_{air}}} \right) = K_{liner} \left(\frac{1}{1 + \frac{K_{liner}}{l_{liner}} \times \frac{d}{K_{air}}} \right) \qquad (7.18)$$

$$d = \frac{\left(0.14 \big/ K_{eff} \right) - 1}{38900}$$

For an effective thermal conductivity of 0.0426W˚C^{-1}m^{-1} determined from the thermal FE model, the depth *d* of the gap between the liner and tooth is 0.059mm. This is 12.3% less than the value predicted by the motorCAD model, giving an idea of the thickness of the gap between the liner and tooth.

Figure 7.9 below shows the temperature gradient between the hottest spot in the middle of the slot to the middle of the stator tooth, from the slope it can be seen that there is a temperature drop 46˚C, as heat flows out of the slot and drops between the winding and tooth.

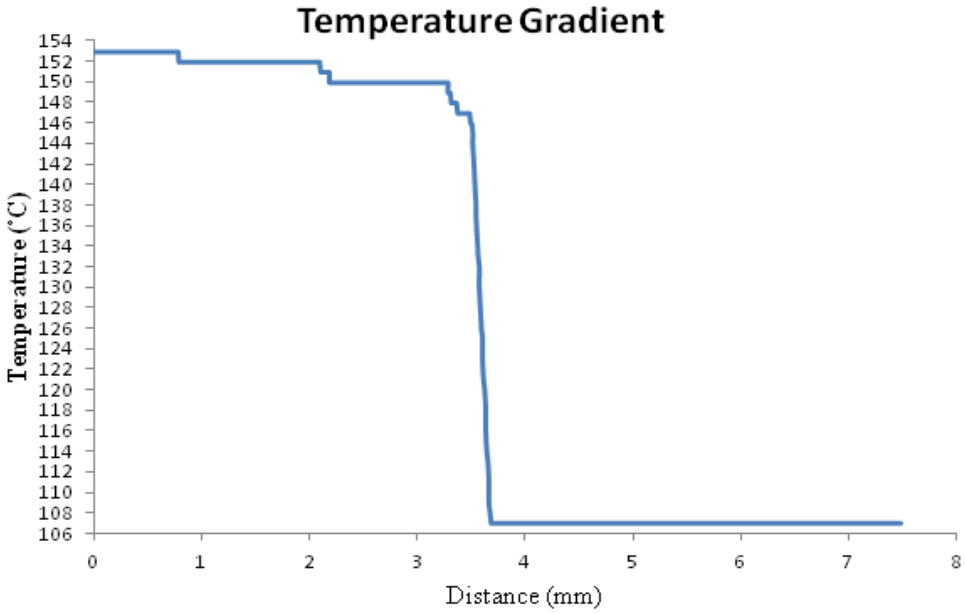

Figure 7.9. Temperature Gradient between slot centre to tooth centre.

7.4 Conclusion

This chapter has presented a method to optimise the mean torque for different slot and pole combinations by setting a peak slot temperature limit and implementing a set of equations to achieve the objective of the optimisation. The optimisation result showed that in order to reduce the temperature drop in the slot while maintaining a good electrical loading, the slot width has to be reduced while the depth increased. The 72slot/64pole and 60slot/56pole machines were shown to have a strong performance for a given slot temperature limit. Two thermal models were applied to determine the temperature flow and loss distribution through the machine, using motorCAD and Infolytical ThermNet™. The models were solved at a speed of 100rpm and winding phase current of 24.18A_{rms}, at this operating point the maximum winding temperature was found to be 153.3˚C and magnet temperature found to be 65.35˚C. As a result of the thermal modelling, the size of gap between the slot liner and tooth has been quantified as 0.059mm to 0.066mm. Finally the graph of temperature gradient between the centre of the slot to the centre to the tooth was plotted and the temperature drop was found to be 46˚C, this is a large drop indicating that the thermal path for the machine is not good enough to adequately remove the heat generated in the slot.

Chapter 8

Testing and Performance of Prototype Machine

The 72slot/64pole machine has been constructed and assembled for testing and performance evaluation, chapters 4 to 7 presented the electromagnetic and thermal simulation study conducted on this machine. This section will present the various tests carried out on the prototype machine and the results compared to that of a machine built in-house by Protean. All tests were performed on a test bed, the prototype machine was connected to a dynamometer and the following tests carried out:

- No-load tests to determine back EMF, resistance and inductance.
- Static and running load test (cold and hot peak torque tests).
- A drive cycle test, to find the cooling system efficiency and thermal characteristics.

The thermal test examines the hot spots in the machine as the speed changes, while the cooling system efficiency evaluates the effective removal of heat from the machine at various speeds.

8.1 Introduction

The testing of the prototype machine was conducted at the Protean Electric testing facility, where a high level test rig was set up with the capability of carrying out various machine tests. Figure 8.1 is the layout of the rig; showing the points of connection and the instrumentation needed to log the measured data.

8.2 No-load test

The initial test was the no-load test. This test can be split in two types, static and running. The static test determines the inductance and resistance of the machine's coils, while the running test gives the back EMF and no-load losses in the machine.

8.2.1 Static no-load

The inductance and resistance tests are to be carried out first on a newly built machine. These tests determine the integrity of the coils after they have been inserted on the tooth of the stator. Any short circuit or open circuit of the coil or phase connection can be detected during this test. The test is normally carried out without the rotor in place, however the mutual component of the phase inductance between phases that are linked via the rotor is not accounted for when the rotor is absent. Table 8.1 shows the measured and calculated coil and phase inductances and resistances. The phase values were measured with the machine star connected.

Table 8.1. Inductance and resistance values.

	Single Coil	**Phase**
Measured inductance (mH)	0.421	1.89
Calculated inductance (mH)	0.3698	1.91
Measured resistance (mΩ)	53.87	160.69
Calculated resistance (mΩ)	56.52	169.56

The calculated inductance values were obtained from a 2D FE model, therefore not taking into account the end effect. The calculated resistance values were obtained using equation 6.11, the difference in measured and calculated can be attributed to the estimation of the total length of wire.

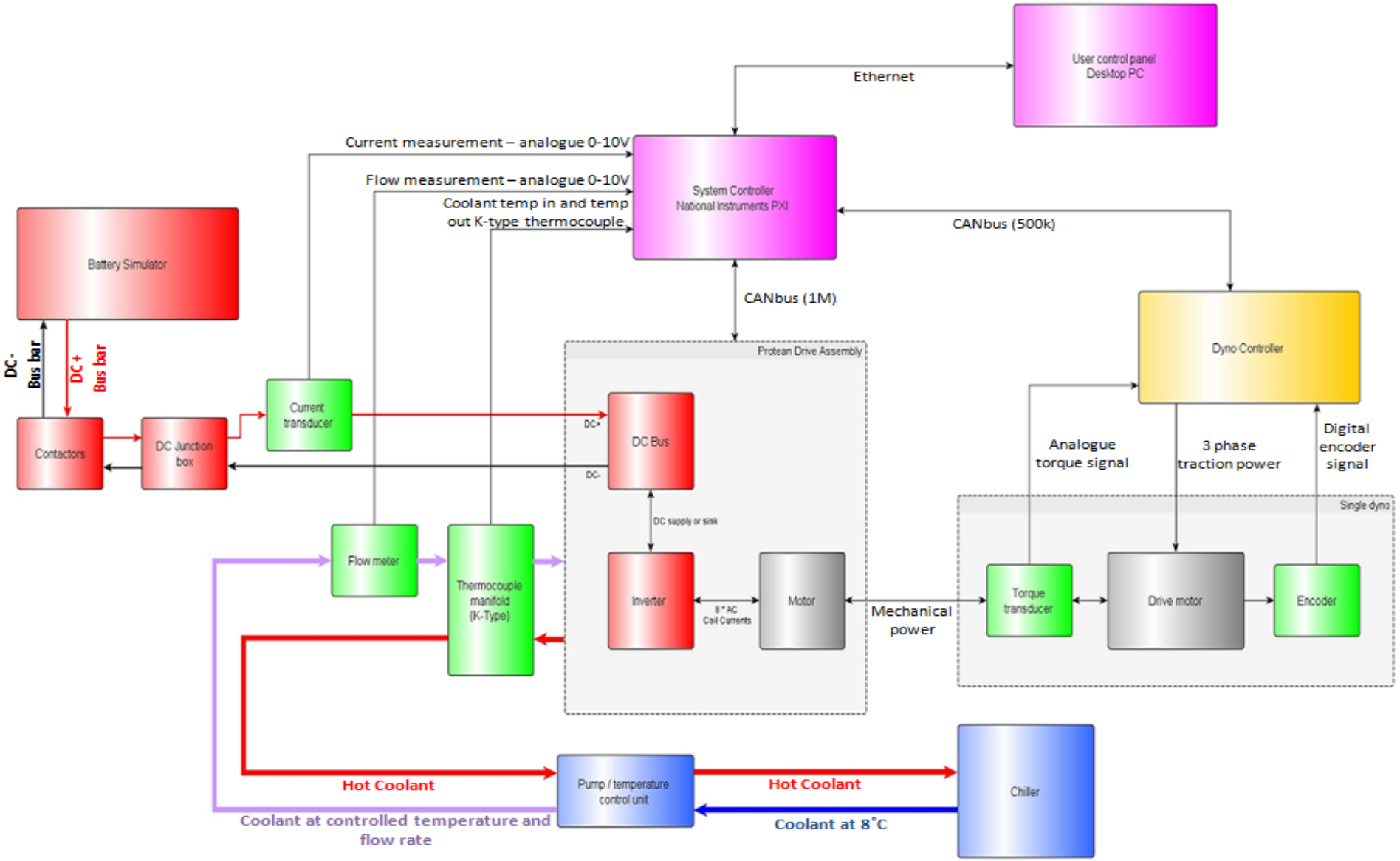

Figure 8.1**. Schematic diagram of the Protean Electric test rig.**

8.2.2 Running no-load

The running no-load test was performed when the machine was fully assembled and mounted on the test rig, the back EMF and no-load losses of the machine were obtained as a result of this test. The test was conducted by mechanically coupling the test machine to a dynamometer that served as a prime mover.

The back EMF test determines the voltage induced in the stator winding by the rotor magnets at a given rotational speed. The dynamometer used was a four pole machine capable of delivering rated power of 132kW, rated torque of 1280Nm at 1700rpm base speed, and the peak torque of 1800Nm. Figure 8.2 (a) shows two cycles of the line back EMF for both the measured and FE predicted values, obtained at a speed of 100rpm. The peak value of the measured line EMF is $37.2V_{peak}$ and the difference between the measured and FE prediction is 7.3%, this discrepancy in values can be attributed to the no-load losses causing the magnet temperature to rise during measurement, thereby reducing the magnet flux. The variation of the voltage with speed is always linear in all types of machine technology and the back EMF constant for this machine was found to be 371.6V/krpm, derived by dividing the peak of the line voltage by the speed at which the voltage was obtained. The harmonic prediction in the measured back EMF waveform is also shown in figure 8.2 (b), the harmonic spectrum shows a good attenuation of all harmonics with the fifth harmonic only 0.9% of the fundamental.

Losses are generated in any machine when running on no-load; the losses that make up the no-load losses are the frictional, windage, iron and in some cases winding loss. The test machine is configured as open circuit whilst driven by the dynamometer at various speeds, the torque is then measured by the torque transducer and the power calculated. Figure 8.3 shows the no-load losses against the speed of the machine with the exception of friction and windage losses. There is a close correlation between the measured and FE model results, and gets up to a difference of 10% at high speed, this difference can be attributed to the FE model's accuracy in predicting the iron losses in a machine. The winding loss in some machines makes up a very small percentage of the total no-load loss and can be ignored. However in the prototype machine the no-load winding loss, although small is expected to increase, due to the winding exposure to the air-gap varying field and the use of a magnetic slot wedge that is 2.2mm thick with a low magnetic permeability; this was discussed in Chapter 6. Figure 8.4 shows an FE prediction of the no-load winding loss as it changes with speed. At a speed of 1200rpm, the no-load winding loss is 13.32% of the total no-load losses, which can lead to

increased power consumption when compared to an equally sized conventional machine without slot wedges. The no-load winding loss that occurs when the phase winding are open circuited can be reduced by placing the windings far away from the air-gap, this is to reduce how much of the air-gap field reaches the coils.

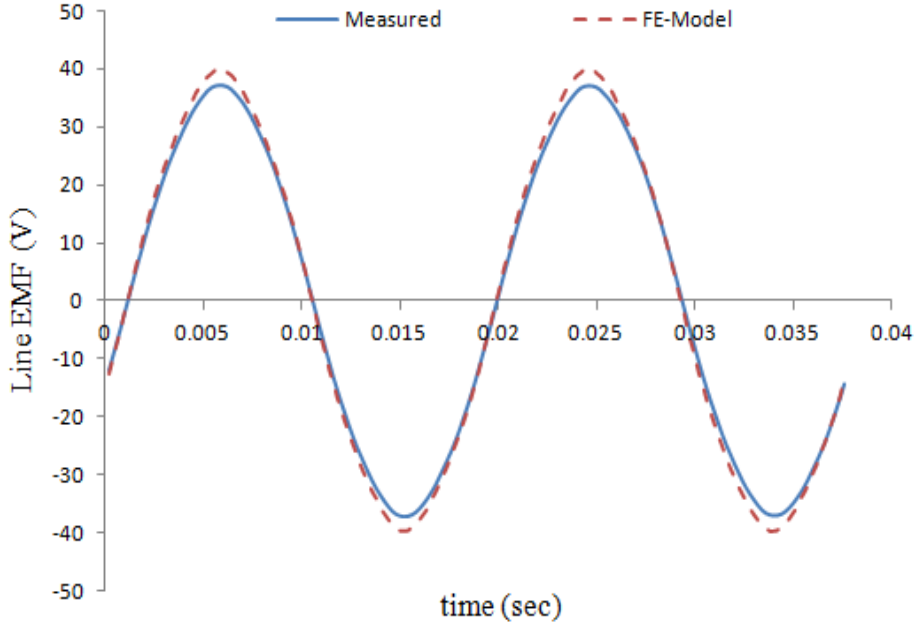

(a) line back EMF waveform

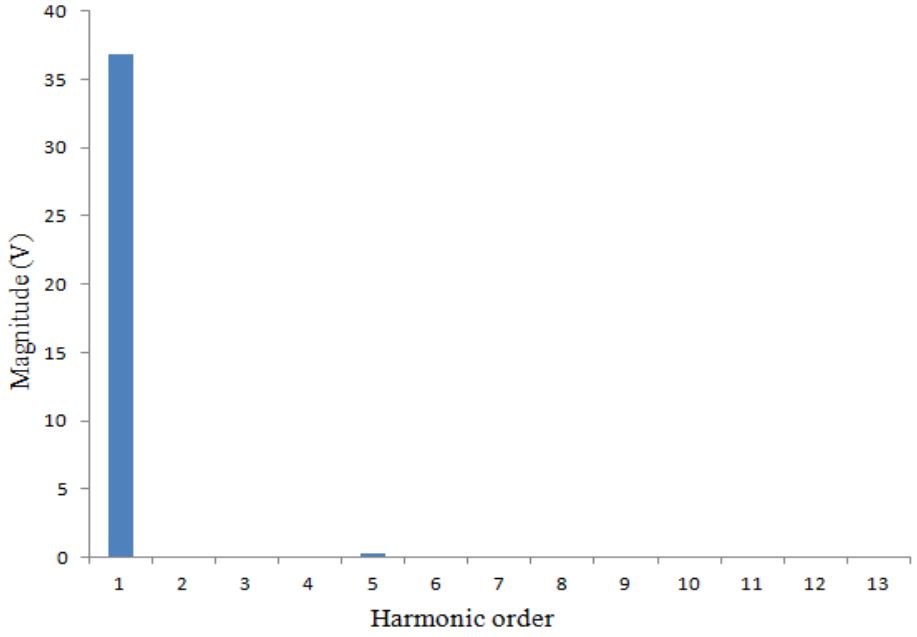

(b) harmonic spectrum of the line back EMF

Figure 8.2. Induced line back EMF measured at 100rpm and harmonic contents.

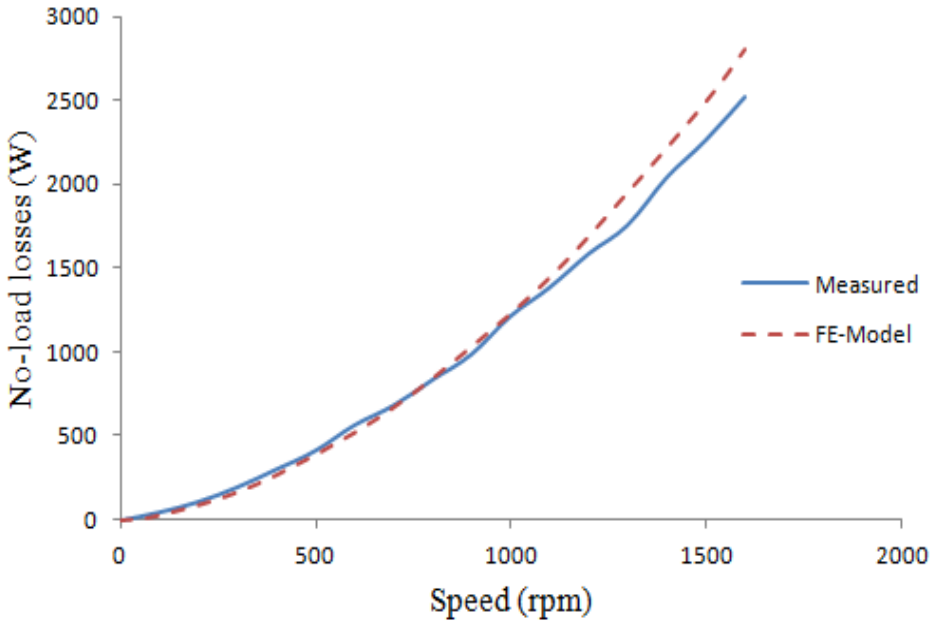

Figure 8.3. No-load machine losses measured at various speeds.

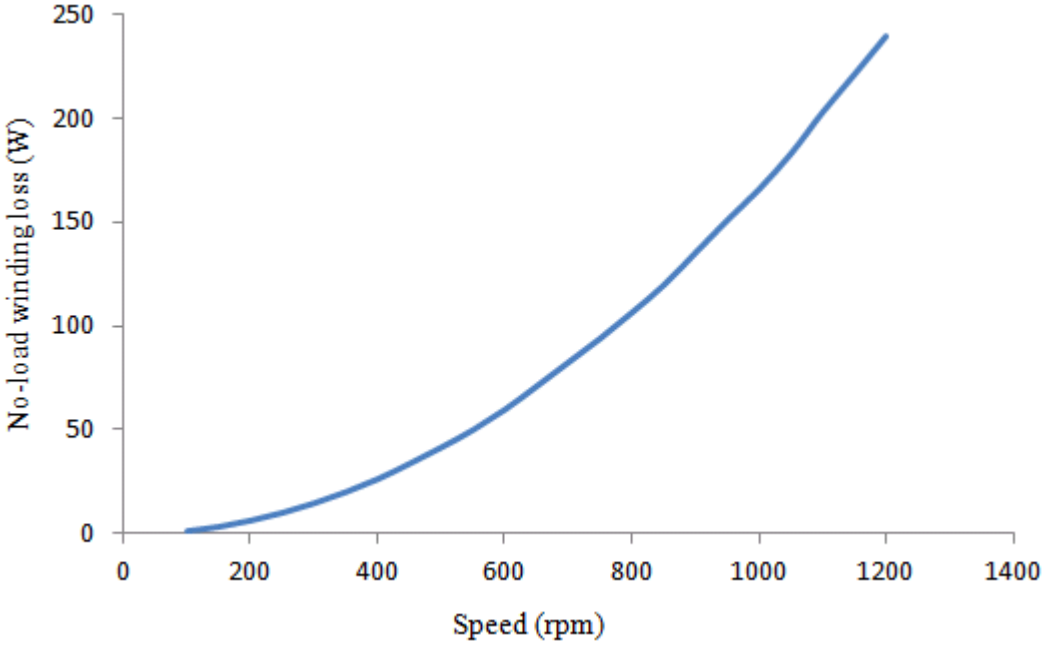

Figure 8.4. No-load winding loss predicted at various speeds.

8.3 Load Test

The load test shows how the machine performs over a range of speeds and loads. In this section the output torque and drive cycle are presented, these will give a general idea of how the machine will behave over its operating range and the machine's requirements with respect to the power source (inverter and batteries). The prototype machine built for this work was compared to a machine designed and built in-house by Protean (MHV), which has similar rotor design and is mounted on a similar type of water jacket

as the prototype machine, however the stator design is different for the two machines. Figure 8.5 shows the flux density at no load for the two machine designs being compared and table C2 in appendix C shows the dimensions for both machines. The saliency in the machine is very little, so there is no reluctance torque contribution. As a result all the current applied to the machine to produce maximum torque is placed in the q-axis, except when field weakening is required above base speed.

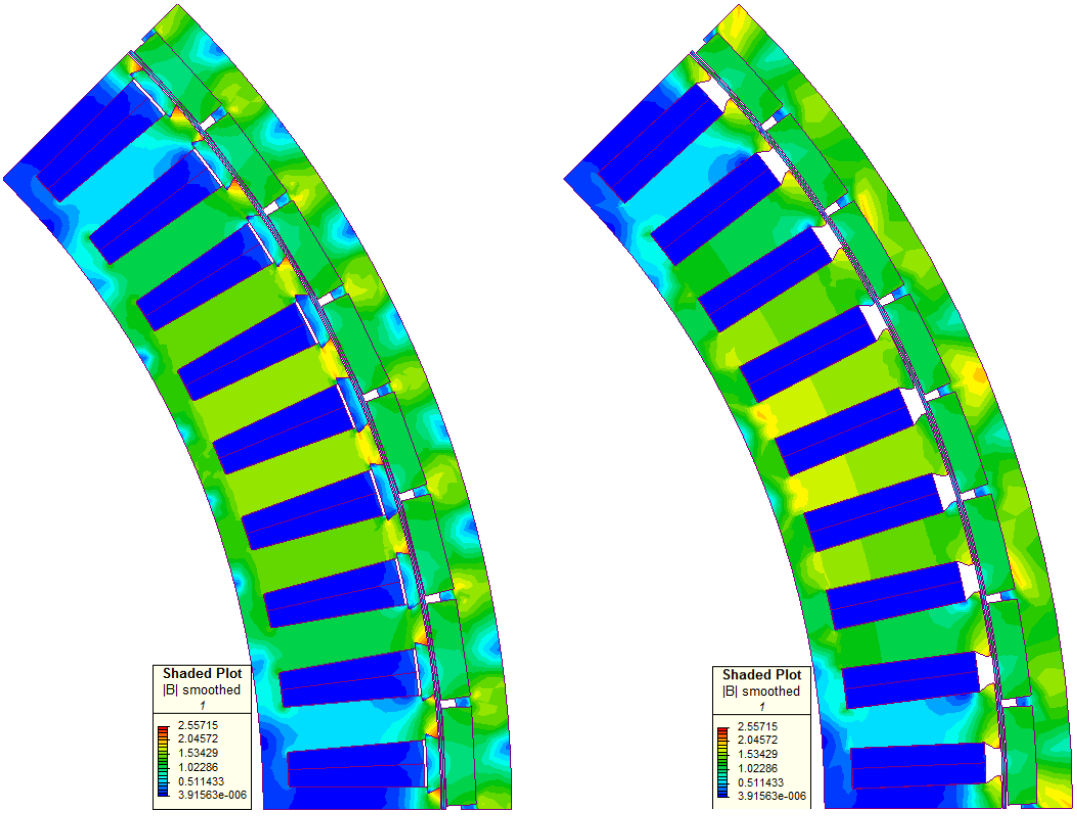

(a) Prototype (b) Protean MHV

Figure 8.5. No load flux density distribution.

The curve in figure 8.6 shows the mean torque variation with machine electric loading; showing how the machines saturate at high electric loading. The difference between the measured and predicted curves can be attributed to the fact that the model does not account for the mechanical effect on the machine loading and since it is a 2D model the end effects produced by the winding are not accounted for, this leads to a difference of up to 10% at high currents. The torque per ampere is shown to be better with the Protean MHV machine compared to the prototype, varying from 12% to 5.8% as the machine loading is increased.

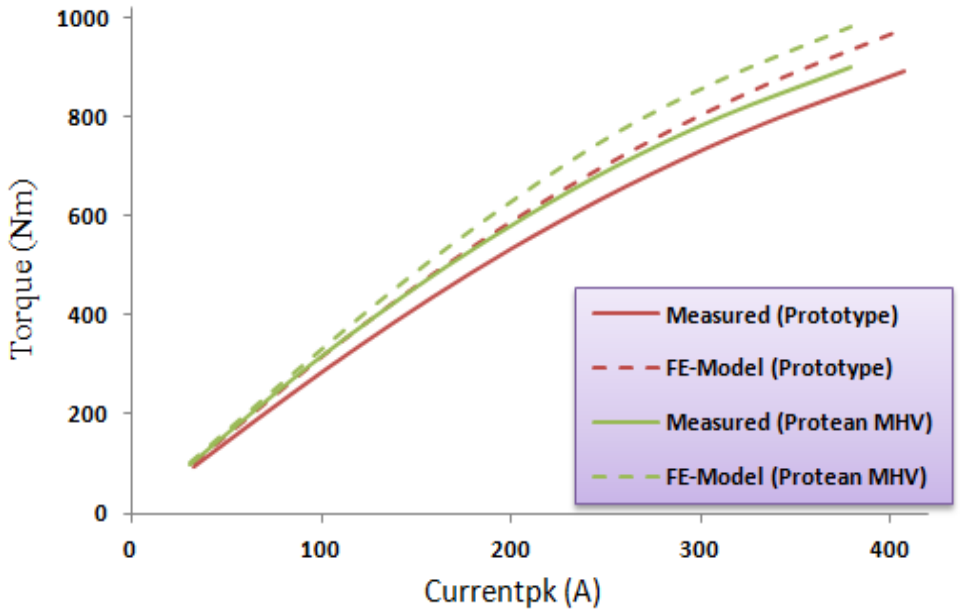

Figure 8.6. Torque variation with electric loading at 200rpm and 100rpm.

Figure 8.7 shows result of torque over a speed range of 50rpm to 1600rpm for both the prototype machine and Protean MHV, with the coil temperature controlled to a maximum of 150˚C. Evidently the prototype machine produces higher torque at lower speeds, but as the machines are driven in the field weakening region, the two machines have identical torque/speed envelopes. During this mode of operation the current is not limited by the coil temperature but is limited by converter voltage. Coil temperature depends on the loss generated in the slot and how well heat is transferred from slot to tooth for effective heat removal; it is worth noting that the thermal resistance between coil and tooth is different for the two machines: the tooth of the Protean MHV is over-moulded with a 0.55mm thick layer of insulation, having a thermal conductivity of 3W/m/˚C, while the prototype has been lined with nomex of thickness 0.18mm with a thermal conductivity of 0.14W/m/˚C, giving the Protean MHV a superior heat transfer out of the slot. However the losses generated in the slot can be the dominant factor that influences coil temperature; equation 8.1 has been applied to determine the various components of loss in the slot, where K_1 is loss constant due to the coil exposure to the air-gap field and K_2 is loss constant due to the proximity loss of the coils. These constants were obtained by curve fitting on FE model result of the coil proximity loss components over a given speed and current range. Table 8.2 shows the calculated values for the losses and the speed ω is in rpm. It can be concluded that at low speed where conduction loss dominates total slot loss, the Protean MHV produces more loss compared to the prototype, because of the better copper to slot ratio achieved in the

prototype. As a point of note, the slot loss in the Protean MHV is 4.6% greater than the prototype machine at 100rpm when the coil temperature limit of 150˚C is reached. This is an indication that the Protean MHV is thermally better. Finally at a speed of 1600rpm, the slot loss in the prototype machine increases by 23.1% compared to the Protean MHV; this is due to the coil proximity loss and loss due to the exposure of the coils to the air-gap field. This leads to greater temperature rise in the prototype machine and must be managed to prevent failure.

$$Slot\_loss = i^2R + K_1\omega^2 + K_2\omega^2\hat{i}^2 \tag{8.1}$$

Table 8.2. Slot Loss calculated values corresponding to 150˚C coil temperature.

	Speed (rpm)	I_{peak} (A)	K_1	K_2	I^2R (W)	$K_1\omega^2$ (W)	$K_2\omega^2i^2$ (W)	Total (W)
Prototype	100	35.56	1.89e-4	7.1e-7	1982	1.89	8.979	1993
	1600	26.28			1082	483.8	1255	2821
Protean MHV	100	32.88	7.98e-6	4.6e-7	2079	0.0798	4.973	2084
	1600	27.06			1408	20.44	862.3	2291

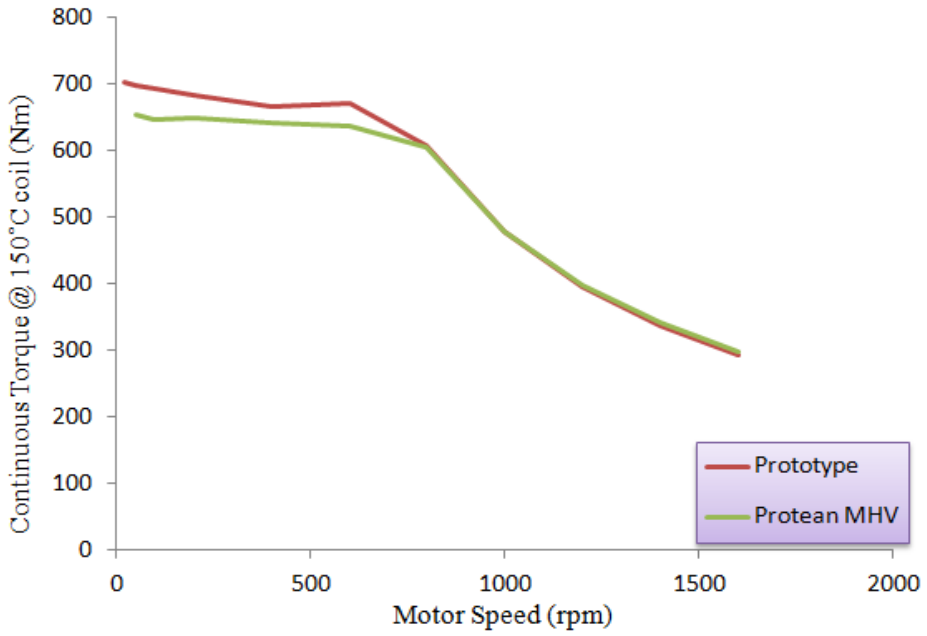

Figure 8.7. Mean torque variation with speed.

8.3.1 Static torque

Static torque measurement could not be carried out, as a rotary table with a dividing head capable of handling the torque produced by the machine was not available. The static torque is a good way to accurately compare the measured torque to the FE predicted torque. When the static torque is measured with varying current, the cogging torque and any contribution from the reluctance torque component can be seen in the electromagnetic torque variation.

An FE prediction of the static torque in the prototype machine was conducted over one electrical cycle. An instant of a balanced three phase current operating system was applied to the phases of the machine, the current is applied at a positive peak in one phase and half of the negative peak is applied to the other two phases. Figure 8.8 shows the static torque variation with rotor position when different electric loading is applied to the phase of one sub-motor. The reluctance torque contribution to the total machine torque is of no significance as the variation of the phase inductance with rotor position is very low. However the shift in the peak of the static torque waveform as the machine is loaded can be attributed to the fact the q-axis is saturated, causing a change in the position of peak torque in the machine.

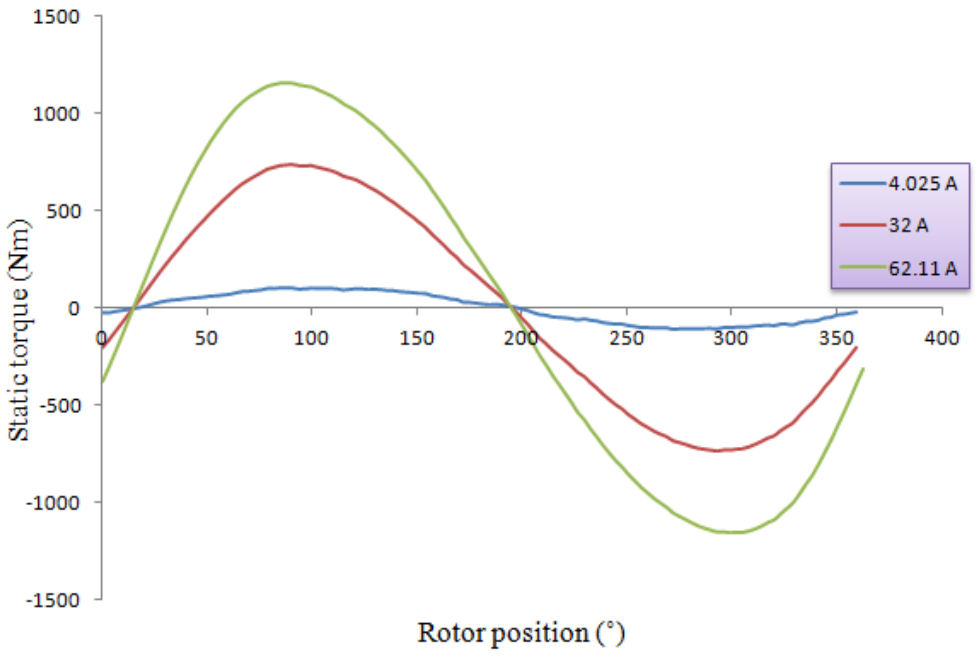

Figure 8.8. Static torque variation with position for different electric loading.

8.3.2 Drive cycle

The prototype motor and Protean MHV motor were simulated against standard drive cycles; extra urban, urban and motorway. The two motors were then compared in terms of energy consumed and winding temperature. Figures 8.9 to 8.11 shows the speed and torque curves for the various drive cycles and table 8.3 shows the temperature and electrical energy consumed over the drive cycles. The coil temperature is higher in the prototype motor, which can be attributed to how thermally poor the motor is compared to the Protean MHV. Also the electrical energy consumed is greater in the prototype machine, due to the proximity loss generated in the winding and the magnet loss due to the no-load air-gap harmonics.

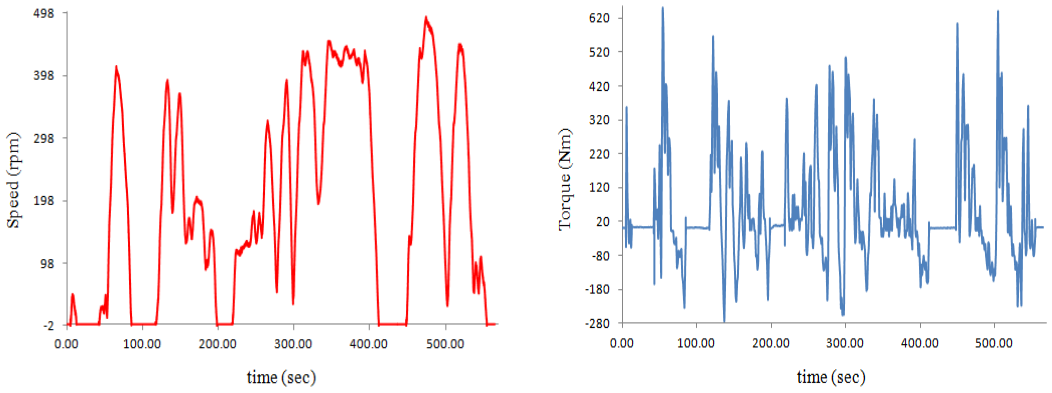

Figure 8.9. Urban drive cycle speed and torque curves.

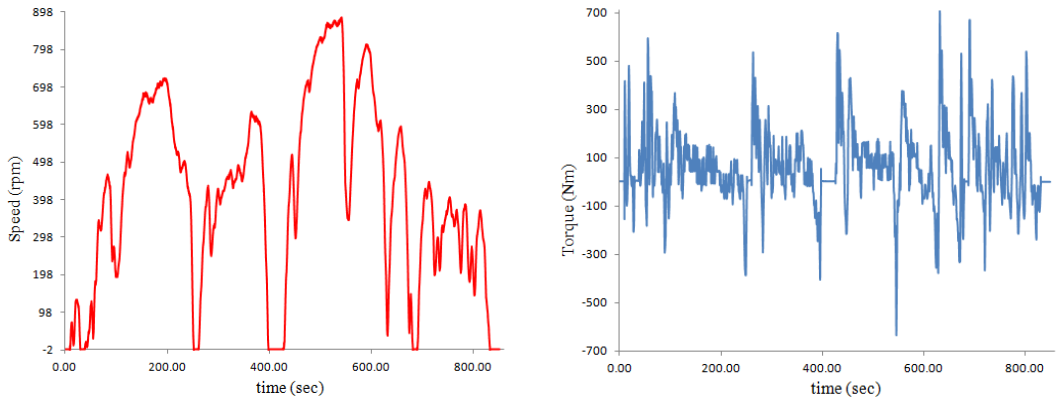

Figure 8.10. Extra urban drive cycle speed and torque curves.

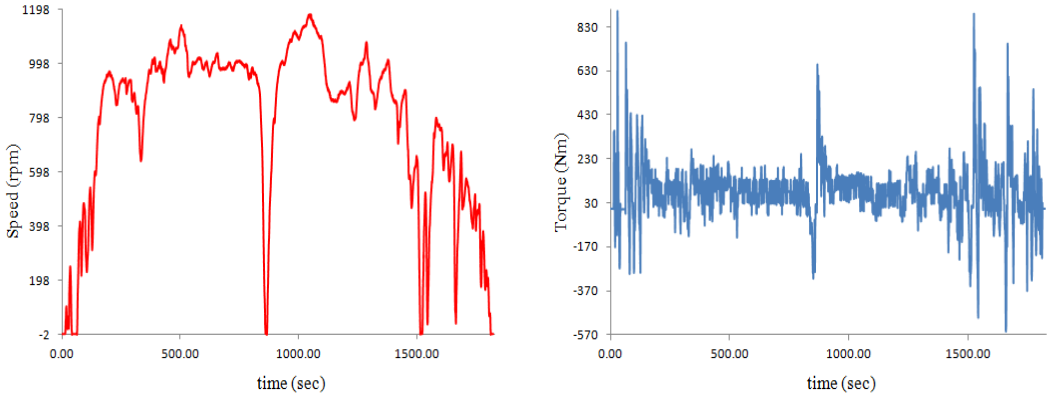

Figure 8.11. Motorway drive cycle speed and torque curves.

Table 8.3. Maximum coil temperature and electrical energy consumed through drive cycles.

	Electrical Energy Consumed (MJ)			Maximum Coil Temperature (˚C)		
	Urban	**Extra urban**	**Motorway**	**Urban**	**Extra urban**	**Motorway**
Prototype	1.09	3.27	16.5	63.3	70.1	77.7
Protean MHV	0.977	2.95	14.2	62.5	68.6	76.1

8.4 Thermal characteristics

This test was performed to determine the machine thermal behaviour over a given speed range at a phase current of 35.98A_{peak} in the constant torque region (up to 600rpm), after which field weakening was applied to the machine. Thermistors were used for the temperature measurement and were placed at various points on the machine, the rotor back iron, rotor housing, outer and inner magnets and coil. The thermistors for the coils were placed in the end-winding region, as shown in figure 8.12 by the red/yellow dots. The test was conducted with the machine loaded, and a cooling liquid made of 50% tap water and 50% ethylene glycol pumped at a flow rate of 15litres/min, while maintaining an inlet temperature of 50˚C.

Figure 8.13 (a), (b) show the temperature change with speed for the various components of the machine and the current into the winding as the machine is field weakened. The temperature distribution in the machine is as expected, with the coils producing the hottest spot in the machine, as shown in figure 8.13 (a). In figure 8.13 (b), it can be seen

that the rotor heating follows the same pattern as the winding excitation current over the speed range; this indicates that the main source of heat in the machine is the stator winding and heat passes through the air-gap to the rotor. So the general idea of the iron loss being the dominant loss component at high speed and causing temperature rise is not the case in this machine.

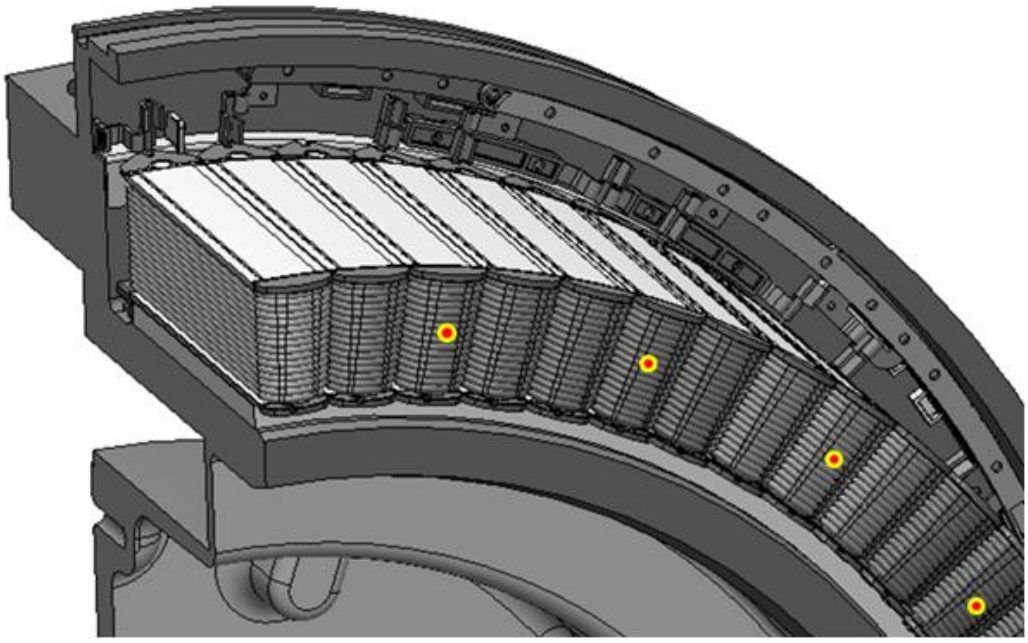

Figure 8.12. Positions of thermistors on stator windings.

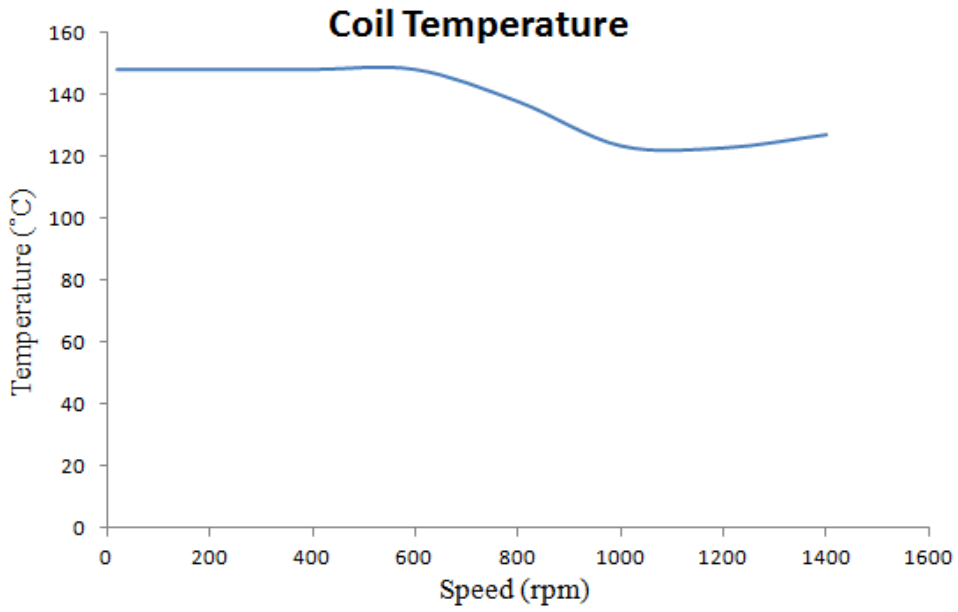

(a) coil temperature variation with speed

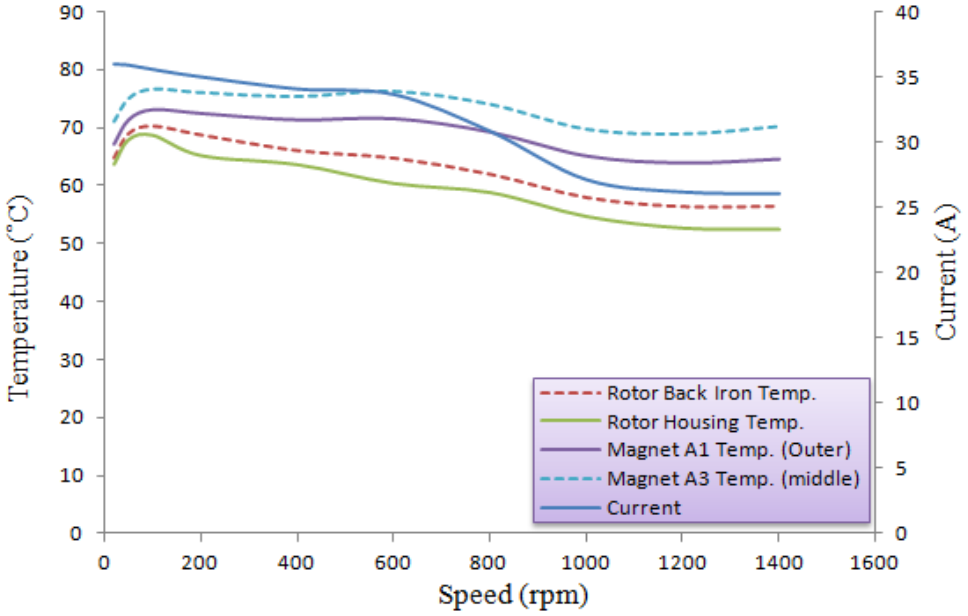

(b) rotor temperature and current variation with speed

Figure 8.13. Machine temperature distribution against speed.

It is worth noting that the temperature distribution in the coils is not uniform; some coils get hotter than others and the current control applied to the machine is temperature limiting, where a peak set point of 150˚C is applied in the control scheme, the current is regulated to maintain this peak coil temperature, which means some coils will be at a lower temperature. As a result of this the machine will not be operating at its optimum. The temperature variations are caused by unbalanced phase currents. The current sensors and the commutation ring (for position sensing) were imperfectly set up, causing a three phase set of currents that were imbalanced. The inverter and machine come as a single package, so stray fields from the machine core-back interfere with the current sensors and commutation ring, thereby causing the sensors to send the wrong signal to the control system and introducing an error in the control system. A method to fix this is to provide shielding for the current sensors and to reduce the diameter of the commutation ring, to keep them away from the machine stray fields.

The coil temperature rise and fall times with a phase current of $30.9A_{peak}$ were recorded, as shown in figure 8.14, the thermal time constants were derived from the graph as shown in table 8.4.

Table 8.4. Thermal time constant calculation for prototype motor.

Thermal time constant	**Rise (min)**	5.134
	Fall (min)	3.983

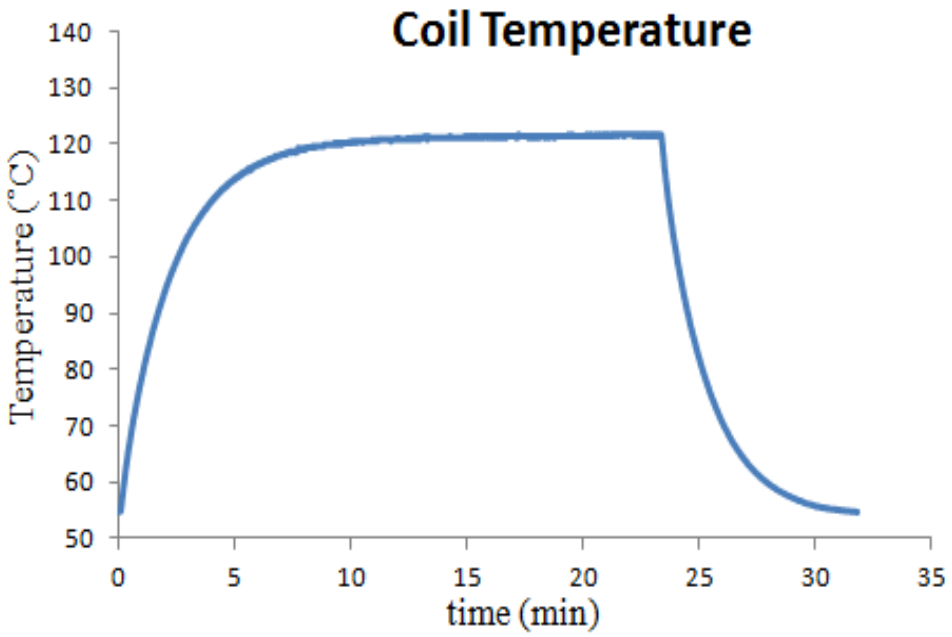

Figure 8.14. Winding temperature behaviour with a phase current of 30.9Apeak applied for 23mins.

8.5 Efficiency of the cooling system

The chosen cooling method has to be capable of removing the heat loss generated in the machine at the chosen slot current density, this is important as it determines how much output power the machine can sustain through its drive cycle.

The machine is cooled by the use of a water jacket around the bore of the stator, with a cooling liquid made of 50% water and 50% ethylene glycol pumped into the machine. The cooling fluid is responsible for cooling the complete drive system; this includes the machine and power electronic board. The flow rate for the coolant, pumped in by the cooling system has been investigated, with the coil peak temperature was set to 150˚C the flow rate was increased and the current into the coil increased in turn, at a speed of 400rpm. The temperature rise between the coolant inlet and outlet was recorded, along with the energy the coolant removes from the machine. Figure 8.15 shows the energy removed at various flow rates and table 8.5 shows the temperature difference between inlet and outlet. At flow rates above 15litre/min the temperature rise showed a reduced

variation, in order to limit the power of the coolant's pump a flow rate of 15litre/min was chosen. Equation 8.2 is the heat energy equation used to calculate the energy removed by the coolant. The specific heat capacity (SHC) was assumed to be 3.4kj/kg/˚C, the coolant's mass density 1.055kg/litre, the mass density of water is 1kg/litre, and ethylene glycol's is 1.11kg/litre.

$$Energy(W) = SHC \times \Delta T \times mass/\sec ond \qquad (8.2)$$

Table 8.5. Effect of changing flow rate on machine cooling for a fixed 150˚C peak coil temperature.

Phase current (A_{peak})	Flow rate (litres/min)	Inlet temperature (˚C)	Outlet temperature (˚C)	ΔT (˚C)
31.79	5.86	50.64	62.05	11.41
33.28	9.03	50.86	58.91	8.05
34.05	11.77	50.88	57.33	6.45
34.62	15	51.04	56.19	5.14
35.02	18.04	50.88	55.24	4.36
35.27	20.87	50.76	54.61	3.85

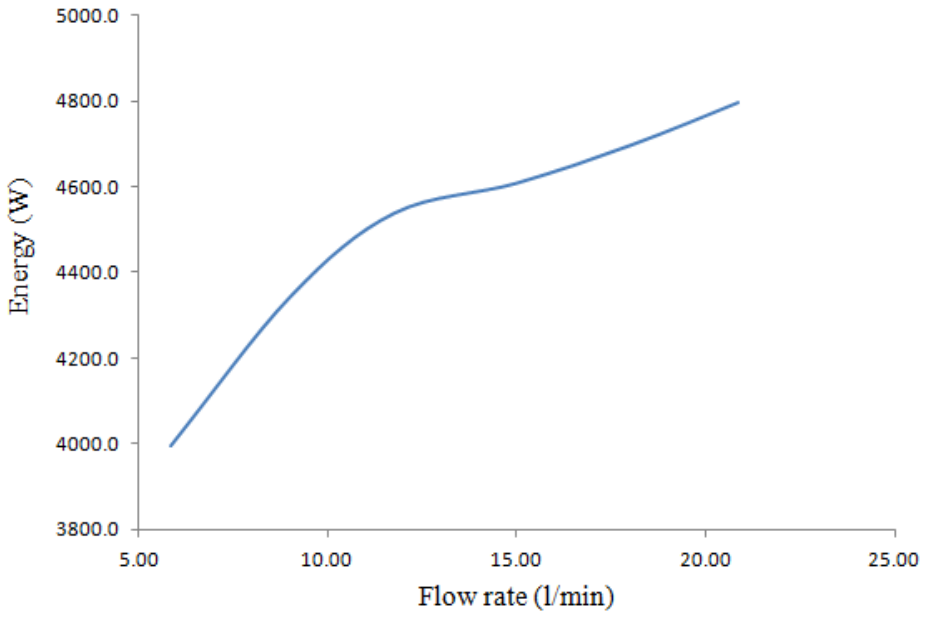

Figure 8.15. Heat energy removed by coolant over various flow rates.

During normal operation of the machine the flow rate of the coolant is 15litres/min, which is maintained over the entire machine torque – speed curve. The effectiveness of

the coolant at removing heat at speeds between 100rpm to 1200rpm was measured, a peak coil temperature of 150˚C was maintained. Table 8.6 shows the variation in the temperature rise between the inlet and outlet coolant, while figure 8.16 shows the energy removed by the coolant over the speed range. The energy removed by the coolant and the temperature rise shows how well the heat loss is removed from the machine over the speed range. As explained earlier the machine iron loss at high speed is not a major concern, as most of the heat produced in the machine is from the windings. In fact it would be more efficient to run the machine at high speeds, where the temperature rise of the coolant is lower and the coolant is required to remove lesser heat energy.

Table 8.6. Cooling of machine at different speeds for a flow rate of 15l/min.

Speed (rpm)	Inlet temperature (˚C)	Outlet temperature (˚C)	ΔT (˚C)
100	50.80	55.93	5.13
400	51.04	56.19	5.14
700	50.86	56.25	5.39
1200	50.74	54.57	3.83

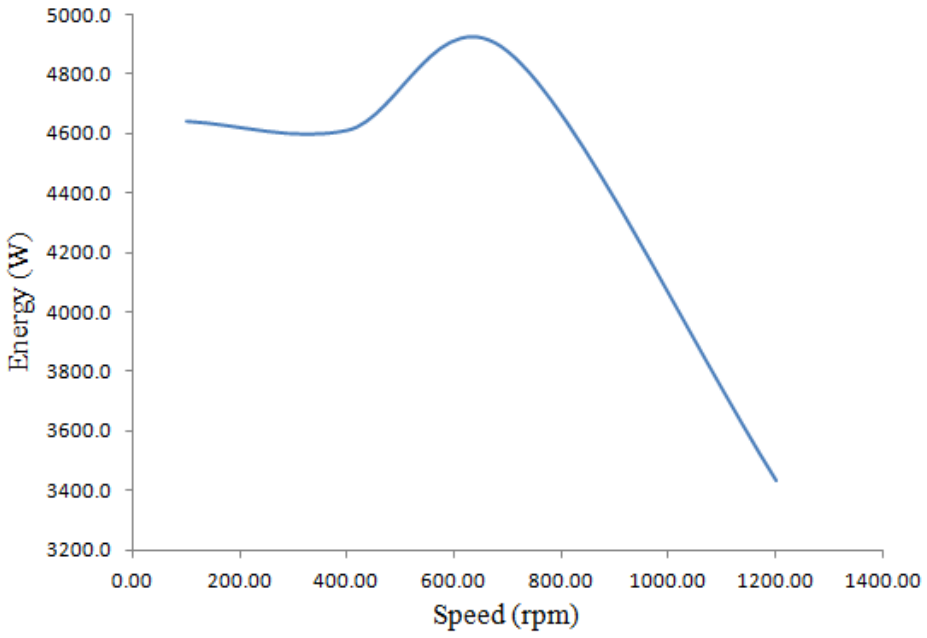

Figure 8.16. Heat energy removed by coolant over a speed range for a flow rate of 15l/min.

8.6 Performance sensitivity to construction tolerance

This section looks at the performance sensitivity to various construction variations. Machine design models are usually not a true representation of the actual machine constructions, due to the dimension tolerance that exists when cutting various machine components. In most manufacturing industries, the effects of dimensional tolerance are very important in providing a quantitative value for the average performance of a series of products manufactured. The effect of variation of magnet span and air-gap length are studied, also the temperature effect on the magnets at various speeds is presented. Studying the variation in the peak of the line to line back EMF waveform has been adopted as a method to determine how the performance is affected.

The magnet span was varied from 160deg to 175deg, the effect on the line to line back EMF is shown in figure 8.17; it can be seen from the waveforms that the percentage variation in the peak value is only within 1.8%, which indicated that this has no significant impact on the machine performance, also this indicates the magnet span can be reduced without losing performance. Changing the magnet span can also change the harmonics of the back EMF.

The machine air-gap was varied from 0.7mm to 1.3mm, figure 8.18 shows the variation in back EMF; the percentage difference is 9.2% for the air-gap lengths chosen. The air-gap length is important for machines designed for a direct drive in-wheel motor application. Having a small air-gap is beneficial to the machine performance, but can lead to a mechanical failure. Also the machine air-gap can be reduced when the rotor expands due to high rotor temperatures.

The magnet temperature was varied based on the actual values presented in figure 8.13 at various speeds; figure 8.19 shows the line back EMF constant, which gives an indication of how the temperature affects the peak value. The percentage difference between the voltage peaks from cold to hot is 6%, indicating that the effect of temperature on the performance is not very significant. The difference between the cold and hot back EMF test can be used to determine the rotor temperature of a permanent magnet motor.

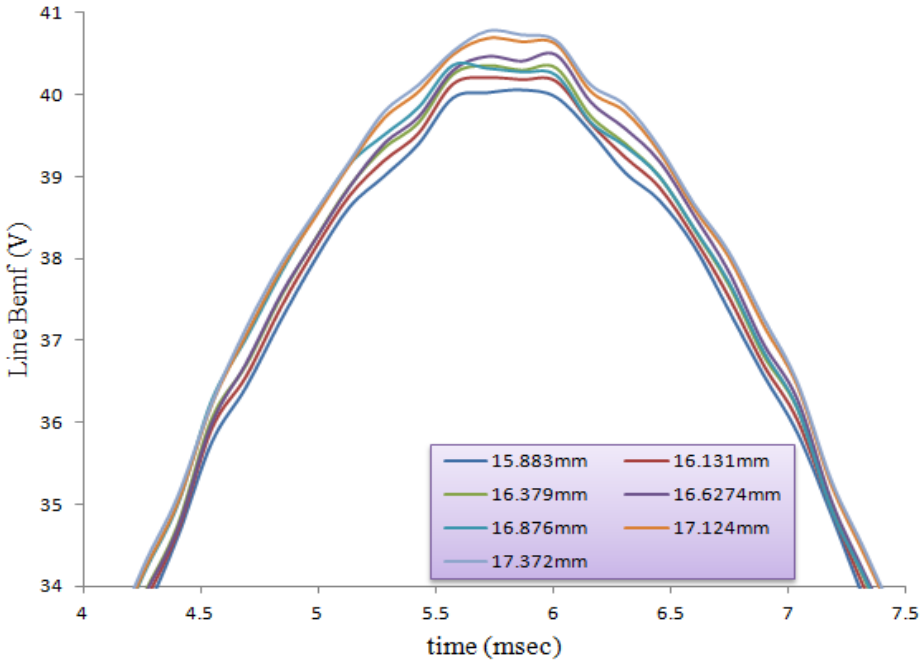

Figure 8.17. Peak point of line – line back EMF for various magnet pole arcs.

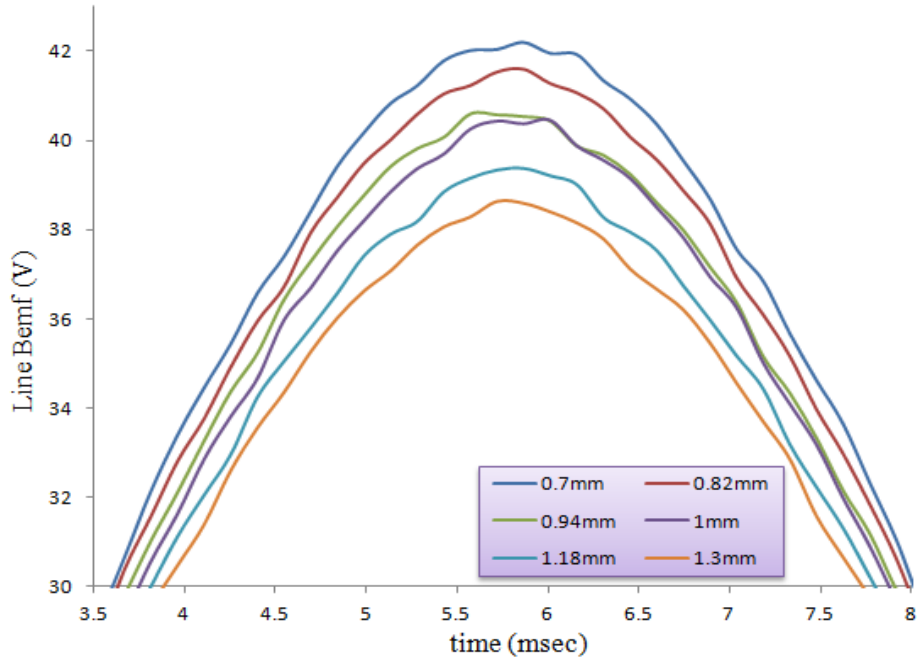

Figure 8.18. Peak point of line – line back EMF for various air-gap length.

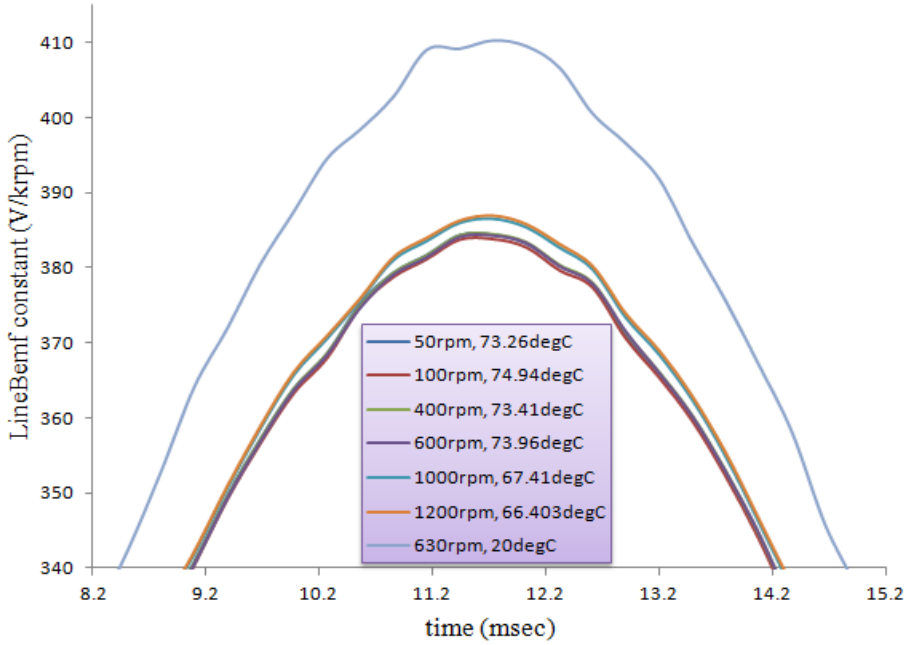

Figure 8.19. Peak point of line – line back EMF, for various speeds and corresponding temperature.

8.7 Conclusion

The results from test data from the prototype machine have been presented in this chapter. The measured results were used to verify the FE predicted results and a good correlation was established between both results.

The no-load test showed that the line back EMF differ from FE calculations by 7.3%, and was found to be near sinusoidal with a very low 5^{th} harmonic content. The no-load losses with the machine terminals open circuited were presented. It was predicted that the winding eddy current loss due its exposure to the varying air-gap field would cause the machine loss to rise, this presents additional loss for the coolant to remove from machine.

The prototype machine was compared to the Protean MHV machine when loaded and driven against standard drive cycles. The torque constant test showed that the Protean MHV has a better torque per ampere compared to the prototype, due to the different tooth designs. However when the continuous torque test was done on both machines, it was found that the prototype machine has about 10% better torque performance for a given temperature rise; this can be attributed to lower conduction. It was found that at high speed the proximity loss of the windings for the prototype machine is significant and is important for the machine efficiency for this to be reduced in future designs. The

increased proximity loss is caused by a larger conductor diameter and increased winding exposure to the air-gap field.

The thermal characteristics and efficiency of the cooling method were studied and it was concluded from the thermal characterisation that the iron loss in the machine was not a major concern, as the rotor temperature followed the curve pattern of the applied current squared over the machine speed range. Removal of heat energy by the coolant was presented, it can be concluded that the heat loss is mostly generated in the slots of the machine. At high speed the coolant is required to remove less heat energy, due to the decrease in slot loss.

Chapter 9

Conclusion

A high torque, fault tolerant, permanent magnet machine has been studied in this thesis. The machine is built for the purpose of providing mechanical propulsion in the EV, as a direct drive in-wheel motor.

The project was initiated by Protean Electric in collaboration with Newcastle University. The company is involved in developing advanced in-wheel electric drives for electric vehicles, whereby the in-wheel electric drive system comes as a packaged unit comprising the power electronics and electric machine, which is then fitted in the vehicle as a hub motor.

By adopting a novel method of construction the performance of the machine was improved in comparison to a pre-existing machine designed by Protean; a machine with higher torque output on a smaller outer diameter was realised. A prototype was built for the purpose of testing and validation and also comparison to a newly built machine by Protean with similar structure and expected output performance.

9.1 Protean in-wheel motor

The design review and critique carried out on the Protean motor was geared towards studying various slot and pole combinations and geometrical variations to improve the electromagnetic performance. The general machine assembly has to conform to certain restrictions such as; having an outer rotor, be capable of being split into a series of sub-motors, have single tooth windings and large number of poles. The optimisation was carried out with the dominant parameter for optimisation being the mean torque per unit volume achieved within a specific efficiency, within specific dimensional constraints. The limits set on the optimisation were; maximum of 64poles, 340mm on the inner stator diameter, 400mm on the outer rotor diameter, 56.6mm on the total axial length and 1mm air-gap length.

Machine design optimisation aimed to maximise torque for a given winding loss. The optimisation of various slot and pole combinations, showed consistence in the outcome of the results; the optimum magnet depth was always towards the maximum allowed, the magnet arc was in the range of 154 – 171 degrees. The active stack length was reduced as the slot number reduced, due to the length of the end-windings, making low pole number machines uncompetitive. The Protean 72slot/64pole machine proved to be the strongest candidate of all the slot and pole combinations, as it combines the highest torque capability with a very low cogging torque and minimal space harmonics in the back EMF.

9.2 Fault tolerance

Fault tolerance is a very important aspect when designing a motor as a direct drive in-wheel motor. The machine must be able to limit any sudden braking torque at the wheel, while limiting a high magnitude of current circulating in the phase and also prevent the propagation of the fault. System studies prove that a large disturbance torque of 280Nm or more at a wheel could lead to loss of vehicle control and an inter-turn fault can lead to a current of very large magnitude flowing in the coil. In order to reduce the braking torque of the Protean motor; the motor has been split into a series of eight parallel sub-motors and the phase coils designed to have a large inductance. This fault tolerant concept has been applied to all subsequent machines designed to be used in the Protean electric drive system. It was demonstrated for the first time that a high performance in-wheel motor can be produced with a high fault tolerance capability.

The fault test carried out on the Protean motor includes; a single phase fault, three phase fault, single coil fault and inter-turn fault. From the results of the fault test and simulation it can be inferred that;

- The Protean machine has a good limit on the drag torque below 280Nm.
- The largest braking torque is seen during a symmetrical three phase short circuit.
- The largest fault current occurs with a single turn – turn fault, due to the single turn resistance being the only limiting component, but the braking torque is very low because the current that circulates is localised.
- The peak drag torque occurs at a very low speed, and poses no danger to the driver.
- The short circuit current increases with speed and converges at a certain speed, where the fault current is not dependent on the speed of the rotor.

- Fault propagation between two adjoining sub-motors is limited as the magnetic coupling between two sub-motors is very low.

9.3 Design concept for machine with slot wedge and pressed coil

The drive behind the work done for this PhD involved improving the torque performance of in-wheel motors. Concepts were applied to an existing Protean machine, while reducing the rotor outer diameter from 400mm to 386mm, reducing the stator inner diameter from 340mm to 302mm and increasing the active axial length from 50mm to 58.3mm. The machine performance was improved by increasing the electrical loading of the machine; achieved by studying an open slot stator design having magnetic slot wedges and the coils pre-pressed to increase the slot fill factor.

The difference between using a magnetic slot wedge to a non-magnetic type was presented during the course of the thesis. A comparison was carried out between magnetic slot wedges, an open slot design option and a design having the conventional tooth tip; it was found that the design with the magnetic wedge conveys the most flux onto the machine tooth, however saturation at the lower section of the tooth causes the flux to drop when compared to the open slot design. On the other hand the design with conventional tooth tip was more effective at screening the winding and consequently showed lower no-load losses than the designs with the wedge and open slot, which had significant winding eddy currents.

The slot fill factor in the machine was greatly increased by the use of pressed coils, whereby a new method of coil pressing was developed. Due to the restriction in the axial length, it was important to ensure the development of coils with short end-wingding, so a new method of pressing the coils was investigated because applying the conventional method of coil pressing means the coils will have a long end-winding. Empirical method had to be adopted in order to realise a final coil pressing method, by applying different bending radii to the coils; from this it was concluded that a bending radius greater than the diameter of the conductor prevents the introduction of weak points at the bends of the coil, even after pressing the coils. This meant that a new method of coil pressing was actualised, whereby the coils are produced with reasonably short end-windings for the purpose of in-wheel application.

The process of winding and pressing the coils were discussed in this thesis; it was also found that the top and bottom turns carry much of the pressing force causing them to

deform irregularly, this uneven distribution of force was mitigated by having a sacrificial layer of aluminium at the top and bottom of the bobbin, this is an important finding that improves the integrity of coils after being pressed. An FE mechanical model was built to determine the conductor behaviour when pressing of the coils; it was found that the conductors can move during the pressing process, which makes it important to hold the turns of the coil properly in place to prevent damage of the wire enamel. A cut through section of an actual sample of the pressed coil was presented, and it was shown that the conductor cross-sectional shape was close to a hexagon.

Finally the method of checking the insulation life expectancy was investigated. It was expected that the breakdown voltage of the wire would be reduced as the coil is pressed, but there was no significant testing to confirm this. A set of coil tests were carried out using a voltage impulse tester, manufactured by Baker Instrument, involving; a megohm, hipot and surge test. These tests, conducted at 2.8kV, revealed no signs of insulation degradation due to pressing.

9.4 Model analysis of machine design having magnetic slot wedge

Machines having slot wedges and pressed coils were modelled with the electromagnetic FE tool used throughout the course of this work. In chapter 6 different slot and pole combinations were researched, using the standardised optimisation procedure adopted for this work; twelve different combinations were studied, some having more slots than poles and others having more poles than slots. The effects of having high number of poles were presented; one of the conclusions drawn showed the higher the number of poles the shallower the core-backs and the bigger the air-gap radius, which means the output torque can be increased.

The various slot and pole combinations chosen for optimisation are; 72slot/64pole, 72slot/60pole, 72slot/48pole, 63slot/56pole, 60slot/64pole, 60slot/56pole, 54slot/60pole, 54slot/48pole, 45slot/50pole, 45slot/40pole, 36slot/48pole and 36slot/40pole. The parameter set for optimisation was the mean torque per unit volume, for a fixed machine winding loss of 2074W, with other geometrical dimensions set at a maximum limit. The structural designs as a result of the optimisation for the various slot and pole combinations were presented in chapter 6, the flux linking the stator coils were shown, along with the flux density in the air-gap and teeth; it can be concluded from the optimisation result of the flux concentration, that the tooth width and core-back depth are reduced to the point of the highest magnetic limit of the lamination, which increases

the slot area and ensures the torque is increased for a given machine winding loss. It is also worth noting that the active stack length of the machine is shortened as the slot number is reduced due to the increase in end-winding length. The combinations show a good attenuation of the spatial harmonics in the back EMF, where the 72slots / 48poles machine has the highest content of 5^{th} harmonic in the line back EMF of about 11.69% of the fundamental. When the electric loading of the machines is increased the 72slot/64pole and 54slot/60pole produce the highest mean torque and finally the torque ripple produced by the various machines was presented. The 72slot/64pole was further analysed in terms of its electromagnetic attributes and its loss components identified from this analysis, finally the prototype was built and tested. The analysis done on the machine include; stator MMF harmonics contribution to rotor loss, the slot proximity loss and total machine winding loss, magnet demagnetisation and machine torque vs speed curve. The proximity loss makes up about 15% of the total slot loss, when the winding current is increased for a given speed. Also the magnet demagnetisation at a speed of 1600rpm, negative d-axis current of 19.3A and temperature of 150˚C was studied and found that the magnet is not likely to experience any irreversible demagnetisation.

Finally thermal analysis was carried out, as below:

The various slot and pole combinations were optimised for a given peak slot temperature of 180˚C, with the mean torque output being the focus of the optimisation. A set of equations were adopted to determine the slot temperature by obtaining the slot loss and iron loss from the model, along with the various thermal resistances of the machine parts. The geometrical structure after optimisation was presented in chapter 7; from this it was shown that the 72slot/64pole and 60slot/56pole produces the most torque for a given slot temperature.

A thermal model was built using motorCAD for analytical calculation and thermNet for FE calculation, to determine the thermal characteristics of the 72slot/64pole machine. Thermal data was obtained from measurement, which was used as a guide to build the thermal models. The steady state thermal resistance network obtained from motorCAD was presented, showing the temperature distribution in the machine; the hottest spot is clearly in the winding as this is where the most heat is generated, the temperature is distributed around the winding and this can be seen in the thermal network. It was recognised that the slot liner would not necessarily be in direct contact with the tooth, leading to an additional thermal resistance. By using measured temperatures in

conjunction with a thermal model, it was possible to estimate the size of this gap. Using motorCAD the thickness of the air-gap between the slot liner and the tooth was found to be 0.066mm. Then from the results of the motorCAD model, an FE thermal model was built using thermNet to determine the temperature distribution in the slot, temperature gradient and heat flow, and using a set of equations the thickness of the air-gap between the slot liner and the tooth was calculated to be 0.059mm. Understanding how the temperature drops from winding to tooth for the prototype machine due to any additional thermal resistance was important, as the prototype machine was compared to another machine with dissimilar thermal path between winding and tooth.

9.5 72slot/64pole prototype testing

The results of the performance test on the 72slot/64pole machine with slot wedges and pressed coils have validated the model results and met the expect output performance which the machine was designed to achieve. The models were solved using 2D FE simulation with the simulation results having a close match to the measured result within an acceptable percentage difference.

The no-load loss test on the machine was used to determine winding loss due to the winding exposure to the air-gap field. It was shown that this is significant at high speeds.

The prototype machine was compared to the Protean MHV machine, which was built in-house by Protean. The Protean MHV machine was designed to produce similar output performance as the prototype machine, with similar cooling methods applied to both machines. The two machines were compared over standard drive cycles. The Protean MHV has a better torque per ampere compared to the prototype, due to the different tooth shape designs. A continuous torque test was performed on both machines, and it was found that the prototype machine has about 10% better torque performance at low speed; this is a result of lower conduction loss. It was found that at high speed the proximity loss of the windings for the prototype machine is an issue and is important for the machine efficiency for this to be reduced. The increased proximity loss is caused by the big conductor diameter and the winding exposure to the air-gap field.

Thermal characterisation of the machine was conducted to determine the temperature distribution around the machine over its speed range, with a coolant pumped through a water jacket at a flow rate of 15l/min and temperature of 50˚C. The temperature change with speed follows the same pattern as the current change with speed, which indicates

that iron loss in the machine is not significant at high speeds. Also the efficiency of the cooling system was presented by calculating the energy dumped into the coolant.

9.6 Future work

The work presented in this thesis explores a new method of construction of a 72slot/64pole, high torque dense permanent magnet machine, designed for direct drive in-wheel motor applications. The purpose of the work was achieved, as the machine delivers the expected performance, however a few key areas are open for further investigation and improvement:

- Further investigation of other slot and pole combinations, particularly the 54slot/60pole machine. It was observed during the optimisation process that pre-pressed coils can help reduce the end-winding while maintaining a longer stack length, as the slot number is reduced. The 54slot/60pole machine combines a high electric and magnetic loading, so having a mock-up of a section of the stator with pressed coils could be used to help determine its actual active length.
- Reduction of the magnet volume and introduction of reluctance torque to help maintain a good torque performance; most work done points at having a distributed winding in order to make use of reluctance torque in a machine. Rotor topologies and radial dimensions can be investigated to improve the reluctance torque.
- The proximity loss in the slot at high speed is an area that could be improved by exploring the use of wires with smaller diameter, however this has the potential of increasing the conduction loss at low speed, presenting a design trade-off that depends on the continuous operating point of the motor.
- The slot loss due to the exposure of the coils to the air-gap field presents another area for improvement; the thickness of the slot wedge can be increased to move the coils further away from the air-gap region. It was found that with a slot depth of 4.2mm, the winding loss due to the magnet air-gap field can be reduced by 87%, figure 9.1 shows the wedge design.

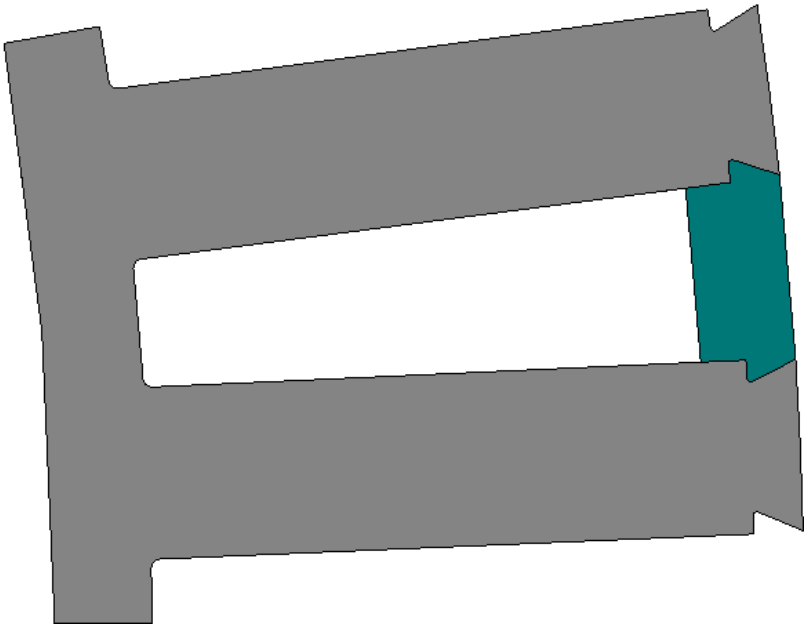

Figure 9.1. Proposed wedge design having a wedge thickness of 4.2mm.

9.7 Published work

The following are conference and journal papers peer-reviewed and published during the course of this work:

a) Ifedi, C.J., Mecrow, B.C., Brockway, S.T.M., Boast, G.S., Atkinson, G.J., and Kostic-Pervoic, D., "Fault Tolerant In-wheel Motor Topologies for High Performance Electric Vehicles," IEEE International Electrical Machines and Drives Conference, IEMDC 2011, Niagara Falls, ON, Canada, 15-18 May, 2011, pp 1310-1315.

b) Ifedi, C.J., Mecrow, B.C., Widmer, J.D., Atkinson, G.J., Brockway, S.T.M., and Kostic-Pervoic, D., "A High Torque Density, Direct Drive In-wheel Motor for Electric Vehicles," IET 6th International Conference on Power Electronics, Machines and Drives, PEMD 2012, Bristol, UK, 27-29 March, 2012, pp. 1-6.

c) Ifedi, C.J., Mecrow, B.C., Brockway, S.T.M., Boast, G.S., Atkinson, G.J., and Kostic-Pervoic, D., "Fault Tolerant In-wheel Motor Topologies for High Performance Electric Vehicles," IEEE Transactions on Industry Applications, vol. 49, no. 3, May/June 2013, pp. 1249-1257.

References

[1] W. Shihua, T. Likun, and C. Shumei, "A comparative study of the interior permanent magnet electrical machine’s rotor configurations for a single shaft hybrid electric bus," presented at the Vehicle Power and Propulsion Conference, 2008. VPPC '08. IEEE, 2008.

[2] P. B. Reddy, T. M. Jahns, P. J. McCleer, and T. P. Bohn, "Design, analysis and fabrication of a high-performance fractional-slot concentrated winding surface PM machine," presented at the Energy Conversion Congress and Exposition (ECCE), 2010 IEEE, 2010.

[3] P. B. Reddy, A. M. El-Refaie, and H. Kum-Kang, "Effect of number of layers on performance of fractional-slot concentrated-windings interior permanent magnet machines," presented at the Power Electronics and ECCE Asia (ICPE & ECCE), 2011 IEEE 8th International Conference on, 2011.

[4] S. Tao, K. Ji-Min, L. Geun-Ho, H. Jung-Pyo, and C. Myung-Ryul, "Effect of Pole and Slot Combination on Noise and Vibration in Permanent Magnet Synchronous Motor," *Magnetics, IEEE Transactions on,* vol. 47, pp. 1038-1041, 2011.

[5] F. Rahman and R. Dutta, "An investigation of a segmented rotor interior permanent magnet (IPM) machine for field weakening," presented at the Power Electronics and Drive Systems, 2003. PEDS 2003. The Fifth International Conference on, 2003.

[6] B. Sneyers, D. W. Novotny, and T. A. Lipo, "Field Weakening in Buried Permanent Magnet AC Motor Drives," *Industry Applications, IEEE Transactions on,* vol. IA-21, pp. 398-407, 1985.

[7] T. M. Jahns, "Flux-Weakening Regime Operation of an Interior Permanent-Magnet Synchronous Motor Drive," *Industry Applications, IEEE Transactions on,* vol. IA-23, pp. 681-689, 1987.

[8] J. Griffin, "World oil outlook," OPEC - Organisation of the petroleum exporting countries, Vienna, Austria2011.

[9] S. Williamson, M. Lukic, and A. Emadi, "Comprehensive drive train efficiency analysis of hybrid electric and fuel cell vehicles based on motor-controller efficiency modeling," *Power Electronics, IEEE Transactions on,* vol. 21, pp. 730-740, 2006.

[10] S. Leitman. and B. Brant. (2009). *Build Your Own Electric Vehicle (Second ed.)*.

[11] F. Didik. History and Directory of Electric Cars [Online]. Available: http://www.didik.com/ev_hist.htm

[12] M. Olszewski, "Report on Toyota/Prius Motor Torque Capability, Torque Property, No-Load Back EMF, and Mechanical Losses," Washington, D.C.2007.

[13] M. Kamiya, "Development of Traction Drive Motors for the Toyota Hybrid System," Japan2007.

[14] Y. Sato, S. Ishikawa, T. Okubo, M. Abe, and K. Tamai, "Development of High Response Motor and Inverter System for the Nissan LEAF Electric Vehicle," *SAE Technical Paper,* pp. 1-8, 2011.

[15] T. M. Corporation, "Toyota Hybrid System THS II," Japan2003.

[16] C. C. Chan, "The state of the art of electric and hybrid vehicles," *Proceedings of the IEEE,* vol. 90, pp. 247-275, 2002.

[17] X. D. Xue, K. Cheng, and N. C. Cheung, "Selection of eLECTRIC mOTOR dRIVES for electric vehicles," presented at the Power Engineering Conference, 2008. AUPEC '08. Australasian Universities, 2008.

[18] M. Jain and S. S. Williamson, "Suitability analysis of in-wheel motor direct drives for electric and hybrid electric vehicles," presented at the Electrical Power & Energy Conference (EPEC), 2009 IEEE, 2009.

[19] W. Jiabin, X. Zhen Ping, and D. Howe, "Three-phase modular permanent magnet brushless Machine for torque boosting on a downsized ICE vehicle," *Vehicular Technology, IEEE Transactions on,* vol. 54, pp. 809-816, 2005.

[20] T. King-Jet and G. H. Chen, "Computer-aided design and analysis of direct-driven wheel motor drive," *Power Electronics, IEEE Transactions on,* vol. 12, pp. 517-527, 1997.

[21] H. C. Lovatt, D. Elton, L. Cahill, H. Duc Hau, A. Stumpf, A. Kulkarni, A. Kapoor, M. Ektesabi, H. Mazumder, T. Dittmar, and G. White, "Design procedure for low cost, low mass, direct drive, in-wheel motor drivetrains for electric and hybrid vehicles," presented at the IECON 2011 - 37th Annual Conference on IEEE Industrial Electronics Society, 2011.

[22] H. C. Lovatt, V. S. Ramsden, and B. C. Mecrow, "Design of an in-wheel motor for a solar-powered electric vehicle," *Electric Power Applications, IEE Proceedings -,* vol. 145, pp. 402-408, 1998.

[23] D. Patterson and R. Spee, "The design and development of an axial flux permanent magnet brushless DC motor for wheel drive in a solar powered vehicle," *Industry Applications, IEEE Transactions on,* vol. 31, pp. 1054-1061, 1995.

[24] S. Wu, L. Song, and S. Cui, "Study on Improving the Performance of Permanent Magnet Wheel Motor for the Electric Vehicle Application," *Magnetics, IEEE Transactions on,* vol. 43, pp. 438-442, 2007.

[25] M. Terashima, T. Ashikaga, T. Mizuno, K. Natori, N. Fujiwara, and M. Yada, "Novel motors and controllers for high-performance electric vehicle with four in-wheel motors," *Industrial Electronics, IEEE Transactions on,* vol. 44, pp. 28-38, 1997.

[26] I. Apex Drive Laboratories. Apex PM Brushless Motors [Online]. Available: http://www.apexdrivelabs.com/brushless-DC-motor-technology.html

[27] F. Caricchi, F. Crescimbini, F. Mezzetti, and E. Santini, "Multistage axial-flux PM machine for wheel direct drive," *Industry Applications, IEEE Transactions on,* vol. 32, pp. 882-888, 1996.

[28] F. Chai, J. Xia, B. Guo, S. Cheng, and J. Zhang, "Double-Stator Permanent Magnet Synchronous in-Wheel Motor for Hybrid Electric Drive System," *Magnetics, IEEE Transactions on,* vol. 45, pp. 278-281, 2009.

[29] S. P. Enstroj. EMRAX Motors [Online]. Available: http://www.enstroj.si/Electric-products/emrax-motors.html

[30] W. Jiabin, K. Atallah, Z. Q. Zhu, and D. Howe, "Modular Three-Phase Permanent-Magnet Brushless Machines for In-Wheel Applications," *Vehicular Technology, IEEE Transactions on,* vol. 57, pp. 2714-2720, 2008.

[31] K. M. Rahman, N. R. Patel, T. G. Ward, J. M. Nagashima, F. Caricchi, and F. Crescimbini, "Application of Direct-Drive Wheel Motor for Fuel Cell Electric and Hybrid Electric Vehicle Propulsion System," *Industry Applications, IEEE Transactions on,* vol. 42, pp. 1185-1192, 2006.

[32] Y. Yee-Pien, L. Jia-Yuan, and X. Xian-Yee, "Design and application of axial-flux permanent magnet wheel motors for an electric vehicle," presented at the AFRICON, 2009. AFRICON '09., 2009.

[33] D. Luque, E. Ruppert, N. Bianchi, and M. Castiello, "Analysis of a three-phase in-wheel electric motor," presented at the Universities Power Engineering Conference (UPEC), 2009 Proceedings of the 44th International, 2009.

[34] M. Zeraoulia, M. E. H. Benbouzid, and D. Diallo, "Electric Motor Drive Selection Issues for HEV Propulsion Systems: A Comparative Study," *Vehicular Technology, IEEE Transactions on,* vol. 55, pp. 1756-1764, 2006.

[35] Z. Q. Zhu and D. Howe, "Electrical Machines and Drives for Electric, Hybrid, and Fuel Cell Vehicles," *Proceedings of the IEEE,* vol. 95, pp. 746-765, 2007.

[36] M. Ehsani, K. M. Rahman, and H. A. Toliyat, "Propulsion system design of electric and hybrid vehicles," *Industrial Electronics, IEEE Transactions on,* vol. 44, pp. 19-27, 1997.

[37] I. Husain and M. S. Islam, "Design, Modeling and Simulation of an Electric Vehicle System," *SAE Technical Paper,* pp. 1-9, 1999.

[38] R. Mizutani and N. MAtsui, "Optimum Design Approach for Low-Speed, High-Torque Permanent Magnet Motors," presented at the Electrical Engineering in Japan, 2001.

[39] F. Libert and J. Soulard, "Design Study of Different Direct-Driven Permanent-Magnet Motors for a Low Speed Application," presented at the Division of Electrical Machines and Power Electronics, Royal Institute of Technology.

[40] B. C. Mecrow, A. G. Jack, D. J. Atkinson, P. G. Dickinson, and S. Swaddle, "High torque machines for power hand tool applications," presented at the Power Electronics, Machines and Drives, 2002. International Conference on (Conf. Publ. No. 487), 2002.

[41] P. Salminen, M. Niemela, J. Pyhonen, and J. Mantere, "Performance analysis of fractional slot wound PM-motors for low speed applications," presented at the Industry Applications Conference, 2004. 39th IAS Annual Meeting. Conference Record of the 2004 IEEE, 2004.

[42] M. G. Simoes and P. Vieira, Jr., "A high-torque low-speed multiphase brushless machine-a perspective application for electric vehicles," *Industrial Electronics, IEEE Transactions on,* vol. 49, pp. 1154-1164, 2002.

[43] J. Cros and P. Viarouge, "Synthesis of high performance PM motors with concentrated windings," *Energy Conversion, IEEE Transactions on,* vol. 17, pp. 248-253, 2002.

[44] S. E. Skaar, O. Krovel, and R. Nilssen, "Distribution, coil-span and winding factors for PM machines with concentrated windings," presented at the Electrical Machines (ICEM), 2006, 2006.

[45] A. M. El-Refaie, T. M. Jahns, and D. W. Novotny, "Analysis of surface permanent magnet machines with fractional-slot concentrated windings," *Energy Conversion, IEEE Transactions on,* vol. 21, pp. 34-43, 2006.

[46] A. M. El-Refaie, "Fractional-Slot Concentrated-Windings Synchronous Permanent Magnet Machines: Opportunities and Challenges," *Industrial Electronics, IEEE Transactions on,* vol. 57, pp. 107-121, 2010.

[47] A. M. El-Refaie, M. R. Shah, J. P. Alexander, S. Galioto, K. K. Huh, and W. D. Gerstler, "Rotor End Losses in Multiphase Fractional-Slot Concentrated-Winding Permanent Magnet Synchronous Machines," *Industry Applications, IEEE Transactions on,* vol. 47, pp. 2066-2074, 2011.

[48] A. J. Rix, M. J. Kamper, and W. Rong-Jie, "Design and Performance Evaluation of Concentrated Coil Permanent Magnet Machines for In-Wheel Drives," presented at the Electric Machines & Drives Conference, 2007. IEMDC '07. IEEE International, 2007.

[49] D. Ishak, Z. Q. Zhu, and D. Howe, "Permanent-magnet brushless machines with unequal tooth widths and similar slot and pole numbers," *Industry Applications, IEEE Transactions on,* vol. 41, pp. 584-590, 2005.

[50] D. Ishak, Z. Q. Zhu, and D. Howe, "Comparison of PM brushless motors, having either all teeth or alternate teeth wound," *Energy Conversion, IEEE Transactions on,* vol. 21, pp. 95-103, 2006.

[51] L. Parsa, H. A. Toliyat, and A. Goodarzi, "Five-Phase Interior Permanent-Magnet Motors With Low Torque Pulsation," *Industry Applications, IEEE Transactions on,* vol. 43, pp. 40-46, 2007.

[52] K. I. Laskaris and A. G. Kladas, "Internal Permanent Magnet Motor Design for Electric Vehicle Drive," *Industrial Electronics, IEEE Transactions on,* vol. 57, pp. 138-145, 2010.

[53] C. M. Spargo, B. C. Mecrow, and J. D. Widmer, "Application of Fractional Slot Concentrated Windings to Synchronous Reluctance Machines," presented at the IEEE International Electrical Machines and Drives Conference, IEMDC 2013, Chicago, Illinois, USA, 2013.

[54] F. Profumo, Z. Zheng, and A. Tenconi, "Axial flux machines drives: a new viable solution for electric cars," *Industrial Electronics, IEEE Transactions on,* vol. 44, pp. 39-45, 1997.

[55] T. J. Woolmer and M. D. McCulloch, "Axial flux permanent magnet machines: A new topology for high performance applications," presented at the Hybrid Vehicle Conference, IET The Institution of Engineering and Technology, 2006, 2006.

[56] T. J. Woolmer and M. D. McCulloch, "Analysis of the Yokeless And Segmented Armature Machine," presented at the Electric Machines & Drives Conference, 2007. IEMDC '07. IEEE International, 2007.

[57] S. Baserrah, K. Rixen, and B. Orlik, "Transverse flux machines with distributed windings for in-wheel applications," presented at the Power Electronics and Drive Systems, 2009. PEDS 2009. International Conference on, 2009.

[58] G. Youguang, Z. Jian Guo, P. A. Watterson, and W. Wei, "Development of a PM transverse flux motor with soft magnetic composite core," *Energy Conversion, IEEE Transactions on,* vol. 21, pp. 426-434, 2006.

[59] J. G. Washington, G. J. Atkinson, N. J. Baker, A. G. Jack, B. C. Mecrow, B. B. Jensen, L. Pennander, G. L. Nord, Sjo, x, and L. berg, "Three-Phase Modulated Pole Machine Topologies Utilizing Mutual Flux Paths," *Energy Conversion, IEEE Transactions on,* vol. 27, pp. 507-515, 2012.

[60] S. L. Ho, N. Shuangxia, and W. N. Fu, "Design and Analysis of a Novel Axial-Flux Electric Machine," *Magnetics, IEEE Transactions on,* vol. 47, pp. 4368-4371, 2011.

[61] Z. Rahman, "Evaluating radial, axial and transverse flux topologies for 'in-wheel' motor," presented at the Power Electronics in Transportation, 2004, 2004.

[62] C. Anyuan, R. Nilssen, and A. Nysveen, "Performance Comparisons Among Radial-Flux, Multistage Axial-Flux, and Three-Phase Transverse-Flux PM Machines for Downhole Applications," *Industry Applications, IEEE Transactions on,* vol. 46, pp. 779-789, 2010.

[63] K. Sitapati and R. Krishnan, "Performance comparisons of radial and axial field, permanent-magnet, brushless machines," *Industry Applications, IEEE Transactions on,* vol. 37, pp. 1219-1226, 2001.

[64] H. Wei, C. Ming, and Z. Gan, "A Novel Hybrid Excitation Flux-Switching Motor for Hybrid Vehicles," *Magnetics, IEEE Transactions on,* vol. 45, pp. 4728-4731, 2009.

[65] A. Zulu, B. C. Mecrow, and M. Armstrong, "A Wound-Field Three-Phase Flux-Switching Synchronous Motor With All Excitation Sources on the Stator," *Industry Applications, IEEE Transactions on,* vol. 46, pp. 2363-2371, 2010.

[66] A. S. Thomas, Z. Q. Zhu, R. L. Owen, G. W. Jewell, and D. Howe, "Multiphase Flux-Switching Permanent-Magnet Brushless Machine for Aerospace Application," *Industry Applications, IEEE Transactions on,* vol. 45, pp. 1971-1981, 2009.

[67] J. Herbst, J. Hahne, H. Jordan, H. Liu, A. Gattozzi, and W. Ben, "Challenges in the design of a 100 kw induction motor for a PHEV application," presented at the Vehicle Power and Propulsion Conference, 2009. VPPC '09. IEEE, 2009.

[68] D. G. Dorrell, A. M. Knight, M. Popescu, L. Evans, and D. A. Staton, "Comparison of different motor design drives for hybrid electric vehicles," presented at the Energy Conversion Congress and Exposition (ECCE), 2010 IEEE, 2010.

[69] P. C. Desai, M. Krishnamurthy, N. Schofield, and A. Emadi, "Novel Switched Reluctance Machine Configuration With Higher Number of Rotor Poles Than Stator Poles: Concept to Implementation," *Industrial Electronics, IEEE Transactions on,* vol. 57, pp. 649-659, 2010.

[70] J. de Santiago, H. Bernhoff, Ekerg, x00E, B. rd, S. Eriksson, S. Ferhatovic, R. Waters, and M. Leijon, "Electrical Motor Drivelines in Commercial All-Electric Vehicles: A Review," *Vehicular Technology, IEEE Transactions on,* vol. 61, pp. 475-484, 2012.

[71] M. Anderson and D. Harty, "Unsprung Mass with In-Wheel Motors - Myths and Realities," presented at the Society of Automotive Engineers, 2011.

[72] A. Rojas Rojas, H. Niederkofler, and J. Willberger, "Comfort and Safety Enhancement of Passenger Vehicles with In-Wheel Motors," presented at the SAE Technical Paper 2010-01-1146, 2010.

[73] D. J. van Schalkwyk and M. J. Kamper, "Effect of Hub Motor Mass on Stability and Comfort of Electric Vehicles," presented at the Vehicle Power and Propulsion Conference, 2006. VPPC '06. IEEE, 2006.

[74] A. Watts, C. Hilton, A. Fraser, M. Anderson, and D. Harty, "Unsprung Mass "The Myths and Realities - Closing the Circle"," presented at the SAE International, 2011.

[75] Dieselnet. Emission Test Cycles. ECE 15+EUDC/NEDC [Online]. Available: http://www.dieselnet.com/standards/cycles/ece_eudc.php

[76] E. Fornasiero, N. Bianchi, and S. Bolognani, "Slot Harmonic Impact on Rotor Losses in Fractional-Slot Permanent-Magnet Machines," *Industrial Electronics, IEEE Transactions on,* vol. 59, pp. 2557-2564, 2012.

[77] N. Bianchi, S. Bolognani, and E. Fornasiero, "An Overview of Rotor Losses Determination in Three-Phase Fractional-Slot PM Machines," *Industry Applications, IEEE Transactions on,* vol. 46, pp. 2338-2345, 2010.

[78] S. Jang-Ho, K. Sang-Yeop, J. Sang-Yong, L. Cheol-Gyun, C. Tae-Kyung, and J. Hyun-Kyo, "A Research on Iron Loss of IPMSM With a Fractional Number of Slot Per Pole," *Magnetics, IEEE Transactions on,* vol. 45, pp. 1824-1827, 2009.

[79] Z. Q. Zhu and D. Howe, "Influence of design parameters on cogging torque in permanent magnet machines," *Energy Conversion, IEEE Transactions on,* vol. 15, pp. 407-412, 2000.

[80] D. Bochnia, W. Hofmann, and H. Hupe, "Design optimization of permanent magnet motors by evolution strategies and finite element analysis," presented at the Electrical Machines and Drives, 1999. Ninth International Conference on (Conf. Publ. No. 468), 1999.

[81] E. Zitzler, M. Laumanns, and S. Bleuler. (2004, A Tutorial on Evolutionary Multiobjective Optimisation. *535,* 1-32.

[82] N. Bianchi, S. Bolognani, and M. Dai Pre, "Magnetic Loading of Fractional-Slot Three-Phase PM Motors With Nonoverlapped Coils," *Industry Applications, IEEE Transactions on,* vol. 44, pp. 1513-1521, 2008.

[83] N. Bianchi, M. D. Pre, G. Grezzani, and S. Bolognani, "Design considerations on fractional-slot fault-tolerant synchronous motors," presented at the Electric Machines and Drives, 2005 IEEE International Conference on, 2005.

[84] R. V. White and F. M. Miles, "Principles of fault tolerance," presented at the Applied Power Electronics Conference and Exposition, 1996. APEC '96. Conference Proceedings 1996., Eleventh Annual, 1996.

[85] R. N. Argile, B. C. Mecrow, D. J. Atkinson, A. G. Jack, and P. Sangha, "Reliability analysis of fault tolerant drive topologies," presented at the Power Electronics, Machines and Drives, 2008. PEMD 2008. 4th IET Conference on, 2008.

[86] B. A. Welchko, T. A. Lipo, T. M. Jahns, and S. E. Schulz, "Fault tolerant three-phase AC motor drive topologies: a comparison of features, cost, and limitations," *Power Electronics, IEEE Transactions on,* vol. 19, pp. 1108-1116, 2004.

[87] M. T. Abolhassani, "A novel multiphase fault tolerant high torque density permanent magnet motor drive for traction application," presented at the Electric Machines and Drives, 2005 IEEE International Conference on, 2005.

[88] J. J. Wolmarans, H. Polinder, J. A. Ferreira, and D. Clarenbach, "Selecting an optimum number of system phases for an integrated, fault tolerant permanent magnet machine and drive," presented at the Power Electronics and Applications, 2009. EPE '09. 13th European Conference on, 2009.

[89] T. Gopalarathnam, H. A. Toliyat, and J. C. Moreira, "Multi-phase fault-tolerant brushless DC motor drives," *Industry Applications Conference, 2000. Conference Record of the 2000 IEEE,* vol. 3, pp. 1683-1688 vol.3, 2000 2000.

[90] Z. Ping, S. Yi, Z. Jing, T. Chengde, T. A. Lipo, and W. Aimeng, "Investigation of a Novel Five-Phase Modular Permanent-Magnet In-Wheel Motor," *Magnetics, IEEE Transactions on,* vol. 47, pp. 4084-4087, 2011.

[91] M. Villani, M. Tursini, G. Fabri, and L. Castellini, "High Reliability Permanent Magnet Brushless Motor Drive for Aircraft Application," *Industrial Electronics, IEEE Transactions on,* vol. 59, pp. 2073-2081, 2012.

[92] B. C. Mecrow, A. G. Jack, D. J. Atkinson, S. R. Green, G. J. Atkinson, A. King, and B. Green, "Design and testing of a four-phase fault-tolerant permanent-magnet machine for an engine fuel pump," *Energy Conversion, IEEE Transactions on,* vol. 19, pp. 671-678, 2004.

[93] L. Parsa and H. A. Toliyat, "Fault-Tolerant Interior-Permanent-Magnet Machines for Hybrid Electric Vehicle Applications," *Vehicular Technology, IEEE Transactions on,* vol. 56, pp. 1546-1552, 2007.

[94] J. A. Haylock, B. C. Mecrow, A. G. Jack, and D. J. Atkinson, "Operation of fault tolerant machines with winding failures," *Energy Conversion, IEEE Transactions on,* vol. 14, pp. 1490-1495, 1999.

[95] P. H. Mellor, T. J. Allen, R. Ong, and Z. Rahma, "Faulted behaviour of permanent magnet electric vehicle traction drives," presented at the Electric Machines and Drives Conference, 2003. IEMDC'03. IEEE International, 2003.

[96] B. C. Mecrow, A. G. Jack, J. A. Haylock, and J. Coles, "Fault-tolerant permanent magnet machine drives," *Electric Power Applications, IEE Proceedings -,* vol. 143, pp. 437-442, 1996.

[97] N. Bianchi, E. Fornasiero, and S. Bolognani, "Thermal analysis of a five-phase motor under faulty operations," presented at the Diagnostics for Electric Machines, Power Electronics & Drives (SDEMPED), 2011 IEEE International Symposium on, 2011.

[98] A. J. Mitcham, G. Antonopoulos, and J. J. A. Cullen, "Favourable slot and pole number combinations for fault-tolerant PM machines," *Electric Power Applications, IEE Proceedings -,* vol. 151, pp. 520-525, 2004.

[99] D. Ishak, Z. Q. Zhu, and D. Howe, "Influence of slot number and pole number in fault-tolerant brushless dc motors having unequal tooth widths," *Journal of Applied Physics,* vol. 97, pp. 10Q509-10Q509-3, 2005.

[100] A. G. Jack, B. C. Mecrow, and J. A. Haylock, "A comparative study of permanent magnet and switched reluctance motors for high-performance fault-tolerant applications," *Industry Applications, IEEE Transactions on,* vol. 32, pp. 889-895, 1996.

[101] A. J. Mitcham, G. Antonopoulos, and J. J. A. Cullen, "Implications of shorted turn faults in bar wound PM machines," *Electric Power Applications, IEE Proceedings -,* vol. 151, pp. 651-657, 2004.

[102] R. A. Hanna, W. Hiscock, and P. Klinowski, "Failure Analysis of Three Slow-Speed Induction Motors for Reciprocating Load Application," *Industry Applications, IEEE Transactions on,* vol. 43, pp. 429-435, 2007.

[103] D. W. Schmitt and R. A. Hanna, "Mechanical and Electrical Challenges of Large Induction Motors Driving Reciprocating Compressors with Three Years Service," presented at the 2010 Gas Machinery Conference, Phoenix, Arizona, 2010.

[104] G. De Donato, F. G. Capponi, and F. Caricchi, "Influence of magnetic wedges on the no-load performance of axial flux permanent magnet machines," presented at the Industrial Electronics (ISIE), 2010 IEEE International Symposium on, 2010.

[105] H. Simburger, "Technical Report: Investigation of Metal Powder Filled, Glass Fiber Reinforced Resin, used as Slot Wedge in Electrical Engineering Industry," Vienna University of Technology, Vienna Austria29 January 2010 2010.

[106] A. G. Jack, B. C. Mecrow, P. G. Dickinson, D. Stephenson, J. S. Burdess, N. Fawcett, and J. T. Evans, "Permanent-magnet machines with powdered iron cores and prepressed windings," *Industry Applications, IEEE Transactions on,* vol. 36, pp. 1077-1084, 2000.

[107] E. Brancato, "Life expectancy of motors," *Electrical Insulation Magazine, IEEE,* vol. 7, pp. 14-16, 1991.

[108] E. Wire. Shaped Enamelled Wires - MAGNETEMP CA200 [Online]. Available: http://www.spsx.com/magnetwire.aspx?id=3698

[109] B. K. Gupta, W. T. Fink, and R. M. Boggia, "Use of thermal cycling as type test for turn insulation in motor coils," in *Electrical Insulation, 1994., Conference Record of the 1994 IEEE International Symposium on*, 1994, pp. 107-110.

[110] M. F. Beavers, "Determination of Equations and Constants for Life Expectancy Studies for Transformers and Similar Apparatus," *Power Apparatus and Systems, IEEE Transactions on,* vol. PAS-86, pp. 1192-1197, 1967.

[111] W. Xuhui, H. Wei, F. Tao, and L. Jun, "Lifetime model research of motor drive system for electric vehicles," in *Electrical Machines and Systems, 2007. ICEMS. International Conference on*, 2007, pp. 129-132.

[112] DuPont, "Nomex Type 410," Richmond Virginia2003.

[113] B. I. Company, "User's Manual Advanced Winding AWA," 2009.

[114] J. G. Washington, "A Modulated Pole Machine Topology Exploiting Mutual Flux Paths," Engineering Doctorate Thesis, Newcastle University, 2012.

[115] T. Chun, W. L. Soong, G. S. Liew, and N. Ertugrul, "Effect of pole and slot number changes on the performance of a surface PM machine," presented at the Electrical Machines (ICEM), 2012 XXth International Conference on, 2012.

[116] J. S. Hsu, B. P. Scoggins, M. B. Scudiere, L. D. Marlino, D. J. Adams, and P. Pillay, "Nature and assessments of torque ripples of permanent-magnet adjustable-speed motors," presented at the Industry Applications Conference, 1995. Thirtieth IAS Annual Meeting, IAS '95., Conference Record of the 1995 IEEE, 1995.

[117] F. Z. Zhou, J. X. Shen, and W. Z. Fei, "Influence on Rotor Eddy-Current Loss in High-Speed PM BLDC Motors," presented at the Universities Power Engineering Conference, 2006. UPEC '06. Proceedings of the 41st International, 2006.

[118] C. R. Sullivan, "Computationally efficient winding loss calculation with multiple windings, arbitrary waveforms, and two-dimensional or three-dimensional field geometry," *Power Electronics, IEEE Transactions on,* vol. 16, pp. 142-150, 2001.

[119] D. Hanselman, *Brushless Permanent Magnet Motor Design*. 3000 M Hekle Drive, Lebanon, Ohio, USA: Magna Physics Publishing, 2006.

[120] A. M. Technologies. Neodymium-Iron-Boron Magnet Catalogs - N45SH [Online]. Available: http://www.arnoldmagnetics.com/Neodymium_Literature.aspx

[121] P. G. Dickinson, "Application of Soft Magnetic Composites in Electrical Machines," Doctor of Philosophy, Newcastle University, 2003.

[122] D. Staton, A. Boglietti, and A. Cavagnino, "Solving the More Difficult Aspects of Electric Motor Thermal Analysis in Small and Medium Size Industrial Induction Motors," *Energy Conversion, IEEE Transactions on,* vol. 20, pp. 620-628, 2005.

Appendix A

Initial Model Design

A1 Thermal model

The winding information is very important in order to accurately build a thermal model; for the 72slot/64pole slot wedge machine design, table A1 below shows the parameters chosen for the winding.

Table A 1. Winding parameters for thermal model.

Winding type	Air divider	**Slot fill**	0.618
Wdg definition	Conductors / slot	**Liner thickness**	0.18
Wedge model	Wound space	**Liner-Lam gap**	0.0664
Mat [Liner-Lam]	Air	**Coil divider width**	0.1
EWdg definition	EWdg MLT	**EWdg MLT**	34.84
EWdg cavity	Potted	**Imp goodness [Active]**	0.9
Wire diameter	1.48	**Imp goodness [liner-lam]**	0.8
Copper diameter	1.4	**Imp goodness [EWdg]**	0.9

The cooling method chosen for the model was a spiral water jacket; this passes the coolant into a stator side plate on one axial end of the machine, through an axle on the stator core-back and out again through the stator side plate. Table A2 below shows the input parameters into the machine cooling options.

Table A 2. Cooling parameter configuration for thermal model.

Ambient temperature (convection)	25
Ambient temperature (radiation)	25
Shaft speed	100
Lamination stacking factor [Stator]	0.97
Lamination stacking factor [Rotor]	0.97
External fluid data	Air (motor-CAD model)
Internal fluid data	Air (motor-CAD model)

Interface gaps in a machine assembly:

Table A 3. Interface gaps for thermal model.

Stator lam – axle	**Rotor – housing**	**Housing – endcap [F]**	**Magnet – rotor lam**	**Bearing effective gap**
0.005	0.005	0.005	0.171	100

Material thermal properties:

Table A 4. Material Properties for thermal model.

Materials	**Thermal conductivity (W/m/°C)**	**Specific heat capacity (kJ/kg/°C)**	**Weight density (kg/m^3)**
Housing	150	0.833	2790
Endcap	150	0.833	2790
Seal	0.2	1.2	1000

Stator plate	150	0.833	2790
Lamination	28	0.46	7600
Copper	386	0.4	8954
Wire enamel	0.21	1	1400
Slot potting	1.28	1.7	1400
Slot liner	0.14	1.3	1400
Magnet	9	0.42	7400
Axle	150	0.833	2790
Shaft	52	0.46	7800
Bearing	30	0.46	7800
Mount	100	0.9	2700

A2 Magnetic model

Lamination Material:

Table A 5. Lamination for electromagnetic modelling.

Material	Thickness (mm)
M250-35A, EN10106	0.35

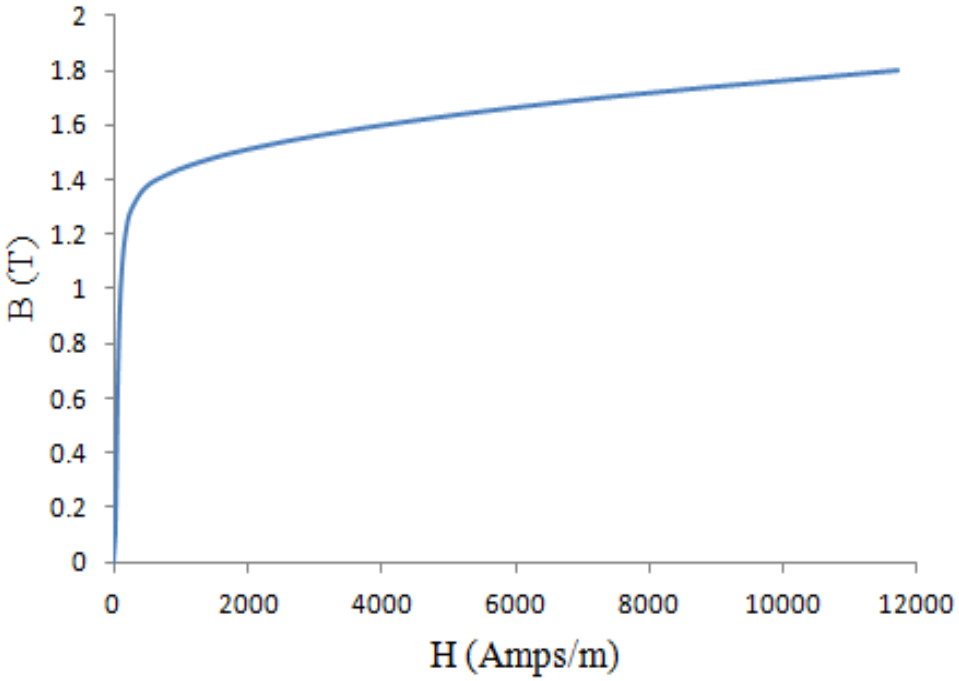

Figure A 1. B-H curve for lamination used in prototype machine.

A3 Wire and insulation

The wire used for the coils is from Essex wire named Magnetemp CA-200; copper enamel polyesterimide, overcoated with polyamide-imide, temperature rating of 210C designed for class H and higher and grade 2 insulation thickness. The slot wall insulation is Nomex type 410.

Appendix B

Optimisation Dimensions

The geometrical dimensions for the different pole and slot combinations optimised based on improving the mean torque for a given winding loss are presented in the drawings of figure B1. These geometrical structures were as a result of the electromagnetic optimisation presented in Chapter 6; the stator outer radius was fixed at 181mm, while the inner radius was fixed at 151mm and wedge depth of 2.2mm, equations B1 to B4 are applied in order to fix winding loss in the parameterisation script, as slot area varies.

$$SA = \frac{\pi(R_{outer\_slot}^2 - R_{inner\_slot}^2)}{TN} - SD \times TW \tag{B1}$$

$$J_{rms} = \sqrt{loss \times \sigma / ff \times SA \times la} \tag{B2}$$

$$MMF = J_{rms} \times SA/2 \times ff \tag{B3}$$

$$I_{peak} = MMF/turns \times \sqrt{2} \tag{B4}$$

The drawings in figure B2 presents the geometrical dimensions for the thermal optimisation done in Chapter 7 based on improving the mean torque output for a given peak slot temperature; the stator outer radius was fixed at 181mm, while the inner stator radius allowed to vary with a set limit of 141mm.

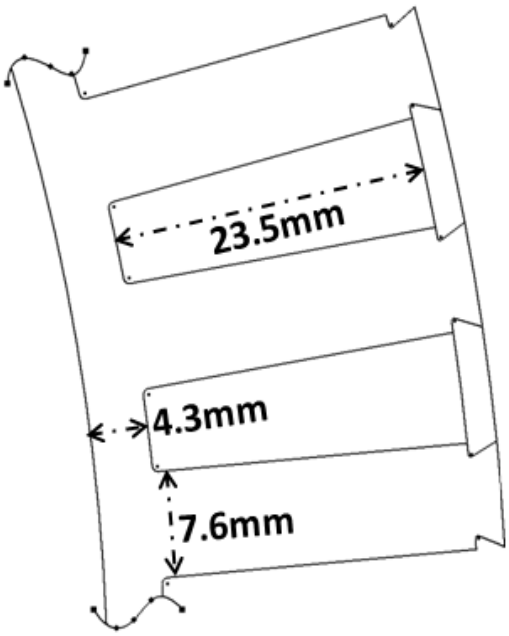

72slots

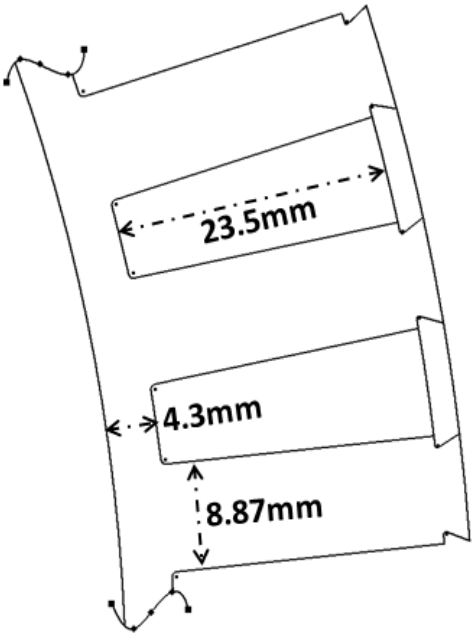

63slots / 56poles

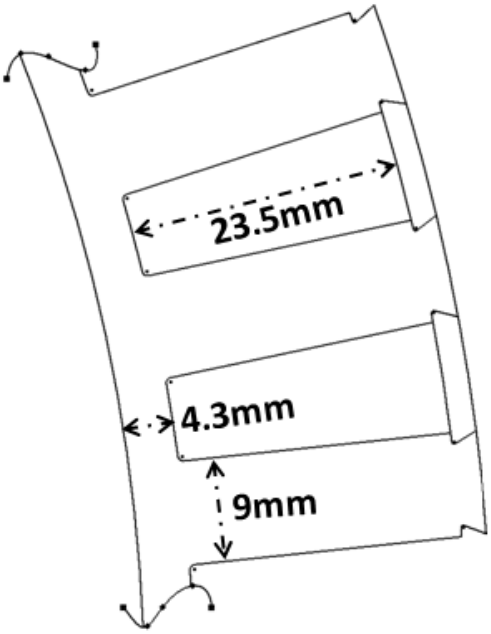

60slots

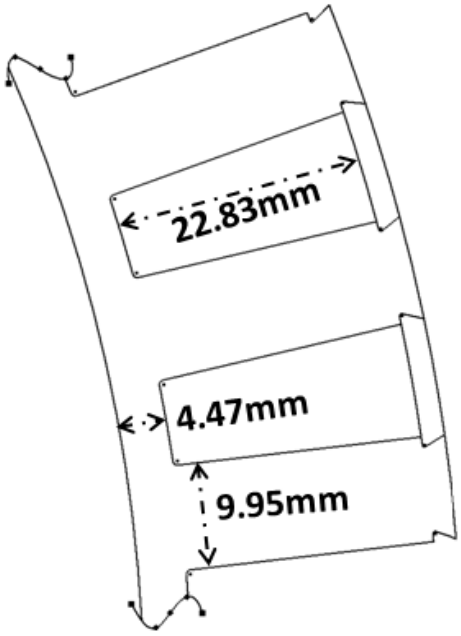

54slots / 48poles

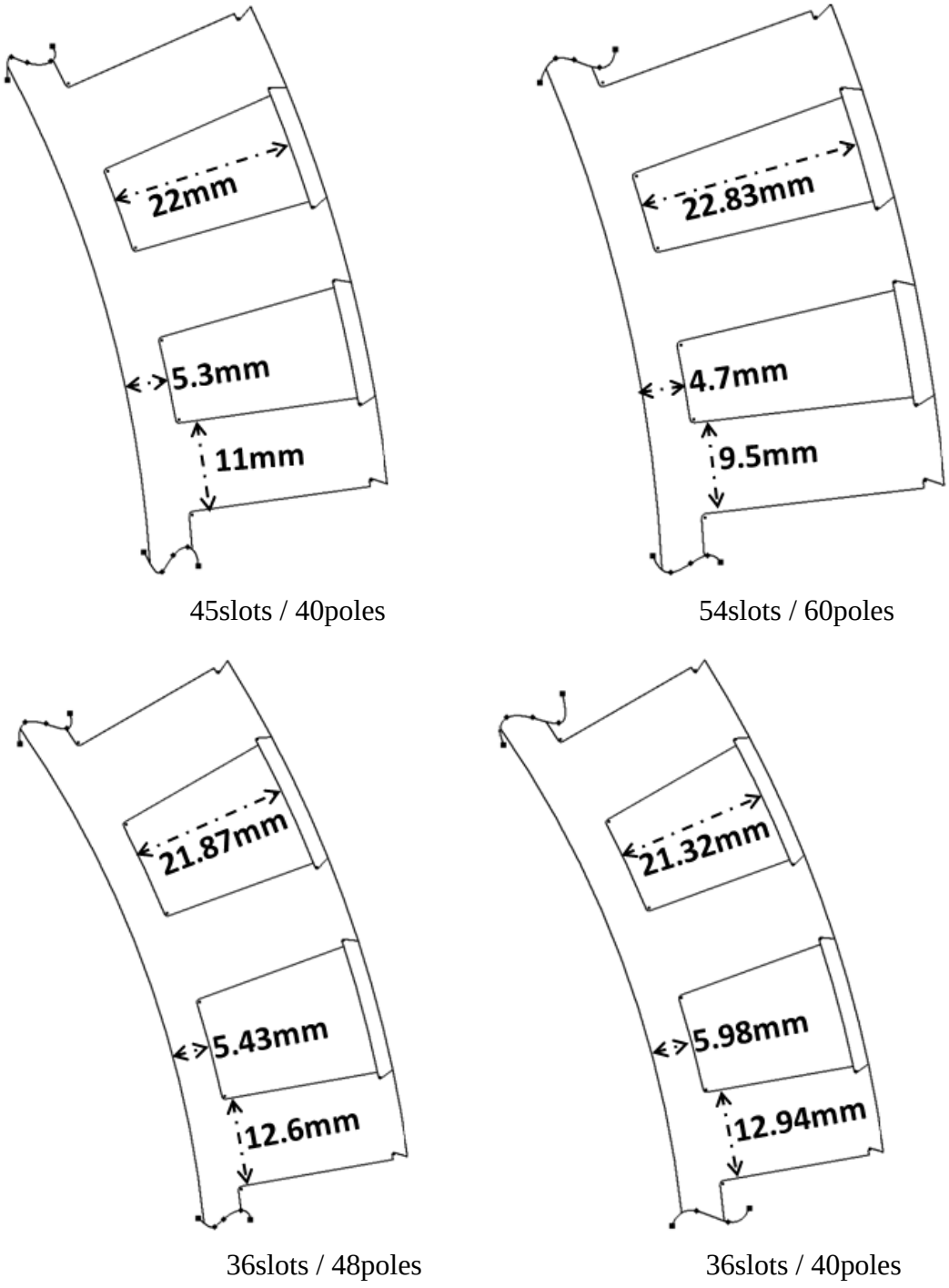

Figure B 1. Geometrical dimensions for slot and pole combinations optimised for a given slot loss.

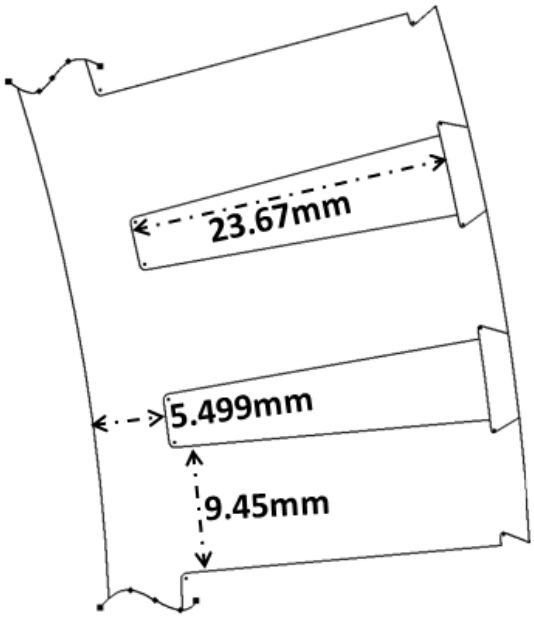

72slots / 60poles

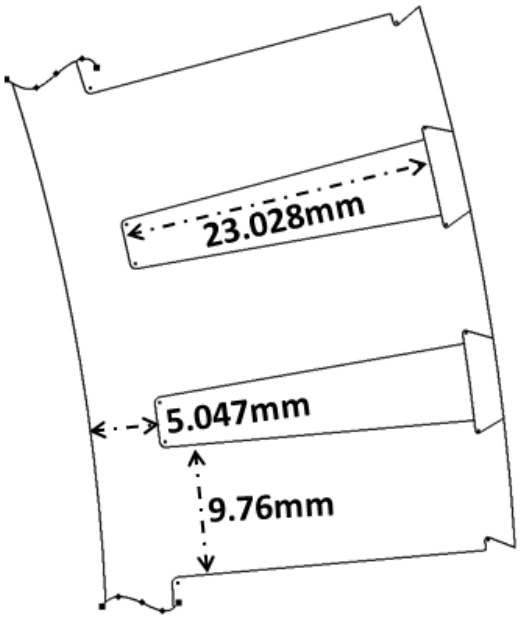

72slots / 48poles

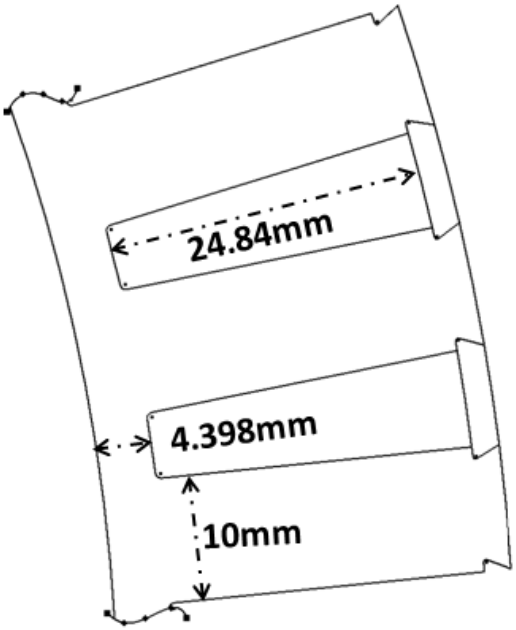

63slots / 56poles

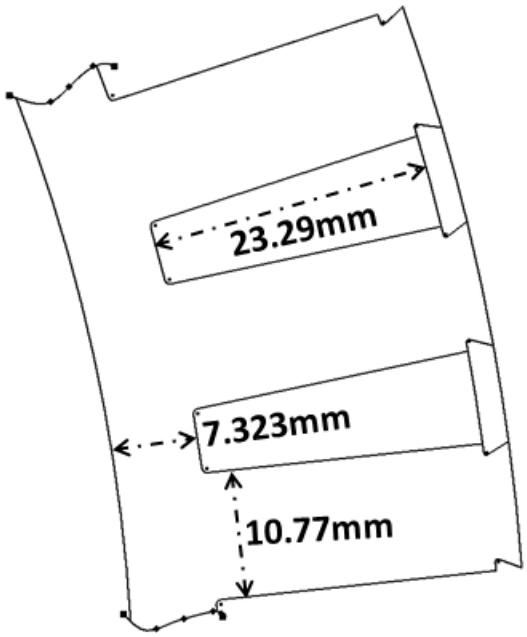

60slots / 56poles

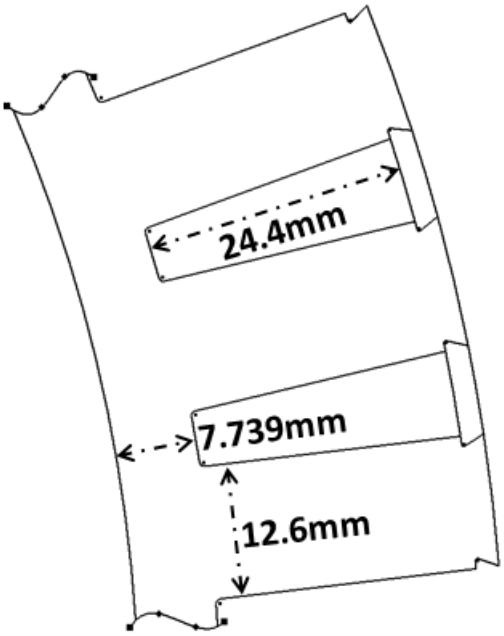

54slots / 48poles

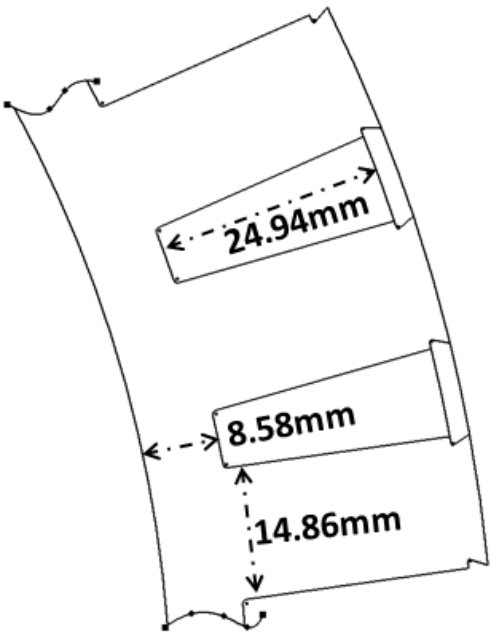

45slots / 40poles

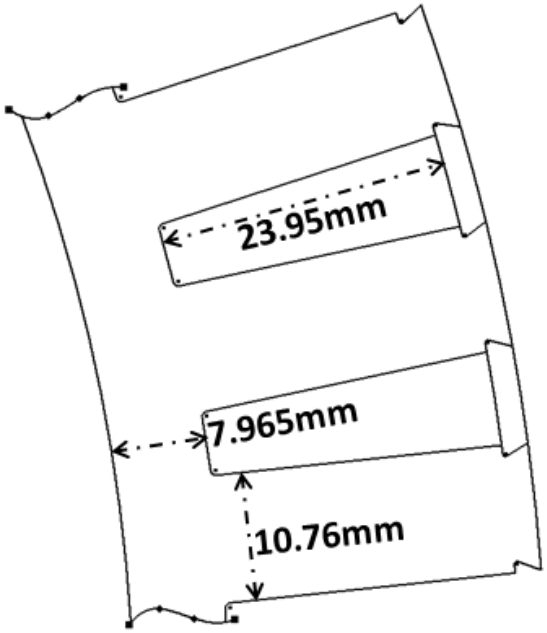

60slots / 64poles

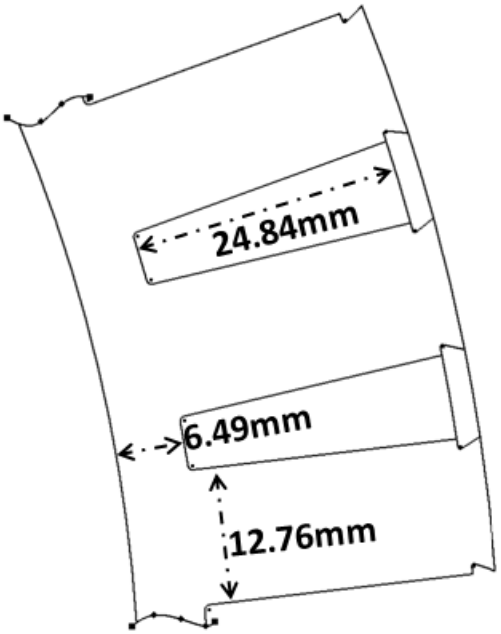

54slots / 60poles

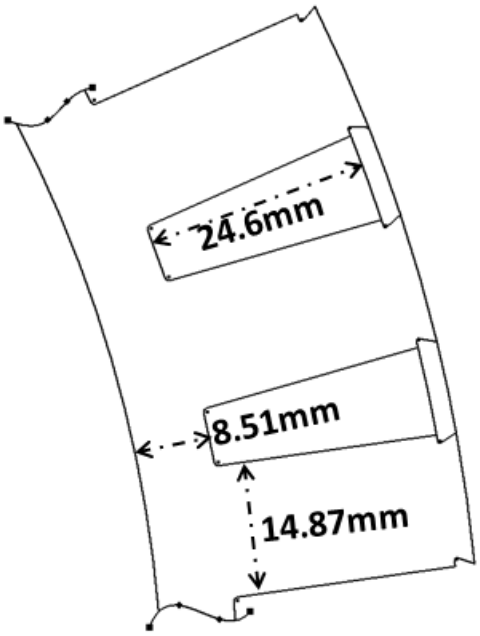

45slots / 50poles

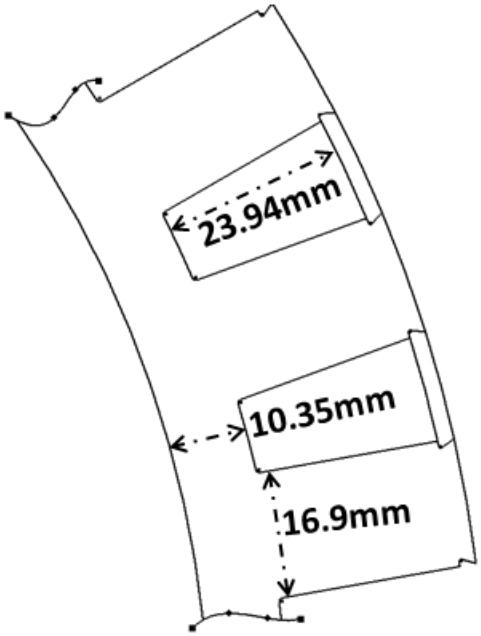

36slots / 48poles

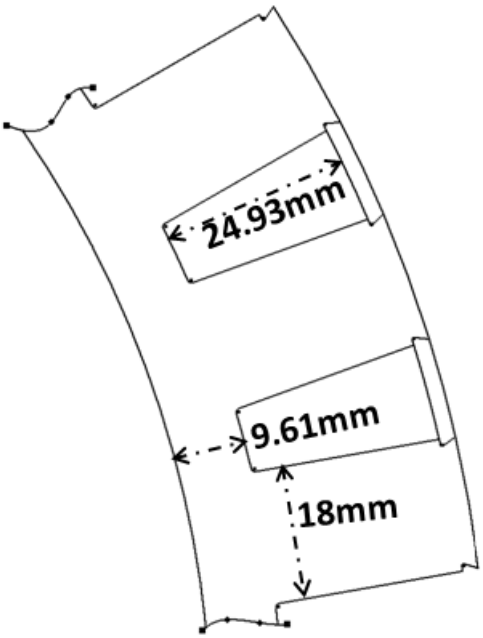

36slots / 40poles

Figure B 2. Geometrical dimensions for slot and pole combinations optimised for a given peak slot temperature.

Appendix C

Pressing Tools and Prototype Machine Drawing

Table C 1. Rotor parameters for prototype machine.

Rotor outer diameter (mm)	386
Rotor inner diameter (mm)	364
Rotor Stack (mm)	61.4
Pole	64
Pole arc (mm)	16.6
Pole span (deg)	167.23
Magnet depth (mm)	5

Table C 2. Stator parameters for prototype machine and Protean MHV.

	Prototype	Protean MHV
Stator inner diameter (mm)	302	302
Stator outer diameter (mm)	362	362
Tooth width (mm)	7.6 (parallel tooth)	6.684, 8.665 (parallel slot)
Slot depth (mm)	23	22.7
Tooth tip span (mm)	7.6	10.795
Stack length (mm)	58.3	58.8
Core-back (mm)	4.3	4.7
Conductor Diameter (mm)	1.4	1.25

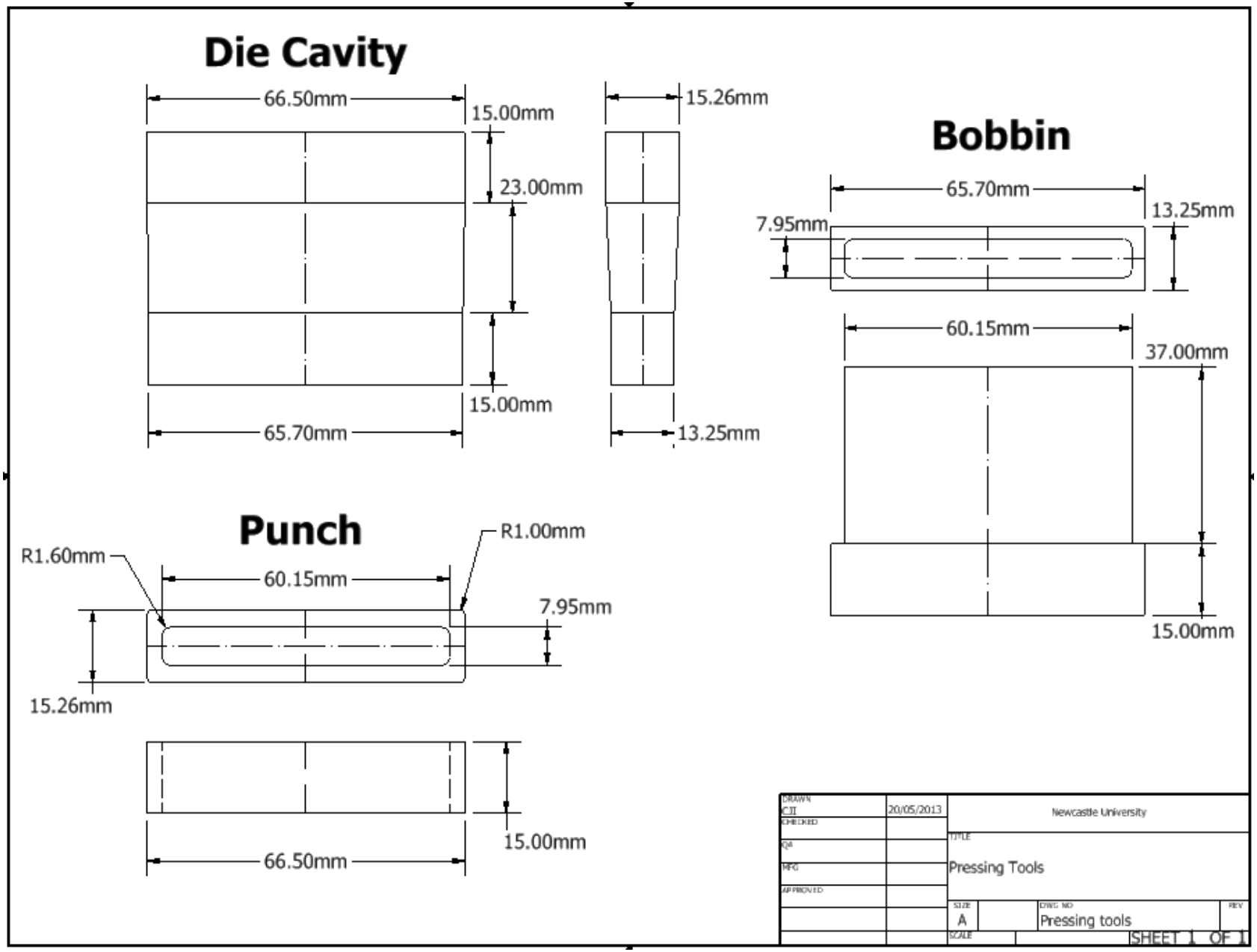
Die Cavity
66.50mm
15.00mm
23.00mm
15.00mm
65.70mm
15.26mm
13.25mm
Bobbin
65.70mm
13.25mm
7.95mm
60.15mm
37.00mm
15.00mm
Punch
R1.60mm
R1.00mm
60.15mm
7.95mm
15.26mm
15.00mm
66.50mm
DRAWN
CJI
20/05/2013
CHECKED
QA
MFG
APPROVED
Newcastle University
TITLE
Pressing Tools
SIZE
A
DWG NO
Pressing tools
REV
SCALE
SHEET 1 OF 1

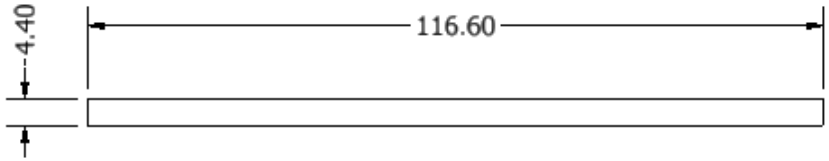

Side View (2:1)

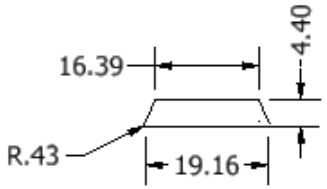

Front View (2:1)

DRAWN CJI	20/05/2013	Newcastle University	
CHECKED			
QA		TITLE	
MFG		Slot wedge	
APPROVED			
		SIZE A	DWG NO Slot wegde REV
		SCALE	SHEET 1 OF 1

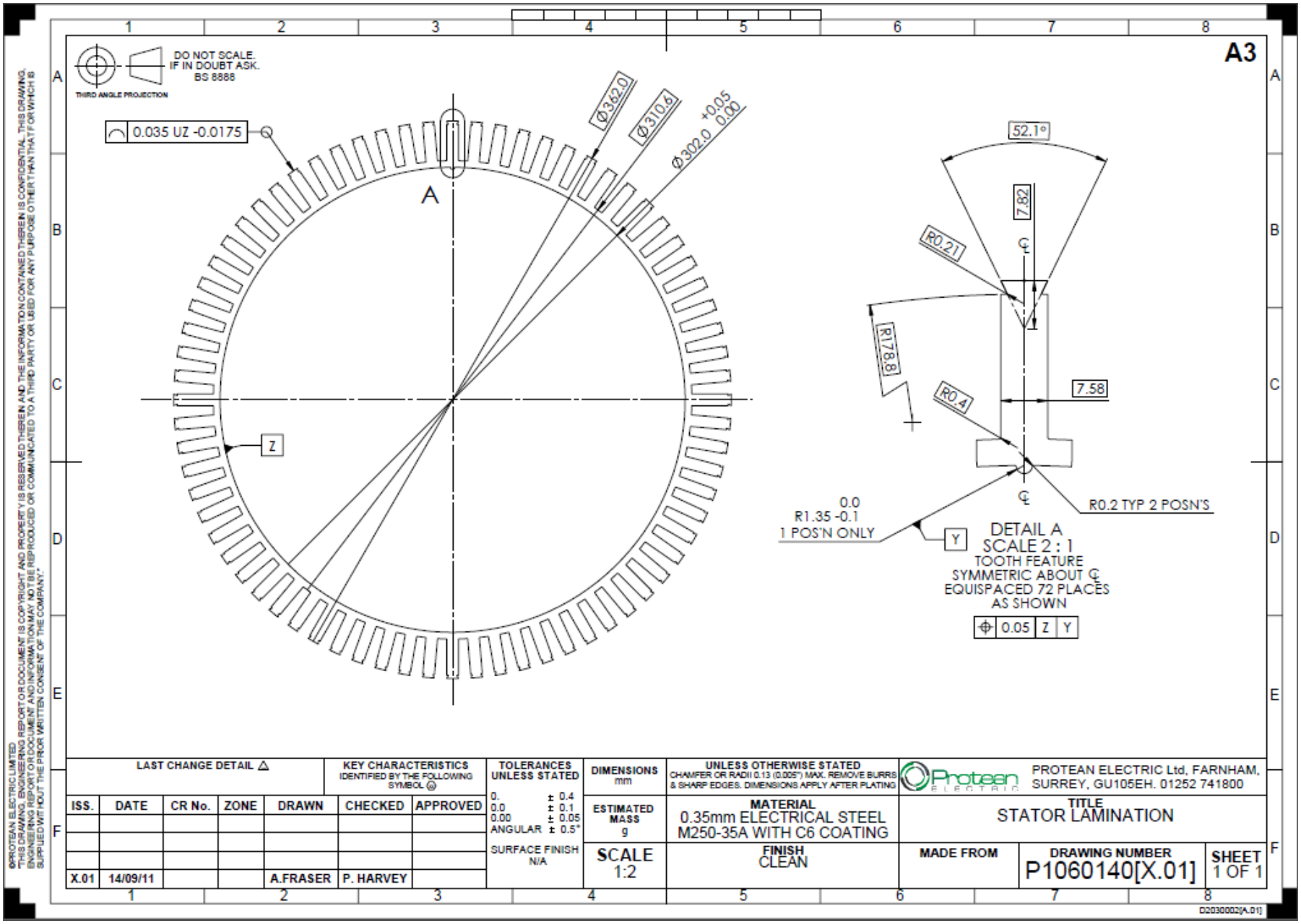
A3
DO NOT SCALE.
IF IN DOUBT ASK.
BS 8888
THIRD ANGLE PROJECTION
0.035 UZ -0.0175
Ø362.0
Ø310.6
Ø302.0 +0.05 0.00
A
Z
52.1°
7.82
R0.21
R178.8
R0.4
7.58
R0.2 TYP 2 POSN'S
0.0
R1.35 -0.1
1 POS'N ONLY
Y
DETAIL A
SCALE 2 : 1
TOOTH FEATURE
SYMMETRIC ABOUT ℄
EQUISPACED 72 PLACES
AS SHOWN
0.05 Z Y
©PROTEAN ELECTRIC LIMITED
THIS DRAWING, ENGINEERING REPORT OR DOCUMENT IS COPYRIGHT AND PROPERTY IS RESERVED THEREIN AND THE INFORMATION CONTAINED THEREIN IS CONFIDENTIAL. THIS DRAWING, ENGINEERING REPORT OR DOCUMENT AND INFORMATION MAY NOT BE REPRODUCED OR COMMUNICATED TO A THIRD PARTY OR USED FOR ANY PURPOSE OTHER THAN THAT FOR WHICH IS SUPPLIED WITHOUT THE PRIOR WRITTEN CONSENT OF THE COMPANY.
LAST CHANGE DETAIL △
KEY CHARACTERISTICS IDENTIFIED BY THE FOLLOWING SYMBOL Ⓚ
ISS. | DATE | CR No. | ZONE | DRAWN | CHECKED | APPROVED
X.01 | 14/09/11 | | | A.FRASER | P. HARVEY |
TOLERANCES UNLESS STATED
0. ± 0.4
0.0 ± 0.1
0.00 ± 0.05
ANGULAR ± 0.5°
SURFACE FINISH N/A
DIMENSIONS mm
ESTIMATED MASS g
SCALE 1:2
UNLESS OTHERWISE STATED CHAMFER OR RADII 0.13 (0.005") MAX. REMOVE BURRS & SHARP EDGES. DIMENSIONS APPLY AFTER PLATING
MATERIAL 0.35mm ELECTRICAL STEEL M250-35A WITH C6 COATING
FINISH CLEAN
MADE FROM
PROTEAN ELECTRIC Ltd, FARNHAM, SURREY, GU105EH. 01252 741800
TITLE STATOR LAMINATION
DRAWING NUMBER P1060140[X.01]
SHEET 1 OF 1
D2030002[A.01]

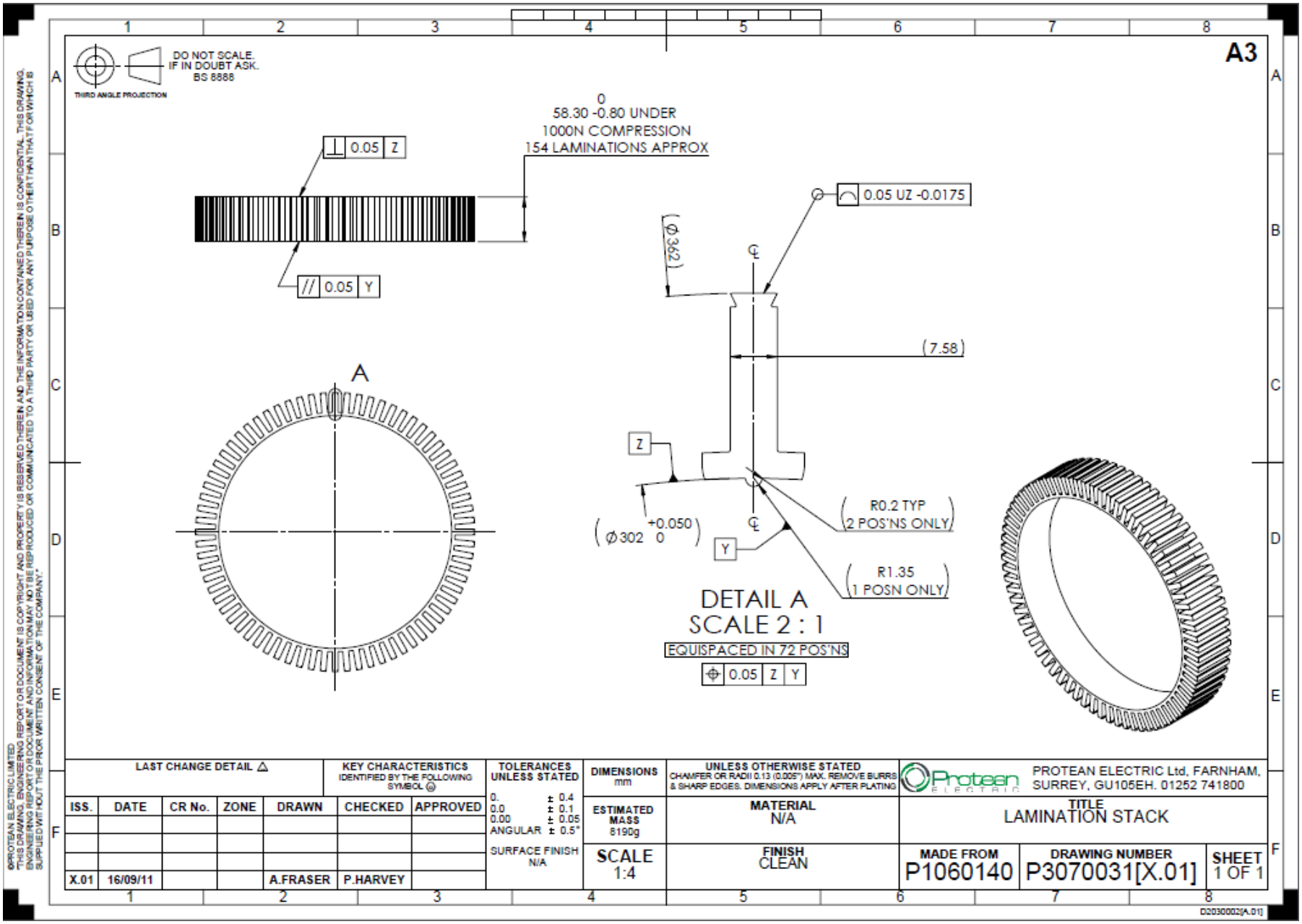
A3
DO NOT SCALE.
IF IN DOUBT ASK.
BS 8888
THIRD ANGLE PROJECTION
0
58.30 -0.80 UNDER
1000N COMPRESSION
154 LAMINATIONS APPROX
0.05 Z
0.05 Y
0.05 UZ -0.0175
Ø362
7.58
A
Z
Y
+0.050
Ø302 0
R0.2 TYP
2 POS'NS ONLY
R1.35
1 POSN ONLY
DETAIL A
SCALE 2 : 1
EQUISPACED IN 72 POS'NS
0.05 Z Y
©PROTEAN ELECTRIC LIMITED
THIS DRAWING, REPORT OR DOCUMENT IS COPYRIGHT AND PROPERTY IS RESERVED THEREIN AND THE INFORMATION CONTAINED THEREIN IS CONFIDENTIAL. THIS DRAWING, REPORT OR DOCUMENT AND INFORMATION MAY NOT BE REPRODUCED OR COMMUNICATED TO A THIRD PARTY OR USED FOR ANY PURPOSE OTHER THAN THAT FOR WHICH IS SUPPLIED WITHOUT THE PRIOR WRITTEN CONSENT OF THE COMPANY.
LAST CHANGE DETAIL
KEY CHARACTERISTICS IDENTIFIED BY THE FOLLOWING SYMBOL
ISS. DATE CR No. ZONE DRAWN CHECKED APPROVED
X.01 16/09/11 A.FRASER P.HARVEY
TOLERANCES UNLESS STATED
0. ± 0.4
0.0 ± 0.1
0.00 ± 0.05
ANGULAR ± 0.5°
SURFACE FINISH N/A
DIMENSIONS mm
ESTIMATED MASS 8190g
SCALE 1:4
UNLESS OTHERWISE STATED
CHAMFER OR RADII 0.13 (0.005") MAX. REMOVE BURRS & SHARP EDGES. DIMENSIONS APPLY AFTER PLATING
MATERIAL N/A
FINISH CLEAN
PROTEAN ELECTRIC Ltd, FARNHAM, SURREY, GU105EH. 01252 741800
TITLE
LAMINATION STACK
MADE FROM P1060140
DRAWING NUMBER P3070031[X.01]
SHEET 1 OF 1
D2030002[A.01]

Appendix D

Prototype Machine

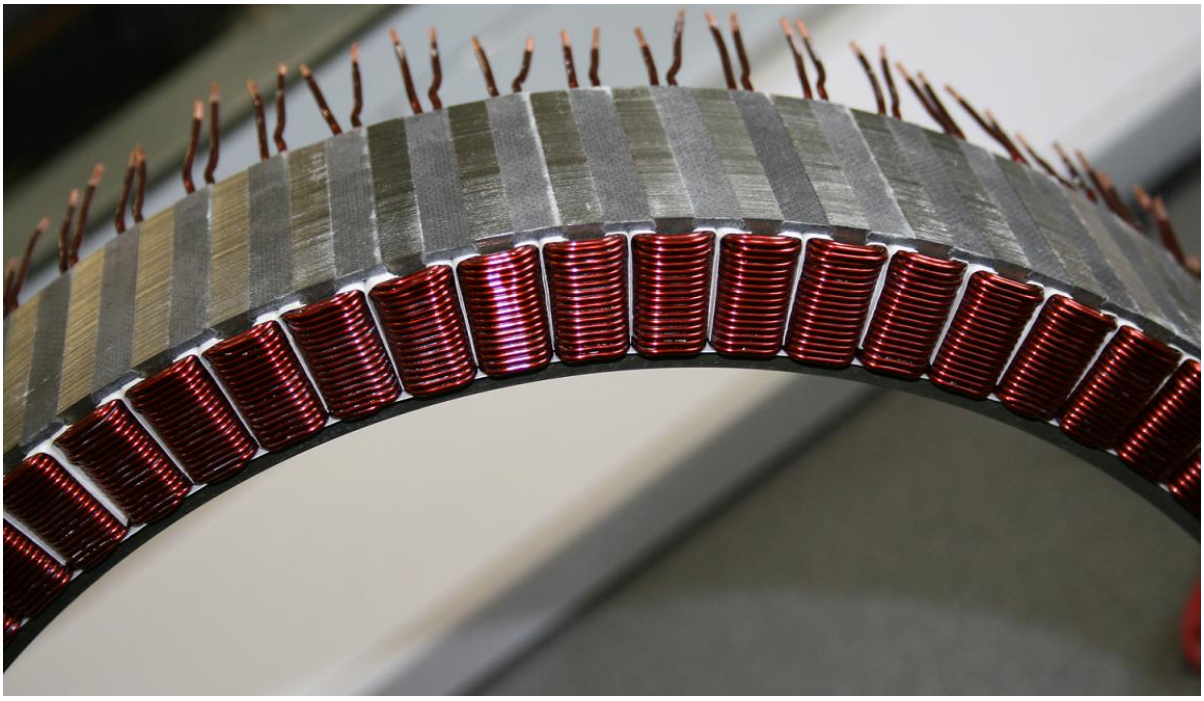

Figure D 1. Section of stator stack showing placement of coils and wedges.

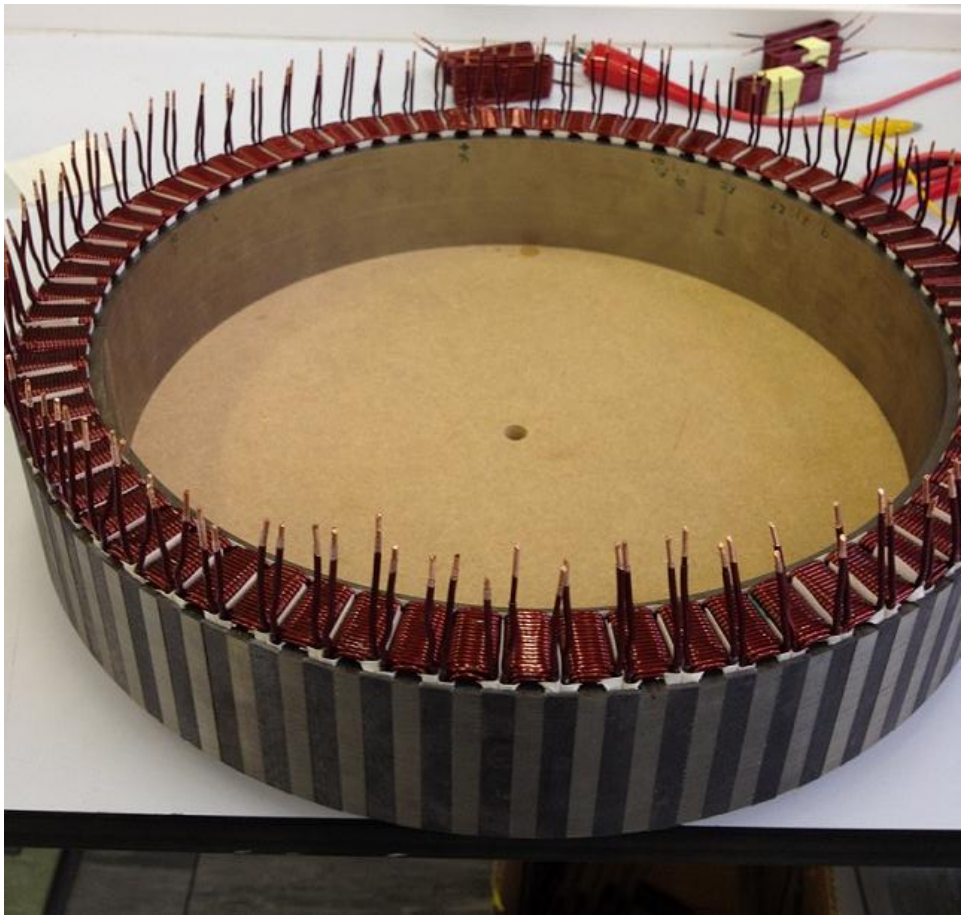

Figure D 2. Complete stator stack, with all coils mounted.

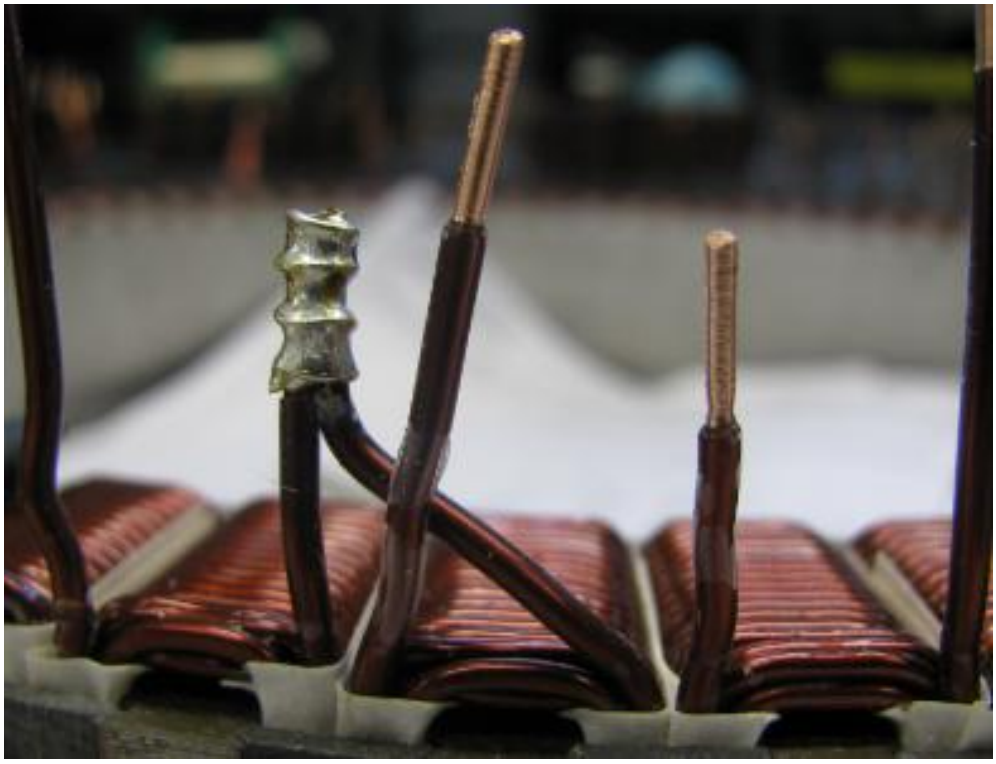

Figure D 3. Method used for coil inter-connection.

Figure D 4. Coil and phase inductance and resistance measurement.

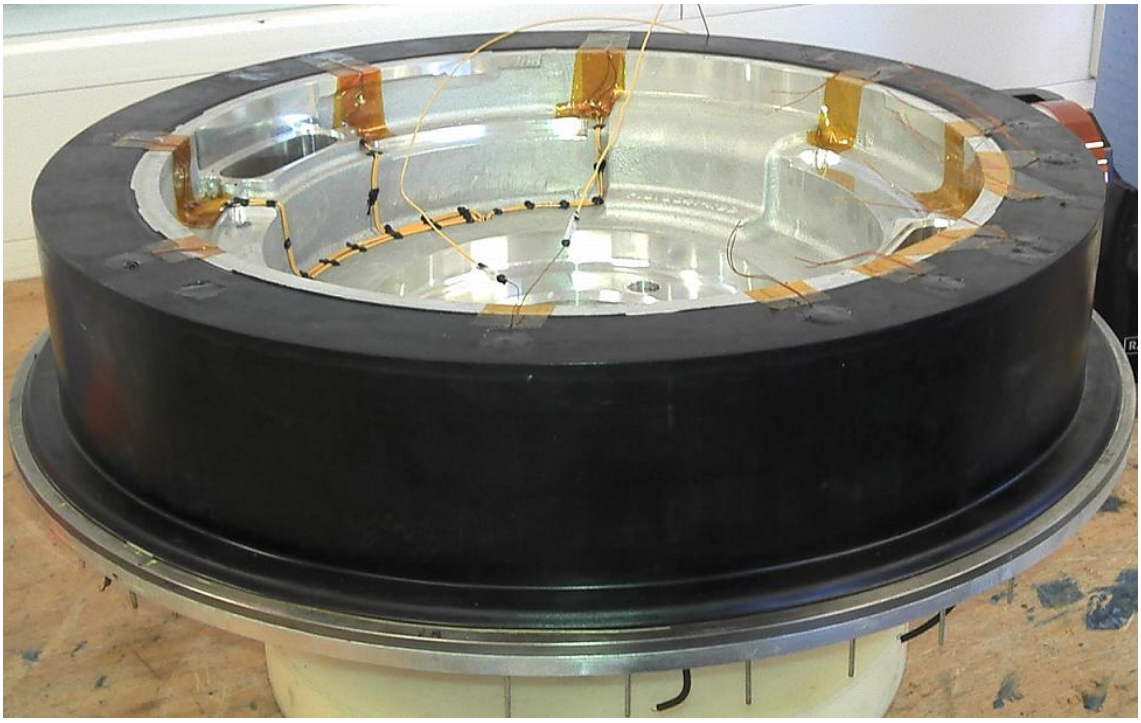

Figure D 5. Stator sealed in its case.

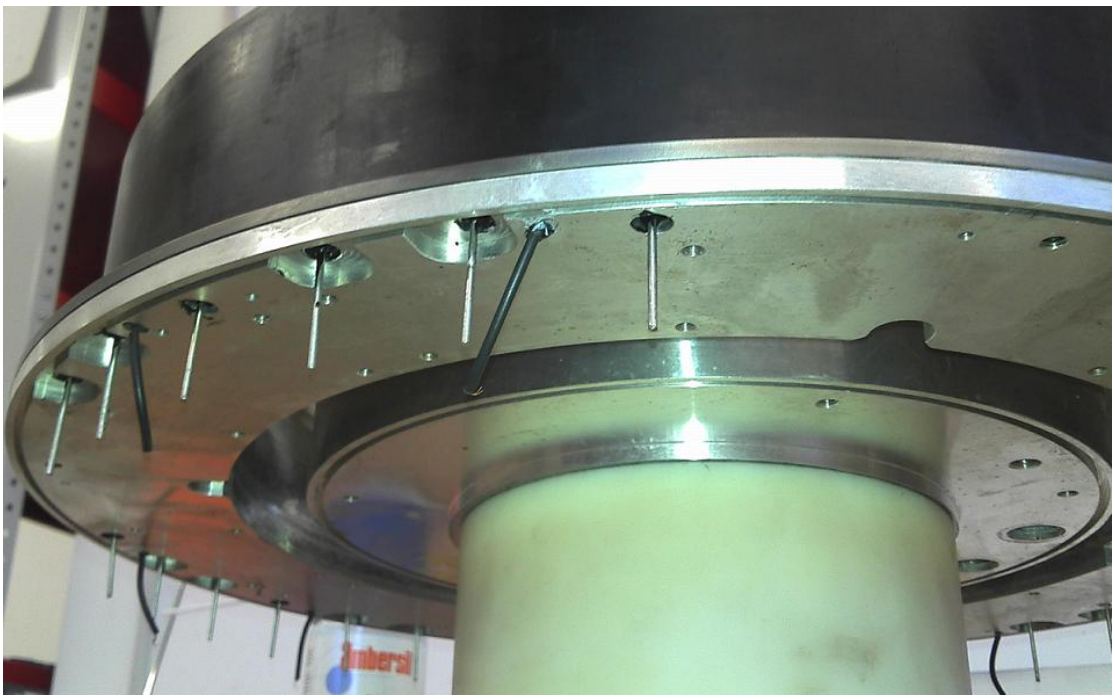

Figure D 6. Seal stator, showing connection pins.